

Chaotic optical communications using delayed feedback systems

A Thesis
Presented to
The Academic Faculty

by

Alexandre Locquet

In Partial Fulfillment
of the Requirements for the Degree
Doctor of Philosophy

School of Electrical and Computer Engineering
Georgia Institute of Technology
May 2006

Chaotic optical communications using delayed feedback systems

Approved by:

William T. Rhodes, Committee Chair
School of ECE
Georgia Institute of technology

Bertrand P. Boussert
School of ECE
Georgia Institute of Technology

David S. Citrin, Advisor
School of ECE
Georgia Institute of Technology

Yves H. Berthelot
School of Mechanical Engineering
Georgia Institute of Technology

Douglas B. William
School of ECE
Georgia Institute of Technology

Date Approved: November 11, 2005

To my loved ones

ACKNOWLEDGEMENTS

I am grateful to Jean-Pierre Goedgebuer, François Malassenet, and Hans Puttgen for having helped me to get into the double PhD program between Georgia Tech and the Université de Franche-Comté. I thank Laurent Larger for having advised my research after the departure of Jean-Pierre Goedgebuer. I have been very lucky that David Citrin agreed to be my Georgia Tech advisor. I thank him sincerely for his help, kindness and wisdom. I am also grateful to the students, staff, researchers, and faculty of the research labs in Metz and Atlanta, to have helped me, in one way or another, to obtain the two PhDs. In particular, I would like to thank warmly Michele Jamrozik, who has always found time for me despite her numerous professional and family obligations. I have been lucky to be involved in interesting collaborations over the years. I am thankful to Vladimir Udaltsov, Silvia Ortin, and Luis Pesquera for their help in the field of multiple-delay systems. I am grateful to Cristina Masoller, Claudio Mirasso, Marc Sciamanna, Ignace Gatare, Fabien Rogister, Patrice Mégret, and Michel Blondel for their help in the field of the synchronization of edge-emitting and vertical-cavity surface-emitting lasers. Finally, I would like to thank the proposal and defense committee members: Steve McLaughlin, Bill Rhodes, Doug Williams, Bertrand Boussert, and Yves Berthelot.

TABLE OF CONTENTS

DEDICATION	iii
ACKNOWLEDGEMENTS	iv
LIST OF FIGURES	viii
SUMMARY	xvii
I INTRODUCTION	1
1.1 Introduction	1
II CHAOS	3
2.1 Introduction	3
2.2 Basic notions about dynamical systems	4
2.3 Delay systems	9
2.4 Chaos in lasers	10
2.4.1 Arecchi's classification	10
2.4.2 Different ways to make a semiconductor laser chaotic	11
2.4.3 Optoelectronic system producing chaos in wavelength	14
2.5 Lyapunov Spectrum, Dimension, and Entropy	16
2.5.1 Definition of the Lyapunov exponents	17
2.5.2 Calculation of the Lyapunov spectrum of non-delay systems when the model is known	21
2.5.3 Dimension and Entropy	25
2.6 Basics of time series analysis	27
2.6.1 Phase-space reconstruction	27
2.6.2 Computation of Lyapunov exponents from time series of non-delay systems	29
2.7 Chaos synchronization	31
2.8 Chaotic communications	33
2.8.1 Chaotic Masking	33
2.8.2 Chaos shift keying	34
2.8.3 Chaotic Modulation	35
2.9 Experimental realizations of chaotic communications	36

2.10	Security aspects	38
III	SYNCHRONIZATION OF UNIDIRECTIONALLY COUPLED EXTERNAL-CAVITY SEMICONDUCTOR LASERS	41
3.1	Introduction	41
3.2	Synchronization of external-cavity edge-emitting semiconductor lasers . . .	42
3.2.1	Semiconductor lasers and rate equations	42
3.2.2	External-cavity semiconductor lasers	46
3.2.3	Unidirectionally coupled external-cavity lasers	51
3.2.4	Time lagged synchronous solutions	54
3.2.5	Synchronization regions	56
3.2.6	Transitions between synchronization regimes	62
3.2.7	Summary	71
3.3	Synchronization of external-cavity vertical-cavity surface-emitting lasers .	73
3.3.1	Introduction	73
3.3.2	Vertical-cavity surface-emitting lasers	74
3.3.3	The Spin-Flip Model and polarization dynamics	76
3.3.4	External-cavity vertical-cavity surface-emitting lasers	83
3.3.5	Synchronization regimes	91
3.3.6	Polarization encoding	112
3.3.7	Summary	116
IV	ANALYSIS OF TIME SERIES PRODUCED BY CHAOTIC DELAY SYSTEMS	118
4.1	Introduction	118
4.2	Principles of the analysis of time series produced by delay systems	119
4.2.1	Scalar delay systems	120
4.2.2	Vectorial delay systems	123
4.3	Estimation of the Lyapunov spectrum of a delay system	125
4.3.1	From the time series	125
4.3.2	From the model – Farmer’s method	127
4.4	Delay identification	128
4.4.1	Identification Techniques	129

4.4.2	Mackey-Glass system	131
4.4.3	Optoelectronic system producing wavelength chaos	137
4.4.4	Optoelectronic system producing chaos in intensity	149
4.4.5	Electronic system producing frequency chaos	152
4.5	Identification of the nonlinear function	154
4.6	Computation of the Lyapunov spectrum, of dimension, and of entropy . .	157
4.6.1	Mackey-Glass system	159
4.6.2	Optoelectronic system producing wavelength chaos	163
4.7	Conclusion	174
V	IDENTIFICATION OF THE DELAY TIMES IN SINGLE- AND MULTIPLE- DELAY SYSTEMS	176
5.1	Motivations	176
5.2	One-delay cryptosystems	177
5.3	Two-delay cryptosystems	184
5.3.1	Delay system subjected to two delays: first configuration	184
5.3.2	Semiconductor laser subjected to two optical feedbacks	187
5.3.3	Delay system subjected to two delays: second configuration	189
5.4	Conclusion and perspectives	200
VI	CONCLUSION	201
	Appendix	206
	APPENDIX A — NEIGHBOR SEARCHING TECHNIQUES	206
	REFERENCES	209

LIST OF FIGURES

1	Bloc diagram of the chaotic delay emitters used at the GTL CNRS Telecom laboratory.	10
2	External-cavity semiconductor laser diode.	13
3	Semiconductor laser subjected to incoherent optical feedback. The arrows represent the direction of linear polarization.	13
4	Optoelectronic system generating wavelength chaos.	15
5	Evolution of a unitary disk under the jacobian of $\vec{\phi}^n$	19
6	Two unidirectionally coupled oscillators.	32
7	Chaotic masking.	34
8	Chaos-shift keying.	35
9	Double heterostructure Fabry-Perot edge-emitting laser.	44
10	Edge-emitting semiconductor laser subjected to external optical feedback. .	47
11	The zeros y_Z of $f(y)$ give the values of $\omega_{Stat}\tau$	50
12	Schematic representation of unidirectionally coupled external-cavity lasers. ML: Master Laser; SL: Slave Laser; OI: Optical Isolator; BS: Beam Splitter; M: Mirror.	53
13	Intensity fluctuations of the ML operating on the coherence collapse regime. The parameters are: $\gamma_m = 10 \text{ ns}^{-1}$, $J_m = 1.85 \times J_{th} = 27.2 \text{ mA}$, $\tau = 1 \text{ ns}$, $\tau_p = 2 \text{ ps}$, $\tau_n = 2 \text{ ns}$, $\alpha = 5$, $G_n = 1.5 \times 10^4 \text{ s}^{-1}$, $N_0 = 1.5 \times 10^8$, $\epsilon = 5 \times 10^{-7}$, $\omega\tau = 0 \text{ rad}$	57
14	(a) Correlation coefficient C_1 as a function of the frequency detuning and the optical coupling strength, when the slave is an external cavity laser subjected to chaotic injection from the master laser. $\gamma_m = \gamma_s = 10 \text{ ns}^{-1}$. (b) Correlation coefficient C_1 as a function of the frequency detuning and the optical coupling strength, when the slave is an external cavity laser subjected to CW injection from the master laser. $\gamma_s = 10 \text{ ns}^{-1}$. All other parameters as Fig. 13.	58
15	(a) Correlation coefficient C_1 as a function of the frequency detuning and the optical coupling strength, when the slave laser is subjected only to chaotic injection from the master laser. $\gamma_m = 10 \text{ ns}^{-1}$, $\gamma_s = 0$. (b) Correlation coefficient C_1 as a function of the frequency detuning and the optical coupling strength, when the slave laser is subjected only to CW injection from the master laser. $\gamma_s = 0 \text{ ns}^{-1}$. (c) Correlation coefficient C_2 as a function of the frequency detuning and the optical coupling strength, when the slave laser is subjected only to chaotic injection from the master laser. All other parameters as Fig. 13.	59

16	Correlation coefficient C_1 as a function of the difference between the phase accumulations in the external cavities of the slave laser, $(\omega\tau)_s$, and of the master laser, $(\omega\tau)_m$. $\Delta\omega=0$, $\eta = 25 \text{ ns}^{-1}$, all other parameters as Fig. 13.	60
17	Correlation coefficient C_2 as a function of the frequency detuning and the optical coupling strength, when $\gamma_s = \gamma_m - \eta$. All other parameters as Fig. 15.	61
18	Synchronization regions in the parameter space (master feedback rate, optical coupling rate). (a) $\gamma_s = \gamma_m$, the value of C_1 is plotted. (b) $\gamma_s = 0$, the value of C_1 is plotted. (c) $\gamma_s = \gamma_m - \eta$, the value of C_2 is plotted. $\Delta\omega = 0$, all other parameters as Fig. 15.	63
19	Correlation coefficients C_1 (a), C_2 (b) as a function of the frequency detuning and the optical coupling strength. $\gamma_m = 10 \text{ ns}^{-1}$, $\gamma_s = 0$, $J_m = J_s = 1.02 = J_{th} = 15 \text{ mA}$. All other parameters as Fig. 15.	64
20	Time traces of the time-averaged intensities. (a) Intensity of the master laser (lagged τ_c in time) for $\gamma_m = 10 \text{ ns}^{-1}$. Intensity of the slave laser for (b) $\eta = \gamma_m$; (c) $\eta = 12 \text{ ns}^{-1}$; (d) $\eta = 9 \text{ ns}^{-1}$. $\Delta\omega = 0$, all other parameters as Fig. 15.	66
21	Time traces of the time-averaged intensities. (a) Intensity of the master laser (lagged τ_c in time) for $\gamma_m = 10 \text{ ns}^{-1}$ and $\tau_{n,m} = 2 \text{ ns}$. Intensity of the slave laser for (b) $\eta = \gamma_m$, $\tau_{n,s} = \tau_{n,m}$; (c) $\eta = \gamma_m$, $\tau_{n,s} = 1.99 \text{ ns}$; (d) $\eta = \gamma_m$, $\tau_{n,s} = 2.01 \text{ ns}$; (e) $\eta = 13 \text{ ns}^{-1}$, $\tau_{n,s} = 2.01 \text{ ns}$. $\Delta\omega = 0$, all other parameters as in Fig. 15.	68
22	Correlation coefficient as a function of the lag-time (as explained in the text). Figs. (a), (b), (c), and (d) are for the same parameters as in Figs. 21 (b), (c), (d), and (e) respectively.	69
23	Synchronization regions in the parameter space (injection current, optical coupling rate). (a) The value of C_1 is plotted. The white line corresponds to the threshold injection rate above which C_1 is larger than 0.95. For $1.15j_{th} < j < 1.4j_{th}$ approximately, the threshold injection rate is larger than 10 ns^{-1} (b) The value of C_2 is plotted. $\Delta\omega = 0$, $\gamma_s = 0$, all other parameters as Fig. 15.	71
24	Vertical-cavity surface-emitting laser.	75
25	Sketch of a four-level model of a quantum-well VCSEL.	76
26	Light-current characteristics of each linearly-polarized component of the electric field (circles: y-polarized, squares: x-polarized). The powers are averaged over 20 ns. The parameters are: $\kappa = 300 \text{ ns}^{-1}$, $\gamma_N = 1 \text{ ns}^{-1}$, $\alpha = 3$, $\gamma_S = 50 \text{ ns}^{-1}$, $\gamma_p = 10 \text{ ns}^{-1}$, and $\gamma_a = 0.1 \text{ ns}^{-1}$.	81
27	Intensities of the x- and y-polarized components of the electric field. (a) $\mu = 1.6$, (b) $\mu = 1.64$, (c) $\mu = 1.68$, (d) $\mu = 1.8$. All the other parameters are the same as in Fig. 26.	81

28	Poincaré sphere representation of the polarization state of light. (a) $\mu = 6$, (b) $\mu = 1.64$, (c) $\mu = 1.68$, (d) $\mu = 1.8$. All the other parameters are the same as in Fig. 26.	82
29	Intensities of the x - and y -polarized components of the electric field of the solitary VCSEL. The parameters of the SFM model are $\mu = 1.5$, $\kappa = 300 \text{ ns}^{-1}$, $\gamma_N = 1 \text{ ns}^{-1}$, $\alpha = 3$, $\gamma_S = 50 \text{ ns}^{-1}$, $\gamma_p = 30 \text{ ns}^{-1}$, and $\gamma_a = 0.5 \text{ ns}^{-1}$. . .	85
30	Intensities of the x - and y -polarized components of the electric field of the external-cavity VCSEL, for a feedback rate $f = 1.4 \text{ GHz}$, a delay $\tau = 3 \text{ ns}$, and a feedback phase $\omega\tau = 6 \text{ rad}$. All other parameters are as in Fig 29. . .	86
31	Carrier number N and n for a feedback rate $f = 1.4 \text{ GHz}$. All parameters are as in Fig 29.	86
32	Intensities of the x - and y -polarized components of the electric field of the external-cavity VCSEL, for a feedback rate $f = 5 \text{ GHz}$. All parameters are as in Fig 29.	87
33	Intensities of the x - and y -polarized components of the electric field of the external-cavity VCSEL, for a feedback rate $f = 30 \text{ GHz}$. All parameters are as in Fig 29.	88
34	Filtered intensities of the x - and y -polarized components of the electric field of the external-cavity VCSEL, for a feedback rate $f = 30 \text{ GHz}$. All parameters are as in Fig 29. A second-order Butterworth filter of 0.1 GHz cutoff frequency is used.	88
35	Intensities of the x - and y -polarized components of the electric field of the external-cavity VCSEL, for a feedback rate $f = 40 \text{ GHz}$. All parameters are as in Fig. 29.	89
36	Total intensity emitted by the external-cavity VCSEL, for a feedback rate $f = 40 \text{ GHz}$. All parameters are as in Fig. 29.	90
37	Filtered intensities of the x - and y -polarized components of the electric field of the external-cavity VCSEL, for a feedback rate $f = 40 \text{ GHz}$. All parameters are as in Fig 29. A second-order Butterworth filter of 0.1 GHz cutoff frequency is used.	90
38	(a) Intensities of the x - and y -polarized components of the master electric field. (b) Intensities of the x - and y -polarized components of the slave. (c) Difference between the synchronized intensities showing anticipating synchronization. Master isotropic feedback rate $f^m = 40 \text{ GHz}$, slave feedback rate $f^s = 0$ (open-loop), injection rate $\eta = 40 \text{ GHz}$. All other parameters are as in Fig. 29.	95
39	Synchronization diagrams for the intensities of the x - and y - polarized components of the electric field, revealing anticipating synchronization. Master isotropic feedback rate $f^m = 40 \text{ GHz}$, slave feedback rate $f^s = 0$ (open-loop), injection rate $\eta = 40 \text{ GHz}$. All other parameters are as in Fig. 29.	95

40	(a) Master carrier number n and (b) synchronized slave carrier number. Master isotropic feedback rate $f^m = 40$ GHz, slave feedback rate $f^s = 0$ (open-loop), injection rate $\eta = 40$ GHz. All other parameters are as in Fig. 29. . .	96
41	Synchronization diagrams for the intensities of the x and y polarized components of the electric field, revealing isochronous synchronization. The correlation coefficients are $C_{1x} = 0.994$ and $C_{1y} = 0.988$. Master isotropic feedback rate $f^m = 40$ GHz, slave feedback rate $f^s = 40$ GHz, injection rate $\eta = 200$ GHz. All other parameters are as in Fig. 29.	97
42	Correlations coefficients C_{1x} (circles) and C_{2x} (crosses) for the synchronization of the x -polarized components of the electric field. Slave feedback rate $f^s = 0$ GHz, injection rate $\eta_x = \eta_y = f^m$. All other parameters are as in Fig. 29.	99
43	(a) Intensity of the x -polarized component of the electric field injected into the slave laser at a time t . (b) Intensity of the x -polarized component of the electric field that will be injected into the slave laser at a time $t + \tau$. (c) Intensity emitted by the x -polarized component of the electric field emitted by the slave at time t . Master isotropic feedback rate $f^m = 30$ GHz, slave feedback rate $f^s = 0$ GHz, injection rate $\eta = 30$ GHz. All other parameters are as in Fig. 29.	100
44	(a) Intensities of the x - and y -polarized components of the master electric field. (b) Intensities of the x - and y -polarized components of the slave. (c) Difference between the intensities. Master isotropic feedback rate $f^m = 40$ GHz, slave feedback rate $f^s = 0$ (open-loop), injection rates $\eta_x = 40$ GHz and $\eta_y = 0$. All other parameters are as in Fig. 29.	103
45	(a) Intensities of the x - and y -polarized components of the master electric field. (b) Intensities of the x - and y -polarized components of the slave. (c) Difference between the intensities. The correlation coefficient between the x -polarized components is 0.996. Injection currents $\mu^m = \mu^s = 2.5$, master isotropic feedback rate $f^m = 25$ GHz, slave feedback rate $f^s = 25$ GHz (open-loop), injection rates $\eta_x = 100$ GHz and $\eta_y = 100$ GHz. All other parameters are as in Fig. 29.	104
46	(a) Intensities of the x - and y -polarized components of the master electric field. (b) Intensities of the x - and y -polarized components of the slave. (c) Difference between the intensities. The correlation coefficient between the x -polarized components is 0.980. Injection currents $\mu^m = \mu^s = 2.5$, master isotropic feedback rate $f^m = 25$ GHz, slave feedback rate $f^s = 25$ GHz (open-loop), injection rates $\eta_x = 100$ GHz and $\eta_y = 0$. All other parameters are as in Fig. 29.	105

47	(a) Intensities of the x - and y -polarized components of the electric field of the solitary slave ($\eta_y = 0$). (b) Intensities of the x - and y -polarized components of the slave when subjected to strong orthogonal injection ($\eta_y = 50$ GHz). (c) Intensity of the injected field, $I_{inj}(t)$, which is the x -polarized output of the master, rotated to y -polarization. The correlation coefficient between $I_y^s(t)$ and $I_{inj}(t)$ is 0.984. Master isotropic feedback rate $f^m = 1.3$ GHz, slave feedback rate $f^s = 0$ GHz (open-loop), injection rates $\eta_y = 0$ GHz (a) or 50 GHz (b), and $\eta_x = 0$. All other parameters are as in Fig. 29.	107
48	Correlation coefficient between the intensity of the injected field and the intensity of the x -polarized component of the slave field (parallel injection) or of the y -polarized component of the slave field (orthogonal injection). The master feedback rate f^m is varied from 0.5 GHz to 50 GHz. The injection rate is of 50 GHz, and the slave feedback rate is $f^s = 0$ GHz (open-loop). All other parameters are as in Fig. 29.	109
49	(a) Intensities of the x - and y -polarized components of the electric field of the slave when subjected to orthogonal injection ($\eta_y = 5$ GHz). (b) Intensity of the injected field, $I_{inj}(t)$, which is the x -polarized output of the master, rotated to y -polarization. The correlation coefficient between $I_y^s(t)$ and $I_{inj}(t)$ is 0.70 and the correlation coefficient between $I_x^s(t)$ and $I_{inj}(t)$ is -0.59. Master isotropic feedback rate $f^m = 1.3$ GHz, slave feedback rate $f^s = 0$ GHz (open-loop), injection rates $\eta_y = 5$ GHz and $\eta_x = 0$. All other parameters are as in Fig. 29.	110
50	(a) Difference between the phases of the x - polarized components of the master and slave electric fields. (b) Information bearing signal m . Master isotropic feedback rate $f^m = 55$ GHz, slave feedback rate $f^s = 0$ GHz (open-loop), injection rates $\eta_x = 55$ GHz and $\eta_y = 55$ GHz. All other parameters are as in Fig. 29.	114
51	(a) Difference between the intensities of the x - polarized components of the master and slave electric fields. (b) Information bearing signal m . Master isotropic feedback rate $f^m = 55$ GHz, slave feedback rate $f^s = 0$ GHz (open-loop), injection rates $\eta_x = 55$ GHz and $\eta_y = 55$ GHz. All other parameters are as in Fig. 29.	115
52	(a) Master carrier number N . (b) Slave carrier number N . (c) Difference between the master and laser carrier numbers showing a period of desynchronization starting after 827 ns approximately. Master isotropic feedback rate $f^m = 55$ GHz, slave feedback rate $f^s = 0$ GHz (open-loop), injection rates $\eta_x = 55$ GHz and $\eta_y = 55$ GHz. All other parameters are as in Fig. 29. . . .	116
53	(a) Chaotic signal and (b) nonlinear function of the Mackey-Glass system. $\tau = 46$, $\tau^R = 10$, $c = 2$	132
54	Autocovariance of $x(t)$. $\tau = 46$, $\tau^R = 10$, $c = 2$, $h = 0.5$	133
55	Mutual information between $x(t)$ and $x(t - \tau^*)$. $\tau = 46$, $\tau^R = 10$, $c = 2$, $h = 0.5$	134

56	Average approximation error. $\tau = 46$, $\tau^R = 10$, $c = 2$, $h = 0.5$, $\epsilon = 1\%$, $N = 41400$ samples.	134
57	Influence of the number of samples N . $\tau = 46$, $\tau^R = 10$, $c = 2$, $h = 0.5$, $\epsilon = 1\%$	135
58	Influence of the neighborhood size ϵ . $\tau = 46$, $\tau^R = 10$, $c = 2$, $h = 0.5$, $N = 20000$	136
59	Influence of the sampling period h . $\tau = 46$, $\tau^R = 10$, $c = 2$, $\epsilon = 0.01$, $N = 20000$	137
60	Bifurcation diagram when β is varied. $\tau^R = 8.4 \mu s$, $\phi = \pi/3$, $\tau = 523 \mu s$. . .	139
61	Bifurcation diagram when β is varied. $\tau^R = 8.4 \mu s$, $\phi = \pi/3$, $\tau = 523 \mu s$. . .	139
62	Bifurcation diagram when τ is varied. $\tau^R = 8.4 \mu s$, $\phi = \pi/3$, $\beta = 8$	140
63	T_2 chaos for $\beta = 2.8$. $\tau = 523 \mu s$, $\tau^R = 8.4 \mu s$, $\phi = \pi/3$	141
64	Chaotic signal for $\beta = 3$. $\tau = 523 \mu s$, $\tau^R = 8.4 \mu s$, $\phi = \pi/3$	142
65	Fully-developed chaos for $\beta = 10$. $\tau = 523 \mu s$, $\tau^R = 8.4 \mu s$, $\phi = \pi/3$	143
66	Fully-developed chaos for $\beta = 25$. $\tau = 523 \mu s$, $\tau^R = 8.4 \mu s$, $\phi = \pi/3$	143
67	Fully-developed chaos for $\tau = 100 \mu s$. $\beta = 8$, $\tau^R = 8.4 \mu s$, $\phi = \pi/3$	144
68	Fully-developed chaos for $\tau = 523 \mu s$. $\beta = 8$, $\tau^R = 8.4 \mu s$, $\phi = \pi/3$	144
69	Fully-developed chaos for $\tau = 1000 \mu s$. $\beta = 8$, $\tau^R = 8.4 \mu s$, $\phi = \pi/3$	145
70	Influence of the number of samples N . $\beta = 7$, $\tau = 523 \mu s$, $\tau^R = 8.4 \mu s$, $\phi = \pi/3$, $h = 1 \mu s$, $\epsilon = 1\%$	146
71	Influence of the neighborhood size ϵ . $\beta = 7$, $\tau = 523 \mu s$, $\tau^R = 8.4 \mu s$, $\phi = \pi/3$, $h = 1 \mu s$, $N = 40000$	146
72	Influence of the sampling period h . $\beta = 7$, $\tau = 523 \mu s$, $\tau^R = 8.4 \mu s$, $\phi = \pi/3$, $N = 80000$, $\epsilon = 2\%$	147
73	Delay identification with and without a message. $\beta = 7$, $\tau = 523 \mu s$, $\tau^R = 8.4 \mu s$, $\phi = \pi/3$, $h = 0.5 \mu s$, $N = 80000$, $\epsilon = 2\%$	149
74	Chaos oscillator in intensity.	150
75	Delay identification. (a) Mutual information. (b) Local linear fits. $N = 80000$ samples, $\epsilon = 1\%$, $h = 50$ ps.	151
76	Nonlinear function realized by three RLC filters in parrallel	154
77	Delay identification by the local linear approximations method. $\epsilon = 1\%$ (a) low pass filter (b) band pass filter. $m = 1$	155
78	Identification of the nonlinear function of a Mackey-Glass system. $\tau = 46$, $\tau^R = 10$, $c = 2$, $h = 0.5$, $N = 46000$	156

79	Identification of the nonlinear function of the optoelectronic generator of wavelength chaos. $h = 1 \mu s$. Experimental estimation of the parameter values: $\beta = 7.2$, $\tau = 523 \mu s$, $\tau^R = 8.4 \mu s$, $\phi = \pi/3$	157
80	Identification of the nonlinear function of the electronic generator of wavelength chaos.	158
81	The twenty largest Lyapunov exponents, computed from the dynamical equations and from a numerically generated time series. $\tau = 46$, $\tau^R = 10$, $c = 2$. $N = 500000$, $\epsilon = 1\%$, $h = 0.5$	160
82	Lyapunov dimension as a function of the number of iterates. The results are obtained by time series analysis. The parameters are the same as in Fig. 81.	160
83	Kolmogorov-Sinai entropy as a function of the number of iterates. The results are obtained by time series analysis. The parameters are the same as in Fig. 81.	161
84	The twenty largest Lyapunov exponents, estimated from time series, for four different delay values. $\tau^R = 10$, $c = 2$. $N = 250000$, $\epsilon = 1\%$, $h = 0.5$	163
85	Lyapunov dimension as a function of the delay τ . The parameters are the same as in Fig. 84.	164
86	Kolmogorov-Sinai entropy as a function of the delay τ . The parameters of the analysis are the same as in Fig. 84.	164
87	The 200 largest Lyapunov exponents, computed by Farmer's method, for four different values of the delay. $h = 0.42 \mu s$, $\beta = 8$, $\tau^R = 8.4 \mu s$, $\phi = \pi/3$	165
88	(a) Dimension as a function of delay. (b) Entropy as a function of delay. $h = 0.42 \mu s$, $\beta = 8$, $\tau^R = 8.4 \mu s$, $\phi = \pi/3$	166
89	The 200 largest Lyapunov exponents, computed by Farmer's method, for four different values of the delays. $h = 0.42 \mu s$, $\tau = 523 \mu s$, $\tau^R = 8.4 \mu s$, $\phi = \pi/3$.	167
90	(a) Dimension as a function of the feedback strength β . (b) Entropy as a function of the feedback strength. $h = 0.42 \mu s$, $\tau = 523 \mu s$, $\tau^R = 8.4 \mu s$, $\phi = \pi/3$	167
91	Delay identification from experimental time series. $h = 1 \mu s$. <i>Experimental</i> estimation of the parameter values: $\beta = 8.1$, $\tau = 523 \mu s$, $\tau^R = 8.4 \mu s$, $\phi = \pi/3$.	169
92	Dimension estimated from experimental time series as a function of the neighborhood size ϵ (solid line). The dotted line corresponds to the dimension computed by Farmer's method. Parameters of the estimation procedure: $N = 300000$, $h = 1 \mu s$. Experimentally estimated values of the system parameters: $\beta = 3.6$, $\tau = 523 \mu s$, $\tau^R = 8.4 \mu s$, $\phi = \pi/3$	171
93	Dimension estimated from experimental time series as a function of the neighborhood size ϵ . The dotted line corresponds to the dimension represented by Farmer's method. Parameters of the estimation procedure $N = 300000$, $h = 1 \mu s$. Experimentally estimated values of the system parameters: $\beta = 9$, $\tau = 523 \mu s$, $\tau^R = 8.4 \mu s$, $\phi = \pi/3$	171

94	Lyapunov spectrum estimated from experimental time series and by Farmer's method. Parameters of the estimation procedure $N = 300000$, $h = 1 \mu s$. Experimentally estimated values of the systems parameters: $\beta = 3.6$, $\tau = 523 \mu s$, $\tau^R = 8.4 \mu s$, $\phi = \pi/3$	172
95	Lyapunov dimension as a function of β . Parameters of the estimation procedure: $N = 300000$, $h = 1 \mu s$. Experimentally estimated values of the system parameters: $\tau = 523 \mu s$, $\tau^R = 8.4 \mu s$, $\phi = \pi/3$	173
96	Entropy as a function of β . Parameters of the estimation procedure: $N = 300000$, $h = 1 \mu s$. Experimentally estimated values of the system parameters: $\tau = 523 \mu s$, $\tau^R = 8.4 \mu s$, $\phi = \pi/3$	173
97	Identification of the delay produced by the optoelectronic emitter of chaos in wavelength. The parameters are: $\beta = 5$, $\tau = 523 \mu s$, $\tau^R = 8,4 \mu s$, $\phi = \pi/3$. The sampling time is $h = 1 \mu s$	180
98	Identification of the delay produced by the optoelectronic emitter of chaos in wavelength. The parameters are: $\beta = 25$, $\tau = 523 \mu s$, $\tau^R = 8,4 \mu s$, $\phi = \pi/3$. The sampling time is $h = 1 \mu s$	181
99	Delayed mutual information for two different values of the feedback strength β . The parameters are: $\tau = 523 \mu s$, $\tau^R = 8,4 \mu s$, $\phi = \pi/3$	182
100	Identification of the delay from a time series of the optoelectronic generator of chaos in wavelength. The parameters are: $\tau = 500 \mu s$, $\beta = 7$, $\tau^R = 8,4 \mu s$, $\phi = \pi/3$. The sampling time is $h = 1 \mu s$	183
101	Identification of the delay from a time series of the optoelectronic generator of chaos in wavelength. The parameters are: $\tau = 1000 \mu s$, $\beta = 7$, $\tau^R = 8,4 \mu s$, $\phi = \pi/3$. The sampling time is $h = 1 \mu s$	183
102	Block diagram of the first configuration of chaotic emitter with two feedback loops.	185
103	Identification of the delays from a time series of the system with two feedback loops given by Eq. (143). The parameters are: $\beta_1 = \beta_2 = 50$, $\tau_1 = 500 \mu s$, $\tau_2 = 385 \mu s$, $\phi_1 = \phi_2 = 0.74\pi$, $\tau^R = 5 \mu s$. The sampling time is $h = 0.25 \mu s$	186
104	Delayed mutual information in the case of an edge-emitter laser diode subjected to two delayed optical feedbacks. The feedback rates are: (a) $\gamma_1 = \gamma_2 = 10$ GHz, (b) $\gamma_1 = \gamma_2 = 100$ GHz, and the delays are $\tau_1 = 1$ ns and $\tau_2 = 0.77$ ns. The other parameters are as in Fig. 13. The sampling time is $h = 5$ ps.	188
105	Block diagram of the second configuration of chaotic emitter with two feedback loops.	189
106	System with one feedback loop. $\beta = 25$, $\tau = 500 \mu s$, $\tau^R = 5 \mu s$, $\phi = 0.74\pi$	190
107	System with two feedback loops. $\beta = 25$, $\tau_1 = 500 \mu s$, $\tau_2 = 385 \mu s$, $\tau^R = 5 \mu s$, $\phi = 0.74\pi$	191

108	Mutual information and local linear fits applied to the system with two feedback loops given by Eq. (147). The parameters are $\beta = 25$, $\tau_1 = 500 \mu s$, $\tau_2 = 385 \mu s$, $\tau^R = 5 \mu s$, $\phi = 0.74\pi$. The sampling time is $h=1 \mu s$. The arrows indicate graphically the delay values.	191
109	Representation of the system described by Eq. (143) in the space $(x_{n+1}, x_n, x_{n-\tau_1})$. The parameters are $\beta_1 = \beta_2 = 25$, $\tau_1 = 500 \mu s$, $\tau_2 = 385 \mu s$, $\tau^R = 5 \mu s$, $\phi = 0.74\pi$. The sampling time is $h=0.25 \mu s$	193
110	Representation of the system described by Eq. (143) in the plane $(x_n, x_{n-\tau_1})$. The parameters are $\beta_1 = \beta_2 = 25$, $\tau_1 = 500 \mu s$, $\tau_2 = 385 \mu s$, $\tau^R = 5 \mu s$, $\phi = 0.74\pi$. The sampling time is $h=0.25 \mu s$	193
111	Representation of the system described by Eq. (147) in the space $(x_{n+1}, x_n, x_{n-\tau_1})$. The parameters are $\beta = 25$, $\tau_1 = 500 \mu s$, $\tau_2 = 385 \mu s$, $\tau^R = 5 \mu s$, $\phi = 0.74\pi$. The sampling time is $h=0.1 \mu s$	194
112	Representation of the system described by Eq. (147) in the plane $(x_{n+1}, x_{n-\tau_1})$. The parameters are $\beta = 25$, $\tau_1 = 500 \mu s$, $\tau_2 = 385 \mu s$, $\tau^R = 5 \mu s$, $\phi = 0.74\pi$. The sampling time is $h=0.1 \mu s$	195
113	Representation of the system described by Eq. (147) in the space $(x_{n+1}, x_{n-\tau_1}, x_{n-\tau_2})$. The parameters are $\beta = 25$, $\tau_1 = 500 \mu s$, $\tau_2 = 385 \mu s$, $\tau^R = 5 \mu s$, $\phi = 0.74\pi$. The sampling time is $h=0.1 \mu s$	196
114	Approximation error as a function of the two unknown delay values τ_1^* , and τ_2^* , in the case of the system with two feedback loops given by Eq. (147). The parameters are $\beta = 15$, $\tau_1 = 500 \mu s$, $\tau_2 = 385 \mu s$, $\tau^R = 5 \mu s$, $\phi = 0.74\pi$	197
115	Approximation error as a function of the two unknown delay values τ_1^* , and τ_2^* , in the case of the system with two feedback loops given by Eq. (147), for a feedback strength $\beta = 5$. The other parameters are $\tau_1 = 500 \mu s$, $\tau_2 = 385 \mu s$, $\tau^R = 5 \mu s$, $\phi = 0.74\pi$	198
116	Approximation error as a function of the two unknown delay values τ_1^* , and τ_2^* , in the case of the system with two feedback loops given by Eq. (147), for a feedback strength $\beta = 10$. The other parameters are $\tau_1 = 500 \mu s$, $\tau_2 = 385 \mu s$, $\tau^R = 5 \mu s$, $\phi = 0.74\pi$	199
117	Approximation error as a function of the two unknown delay values τ_1^* , and τ_2^* , in the case of the system with two feedback loops given by Eq. (147), for a feedback strength $\beta = 25$. The other parameters are $\tau_1 = 500 \mu s$, $\tau_2 = 385 \mu s$, $\tau^R = 5 \mu s$, $\phi = 0.74\pi$	199
118	Matrix BOXES and vector POINTS.	207

SUMMARY

Chaotic dynamics produced by optical delay systems have interesting applications in telecommunications. Optical chaos can be used to transmit secretly, in real-time, a message between an emitter and a receiver. The noise-like appearance of chaos is used to conceal the message, and the synchronization of the receiver with the chaotic emitter is used to decode the message. This work focuses on the study of two crucial topics in the field of chaotic optical communications.

The first topic is the synchronization of chaotic external-cavity laser diodes, which are among the most promising chaotic emitters for secure communications. It is shown that, for edge-emitting lasers, two drastically different synchronization regimes are possible. The regimes differ in terms of the delay time in the synchronization and in terms of the robustness of the synchronization with respect to parameter mismatches between the emitter and the receiver. In vertical-cavity surface-emitting lasers, the two linearly-polarized components of the electric field also exhibit isochronous and anticipating synchronization when the coupling between the lasers is isotropic. When the coupling is polarized, the linearly-polarized component that is parallel to the injected polarization tends to synchronize isochronously with the injected optical field, while the other component tends to be suppressed, but it can also be antisynchronized.

The second topic is the analysis of time series produced by optical chaotic emitters subjected to a delayed feedback. First, we verify with experimental data that chaos produced by optical delay systems is highly complex. This high complexity is demonstrated by estimating chaos dimension and entropy from experimental time series and from models of optical delay systems. Second, by analyzing chaotic time series, it is shown that the value of the delay of a single-delay system can always be identified, independently of the type of system used and of its complexity. Unfortunately, an eavesdropper can use this information on the delay value to break the cryptosystem. We propose a new cryptosystem with two

delayed feedback loops that increases the difficulty of the delay identification problem.

CHAPTER I

INTRODUCTION

1.1 Introduction

Chaotic dynamics produced by optical delay systems have attracted considerable attention in the last decade because of their potential applications in telecommunications. Optical chaos can be used to transmit secretly a message between an emitter and a receiver. The noiselike appearance of chaos is used to conceal the message, and the synchronization of the receiver with the chaotic emitter is used to decode the message. Delay systems are especially attractive for chaotic communications because they can produce highly complex chaos, which can help to ensure a good concealment of the message.

The work presented here focuses on the numerical study of three topics lying in the field of chaotic communications.

We begin, in chapter 2, with an introduction of the basic notions of the fields of chaotic dynamics and chaotic communications. In chapter 3, we study the synchronization process in the context of coupled laser diodes subjected to external optical feedback. This synchronization process is crucial for message recovery. The chaotic receiver is usually a copy of the chaotic emitter, and the receiver chaos must synchronize with the transmitter chaos in order to recover the message. The robustness of the synchronization process is very important from a practical point of view. If the synchronization process is very sensitive to parameter mismatch or noise, it will be difficult even for an authorized listener to realize the synchronization and decode the message. If the synchronization is very robust, then an eavesdropper possessing a rough copy of the chaotic emitter will be able to recover the message, and the security of the system will be low. In this chapter, we propose to study specifically the synchronization mechanisms of semiconductor lasers subjected to the optical feedback produced by an external mirror. We consider dynamical regimes in which coherence collapse occurs because of the optical feedback, and the the laser output becomes

chaotic. These external-cavity lasers constitute one of the most promising sources of optical chaos for chaotic communications. Their synchronization has been obtained experimentally but the underlying synchronization mechanisms are not clearly understood. We will investigate the synchronization of edge-emitting lasers as well as of vertical-cavity surface emitting lasers, which present some specific polarization instabilities.

In chapter 4, we study the complexity of the chaos produced by an optoelectronic generator of wavelength chaos, and of the Mackey-Glass delay system, in order to determine the operational conditions under which highly complex chaos occurs. We calculate this complexity from the dynamical model of the system, and also assuming that we only know the experimental time series produced by the chaotic emitter, using specific techniques for delay systems. A measure of the effectiveness of the encryption is the difficulty with which the parameters of the chaotic system can be extracted by time series analysis. It is particularly important to be able to hide the value of the delay time of a chaotic cryptosystem, because if it is known, it is possible to break the system despite its high dimensionality. We show that time series analysis techniques can be used to identify the delay value and the nonlinear function of several chaotic delay systems. These results imply that the security of chaotic communications is compromised.

Multiple-delay delay systems have been suggested to provide a better security level than single-delay systems. In chapter 5, we study the delay identification problem in the specific context of multiple-delay chaotic systems, with the objective of trying to determine if some architectures of multiple-delay systems can make the delay identification a difficult task.

The next chapter 2, presents some basic concepts that it is necessary to master in order to understand the remainder of the manuscript. In particular, we introduce the notions of dynamical system, of chaotic dynamics, of delay system, of Lyapunov spectrum, of time series analysis, of chaos synchronization, and of chaotic communications.

CHAPTER II

CHAOS

2.1 *Introduction*

The study of chaotic phenomena is part of the broader theory of nonlinear dynamical systems. The birth of the science of dynamical systems goes back to the second half of the seventeenth century, when Newton invented differential calculus, the laws of motion, and the theory of gravity. Physicists have long believed that periodic solutions are sufficient to describe the oscillatory behavior of dynamical systems after transients have died out. The seminal research performed by Henri Poincaré at the end of the nineteenth century showed, however, that simple dynamical laws can lead to very complex steady-state behaviors, that we now call *chaotic behaviors*. It was only at the end of the 1960s that a significant part of the scientific community drew its attention toward this type of phenomena, and that a new science, the “science of chaos” started to grow. In parallel to the research on the theory of dynamical systems¹, the widespread use of computers has enabled a large number of research groups, in different scientific fields, to observe chaotic behaviors. Edward Lorenz is a pioneer of this approach. While simulating fluid convection in the atmosphere, he observed in 1963 irregular oscillations of a new type [1]. He also discovered that if the numerical integration is repeated with slightly different initial conditions, the steady-state regime has again irregular oscillations but looks very different. Li and Yorke [2] have proposed to use the term “chaos” to designate this kind of behavior. Scientists have now discovered that chaos can appear in a huge number of biological, chemical, physical, and economic systems.

In sections 2.2 and 2.3, we explain the basic notions and properties associated with dynamical systems and delay systems respectively. In section 2.4, we present the different ways in which a laser can be made to oscillate chaotically, with a special focus on lasers subjected

¹For example, the seminal work by Steve Smale and David Ruelle.

to a delayed feedback. In sections 2.5, we introduce the notions of the Lyapunov spectrum, dimension, and entropy, which are quantities that are typically used to characterize a chaotic regime. We also show how these quantities can be computed when the dynamical model is known. Section 2.6 then explains the procedures to compute these quantities when all that is known about the system is an experimental time series. Specific difficulties encountered in the case of chaotic delay systems are also pointed out. Section 3.2.4 presents the chaos synchronization phenomenon which is fundamental to chaotic communications, whose principles are explained in section 2.8. The last two sections (2.9 and 2.10) present some experimental realizations of chaotic communications and explain in what sense this type of communication can be considered secure respectively.

2.2 *Basic notions about dynamical systems*

A dynamical system consists of a set of possible states, together with a rule that determines the present state in terms of past states. If the rule is applied at discrete times, it is called a discrete-time dynamical system. In the case of continuous-time systems, the governing rule is usually a set of differential equations.

2.2.0.1 *Continuous-time systems*

Continuous-time systems can be described by a system of k first-order ordinary differential equations² with initial conditions

$$\begin{aligned}\frac{d\vec{x}(t)}{dt} &= \vec{F}[\vec{x}(t), t] \\ \vec{x}(t_0) &= \vec{x}_0,\end{aligned}\tag{1}$$

where $\vec{x} \in \mathbb{R}^m$ is the state vector, \vec{x}_0 is the initial state vector, t represents time, t_0 is the initial time, and $\vec{F} : \mathbb{R}^m \rightarrow \mathbb{R}^m$ is a vector field. We assume that the field \vec{F} verifies the conditions that ensure the existence and unicity of the solution of (1) for all $t \geq t_0$ and for all initial conditions. When the vector field depends explicitly on time, as in (1), the system is said to be non-autonomous. If it is not the case, the system is said to be autonomous and

²The reader should keep in mind that it is always possible to find a change of variables that transforms an n^{th} order differential equation in a system of n first order differential equations.

the system of differential equations describing its dynamical behavior can be written as

$$\begin{aligned}\frac{d\vec{x}(t)}{dt} &= \vec{F}[\vec{x}(t)] \\ \vec{x}(t_0) &= \vec{x}_0.\end{aligned}\tag{2}$$

It is common to represent the evolution of an autonomous system in its phase space. This space is generated by the set of all the variables that are necessary to describe the dynamical state of the system. The state of a dynamical system is the set of variables whose knowledge is necessary to describe, at a given time, the evolution or the history of this system. In the case of system described by (2), the phase space is \mathbb{R}^m . It is interesting to notice that for a finite-dimensional system like (2), the dimension of the phase space is equal to the number of initial conditions that are necessary to integrate (1).

If we designate by $\vec{\phi}_t(x_0)$ the solution of the system of *autonomous* equations (2), the family of applications

$$\vec{\phi}_t : \mathbb{R}^m \rightarrow \mathbb{R}^m; x \mapsto \vec{\phi}_t(x),\tag{3}$$

is called the flow or the "time- t " map of the dynamical system. This map associates to every state \vec{x} , the state of the system t units of time later. The set of points³ $\{\vec{\phi}_t(x_0) : -\infty < t < +\infty\}$ is called the trajectory of the system going through \vec{x}_0 . It is easily understood that the unicity of the solution of the initial value problem implies that two trajectories of an autonomous system cannot intersect in phase space. This also means that we can talk of *the* trajectory going through \vec{x}_0 , without specifying the time at which the trajectory reaches \vec{x}_0 .

2.2.0.2 Discrete-time systems

A map $\vec{\phi} : \mathbb{R}^m \rightarrow \mathbb{R}^m$ defines a discrete-time dynamical system by the iteration of

$$\vec{x}_{n+1} = \vec{\phi}(\vec{x}_n),\tag{4}$$

where \vec{x}_n is the state of the system at the n^{th} iteration and $\vec{\phi}$ assigns to each state \vec{x}_n , the next state \vec{x}_{n+1} . Starting from an initial state \vec{x}_0 , the iteration of the map $\vec{\phi}$ leads to a sequence of vectors (\vec{x}_n) that is called an "orbit" or "trajectory".

³In the following, we will designate \vec{x} by the term *vector* or *point*.

2.2.0.3 Attractors

In the remainder of this manuscript, we only consider the case of dissipative systems⁴. Dissipation implies that any volume in phase space will contract over time. Any trajectory will tend asymptotically, *i.e.* when $t \rightarrow +\infty$, toward a subset of the phase space. Such a subset is called an *attractor*. The set of initial states that lead to trajectories that converge toward the attractor is called the *basin of attraction* of the attractor.

The knowledge of the geometry of the attractor helps greatly in the characterization of the type of asymptotic (or steady-state) behavior a system experiences. The following attractors can be observed:

- **fixed point.** The asymptotic behavior is stationary. Therefore the Fourier transform of the steady-state solution is a Dirac impulse.
- **limit cycle**, *i.e.* a closed curve. The steady state solution is periodic and the spectrum is discrete and constituted by a fundamental frequency and its harmonics.
- **torus** T^r . The asymptotic solution is quasi-periodic and its spectrum has r base frequencies. In the case of a two-dimensional torus ($r = 2$), this obviously means that the spectrum has two base frequencies. When the ratio of the two frequencies is irrational, the trajectories lie on the torus in a dense way and the spectrum is itself dense⁵. When the ratio is rational, the solution is periodic and the period is the smallest common multiple of the two base frequencies. The asymptotic solution is a closed curve on the torus and the spectrum is discrete.
- **strange attractor.** The steady-state is chaotic⁶. Chaos is sometimes defined by exclusion: a steady state solution of a deterministic system can be said to be chaotic if it is neither stationary, nor periodic, nor quasi-periodic. Practically, a series of properties are used to characterize a chaotic signal. We are going to enumerate the most important ones. A first property is that the spectrum of a chaotic signal is

⁴Systems which do not experience dissipation are said to be conservative or Hamiltonian.

⁵This does not mean, however, that the spectrum is a continuous function

⁶It is possible to observe strange attractors (geometric notion) on which typical trajectories are not chaotic (dynamical notion) [3].

continuous and broadband . The spectrum usually resembles that of a noisy process with sometimes a few dominant frequencies appearing. This also means that the autocorrelation function, which is the inverse Fourier transform of the power spectral density, tends rapidly toward zero. Therefore the temporal correlation of the signal with itself decreases rapidly with time. Another important property is the sensitivity to initial conditions: two trajectories, initially even very close, diverge over time and the distance between the trajectories increases, on average, exponentially over time. The concept of Lyapunov exponent helps quantify the sensitivity of the system to initial conditions. A Lyapunov exponent measures the divergence or convergence rate of initially close trajectories. This sensitivity is also linked to the unpredictability of chaotic systems. Indeed, if the same experience is repeated two times on the same chaotic systems, two completely different evolutions of the system over time will be observed. We see that chaotic signals have common characteristics with random processes even if chaotic systems are fundamentally deterministic.

In addition to knowing the geometry of an attractor, it is interesting to determine its stability. Intuitively, an attractor A is asymptotically stable if every trajectory that reaches a neighborhood of A is attracted to it over time. On the contrary, an attractor is unstable if all trajectories that reach a neighborhood of A move away from A over time. This means that it is only the trajectories that lie exactly on A that stay on A and any perturbation, even infinitesimal, will make the trajectories move away from the attractor. We understand easily that in a real system a trajectory can stay permanently on a stable attractor only.

2.2.0.4 An important consequence of the Poincaré-Bendixson theorem

Some necessary conditions must be verified in order to observe chaos in a dynamical system. One of these is that the vector field \vec{F} (continuous-time system) or the map $\vec{\phi}$ (discrete-time system) must be non-linear. The famous Poincaré-Bendixson theorem (see *e.g.* [4, p. 337]) gives another essential condition for the case of a continuous-time dynamical system. This condition is that the dimension of the phase space must be at least equal to 3 to observe chaos. This means that a continuous system must have at least three degrees of freedom to

produce chaotic behaviors.

2.2.0.5 Bifurcation - Routes to chaos

We end this brief introduction on dynamical systems with the notion of bifurcation diagram. In addition to the state variables, the equations of a dynamical system also involve parameters which keep fixed values for a given experience or simulation. The type of steady-state solution experienced by a dynamical system depends on the values of these parameters. A bifurcation diagram represents the evolution of the type of steady-state solution when one or more parameters are modified. The type of steady state solution is usually represented by displaying the extrema of an observable when a parameter is varied. A bifurcation, which corresponds to a qualitative change of a steady-state solution, can be easily spotted in a bifurcation diagram. One of the main uses of bifurcation diagrams is to determine the “route to chaos” of the system under consideration *i.e.* the way in which chaos is reached when a parameter value is varied continuously. Several typical routes to chaos have been observed for low-dimensional systems. One of them is the period-doubling cascade (or sub-harmonic cascade or Feigenbaum cascade [5]). In this route, limit cycles give rise to other limit cycles with two times bigger periods until chaos is reached (in which case the steady-state is obviously aperiodic). Another route to chaos is by quasi-periodicity: a fixed point regime leads to a limit cycle, then to a torus T^2 , and to chaos (Curry-Yorke route) or to a T^2 torus, then to a T^3 torus, and finally to chaos (Ruelle-Takens route)). Finally, scientists have also identified an intermittency route in which phases of periodic behavior and chaos alternate. The duration of the chaotic phases increases until fully-developed chaos is reached.

In addition to bifurcations, another interesting phenomenon called a crisis can be observed in a bifurcation diagram. It corresponds to the brusque appearance or disappearance of a strange attractor or to a discontinuous change in the size or shape of an attractor. The appearance of a crisis can be due to the collision, in phase space, of a strange attractor with an unstable fixed point or an unstable limit cycle.

2.3 Delay systems

In the preceding introductory section on dynamical systems (§2.2), we have considered systems that can be modeled by a set of first-order ordinary differential equations. Delay systems belong to a different class of systems. These possess a delayed feedback loop and can often be modeled by a system of first-order delay-differential equations

$$\frac{d\vec{x}(t)}{dt} = \vec{F}[\vec{x}(t), \vec{x}(t - \tau)] , \quad (5)$$

where τ is the delay of the system and \vec{F} is a vector field. We see that for these systems, the derivative of \vec{x} at time t depends on the value of \vec{x} at the same time t but also on the value that \vec{x} took in the past (at time $t - \tau$). We understand that the evolution of \vec{x} , after a time t , can only be determined if we know the values of \vec{x} on the time interval $[t, t - \tau]$. This means that it is necessary to know a vectorial function on a time interval of length τ to determine the state of the system and therefore also its evolution. The phase space is thus, grossly speaking, the space of vectorial functions defined on an interval of length τ , which is an *infinite-dimensional* functional space. This infinite dimensionality of the phase space means that delay systems have the potential to produce very high-dimensional dynamics. This makes delay systems interesting candidates for secure communications, as will be explained later in this manuscript.

Delay systems are common in scientific fields such as physiology, biology, epidemiology, and controls systems. It is well known that a delayed feedback can induce instabilities, and in chaotic communications, these instabilities are exploited to hide a message, but it should be noted that a delayed feedback loop can also be added to a system to stabilize it [6, 7].

One of the most famous delay systems is Mackey-Glass system that was proposed in 1977 to model the production of red cells in the bone marrow [8]. The Mackey-Glass system is often considered the archetype of delay systems and it will be used in chapter 4 as a benchmark for our time series analysis algorithms.

We end this section by mentioning that most chaotic systems studied at the GTL-CNRS Telecom laboratory (Metz) and at the laboratoire d'optique Pierre-Michel Duffieux

(Besançon), in the context of chaotic communications, are delay systems that can be modeled by equations of the form (5). Figure 1 represents the bloc diagram of these chaotic generators. A tunable source is subject to feedback on its control electrode. The feedback

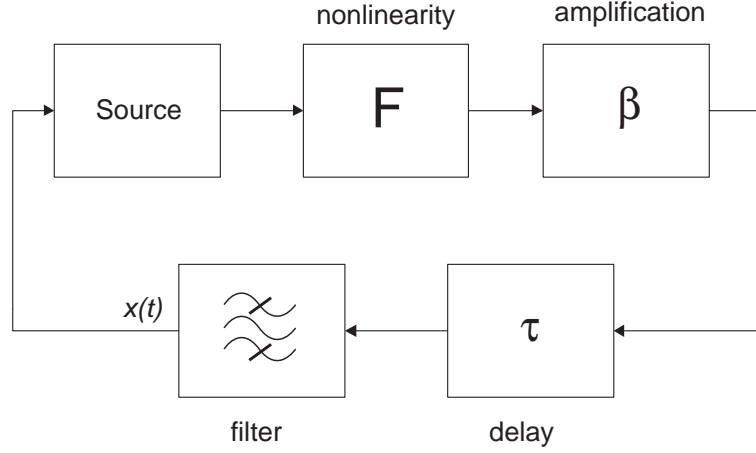


Figure 1: Bloc diagram of the chaotic delay emitters used at the GTL CNRS Telecom laboratory.

loop comprises a nonlinear element, a delay line, an amplifier (in the remainder of this manuscript, β will be a parameter proportional to the amplification), and a filter. It is to be noted that the block diagram representation leads to a conceptual separation of the elements of the system that does not necessarily correspond to the way things are realized experimentally. Section 2.4 and chapter 4 present different experimental realizations based on this bloc diagram.

2.4 *Chaos in lasers*

The topic of this thesis lies in the field of chaotic optical communications. Generators of optical chaos are a key element of these communications systems. In this section, we show how the most common source of coherent light used in optical communications, the semiconductor laser, can be made to produce optical chaos.

2.4.1 Arecchi's classification

Numerous laser types can be described by equations that resemble those of Maxwell–Bloch. These equations are a system of three differential equations, one for the complex

electric field, one for the complex polarization, and one for the population inversion. Arecchi [9] has proposed to classify lasers based on their number of degrees of freedom. The classification is realized by comparing the typical response times of polarization, electric field, and population to a perturbation. This information tells us which variables can be adiabatically eliminated from the Maxwell-Bloch-like equations. Class A corresponds to lasers whose polarization and populations adapt instantaneously to changes in the electric field (He-Ne lasers, Ar^+ and Kr^+ lasers, dye lasers). These lasers have thus only one degree of freedom since they can be modeled by a single rate equation for the electric field. For class-B lasers (Ruby, Nd:Yag, CO_2 lasers, semiconductor lasers), it is only the polarization that can be eliminated adiabatically and the lasers have two degrees of freedom. In class C lasers, no variable can be eliminated adiabatically and the full Maxwell-Bloch system is needed to describe their dynamical behavior.

In this manuscript, we will only consider the case of semiconductor lasers. Since they are class B lasers and therefore have only two degrees of freedom, the Poincaré–Bendixson theorem (*cf.* §2.2.0.4) predicts that they cannot be intrinsically chaotic. At least one degree of freedom must be added to make it chaotic. In the following, we show how this can be realized.

2.4.2 Different ways to make a semiconductor laser chaotic

- 1. Modulation of the cavity losses.

This process called Q-switching is typically used to generate pulse trains but can lead to chaos under certain conditions [10].

- 2. Modulation of the resonance frequency of the laser cavity.

This can be realized by an electro-optic modulator placed inside the laser cavity that modifies its refraction index. In this way, the optical path and therefore the resonance frequency are modified.

- 3. Modulation of the injection current.

Chaos can be observed under suitable conditions [11]. This technique is convenient to

realize because of the easy access for the experimentalist to the injection current and the semiconductor laser does not need to be modified.

- 4. External optical injection [12].

The light produced by a laser diode, the master, is optically injected into the active layer of a slave laser. The master is in a continuous wave (CW) regime and its frequency is slightly detuned with respect to that of the master. A wealth of dynamical regimes, including chaos, can be observed in this configuration.

- 5. Delayed feedback.

The effect of the feedback is to reinject into the laser dynamics one or more state variables, with a delay. These systems are of the type described in section 2.3 and are of major interest to us. In the following, we present the main types of systems in which a semiconductor laser is subjected to delayed feedback.

- 5.1 Optoelectronic feedback on the injection current of the laser. In this case, a fast repoding photodiode (bandwith of a few GHz) produces a current that is an image of the laser output power and that is added, after a delay τ , to the laser injection current. Chaos has been observed for this setup [13, 14, 15].
- 5.2 External Optical Feedback. Lasers subjected to external optical feedback are often called "external-cavity lasers". Figure 2 represents a laser diode subject to external optical feedback. An external mirror is used to optically reinject a fraction of the light produced by the laser into its active laser. The round-trip time of light in the external-cavity introduces a delay in the system. A variable attenuator placed between the external mirror and the laser is used to modify the reinjected power. A very large number of dynamical behaviors has been observed numerically and experimentally. In particular, the output power can vary in a very hyperchaotic way, which is interesting for secure communications. Chapter 3 examines in detail the synchronization of the chaos produced by two unidirectionally coupled external-cavity lasers. The optical feedback that we have described above is called *coherent* optical feedback because

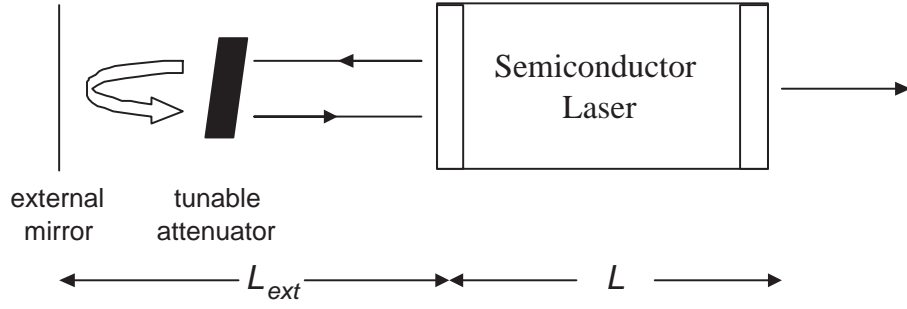


Figure 2: External-cavity semiconductor laser diode.

the optical field is injected "coherently" into the slave laser cavity (the cavity length is smaller than the coherence length of the laser light and no polarization-sensitive element is placed inside the cavity). Other types of optical feedback exist. The case of incoherent (or polarization-rotated) optical feedback [16, 17, 18, 19] is represented in figure 3. A Faraday rotator or a birefringent plate is inserted in the external cavity and is used to rotate the (linear) polarization of the light emitted by the laser in such a way that the polarization reinjected into the laser cavity is perpendicular to the direction of polarization of the laser light. In this way, the optical field reinjected into the laser cavity does not interfere coherently with the field inside the cavity. It has also been proposed to use a phase-conjugating mirror as an external feedback source. This configuration has been called naturally phase-conjugate feedback. Lasers subjected to phase-conjugate feedback as well as lasers subjected to incoherent optical feedback can present chaotic behaviors that can be used in chaotic communications [20, 21].

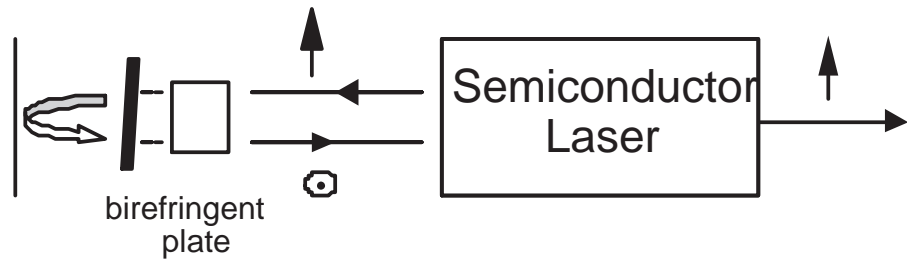


Figure 3: Semiconductor laser subjected to incoherent optical feedback. The arrows represent the direction of linear polarization.

- 5.3 Several chaotic delay systems have been realized at the Laboratoire d'Optique Pierre-Michel Duffieux and at GTL-CNRS Telecom on the basis of the block diagram represented in Fig. 1. These systems are used as emitters and receivers in chaotic secure communications systems (*cf.* §2.8). The first system that has been realized experimentally is an optoelectronic generator of chaos in wavelength [22, 23]. This wavelength chaos is emitted by a DBR laser subject to a delayed and nonlinear feedback applied to its wavelength-changing electrode. After this first setup, optoelectronic systems have been built that experience fluctuations of the intensity of the electric field [24, 25], of its phase [26], and of the optical path difference in a coherence modulator [27, 28]. These last three systems all use electro-optic modulators subject to delayed feedback on their driving electrode. It is important to notice that contrary to all previously described systems, the chaos generators presented here (5.3) do not use intrinsic semiconductor laser nonlinearities. External elements (birefringent plate, electro-optic modulators) are used to produce nonlinearities, and the laser diode is used only as a light source. In the next section, we describe in greater detail the above-mentioned wavelength chaos emitter since it is the optoelectronic system that has attracted most of our attention during the thesis work. We have taken most of the experimental time series that we analyze in chapter 4 on this system.

2.4.3 Optoelectronic system producing chaos in wavelength

Figure 4 represents schematically the constitutive elements of the system. This chaos generator has been described in great detail in references [22, 23, 29, 30] and we will therefore describe it relatively concisely here. A DBR laser diode is used as a light source whose wavelength can be tuned by changing the current injected in its driving electrode. The link between this current and the laser wavelength $\lambda(t)$ is strictly linear. A constant current applied to the electrode determines the mean wavelength and a variable current coming from a delayed nonlinear feedback is also applied to it to create the chaotic fluctuations. The nonlinearity is purely optical and realized by a birefringent plate placed between two crossed polarizers. The power $P(t)$ detected by a photodiode after the second polarizer is a

nonlinear function of the wavelength. The current produced by the photodiode is delayed by an analog delay line, amplified, and applied to the wavelength-changing electrode. We have actually slightly modified the experimental setup described in [22, 23, 29, 30] with the aim of realizing the non-linearity with optical fibers instead of using free-space optics. As figure 4 shows, the laser light, after going through the waveplate, is injected in an optical fiber and goes through a fiber-optic polarization controller to counter-balance the polarization fluctuations induced by the optical fiber. The light then goes through a portion of polarizing fiber which plays the role of a second polarizer, and the power $P(t)$ is detected at the output of this fiber. The next step in the evolution of this chaos generator will be to replace the birefringent plate by a highly birefringent optical fiber (polarization-maintaining fiber).

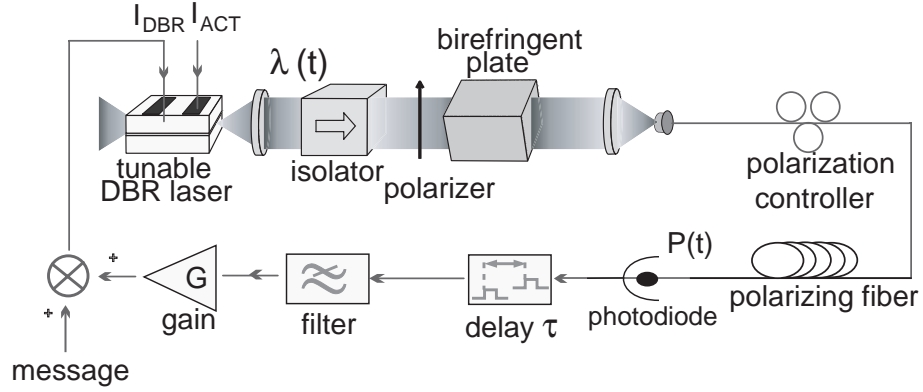


Figure 4: Optoelectronic system generating wavelength chaos.

It can be easily shown that this system is described by the following scalar delay-differential equation

$$\tau^R \dot{x}(t) = \beta \sin^2[x(t - \tau) + \phi] - x(t), \quad (6)$$

where x is a dimensional variable proportional to the wavelength, τ^R represents the response time of the system, β represents the feedback strength, τ is the delay time of the feedback loop, and ϕ is an optical phase shift. This kind of system is described by the block diagram shown in Fig. 1. It is easy to understand that the filter in this case is a low-pass filter. Parameters β , τ , and ϕ can be tuned experimentally by modifying the gain G of the amplifier, the frequency of the oscillator that drives the analog delay line, and the mean current of the

wavelength-changing electrode respectively. The time series analyses presented in chapter 4 have been mostly performed on this system. Since we needed to compare results obtained from experimental time series with theoretical results coming from the model, it has been necessary to estimate accurately the parameters of the experimental system. The interested reader can find details on the estimation procedure in the theses manuscripts [29, 30]. More details on the experimental setup and its constitutive elements can be found in [22, 23, 29, 30].

2.5 *Lyapunov Spectrum, Dimension, and Entropy*

As we have mentioned in the introduction, we believe that a complex chaos is necessary to mask efficiently an information-bearing signal. An interesting quantity that provides a measure of this complexity is the dimension of the chaotic attractor, *i.e.* of the limit set in phase space toward which chaotic trajectories converge. The dimension gives an order of magnitude of the number of variables that have to be used to model the dynamics. Another very interesting quantity is the entropy of the chaotic system. Entropy measures the “randomness” of the signal. In the context of chaotic regimes, it gives an idea of the predictability of the system (the larger the entropy, the less the system is predictable). An indispensable tool to determine dimension and entropy is the Lyapunov spectrum of the chaotic system. As will be shown later, dimension and entropy can be computed trivially once the Lyapunov spectrum is known. Chapter 4 is devoted mainly to the characterization, in terms of Lyapunov spectrum, dimension, and entropy, of the chaotic regimes produced by various chaotic emitters used in chaotic communication systems.

The Lyapunov spectrum is the collection of all the Lyapunov exponents of the system. Lyapunov exponents are used to characterize the stability of any kind of attractor since their definition is sufficiently general to be applied even to sets as complex as strange attractors (and therefore also to simpler sets like fixed points, limit cycles, and tori). It can be considered that these exponents are a generalization of standard quantities used to characterize the stability, like eigenvalues in the case of stationary solutions, and Floquet multipliers for periodic solutions. In a phase-space of dimension m , there are m Lyapunov exponents

that correspond to the exponential divergence or contraction rates of infinitesimally close trajectories, in m orthogonal directions. A positive exponent is the fingerprint of a chaotic system. When a system has at least two positive exponents, it is called *hyperchaotic*. Since the trajectories are supposed to be infinitesimally close, the Lyapunov spectrum is a linearized quantity, *i.e.* it is computed taking only into account the *linear part* of the system in every point of the phase space.

In this section, we give a relatively detailed presentation of the notion of Lyapunov spectrum, of its numerical calculation when the dynamical model is known, and of the notions of dimension and entropy. This presentation is largely inspired by references [31, 32, 4]. We consider only the cases of discrete-(4) and continuous-time (2) dynamical systems that are *not* subjected to delayed feedback. The important case of delay systems will be treated in sections 4.3.1 and 4.3.2.

2.5.1 Definition of the Lyapunov exponents

2.5.1.1 Discrete-time systems – One-dimensional iteration

We consider first the case of a discrete-time system which can be described by an iterative model involving a single variable

$$x_{n+1} = \phi(x_n), \quad (7)$$

where $x \in \mathfrak{R}$ is the system's state variable. The trajectory coming out of the initial state x_0 is the sequence $(x_n), n = 0, 1, \dots$. To determine the stability of the system, we must analyze in which way the distance between two initially close trajectories evolves. We will consider trajectory (x_n) that starts from x_0 and (y_n) that starts from $x_0 + \delta x_0$, where δx_0 is infinitesimally small. Since the distance between the trajectories is infinitesimal, ϕ can be replaced by its first-order limited Taylor series and we get

$$y_1 = x_1 + \delta x_1 = \phi(x_0 + \delta x_0) = \phi(x_0) + \phi'(x_0)\delta x_0.$$

The distance between the two trajectories is therefore initially

$$|\delta x_1| = |\phi'(x_0)\delta x_0| = |\phi'(x_0)| |\delta x_0|$$

and after a second iteration it becomes

$$|\delta x_2| = |\phi'(x_1)| |\delta x_1| = |\phi'(x_1)| |\phi'(x_0)| |\delta x_0|.$$

It is easily found that the distance after k iterations is

$$|\delta x_n| = \left(\prod_{l=0}^{n-1} |\phi'(x_l)| \right) |\delta x_0|.$$

It is well known that if we had wanted to study the stability of a fixed point x^* of ϕ , we would have chosen $x_0 = x^*$ and would have obtained $|\delta x_k| = L^k |\delta x_0|$, where $L = |\phi'(x^*)|$. The stability of the fixed point could then be determined by comparing L to unity. In the case of an arbitrary trajectory, we can define, in a similar way, an effective multiplicative coefficient

$$L = \lim_{n \rightarrow \infty} \left(\prod_{l=0}^{n-1} |\phi'(x_l)| \right)^{1/n}. \quad (8)$$

L is called the Lyapunov number of x_0 and the Lyapunov exponent λ is the natural logarithm of L

$$\lambda = \ln(L) = \lim_{n \rightarrow \infty} \frac{1}{n} \sum_{l=0}^{n-1} \ln |\phi'(x_l)|. \quad (9)$$

The existence of the limits defined hereabove and their independence of the initial state x_0 can be proved with the help of Birkhoff's ergodic theorem. Because it is independent of the initial state, it is meaningful to talk of *the* Lyapunov exponent of an attractor, without specifying the initial state. The Lyapunov exponent corresponds therefore to the average of the local divergence and convergence rates, $\ln(|\phi'(x_n)|)$, along the trajectory.

2.5.1.2 Discrete-time systems–Multidimensional iterations

We consider now a map $\vec{\phi} : \mathbb{R}^m \rightarrow \mathbb{R}^m$ that defines an iteration involving several variables (that together form the vector \vec{x})

$$\vec{x}_{n+1} = \vec{\phi}(\vec{x}_n). \quad (10)$$

We will present the intuitive notion of Lyapunov exponent in this case. We consider a unitary sphere U centered on the initial state \vec{x}_0 and lying in the basin of attraction of

the attractor under consideration. Since we are interested in the evolution of states that are initially infinitesimally close to \vec{x}_0 , we will consider the linear part of $\vec{\phi}$ which is its Jacobian matrix. We call $J_l = J\vec{\phi}(\vec{x}_l)$ the Jacobian matrix of $\vec{\phi}$ at \vec{x}_l and $J^{(n)} = J\vec{\phi}^n(\vec{x}_0)$, the Jacobian matrix of $\vec{\phi}^n$, where $\vec{\phi}^n$ is the result of the convolution of $\vec{\phi}$, n times with itself. We have of course that $J^{(n)} = J_0 J_1 \cdots J_{n-1}$. When $J^{(n)}$ is applied to U , the unitary sphere is transformed into the ellipsoid $J^{(n)}U$. This ellipsoid has m orthogonal axes, which are larger than unity in the expanding directions of $J^{(n)}$, and smaller than unity in contracting directions. In the following, we call $r_k^{(n)}$, for $k = 1, \dots, m$, the k^{th} longest semi-axis of the ellipsoid $J^{(n)}U$. The k^{th} Lyapunov number is defined as

$$L_k = \lim_{n \rightarrow \infty} (r_k^{(n)})^{1/n}. \quad (11)$$

The k^{th} Lyapunov exponent is defined by

$$\lambda_k = \ln(L_k) = \lim_{n \rightarrow \infty} \frac{1}{n} \ln(r_k^{(n)}). \quad (12)$$

The way the Lyapunov numbers and exponents are defined implies that they are ordered

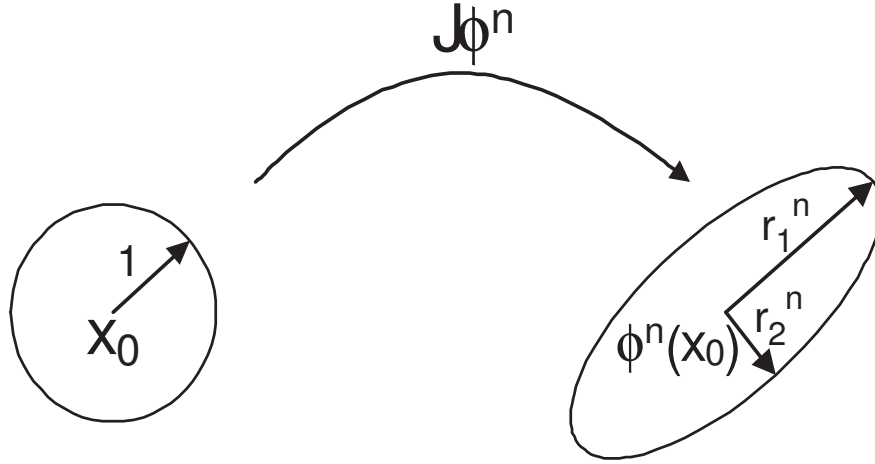


Figure 5: Evolution of a unitary disk under the jacobian of $\vec{\phi}^n$.

by decreasing values

$$L_1 \geq L_2 \geq \cdots \geq L_m \quad (13)$$

$$\lambda_1 \geq \lambda_2 \geq \cdots \geq \lambda_m. \quad (14)$$

It can be easily shown that the semi-axis lengths of the ellipsoid $J^{(n)}U$ are the square roots of the m eigenvalues of the matrix $J^{(n)T}J^{(n)}$, where T is the transposition operator. Additionally, the axis directions correspond to the eigenvectors of this matrix. The following definition of the Lyapunov exponents is therefore equivalent to the preceding one

$$\lambda_k = \lim_{n \rightarrow \infty} \frac{1}{2n} \ln \left| \Lambda_k^{(n)} \right|, \quad (15)$$

where $\Lambda_k^{(n)}$ is the k^{th} largest eigenvalue of $J^{(n)T}J^{(n)}$ which means that

$$\left(\prod_{l=0}^{n-1} J_l \right)^T \left(\prod_{l=0}^{n-1} J_l \right) \vec{u}_k^{(n)} = \Lambda_k^{(n)} \vec{u}_k^{(n)}, \quad (16)$$

where $\vec{u}_k^{(n)}$ is the eigenvector associated to the eigenvalue $\Lambda_k^{(n)}$. Oseledec's ergodic multiplicative theorem [33] can be used to prove that the limit (12, 15) exists and that it is the same for all initial vectors \vec{x}_0 belonging to the basin of attraction of the attractor under consideration. It should be noted that the set of all eigenvectors \vec{u}_k^∞ constitutes a basis of tangent space in \vec{x}_0 , that gives the directions in which infinitesimal perturbations evolve over time, with an exponential rate that is given by the corresponding Lyapunov exponent⁷.

In the following, we call E_k the vector subspace spanned by all the eigenvectors \vec{u}_k^∞ , except the $k - 1$ first ones. The essential property that will be exploited to determine numerically the Lyapunov spectrum is

$$\lambda_k = \lim_{n \rightarrow \infty} \frac{1}{n} \ln \left\| \left(\prod_{l=0}^{n-1} J_l \right) \vec{u} \right\| \Leftrightarrow \vec{u} \in E_k, \quad (17)$$

where \vec{u} is a unitary vector. This property means that any infinitesimal perturbation belonging to the subspace E_k increases or decreases, on average, as $e^{\lambda_k t}$.

⁷It is important to realize that the eigenvalues and eigenvectors of J_l only have a *local* meaning.

2.5.1.3 Continuous-time systems

The definitions presented in the case of a discrete-time system are useful to introduce the notion of Lyapunov spectrum in the context of autonomous continuous-time systems (2). This is because the Lyapunov exponents of the continuous-time system are the Lyapunov exponents of the discrete-time system defined by the "time-1 map" that corresponds to the integration of the continuous time system over a unit of time. The time- h map of a continuous-time autonomous system is defined as

$$\vec{\phi}_h : \mathbb{R}^m \rightarrow \mathbb{R}^m; \vec{x}_n \mapsto \vec{x}_{n+1} = \vec{\phi}_h(\vec{x}_n), \quad (18)$$

where $\vec{\phi}_h$ is the map that associates to the state \vec{x}_n of the continuous system (2), its state h units of time later. When the continuous process is integrated numerically, the time h can be the integration step. When the system is known through a measure of some observables, h can be the sampling period⁸. The Lyapunov exponents of the time-1 map are obtained by dividing the exponents of the time- h map by h .

A peculiarity of continuous-time systems is that, except in the case of a fixed point attractor, one Lyapunov exponent is always equal to zero. The existence of this exponent is linked to the fact that the distance between two points on the same trajectory cannot increase indefinitely, nor it can tend toward zero.

2.5.2 Calculation of the Lyapunov spectrum of non-delay systems when the model is known

In theory, all that has to be done is to compute the set of eigenvalues of the product of Jacobian matrices given in (16). The Lyapunov exponents would then be obtained by formula (15). It is not possible of course, to compute an infinite number of Jacobian matrices and the product (16) has to be truncated. This is not the main problem of the computation procedure however. We should recall that the eigenvalues $\Lambda_k^{(n)}$ correspond to the lengths of the semi-axis of the ellipsoid $J^{(n)}U$. When a chaotic attractor is considered, the ellipsoid will be stretched along certain directions and will shrink along other ones. The ellipsoid will tend to be crushed along the direction of the eigenvector that is associated to

⁸*i.e.* the time interval between two consecutive measurements.

the largest eigenvalue. This means that the ellipsoid will become very long and very thin. The eigenvalues that have to be estimated have therefore very different magnitudes, which results in an ill-conditioned problem that cannot lead to accurate numerical results.

Another approach has to be considered. The computation technique, proposed for the first time in [34, 35], is based on the relation (17). The starting point is to consider a basis of orthogonal vectors $(\vec{w}_1^0, \dots, \vec{w}_m^0)$. The Jacobian matrices J_n are applied in chronological order to the vectors of the basis which transform into

$$\begin{aligned}\vec{z}_1 &= (J_0 J_1 \cdots J_r) \vec{w}_1^{(0)} \\ \vec{z}_2 &= (J_0 J_1 \cdots J_r) \vec{w}_2^{(0)} \\ &\vdots \\ \vec{z}_m &= (J_0 J_1 \cdots J_r) \vec{w}_m^{(0)},\end{aligned}\tag{19}$$

where r corresponds to the number of jacobian matrices taken into account at this stage of the procedure. Since all of the vectors $\vec{w}_i^{(0)}$ belong to E_1 , they increase with a mean exponential rate equal to λ_1 and tend to align along the direction of the corresponding eigenvector. Before the transformed vectors $\vec{z}_1, \dots, \vec{z}_m$ become degenerate (*i.e.* for a sufficiently small value of r), an orthonormalization procedure is applied (of Gram-Schmidt type), leading to a new basis $(\vec{w}_1^{(1)}, \dots, \vec{w}_m^{(1)})$ of orthonormal vectors. The first vector $\vec{w}_1^{(1)}$ is obtained by normalizing \vec{z}_1 . The second, $\vec{w}_2^{(1)}$, is obtained by subtracting from the vector \vec{z}_2 its projection on $\vec{w}_1^{(1)}$ and by normalizing the resulting vector. The third vector, $\vec{w}_3^{(1)}$, is obtained by subtracting from \vec{z}_3 its projections on $\vec{w}_1^{(1)}$ and $\vec{w}_2^{(1)}$ and by normalizing the result. The other vectors of the new basis are obtained in an analog way. Mathematically,

the orthonormalization can be written as

$$\begin{aligned}
\vec{w}_1^{(1)} &= \frac{\vec{z}_1}{\|\vec{z}_1\|} = \frac{\vec{y}_1^1}{\|\vec{y}_1^1\|} \\
\vec{w}_2^{(1)} &= \frac{\vec{z}_2 - \frac{\langle \vec{z}_2, \vec{y}_1^1 \rangle \vec{y}_1^1}{\|\vec{y}_1^1\|^2}}{\left\| \vec{z}_2 - \frac{\langle \vec{z}_2, \vec{y}_1^1 \rangle \vec{y}_1^1}{\|\vec{y}_1^1\|^2} \right\|} = \frac{\vec{y}_2^1}{\|\vec{y}_2^1\|} \\
\vec{w}_3^{(1)} &= \frac{\vec{z}_3 - \frac{\langle \vec{z}_3, \vec{y}_1^1 \rangle \vec{y}_1^1}{\|\vec{y}_1^1\|^2} - \frac{\langle \vec{z}_3, \vec{y}_2^1 \rangle \vec{y}_2^1}{\|\vec{y}_2^1\|^2}}{\left\| \vec{z}_3 - \frac{\langle \vec{z}_3, \vec{y}_1^1 \rangle \vec{y}_1^1}{\|\vec{y}_1^1\|^2} - \frac{\langle \vec{z}_3, \vec{y}_2^1 \rangle \vec{y}_2^1}{\|\vec{y}_2^1\|^2} \right\|} = \frac{\vec{y}_3^1}{\|\vec{y}_3^1\|} \\
&\vdots \\
\vec{w}_m^{(1)} &= \frac{\vec{z}_m - \frac{\langle \vec{z}_m, \vec{y}_1^1 \rangle \vec{y}_1^1}{\|\vec{y}_1^1\|^2} - \dots - \frac{\langle \vec{z}_m, \vec{y}_{m-1}^1 \rangle \vec{y}_{m-1}^1}{\|\vec{y}_{m-1}^1\|^2}}{\left\| \vec{z}_m - \frac{\langle \vec{z}_m, \vec{y}_1^1 \rangle \vec{y}_1^1}{\|\vec{y}_1^1\|^2} - \dots - \frac{\langle \vec{z}_m, \vec{y}_{m-1}^1 \rangle \vec{y}_{m-1}^1}{\|\vec{y}_{m-1}^1\|^2} \right\|} = \frac{\vec{y}_m^1}{\|\vec{y}_m^1\|}, \tag{20}
\end{aligned}$$

where $\langle \dots, \dots \rangle$ is the dot product and \vec{y}_k^1 is the k^{th} vector of the orthogonalization process, before normalization has been applied.

We then apply the next r Jacobian matrices (the matrices from J_{r+1} to J_{2r}) in chronological order to the new basis $(\vec{w}_1^{(1)}, \dots, \vec{w}_m^{(1)})$. We thus obtain a new set of vectors to which the orthonormalization procedure is applied, leading to another orthonormal basis $(\vec{w}_1^{(2)}, \dots, \vec{w}_m^{(2)})$. After repeating this procedure n times, the basis $(\vec{w}_1^{(n)}, \dots, \vec{w}_m^{(n)})$ is obtained.

Since the first vector of the Gram-Schmidt procedure is only normalized, it will point toward the most unstable direction (associated to λ_1) after a sufficiently large number of stages. The mean rate of change, per iteration, of its length is the Lyapunov exponent λ_1 . The other vectors of the Gram-Schmidt procedure lie in the subspace E_2 which is spanned by all the transformed vectors except the first one. Specifically, the second vector of the procedure does not contain any contribution coming from the first exponent λ_1 but contains a contribution from λ_2 . The mean rate of change of the length of the second vector thus leads to λ_2 . The other exponents are calculated in a similar way.

Therefore, the expression

$$\frac{\ln \left\| \vec{y}_k^{(1)} \right\| + \dots + \ln \left\| \vec{y}_k^{(n)} \right\|}{n} \tag{21}$$

gives an estimation of the k^{th} largest Lyapunov exponent λ_k .

We have assumed so far that the Jacobian matrices J_l are known. In case the dynamical

model is known, the Jacobians can be computed directly from it. In case the model is unknown, they must be estimated from experimental time series. The estimation of Jacobians from time series is described in section (§2.6.2) for the case of systems that can be modeled by a system of ordinary differential equations and in section (§4.3.1) in the case of delay systems. In the remainder of the section, we explain how the Jacobian matrices can be computed, *when the model is known, in the case of systems that do not have delays*.

In the case of a discrete-time system (4), the matrices J_l are simply the Jacobians of the map $\vec{\phi}$ at the different points \vec{x}_l of the orbit under consideration. Their determination is therefore straightforward when the model, and therefore also the map $\vec{\phi}$, are known.

In the case of a continuous-time system, it is necessary to compute the jacobian matrices of $\vec{\phi}_h$, which is the time- h map which associates to a vector \vec{x} , the solution of (2), h units of time after the system has gone through the state \vec{x} . The jacobians $J_l = J\vec{\phi}_h(\vec{x}_l)$ of $\vec{\phi}_h$ at \vec{x}_l cannot be determined explicitly in general, but can be found as solutions of a differential equation, called the variational equation. Consider $\vec{\phi}_t(\vec{x})$, the time- t map applied to the state \vec{x} , which is a function of t and \vec{x} . By definition of the time- t map, we have

$$\frac{d\vec{\phi}_t(\vec{x})}{dt} = \vec{F}(\vec{\phi}_t(\vec{x})).$$

By taking the jacobian of the two terms of the preceding expression, the variational equation is obtained

$$\frac{dJ\vec{\phi}_t(\vec{x})}{dt} = J\vec{F}(\vec{\phi}_t(\vec{x}))J\vec{\phi}_t(\vec{x}). \quad (22)$$

It is a system of linear non-autonomous⁹ differential equations. The matrix $J\vec{F}(\vec{\phi}_t(\vec{x}))$ appearing in (22) can be computed explicitly when the model (2) is known. Since $\vec{\phi}_0(\vec{x}) = \vec{x}$, the initial condition of the variational equation is $J\vec{\phi}_0(\vec{x}) = I$, where I is the identity matrix. The integration of the variational equation and of the dynamical equation of the system must be performed in parallel. Let's assume that $\vec{x}_0, \vec{x}_1, \vec{x}_2, \dots$ represent successive states of the dynamical system (2), on the same trajectory, and separated by a time step h . Starting from an initial state \vec{x}_0 , the dynamical equation (2) is integrated during h units

⁹since its coefficients are not constant.

of time, leading to the value of \vec{x}_1 . The variational equation is also integrated, at \vec{x}_0 , for a time h , giving the sought-after matrix $J_0 = J\vec{\phi}_h(\vec{x}_0)$. It is important to understand that this integration of the variational equation necessitates the knowledge of the matrix $J\vec{F}(\vec{x}_1)$ [footnote ¹⁰], which can only be known because the dynamical equation has also been integrated. The integration of the dynamical and variational equations starting from \vec{x}_1 leads to J_1 . The repetition of this procedure all along the trajectory under consideration gives the different jacobian matrices.

2.5.3 Dimension and Entropy

The notions of dimension and entropy are used to characterize in a quantitative way chaotic dynamical regimes.

Intuitively, the dimension corresponds to the quantity of information necessary to specify the position of a point on the attractor with a given precision [36]. The dimension also gives an order of magnitude of the number of variables that are needed to model the dynamics. The classic topological dimension is not adapted to characterize strange attractors, and a series of generalized definitions of dimension have been proposed. These definitions can be applied to sets as complex as strange attractors and lead in these cases to non-integer values of the dimension. The values of the different dimensions for low-dimensional attractors are usually similar. The different definitions can be classified based on the fact that only metric properties are used in the definition or that both metric and probabilistic properties are used. This latter type of dimension divides an attractor into a set of regions of the phase space and integrates in its definition the probability of visiting these regions. The capacity dimension ¹¹ and the correlation dimension are examples of the first type of dimension, while the information dimension is an example of the second type. We present here, in a relatively non-formal way, the definitions of capacity and information dimension only.

The capacity dimension D_C of an attractor is

$$D = \lim_{\varepsilon \rightarrow 0} \frac{\ln N(\varepsilon)}{\ln(1/\varepsilon)}, \quad (23)$$

¹⁰that is a function of time.

¹¹or capacity or Hausdorff dimension or Hausdorff-Besicovitch dimension.

where $N(\epsilon)$ is the number of hypercubes of side ϵ that are necessary to cover the attractor. This capacity dimension gives the same "weight" to all the hypercubes.

The definition of the information dimension D_I gives more weight to the regions that are more frequently visited. It is defined as

$$D_I = \lim_{\epsilon \rightarrow 0} \frac{I(\epsilon)}{\ln(1/\epsilon)}, \quad (24)$$

where $I(\epsilon) = -\sum_{i=1}^{N(\epsilon)} p_i \ln(p_i)$, and p_i is the probability that the trajectory goes through the i^{th} hypercube. The quantity $I(\epsilon)$ corresponds to the information (in the Shannon sense) necessary to specify a state of the system with a precision ϵ .

The notion of entropy comes from information theory. It is used to quantify the "randomness" of a random variable. The definition of entropy, in the Shannon sense, is given in section 4.4.1.2. In the context of chaotic regimes, the entropy gives an idea of the predictability of a system (the larger the entropy, the less a system is predictable). As for the case of dimension, several definitions of entropy exist, for example the Renyi entropies (of which the Shannon entropy is a special case) and the Kolmogorov-Sinai entropy H_{KS} . We refer the reader to [31] for the definitions of the aforementioned quantities.

One of the reason why the Lyapunov spectrum is particularly interesting to determine is because a dimension and entropy can be computed trivially from it. Specifically, the sum of the positive Lyapunov exponents is an upper bound of the Kolmogorov-Sinai entropy [37], as shows the following inequality, called the Pesin inequality

$$H_{KS} \leq \sum_{k: \lambda_k > 0} \lambda_k. \quad (25)$$

Under certain conditions, it has been proved that the two sides of inequality are equal [31]. Even more, it is actually often considered in the literature that the sum of the positive exponents is equal the Kolmogorov-Sinai entropy (and the Pesin inequality is thus called the Pesin identity).

A dimension, called the Lyapunov or Kaplan-Yorke dimension, can be computed from the spectrum by

$$D_L = k + \frac{\sum_{i=1}^k \lambda_i}{|\lambda_{k+1}|}, \quad (26)$$

where $\sum_{i=1}^k \geq 0$ and $\sum_{i=1}^{k+1} \leq 0$. This means that the Lyapunov dimension is equal to the (linearly interpolated) index for which the sum of the Lyapunov exponents, ordered by decreasing values (13), is equal to zero. The Kaplan-Yorke conjecture [38] states that the Lyapunov dimension is equal to the information dimension D_I . This conjecture has been proven to be true for certain low-dimensional systems. Even though there is no proof for the general case, this conjecture is deemed to be valid in a great number of systems and is frequently used in the literature.

2.6 Basics of time series analysis

Often the knowledge a scientist has of a physical system is a set of times series corresponding to measured values, at discrete sampling times, of one or more variables of a continuous-time dynamical system. One of the main challenges is to determine the characteristics of a dynamical system from these experimental times series, with maybe the help of some additional information on the nature of the system. Examples of characteristics that are of particular interest are the type of dynamical regime, the geometry and dimension of the attractor, and the Lyapunov spectrum. It can also be interesting to be able to predict the system behavior and to perform noise reduction on experimental time series. Our aim here is not to present all the different time-series analysis techniques, but only the ones that have been used during the thesis work. In section 2.6.1, we explain how the phase space can be reconstructed, which is the starting point of numerous time-series analysis techniques; in section 2.6.2, we present the procedure to determine the Lyapunov spectrum from time series in the case of a system that is not subjected to feedback. Section 4.3.1 in chapter 4 treats the case of delay systems.

2.6.1 Phase-space reconstruction

Knowing the state of a deterministic system and therefore of its phase space is of fundamental importance. We understand easily that a prediction of the behavior of a system can only be performed if its state is known. This knowledge is also necessary for numerous time series analysis techniques, for example for computing the Lyapunov exponents, for noise reduction and to determine the geometry of the attractor. Unfortunately, the scientist often

only has the measure of a single state variable. It is therefore necessary to know ways to reconstruct the phase space from the measured time series.

Mathematicians have found an answer to this problem in the notion of embedding of an attractor. An embedding is a continuous and bijective function from a compact set of phase space \mathbb{R}^k to \mathbb{R}^m , where m is called the embedding dimension¹². This notion is particularly interesting since it means that every state of the compact set (imagine it is an attractor) can be represented in a unique way in \mathbb{R}^m . In the following, \mathbb{R}^m will be called the reconstructed phase space. There are several ways to reconstruct a phase space but we will present here only the most famous of all, which is called the method of delays. In this method, the measure $x(t)$ of a dynamical variable, is associated, for every t , to the vector $\vec{S}(t) = (x(t), x(t - \Delta), x(t - 2\Delta), \dots, x(t - (m - 1)\Delta))$, which is made up of $x(t)$ and the values that x took at different times in the past, separated by a time interval Δ . Takens' embedding theorem and its generalizations [39, 4] prove that an attractor reconstruction by the delays method is an embedding if $m > 2D$, where D is the Hausdorff dimension of the attractor. Moreover, it has also been proved that important quantities such as the Lyapunov spectrum, attractor dimension, and Kolmogorov-Sinai entropy are invariant with respect to this type of phase space embedding. This means that these quantities have the same values in the "real" phase space and in the reconstructed space, which is a particularly interesting and useful property. Practically, one often has a time series (x_n) which is a set of measures of a dynamical variable, at different moments in time, separated by a time interval h called the sampling time. The method of delays in this discrete case associates to every element x_n of the time series, a vector \vec{S}_n

$$\vec{S}_n = (x_n, x_{n-\Delta}, x_{n-2\Delta}, \dots, x_{n-(m-1)\Delta}), \quad (27)$$

where Δ is the number of samples corresponding to the delay used in the method of delays. It should be noticed that we use here, for simplicity reasons, the same notation for the delay time in time units and for the number of samples corresponding to this delay. A common misuse of the term "embedding", which we will use in the following, consists in saying that

¹²Contrary to the preceding notations, the phase space is noted here \mathbb{R}^k .

the time series has been embedded.

We end this section by giving some information on how to implement the method of delays. It is essential to determine "good" values of the number m of delayed variables and of the delay Δ used in the reconstruction. Takens' embedding theorem tells us that a lower limit of m is equal to two times the attractor dimension. When a time series analysis is performed, however, this dimension is not generally known. Moreover, Takens' theorem does not give any information on the choice of Δ . From a mathematical point of view, the embeddings for different values of Δ are equivalent when applied to noiseless data. When real-world (and therefore noisy) data is used, however, a good choice of Δ greatly helps the analyst. It is outside the scope of this manuscript to present and explain the motivations of the different techniques that can be used to determine m and Δ . We only mention that the so-called false nearest neighbors technique [40] is often used to determine m , and that an order of magnitude of Δ can be found by analyzing the autocorrelation function of the time series as well as the mutual information¹³ between the time series and a translation in time of this time series. A description of these techniques can be found in [31].

2.6.2 Computation of Lyapunov exponents from time series of non-delay systems

Section 2.5.2 showed how the Lyapunov spectrum could be computed if the jacobians J_l were known. These jacobians cannot be found by integrating the variational equation, which is unknown since the dynamical model is itself unknown. We explain in this section how these jacobians can be computed from a time series (x_n) . The estimation technique has been proposed by Eckmann and Ruelle [41] and has been applied for the first time to time series by Sano and Sawada [42] and by Eckmann *et al.* [43].

The first step is an embedding of the time series by the method of delays, leading to the time series (\vec{S}_n) defined in the preceding section. In the reconstructed phase space spanned by the vectors \vec{S}_n , a map $\vec{\phi}_h$

¹³The concept of mutual information, which comes from information theory, is described in section 4.4.1.2.

$$\vec{\phi}_h : \mathbb{R}^m \rightarrow \mathbb{R}^m; \vec{S}_n \mapsto \vec{\phi}_h(\vec{S}_n) = \vec{S}_{n+1}, \quad (28)$$

that associates to every state of the reconstructed phase space, the following state in this same space, can be defined univocally. This map is a discrete model of the continuous-time system.¹⁴

The second step consists in computing the jacobian matrices $J_n = J\vec{\phi}_h(\vec{S}_n)$. Of course, the analytic expression of $\vec{\phi}_h$ is unknown and the jacobians cannot be computed by a direct derivation of the map $\vec{\phi}_h$. The technique used to compute the jacobians stems from the fact they represent the linear part of the dynamics in a local approximation. Consequently, if we determine the set $\mathcal{U}_n(\epsilon) = \{i : \|\vec{S}_i - \vec{S}_n\| < \epsilon\}$ ¹⁵ of neighbors of \vec{S}_n , for a neighborhood size ϵ , the jacobian can be obtained by minimizing

$$\sum_{i \in \mathcal{U}_n} \left\| \vec{S}_{i+1} - \hat{J}_n \vec{S}_i - \vec{a}_n \right\|^2 \quad (29)$$

with respect to the elements of the estimated Jacobian matrix \hat{J}_n , and with respect to the vector \vec{a}_n which is the constant part of the linear approximation of the dynamics in a neighborhood of \vec{S}_n . This corresponds to a local linear approximation of the dynamics. Of course, \hat{J}_n can be a good estimation of J_n if the neighborhood size is small enough to justify a linear approximation. Determining the size of the neighborhoods that have to be used in the numerical calculation is a non-trivial task. Neighborhood sizes must be greater than the noise level to avoid fitting the noise rather than the deterministic dynamics. Additionally, small neighborhoods can lead to a number of neighbors that is too small to give statistically well determined values of the matrix \hat{J}_n and the vector \vec{a}_n . On the contrary, if the neighborhoods are big, the influence of the nonlinearity of the map $\vec{\phi}_h$ can be important and the linear approximation (29) can lose its meaning. Even when the neighborhood size has been determined, the search for neighbors itself (in high-dimensional spaces) is nontrivial and necessitates specific search methods to limit the CPU and memory

¹⁴The reader should keep in mind that by numerically integrating a continuous-time system, a discrete iterative model of the system is created.

¹⁵We choose arbitrarily the euclidian norm, which implies that the neighborhoods are hyperspheres of radius ϵ .

resources used. The appendix A briefly describes the "box method" that we have used in this work to search for neighbors.

The third and last step is the application of the computation technique of the Lyapunov spectrum previously described in section 2.5.2, where the Jacobians J_n are here estimated from time series in the way described in the second step.

Though this procedure can be applied in theory to time series produced by a delay system, the high dimensionality of the attractors of delay systems make it practically impossible to reconstruct the attractors with an embedding technique. The specific analysis techniques that have to be used for delay systems are described in sections 4.2 and 4.3.

2.7 *Chaos synchronization*

The synchronization of periodic oscillators is a well-known phenomenon that was described for the first time by Huygens in the seventeenth century. He observed that two pendulums positioned close to each other on a wall could synchronize their movements thanks to the vibrations going from one pendulum to the other through the wall. It was long thought that chaotic systems could not synchronize because of the property of sensitivity to initial conditions. Fujisaka and Yamada [44, 45, 46] and Pecora and Carroll [47, 48, 49] proved however this assumption to be false. In particular, Pecora and Carroll proved theoretically, numerically, and experimentally that two unidirectionally coupled chaotic systems can be synchronized. Chaos synchronization has since been observed in a large number of chaotic systems. The main drive of this research on synchronization is the possibility to use it for chaotic communication and encryption (*cf.* §2.8). More precisely, the synchronization of chaos is used to recover an information-bearing message that has been hidden by mixing it with a chaotic carrier.

Generally, synchronization can occur if two identical or similar chaotic oscillators are used and if these oscillators are coupled. Figure 6 represents two oscillators that are unidirectionally coupled by a coupling signal $s(t)$ ¹⁶. One of the oscillators will be called the

¹⁶The coupling can also be bidirectional.

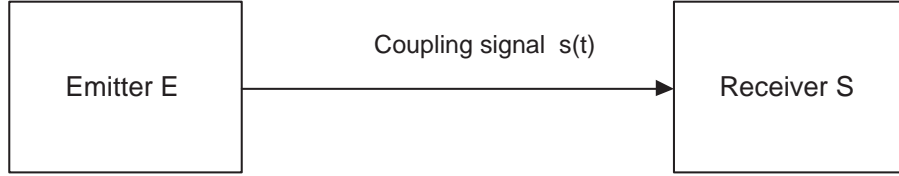


Figure 6: Two unidirectionally coupled oscillators.

”emitter” (E) and the other one the ”receiver” (R). We call $\vec{x}_e(t)$ the vector of the dynamical variables of the emitter and $\vec{x}_r(t)$ the vector of the dynamical variables of the receiver. The oscillators are also often designated by the terms ”master” and ”slave” in the case of unidirectional coupling; we use this latter terminology in chapter 3 that is devoted to the study of the synchronization of unidirectionally coupled external-cavity lasers.

The synchronization is said to be identical or complete when $\vec{x}_e(t) \approx \vec{x}_r(t)$ is obtained a certain time after the systems are coupled and up to a sufficiently small error. The synchronization is said to be generalized [50] when a functional relation of the form $\vec{x}_e(t) \approx \vec{F}(\vec{x}_r(t))$ is obtained¹⁷. There are other forms of synchronization but they are out of the scope of this manuscript. Complete synchronization has been observed numerically and experimentally for a wide range of systems and we refer the reader to section 2.9 for references. Generalized synchronization is more difficult to observe but has been found in a limited number of systems. It has been observed for example in the case of a laser that is optically pumped by another chaotic laser [51]. It is also worth remembering that it has been conjectured [51] that numerous results that have been interpreted as an absence of synchronization due to a too weak coupling could actually correspond to generalized synchronization. The synchronization of chaotic systems is an essential phenomenon in chaotic communications. The principles of chaotic communications and how the synchronization of chaos is exploited is presented in the next section.

¹⁷Complete synchronization can be considered a special case of generalized synchronization for which \vec{F} is the identity function.

2.8 Chaotic communications

Keven Cuomo and Alan V. Oppenheim [52] were the first to realize chaotic communications experimentally. They built a circuit version of the Lorenz equations and showed the possibility of using this system as a communication scheme to transmit a small speech signal. The signal was hidden in the fluctuations of the x signal of the master circuit. The slave circuit generated its own synchronized x' signal and by subtracting $x - x'$ the speech signal could be recovered. Since then, a large number of schemes that use the synchronization of unidirectionally coupled chaotic systems for secure communication have been proposed. These schemes fall into three main categories which we present in this section: chaotic masking, chaos shift keying, and chaotic modulation. It is important to understand that the encryption is realized at the physical level and that it is possible to also encrypt the information-bearing signal with standard algorithmic techniques, as a complement.

We assume in the following that we have two unidirectionally coupled chaotic systems, E and R , that synchronize in a finite time. To remain general, we do not specify the type of chaotic system used or the way the synchronization is realized.

2.8.1 Chaotic Masking

In the case of chaotic masking, represented in Fig. 7, the information-bearing signal $m(t)$ is mixed with the chaotic output of the emitter $x_e(t)$. We have represented the special case of an addition of these two signals. It is thus the sum $s(t) = x_e(t) + m(t)$ that propagates through the transmission channel and that is injected into the receiver. A certain degree of security will be associated with this form of communication if the properties of the chaotic “carrier” are exploited correctly, namely its large spectrum and the noiselike appearance of its time series. In particular, the amplitude of $m(t)$ should be small compared to that of $x_e(t)$ and its spectrum should be contained in the spectrum of $x_e(t)$. In this way, it will be difficult to extract the message by an analysis of a time series or of the spectrum of the transmitted signal $(x_e(t) + m(t))$. Since a message m of small amplitude is added to a chaotic carrier of much larger amplitude with large noiselike fluctuations, it is easy to understand that the observation of the time series will hardly give any information on the message.

Moreover the fact that the spectrum of the message is contained in that of the carrier means that first, the fluctuations of the message will occur at a frequency similar to those of the carrier, which contributes to hide the message at the temporal level, and second, that it will be difficult to extract the signal through spectral filtering and spectral analysis. The recovery of the message $m(t)$ is possible in reason of the robustness of the synchronization of chaotic systems. This means that the synchronization occurs even if small perturbations are applied to the coupling signal or to the structure of the chaotic systems. The message can be considered as a small perturbation which does not significantly affect the synchronization process. Therefore, the chaos produced by the receiver, $x_r(t)$, follows its natural tendency to synchronize with the carrier $x_e(t)$ *only*, and the message can be recovered by subtracting $x_r(t)$ from $x_e(t)$. Of course, the synchronization of $x_r(t)$ with $x_e(t)$ is not perfect when a perturbation is present and the smaller the perturbation (here it is the message), the better the synchronization quality is. We understand that since the spectrum of the message must

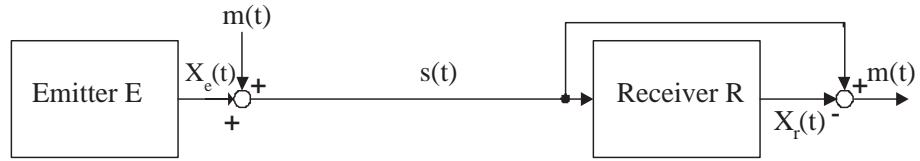


Figure 7: Chaotic masking.

be contained in the spectrum of the chaotic carrier, the extent of the chaos spectrum sets the maximal values of the bit rate that can be used to ensure the secrecy of the communication.

2.8.2 Chaos shift keying

In the case of the chaos shift keying technique, represented in Fig. 8, a parameter p of the emitter system can take either of two values p_0 or p_1 depending on the value of the binary information-bearing signal. The value of parameter p in the receiver, which is a copy of the transmitter, is set to p_0 . Depending on the value of the binary message, the receiver synchronizes or does not synchronize with the emitter. The message can therefore be recovered by an analysis of the synchronization error $e(t)$, which is the difference between the

the emitter chaotic signal $x_e(t)$ and the receiver chaotic signal $x_r(t)$. This type of communication will provide a certain degree of security if the chaotic attractors corresponding to the different values of p are difficult to distinguish. The bit rate of the message is limited by the synchronization time, *i.e.* the time needed for the receiver to synchronize with the emitter, when the value of the emitter parameter p is turned to p_0 . It is easy to understand

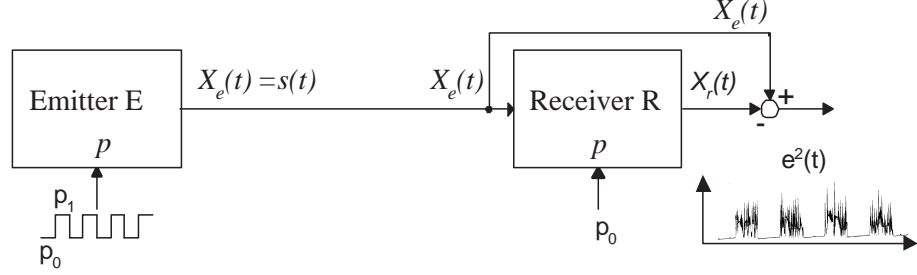


Figure 8: Chaos-shift keying.

that the duration of a bit must be larger than the synchronization time of the receiver. This synchronization time thus limits the bit rate of the message.

2.8.3 Chaotic Modulation

Finally, the chaotic modulation technique is a concept that corresponds to the generic case in which the information-bearing signal $m(t)$ participates directly to the dynamics of the chaotic emitter. More specifically, this means that $m(t)$ must appear *inside* the equations of the chaotic emitter. This is clearly not the case for chaotic masking but it could be considered that chaos-shift keying is a special case of chaotic modulation. Figure 4 shows that in the case of the optoelectronic emitter of wavelength chaos, the message is a current that is injected in the electrode that tunes laser wavelength. This corresponds to chaotic modulation. Chaotic modulation is the technique that has been used the most in the chaotic communication schemes developed at the GTL-CNRS Telecom laboratory [25, 53, 54]. Since the message participates directly to the system dynamics, it is reasonable to assume that the masking can be made more efficient with this type of technique.

We have presented so far different ways of using chaotic dynamics to realize *secure* communications. We will end this section by mentioning that there is another branch of

chaotic communications that focuses on exploiting the information theoretic formalism of chaos to code a message [55, 56, 57]. The idea is to manipulate the chaotic system to cause its symbolic dynamics¹⁸ to track a prescribed symbol sequence.

In the next section, we present several experimental realizations of chaotic synchronization and communication, with a focus on optical chaos.

2.9 *Experimental realizations of chaotic communications*

Since the discovery of chaos synchronization, a large number of research groups have demonstrated chaos synchronization and communication experimentally. The first realizations were based on nonlinear electronic circuits. Pecora and Carrol proved chaotic synchronization using an unstable second-degree oscillator coupled to a hysteretic circuit [47, 49]. The first demonstrations of chaotic communications have used a famous nonlinear circuit called the Chua circuit [58, 59, 60] and an analog implementation of the Lorenz system [52, 61]¹⁹. A host of other electronic systems have been used since then for chaotic communications but it is beyond the scope of this work to list them all.

Synchronization of chaos produced by optical systems has also raised the interest of a large number of researchers because of the potential applications in optical telecommunications and the higher bit rates than can be obtained. The first experimental realization of optical synchronization goes back to 1994 when R. Roy and K. S. Thornburg obtained the synchronization of two mutually coupled solid-state Nd:YAG lasers lying in the same crystal [62]. In the same year, P. Colet and R. Roy proved numerically that a digital communication between two unidirectionally coupled chaotic solid-state Nd:YAG lasers was possible [63]. After these early experiments in solid-state lasers, interest has shifted toward chaotic erbium-doped fiber ring lasers (EDFRLs) and semiconductor lasers. Pioneering work in synchronization of EDFRL has been performed by G. D. VanWiggeren and R.

¹⁸The symbolic dynamics is the dynamics in a finite partition of the phase space, where each element of the partition is associated with a symbol.

¹⁹The Lorenz system is a system of three coupled nonlinear ordinary differential equations modeling fluid convection in the atmosphere. Edward Lorenz is well known for having been the first to observe chaotic behavior numerically by integrating the aforementioned system of equations, which has been named after him.

Roy [64, 65] who showed that a 126 Mbit/s pseudorandom binary message could be transmitted in a secure way. In later work [66], transmission of a 1 GHz sinusoidal signal was demonstrated.

It is the synchronization of chaotic semiconductor lasers that has drawn most of the attention because of their predominance in optical communications. There are different ways of making the intensity of the light produced by a semiconductor laser vary in a chaotic way as explained in section 2.4. But by far the most popular method is to use an external feedback loop. The feedback can be either optoelectronic or fully optical. In the case of external optical feedback, an external mirror reinjects in the laser cavity a fraction of the light emitted by this laser. Lasers subject to this type of feedback are called external-cavity laser diodes (ECLs). The first simulation of the synchronization of unidirectionally coupled chaotic ECLs goes back to 1996 [67] and the first experimental observations to 1999 [68] for synchronization on the microsecond timescale and 2000 [69] for synchronization on the nanosecond timescale. Transmission of a 1 GHz sinusoidal signal with a chaotic masking technique has been obtained in 2000 [70] and a very recent result (2005) proves the experimental transmission of a 3.5 GHz signal [71]. It has also been proved numerically [72, 73] and experimentally²⁰ [70] that the synchronization process is robust enough to allow the extraction of an information-bearing signal even when the distortions induced by an optical channel are taken into account. Chapter 3 is devoted to the numerical study of the synchronization regimes of external-cavity edge-emitting and vertical-cavity surface-emitting lasers. Another interesting type of feedback is the optoelectronic feedback. A big advantage of using this type of system in chaotic communications is that the synchronization process does not depend on the polarization state of the optical field that gets to the receiver. A first type of electronic feedback is being studied by the group of Jia-Ming Liu, in UCLA. In their scheme, the output power of a semiconductor laser is detected by a fast photodiode and then added, after a delay, to the diode's injection current. Transmission of 2.5 Gbit/s pseudorandom bit sequences has been demonstrated experimentally with this scheme [74]. A second class of systems with optoelectronic feedback has been developed at the University

²⁰For an optical channel constituted by a short optical fiber only.

of Franche-Comté and at the Georgia Tech Lorraine-CNRS Telecom laboratory, as explained in section 2.4. This kind of setup is characterized by the fact that the laser diode is used only as a light source and the nonlinear elements and the feedback loop are external to the laser. This means that the parameters of the laser itself do not influence the chaotic dynamics of the system. As an example of this type of realization, reference [25] presents a generator of optical chaos in intensity which uses a Mach-Zehnder modulator subjected to an optoelectronic delayed feedback from its output to its control electrode. A 3 Gbit/s pseudo-random bit stream has been successfully transmitted with this type of generator, using a chaotic modulation technique. Other realizations belonging to this class of feedback include a generator of chaotic variations of the wavelength (*cf.* § 2.4.3) and of the phase [26] of the optical field.

Some considerations on the security of chaotic communications are presented in next section.

2.10 Security aspects

One way an eavesdropper can break a chaotic cryptosystem is by making a copy of the chaotic emitter and by using this copy to obtain chaos synchronization and ultimately recover the message. This supposes that the eavesdropper has some notion of the chaos-generating system. It is easy to understand that the robustness of the synchronization process plays an important and contrasting role. If the synchronization process is not robust at all, even the authorized receiver will have a hard time extracting the message, especially in the presence of a long optical channel. If the synchronization process is very robust, even an eavesdropper with an approximate notion of the emitter's architecture might be able to recover the information-bearing signal. The very important process of synchronization and its robustness is studied in great detail in chapter 3 in the case of coupled external-cavity edge-emitting and surface-emitting lasers.

An eavesdropper might also try to break a chaotic cryptosystem by intercepting and analyzing the signal transmitted between the emitter and the receiver. As we have explained previously (*cf.* § 2.6), time series analysis usually begins with a reconstruction of the phase

space of the system, based on the measured time series (x_n) . This means that the full dynamics of the system is reconstructed based only on the knowledge of a sequence of measurements (x_n) . As we have seen in section 2.6, this is usually done by associating to the sequence (x_n) , a sequence of vectors $(x_n, x_{n-\Delta}, x_{n-2\Delta}, \dots, x_{n-(m-1)\Delta})$ which are constituted by the measurement x_n and m values of that measurement at different times in the past, separated by a suitably chosen number of iterates Δ . Once the phase space has been reconstructed, nonlinear time series analysis techniques can be used to estimate the system parameters and for dynamical forecasting. This capability to predict the behavior of the system has been used to break certain chaotic cryptosystems [75, 76]. This works because the chaotic carrier *only* is predicted and the message can be obtained by comparing the predicted time series with the measured one. In order to counter these attacks, it has been proposed to use high-dimensional chaotic signals to hide the message [77, 78]. This is due to the fact that the number m of delayed measurements that have to be taken into account in the reconstruction of the phase space increases linearly with the dimension of chaos. It is very difficult to work in very high-dimensional spaces because of the inevitable large sizes of the vectors involved, of the long computations times and above all because unreasonably long time series would have to be used to obtain statistically significant results. For this reason, delayed systems seem to be good candidates for chaotic cryptosystems. They are easy to realize and can at the same time produce very high-dimensional dynamics. For example, we have seen that the generator of wavelength chaos described in section 2.4.3 can be modeled by the following scalar nonlinear delay-differential equation

$$\tau^R \dot{x}(t) = \beta \sin^2[x(t - \tau) + \phi] - x(t) , \quad (30)$$

where τ is the delay in the feedback loop, β is the feedback strength, ϕ is a phase shift, and τ^R is the response time. Only one variable is present in this model, but at the same time the phase space is infinite-dimensional: it is the functional space of differentiable functions on an interval of length τ . This means that very high-dimensional dynamics can occur. Hegger *et al.* [79] have shown, however, that in spite of the high dimensionality of delay systems, it is possible to analyze these system in a low-dimensional projection of their phase space.

And certain time-delay cryptosystems have been broken by working in this low-dimensional system [80, 81]. This projection of the phase space can only be constructed however if the value of the delay τ of the system is known. This is why it is particularly critical to hide this value and we propose to examine the problem of the identification of the delay time in chapters 4 and 5.

CHAPTER III

SYNCHRONIZATION OF UNIDIRECTIONALLY COUPLED EXTERNAL-CAVITY SEMICONDUCTOR LASERS

3.1 Introduction

Semiconductor lasers are ubiquitous in the modern world. They are the principal source of coherent light in optical telecommunications, they are used in optical storage devices, in laser pointers, to cite only a few applications. It has rapidly appeared to the scientific community that these devices are very sensitive to optical feedback, particularly because of the low reflectivities of their facets. Optical feedback first appeared as a parasitic effect due to unwanted reflections on an optical channel or on an optical storage device. Later, the scientists realized that the large variety of dynamical regimes produced by laser diodes subjected to optical feedback could be exploited in useful applications. Depending on the operating conditions, the feedback can lead to a decrease of the linewidth, to a shift of the laser frequency, or to a loss of coherence and to chaotic fluctuations of the dynamical variables of the laser. The frequency shift induced by the optical feedback is being currently exploited in commercially available wavelength-tunable laser diodes used in wavelength-multiplexed systems. External-cavity lasers in the coherence collapse regime are one of the most studied sources of optical chaos for chaotic communications. They are easy to realize experimentally and the parameters of the feedback can be easily tuned experimentally. We study in this chapter the synchronization of two unidirectionally coupled external-cavity laser diodes. As was explained in the preceding introductory chapter, the details of this synchronization process have important consequences for chaotic cryptosystems, in terms of easiness of realization and security. It is therefore crucial to master this process to realize efficient chaotic communications.

In section 3.2, we study the synchronization of edge-emitting semiconductor lasers, while in section 3.3, we study the synchronization of vertical-cavity surface-emitting lasers.

3.2 Synchronization of external-cavity edge-emitting semiconductor lasers

In section 3.2.1, we present the main characteristics of edge-emitting semiconductor lasers and the rate equation model we use to simulate their dynamical behavior. In section 3.2.2, we present the Lang and Kobayashi model for the dynamical behavior of a semiconductor laser subjected to external optical feedback, and section 3.2.3 presents the model for unidirectionally coupled external-cavity lasers. Two types of synchronization regimes are identified in section 3.2.5; the regions of parameter space in which these occur are presented in section 3.2.5; and finally, section 3.2.6 shows under which conditions it is possible to observe a transition between the two synchronization regimes.

3.2.1 Semiconductor lasers and rate equations

We present here very briefly some of the characteristics of semiconductor lasers, and the rate equation model that we use to model their dynamical behavior.

Most semiconductor lasers nowadays employ either a double heterostructure or a quantum-well heterostructure [82]. We have represented in Fig. 9 a Fabry-Pérot edge-emitting double-heterostructure semiconductor laser. A thin active layer of InGaAsP semiconductor material is sandwiched between two layers of a different semiconductor material, InP , which has approximately the same lattice constant. This creates a forward-biased diode when an external voltage is applied, and the injection current J ensures a permanent supply of electrons and holes (carriers¹) in the active layer. The use of an heterostructure (*i.e.* of different semiconductor materials) leads to a good transverse confinement of the carriers and of the optical field. The carriers are trapped into the active region by the electrostatic barriers created by the bandgap difference between the active and cladding layers². The

¹The two highest energy bands are the valence and conduction bands. In semiconductor materials, the conduction band is separated from the valence band by an interval of forbidden energies, called the bandgap. Free electrons in the conduction band and holes in the valence band are designated by the term *carriers*.

²The active layer material has a smaller bandgap than the semiconductor material of the cladding layers.

optical confinement comes from the fact that the active layer has a higher refractive index than the surrounding cladding layers, and therefore behaves like a dielectric waveguide which confines the photons by total internal reflection. It is in this active layer that the interactions that lead to the laser effect take place. The fundamental mechanism that leads to the emission of coherent light is stimulated emission. Stimulated emission corresponds to an electron-hole recombination stimulated by a photon existing in the semiconductor material, which leads to the coherent amplification of the incoming photon through the creation of a second photon, with the same energy, phase, propagation direction, and polarization as the incoming photon³. Stimulated emission has to compete against photon absorption processes. The state at which the rates of stimulated emission and photon absorption are equal is called *transparency*, which corresponds to the appearance of population inversion [82]. While above transparency there is a net amplification in the medium, it is not enough to overcome the losses at the facets (mirrors), through which the light is emitted. Coherent light is emitted only when the net optical gain overcomes both the internal losses and the mirror losses. Practically, this means that the injection current must be larger than a minimal value, called the threshold current. The remaining requirement to have an autonomous laser is to have a resonant cavity which provides a feedback mechanism. The resonant cavity provides frequency selection and the waves that verify the resonance condition are called the longitudinal modes of the laser. There are different ways to realize the resonant cavity. In Fabry-Pérot lasers, the resonator is a Fabry-Pérot cavity formed by cleaving the wafer along parallel crystal planes, to create partially reflecting flat mirror facets at the edges of the wafer. This type of edge-emitting laser usually emits several longitudinal modes, separated several hundreds of GHz. Other realizations of the resonant cavity have been proposed (most importantly in DBR and DFB edge-emitting lasers) which lead to a single-mode emission which is highly desirable in optical telecommunications. A different type of laser architecture is used in vertical-cavity surface-emitting lasers (VCSELs). In these lasers, the cavity is vertical, and the mirrors are parallel to the wafer surface, resulting

³Spontaneous emission can also occur randomly, creating photons with no phase relation with those resulting from stimulated emission.

in vertical surface emission. These surface-emitting lasers are always single-mode because of the very short length of their resonant cavity. A more detailed description of VCSELs can be found in section 3.3.

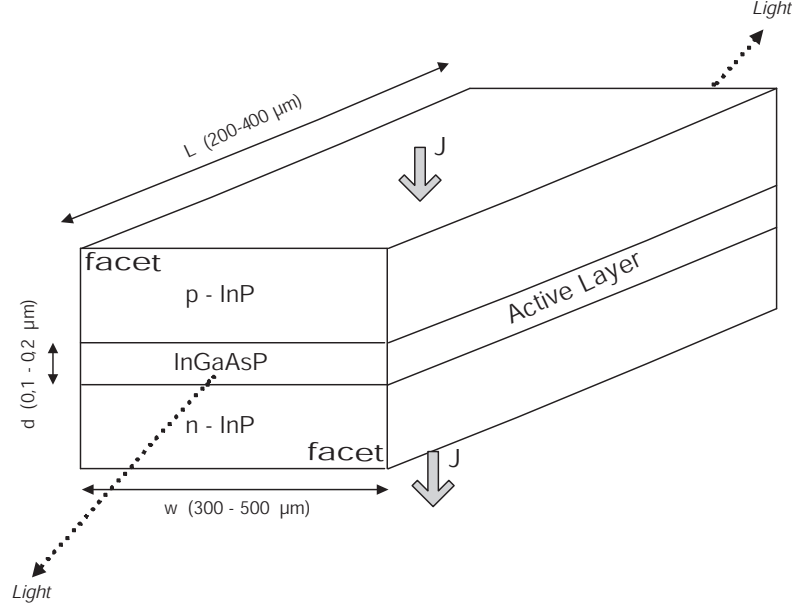


Figure 9: Double heterostructure Fabry-Perot edge-emitting laser.

In this work, we only consider single-mode semiconductor lasers, and until stated otherwise, we will assume that the lasers are edge-emitters.

The dynamical behavior of a semiconductor laser can be modeled by a system of ordinary differential equations called rate equations. These equations result from a semiclassical approach in which the electric field is treated classically and the carrier population and material polarization are treated according to quantum mechanics. Additionally, in a semiconductor medium, the material polarization reflects almost instantly any change in the electric field and in the carrier population. The polarization is therefore adiabatically eliminated in the equations, leading to a system of two equations, one for the complex electric field, and one for the carrier number

$$\frac{dE(t)}{dt} = \left\{ \frac{1}{2}(1 + i\alpha) \left[G(N, |E|^2) - \frac{1}{\tau_p} \right] \right\} E(t), \quad (31)$$

$$\frac{dN(t)}{dt} = \frac{J}{e} - \frac{N(t)}{\tau_n} - G(N, |E|^2)|E|^2(t), \quad (32)$$

where:

- $N(t)$ [dimensionless] is the normalized carrier number *i.e.* the normalized number of electron-hole pairs in the active region.
- $E(t) = A(t)e^{i\phi(t)}$ [dimensionless] is the slowly-varying complex electric field, corresponding to the only longitudinal mode present. The complete complex electric field is of the form $F(t) = E(t)e^{i\omega t} = A(t)e^{i\Omega(t)}$, where ω is the angular frequency of the laser in a CW (continuous wave) regime, and $\Omega(t)$ is the total phase of the electric field. The variable $A(t)$ is the amplitude of the electric field, and $\phi(t)$ is sometimes called the slowly-varying phase. The electric field is normalized in such a way that the total number of photons in the active layer is equal to $|E(t)|^2 = A(t)^2$.
- α is the linewidth enhancement factor. It introduces a coupling between the amplitude and the phase of the electric field. This coupling is due to the fact that a change in the amplitude induces a change in the carrier number through (32), and that, in semiconductor medium, a change in carrier number induces a change of the index of refraction, and therefore also of the phase of the electric field.
- $G(N, |E|^2)$ [s^{-1}] is the optical gain. The following expression is often used

$$G(N, |E|^2) = G_N(N - N_0)/(1 + \epsilon|E|^2), \quad (33)$$

where G_N [s^{-1}] is the differential gain, N_0 is the carrier density at transparency, and ϵ [dimensionless] is the gain saturation coefficient, which takes into account phenomenologically the gain reduction with the optical power due to spatial and spectral hole burning.

- τ_p [s] is the photon lifetime. The quantity $1/\tau_p$ represents the total losses (in the active layer and at the cleaved facets) per unit time.

- τ_n [s] is the carrier lifetime. The quantity $1/\tau_n$ represents the carrier recombination rate by all processes other than stimulated emission.
- J [A] is the injection current and e is the absolute value of the electron charge.

Starting from (31), it is easy to determine the equation for the amplitude A and slowly-varying phase ϕ of the electric field

$$\frac{dA(t)}{dt} = \left\{ \frac{1}{2} \left[G(N, A^2) - \frac{1}{\tau_p} \right] \right\} A(t), \quad (34)$$

$$\frac{d\phi(t)}{dt} = \frac{\alpha}{2} \left[G(N, A^2) - \frac{1}{\tau_p} \right], \quad (35)$$

The rate equation for the amplitude (34) expresses a competition between a gain term, $\frac{1}{2}G(N, A^2)$, and a loss term, $-1/(2\tau_p)$. Laser emission occurs only if the gain is larger than the losses. In the equation for the carrier number N , the term J/e represents the number of carriers per unit time supplied by the injection current, and the terms $-G(N, A^2)A^2(t)$ and $-N(t)/\tau_n$ represent the carriers consumed by unit time, by stimulated emission and by all the processes other than stimulated emission, respectively.

It is important to notice that only two variables, A and N , are independent. These two variables can be found by solving the two equations (34) and (32) only, and the phase is then obtained by solving Eq. (35). This means that a solitary semiconductor laser has only two degrees of freedom and is therefore a class B laser in Arecchi's classification (*cf.* §2.4.1). The Poincaré-Bendixon theorem (*cf.* § 2.2) allows us to conclude that an autonomous solitary edge-emitting semiconductor laser cannot behave chaotically.

3.2.2 External-cavity semiconductor lasers

3.2.2.1 The Lang and Kobayashi model

An experimental realization of coherent optical feedback is represented in Fig 10. In this setup, an external mirror is used to reinject in the active layer, after a delay, a fraction of the light emitted by the laser. This type of system is called an external-cavity laser. A tunable attenuator in the external cavity is used to vary the power reinjected into the cavity.

Depending on the operating parameters, the laser can be stabilized or destabilized by the optical feedback. Under certain conditions, very hyperchaotic behaviors can be observed, making these systems interesting for chaotic communications.

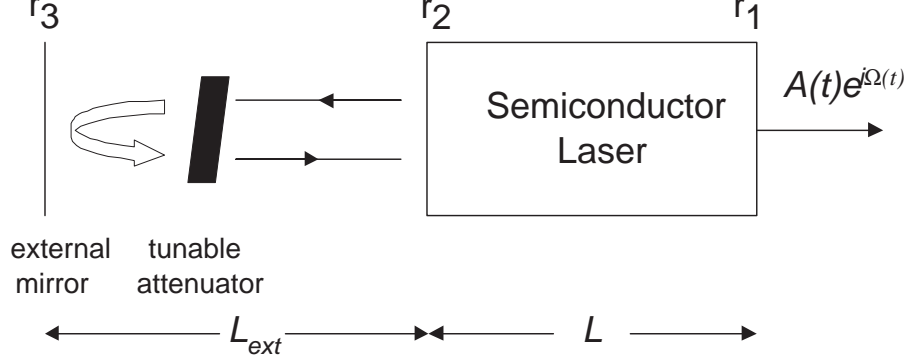


Figure 10: Edge-emitting semiconductor laser subjected to external optical feedback.

In 1980, Lang and Kobayashi [83] propose the following model to describe the dynamical behavior of a single longitudinal mode external-cavity laser

$$\frac{d[A(t)e^{i\phi(t)}]}{dt} = \left\{ \frac{1}{2}(1 + i\alpha) \left[G(N, A^2) - \frac{1}{\tau_p} \right] \right\} A(t)e^{i\phi(t)} + \frac{\kappa}{\tau_{in}} A(t - \tau) e^{i\phi(t-\tau)} e^{-i\omega\tau}, \quad (36)$$

$$\frac{dN(t)}{dt} = \frac{J}{e} - \frac{N(t)}{\tau_n} - G(N, A^2)A^2(t). \quad (37)$$

The only difference with respect to the solitary⁴ laser, is the term $\frac{\kappa}{\tau_{in}} A(t - \tau) e^{i\phi(t-\tau)} e^{-i\omega\tau}$, which represents the complex electric field fed back into the active layer by the external mirror. The meaning of the additional quantities is the following

- κ is the dimensionless feedback parameter. The quantity κ^2 corresponds to the ratio between the power that enters the laser cavity because of the external feedback, to the power that is reflected inside the cavity by the cavity mirrors. Experimentally, κ is modified by varying the attenuation of the tunable attenuator present in the external cavity.
- τ_{in} is the roundtrip time of light in the laser cavity. In the remainder of this manuscript, we often use the quantity $\gamma = \kappa/\tau_{in}$ which is called the feedback rate.

⁴*i.e.* not subjected to external optical feedback.

- τ is the roundtrip time of light in the external cavity. Typical values of τ are in the range going from 0.1 ns to 10 ns, which correspond to cavity lengths going from 10 cm to 1m. *Short cavities* that are only a few centimeters long have been recently studied [84, 85].

The quantity $\omega\tau$ is often called the *phase accumulation* in the external cavity or the *feedback phase*. Obtaining a specific value of $\omega\tau$ necessitates an extremely precise (sub-wavelength and therefore sub-micrometric) positioning of the external mirror. It is important to note that the three variables A , ϕ , and N are no longer independent, and that chaotic solutions can therefore exist. Additionally, the presence of a delay creates an infinite number of degrees of freedom and potentially very high-dimensional dynamics. This model neglects multiple reflections on the external mirror and is valid only for "weak to moderate" feedback ($\kappa \ll 1$).

From Eq. (36), it is easy to determine the equations of the amplitude and the phase of the electric field

$$\frac{dA(t)}{dt} = \left\{ \frac{1}{2} [G(N, A^2) - \frac{1}{\tau_p}] \right\} A(t) + \gamma A(t - \tau) \cos[\omega\tau + \phi(t) - \phi(t - \tau)], \quad (38)$$

$$\frac{d\phi(t)}{dt} = \frac{\alpha}{2} [G(N, A^2) - \frac{1}{\tau_p}] - \gamma \frac{A(t - \tau)}{A(t)} \sin[\omega\tau + \phi(t) - \phi(t - \tau)]. \quad (39)$$

Despite its simplicity, this model has proved to be extremely successful. A great number of experimentally observed dynamical behaviors have been reproduced with this model, and some unknown behaviors have been predicted and later confirmed experimentally.

3.2.2.2 Stationary solutions and dynamical behavior

In the case of a solitary laser, the stationary solutions, which correspond to a laser in a continuous-wave regime, can be easily found by imposing the following conditions in the rate equations (32), (34), (35)

$$A(t) = A_{Stat}, \quad (40)$$

$$\Omega(t) = \omega t + \phi(t) = \omega_{Stat}, \quad (41)$$

$$N(t) = N_{Stat}, \quad (42)$$

where A_{Stat} , ω_{Stat} , and N_{Stat} are constants that correspond to the values of the amplitude, frequency, and carrier number in a stationary regime. Neglecting the gain saturation, we obtain the following stationary solution

$$N_{Stat} = N_0 + \frac{1}{G_N \tau_p}, \quad (43)$$

$$A_{Stat} = \sqrt{\frac{\frac{J}{e} - \frac{N_{Stat}}{\tau_n}}{G_N(N_{Stat} - N_0)}}, \quad (44)$$

$$\omega_{Stat} = \omega. \quad (45)$$

This solution exists only if the quantity in the square root in (44) is positive, which occurs if the injection current is larger than the threshold current J_{th} given by

$$J_{th} = \frac{e N_{Stat}}{\tau_n} = \frac{e N_{th}}{\tau_n}, \quad (46)$$

where $N_{th} = N_{Stat}$ is the carrier concentration at threshold. When the injection current is larger than the threshold value, the laser emits coherent light whose intensity increases with J , while the frequency and the carrier number remain clamped to the threshold values.

We consider now the case of a laser subjected to external optical feedback. Proceeding similarly to the preceding case, and neglecting the gain saturation, it is found that an external cavity laser has several stationary solutions whose frequencies ω_{Stat} are of the form $(1/\tau)y_Z$, where y_Z are the zeros of the function

$$f(y) = y - \omega\tau + \gamma\tau\sqrt{1 + \alpha^2} \sin[y + \arctan(\alpha)]. \quad (47)$$

The values of the stationary carrier number and of the amplitude of the electric field are given by

$$N_{Stat} = N_{th} - \frac{2\gamma\tau_p}{G_N} \cos(\omega_{Stat}\tau), \quad (48)$$

$$A_{Stat} = \sqrt{\frac{\frac{J}{e} - \frac{N_{Stat}}{\tau_n}}{G_N(N_{Stat} - N_0)}}. \quad (49)$$

The number of stationary solutions of an external-cavity laser is therefore equal to the number of zeros of the function $f(y)$, represented in Fig. 11. A linear stability analysis

shows that the zeros for which $f(y)$ cuts the y axis with a negative slope correspond to unstable stationary solutions called antimodes. When the y axis is cut with a positive slope, the corresponding stationary solutions can be stable and are called external-cavity modes.

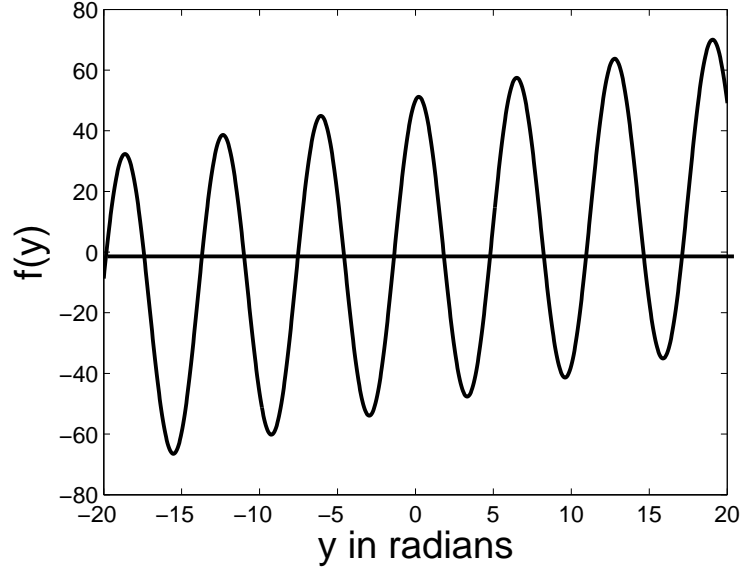


Figure 11: The zeros y_Z of $f(y)$ give the values of $\omega_{Stat}\tau$.

It is easy to see that when the feedback rate γ or the delay τ are increased, additional stationary solutions appear by mode–antimode pairs, corresponding to saddle-node [4] bifurcations. When γ or τ are further increased, some of the modes can be destabilized and chaotic attractor can appear near (in phase space) the formerly stable modes. Several nearby chaotic attractors can merge and lead to a trajectory in phase space that visits all of them in a process called chaotic itinerancy. The corresponding chaotic state is named “fully-developed coherence collapse” and is an indication of high-dimensional chaos [86, 87].

A classification of the dynamical behaviors of external-cavity laser diodes has been established for increasing feedback rates:

- Regime I: For very low feedback rates, only one external-cavity mode exists. The laser linewidth is smaller or larger than that of the solitary laser, depending on the value of the feedback phase.

- Regime II: For larger feedbacks, mode hopping between the different existing external cavity modes occurs.
- Regime III: When the feedback rate is increased, the frequency of mode hopping decreases and in regime III, the laser oscillates in only one external cavity mode, which is the mode of minimum linewidth.
- Regime IV: In this regime of moderate feedback, coherence collapse occurs. The linewidth of the laser increases greatly and the output power varies chaotically.
- Regime V: In this regime of strong feedback, the laser oscillates in only one stable mode and the linewidth is greatly decreased.

These different regimes have been observed both numerically with the Lang and Kobayashi model and experimentally. Another interesting dynamical regime is the regime of “low-frequency fluctuations” (LFF), which usually occurs for an injection current close to the solitary laser threshold. A LFF regime is characterized by brutal dropouts of the mean power of the laser, followed by progressive power buildups [88]. The brutal power dropouts often occur at irregular times but, in certain cases, the time interval is almost constant, and the regime is named “periodic LFF”. We refer the reader to the thesis manuscripts [89] and [90] for more details on the various dynamical regimes of external-cavity lasers.

3.2.3 Unidirectionally coupled external-cavity lasers

As mentioned in the introduction, the synchronization of chaotic semiconductor lasers has been extensively studied since these devices are key elements of all-optical communication systems. In particular, external-cavity semiconductor lasers have attracted considerable attention (see for example [91] and references therein). When we started our work on the synchronization of ECLs, however, despite the relatively large literature on the subject, it was not clear that there existed two different types of synchronization. We can cite as an example the experimental paper [92] called “Experimental verification of the synchronization condition for chaotic external-cavity diode lasers”. The authors claim to have verified *the* synchronization condition, when it is only *a* synchronization condition for a specific regime.

Moreover, the authors cite references that correspond to very different operating conditions as if they corresponded to the same. We contributed to put the existence of two types of synchronization into light [93, 94, 91], and we studied the robustness and stability regions of these two synchronization regimes. As we mentioned before, the synchronization is a particularly critical phenomenon for chaotic communications, thus we think this work can be useful in real applications of secure communications using ECLs. When we began this research, the importance of the presence or the absence of an external-cavity at the slave laser was not clearly understood. We have studied this aspect also, in light of the results on the two synchronization regimes. We should also cite the work that has been done during a similar time frame by Murakami and Ohtsubo [95] and by Koryukin and Mandel [96].

We present in this section the model used for unidirectionally coupled external-cavity lasers. In section 3.2.4, we describe the different possible synchronized solutions. In Section 3.2.5, we discuss the parameter regions in which the two types of synchronization occur, and section 3.2.6 explains under which circumstances transitions between synchronization regimes may occur.

Figure 50 shows schematically the setup of the system under study. The master laser (ML) and the slave laser (SL) are identical semiconductor lasers with optical feedback from external mirrors. We assume that the mirrors are positioned in such a way that the external cavity length (defined as the distance between the laser facet and the mirror) is the same for both lasers. The output of the ML is injected into the SL via the optical isolator (OI). The rate equations for the complex electric fields and carrier densities in the lasers are the Lang-Kobayashi equations, where the equation for the field in the SL contains an additional term that accounts for the optical injection from the ML [97]. The equations are

$$\begin{aligned} \dot{E}_i = & \frac{1+i\alpha}{2}[G_i(t) - 1/\tau_{p,i}]E_i(t) + \gamma_i E_i(t-\tau) \exp[-i(\omega\tau)_i] \\ & + \eta E_m(t-\tau_c) \exp[-i(\omega_m\tau_c - \Delta\omega t)] , \end{aligned} \quad (50)$$

$$\dot{N}_i = J_i/e - N_i(t)/\tau_{n,i} - G_i(t)|E_i(t)|^2 . \quad (51)$$

Here, the indices $i = m, s$ refer to the ML and the SL respectively. The term $\eta E_m(t - \tau_c) \exp[-i(\omega_m\tau_c - \Delta\omega t)]$ in Eq. (50) exists only for the SL, and accounts for the light

injected from the ML. The quantity $\Delta\omega = \omega_m - \omega_s$ is the frequency detuning between the lasers, and η , the injection rate, measures the fraction of the output power of the master laser that is injected into slave laser cavity.

We have assumed that the optical field does not experience any distortion during its propagation from the master to the slave laser. We have also neglected the spontaneous emission noise, which degrades the synchronization quality [98, 94].

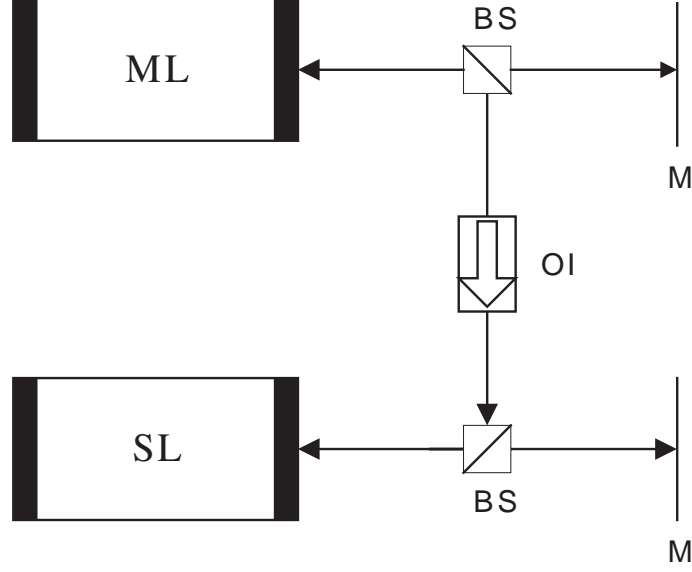


Figure 12: Schematic representation of unidirectionally coupled external-cavity lasers. ML: Master Laser; SL: Slave Laser; OI: Optical Isolator; BS: Beam Splitter; M: Mirror.

To characterize the quality of the synchronization between the output intensities of the lasers we calculate two correlation coefficients:

$$C_1 = \frac{\langle [I_m(t + \tau_1) - \langle I_m \rangle][I_s(t) - \langle I_s \rangle] \rangle}{[\langle (I_m(t) - \langle I_m \rangle)^2 \rangle \langle (I_s(t) - \langle I_s \rangle)^2 \rangle]^{1/2}}, \quad (52)$$

$$C_2 = \frac{\langle [I_m(t + \tau_2) - \langle I_m \rangle][I_s(t) - \langle I_s \rangle] \rangle}{[\langle (I_m(t) - \langle I_m \rangle)^2 \rangle \langle (I_s(t) - \langle I_s \rangle)^2 \rangle]^{1/2}}, \quad (53)$$

where $\tau_1 = -\tau_c$, $\tau_2 = \tau - \tau_c$, and $\langle \dots \rangle$ represents time averaging. The regime of isochronous synchronization with lag-time τ_c is characterized by a large value of C_1 , while the regime of anticipated synchronization with lag-time $\tau_c - \tau$, is characterized by a large

value of C_2 .

3.2.4 Time lagged synchronous solutions

If there is no frequency detuning ($\omega_m = \omega_s = \omega$), Eqs. (50) and (51) can be rewritten as

$$\dot{I}_m(t) = [G_m(t) - 1/\tau_{p,m}]I_m(t) + 2\gamma_m\sqrt{I_m(t-\tau)I_m(t)}\cos\xi_m(t,\tau), \quad (54)$$

$$\dot{\psi}_m(t) = \frac{\alpha}{2}[G_m(t) - 1/\tau_{p,m}] - \gamma_m\sqrt{\frac{I_m(t-\tau)}{I_m(t)}}\sin\xi_m(t,\tau), \quad (55)$$

$$\dot{N}_m(t) = J_m/e - N_m(t)/\tau_{n,m} - G_m(t)I_m(t), \quad (56)$$

$$\begin{aligned} \dot{I}_s(t) = & [G_s(t) - 1/\tau_{p,s}]I_s(t) + 2\gamma_s\sqrt{I_s(t-\tau)I_s(t)}\cos\xi_s(t,\tau) \\ & + 2\eta\sqrt{I_m(t-\tau_c)I_s(t)}\cos\xi_{ms}(t,\tau_c), \end{aligned} \quad (57)$$

$$\begin{aligned} \dot{\psi}_s(t) = & \frac{\alpha}{2}[G_s(t) - 1/\tau_{p,s}] - \gamma_s\sqrt{\frac{I_s(t-\tau)}{I_s(t)}}\sin\xi_s(t,\tau) \\ & - \eta\sqrt{\frac{I_m(t-\tau_c)}{I_s(t)}}\sin\xi_{ms}(t,\tau_c), \end{aligned} \quad (58)$$

$$\dot{N}_s(t) = J_s/e - N_s(t)/\tau_{n,s} - G_s(t)I_s(t) \quad (59)$$

where I_m , ϕ_m , I_s , and ϕ_s are the intensity and the phase of the master and the slave lasers [$E_m = \sqrt{I_m}e^{i\phi_m}$, $E_s = \sqrt{I_s}e^{i\phi_s}$, $\xi_m(t,\tau) = \phi_m(t) - \phi_m(t-\tau) + \omega\tau$, $\xi_s(t,\tau) = \phi_s(t) - \phi_s(t-\tau) + \omega\tau$ and $\xi_{ms}(t,\tau_c) = \phi_s(t) - \phi_m(t-\tau_c) + \omega\tau_c$].

The two synchronization regimes are the following:

1. *Anticipated synchronization.* If the operating conditions and the internal parameters of the lasers are identical, and the feedback levels of the master and the slave lasers are related by the condition $\gamma_m = \gamma_s + \eta$, it can be shown that the synchronization manifold is

$$I_s(t-\tau) = I_m(t-\tau_c), \quad (60)$$

$$\xi_s(t,\tau) = \xi_{ms}(t,\tau_c) \Rightarrow \phi_s(t-\tau) - \omega\tau = \phi_m(t-\tau_c) - \omega\tau_c, \quad (61)$$

$$N_s(t-\tau) = N_m(t-\tau_c). \quad (62)$$

This corresponds to the complete (or identical) synchronization of the coupled systems with a lag time $\tau_c - \tau$. In the expression of the time lag, the term τ_c is due to the

propagation time of light between the two lasers, while the term τ is due to the fact that the master is a time-delayed system [99, 100]. When $\tau_c < \tau$, the optical field of the slave laser at time t anticipates the optical field of the master laser at time t [99]; otherwise it lags behind. The lag time $\tau_c - \tau$ is typical of unidirectionally coupled time-delayed systems.

2. *Isochronous synchronization.* If the lasers have the same operating conditions, equal feedback levels ($\gamma_m = \gamma_s$), equal internal parameters except maybe for the cavity decays and the laser frequencies⁵, the following *approximative* synchronized solution can be found

$$I_s(t) = aI_m(t - \tau_c), \quad (63)$$

$$\phi_s(t) = \phi_m(t - \tau_c) - \omega\tau_c + \Delta\phi + \Delta\omega t, N_s(t) = N_m(t - \tau_c) + \Delta_N, \quad (64)$$

where a , $\Delta\phi$, and Δ_N are constants. In this case, the slave laser synchronizes with the injected field, and due to the finite speed of propagation, the slave laser always lags in time behind the master laser. Since there is a functional relation between the states of the master and slave systems, this corresponds to generalized synchronization [50] of the coupled systems, with a lag time τ_c . The solution is approximative because certain approximations have to be made to find it. We have not included here the relatively long analytical developments that have to be performed to determine this solution and refer the interested reader to the reference [101].

We can also consider the case in which the slave laser is a solitary laser, subjected only to optical injection from the master laser (open-loop scheme). In this case, when the injection rate is equal to the master feedback rate ($\eta = \gamma_m$) a synchronized solution with a lag time $\tau_c - \tau$ exists. This synchronized solution is simply a special case of solution (60)-(62) when the slave is not subjected to feedback ($\gamma_s = 0$). Several authors [102, 96, 103, 95] have found that it is also possible to obtain a certain degree of synchronization with a lag time τ_c with an open-loop scheme. With an open-loop scheme, however, a chaotic synchronized

⁵therefore this solution exists even in presence of a frequency detuning

solution with a lag time τ_c does not exist, because in case 2 the lasers must be subjected to the same feedback level. Koryukin and Mandel have shown [96] that, in the special case $\eta = \gamma_m$, a perfectly synchronized solution with a lag time τ_c exists if the amplitude and the phase of the slowly-varying optical field are periodic, with a period τ/N , where N is a positive integer.

3.2.5 Synchronization regions

We have simulated Eqs. 50 and 51 for the realistic parameter values $\tau = 1$ ns, $\tau_p = 2$ ps, $\tau_n = 2$ ns, $\alpha = 5$, $G_n = 1.5 \times 10^4$ s⁻¹, $N_0 = 1.5 \times 10^8$, $\epsilon = 5 \times 10^{-7}$, $\omega\tau = 0$ rad. We assume that the internal parameters are identical for the two lasers.

First, we characterize the synchronization regions in the parameter space (frequency detuning, injection rate). The synchronization regions strongly depend on the chaotic behavior of the master laser, which in turn is determined by the injection current and the feedback level. Let us consider a situation in which the lasers operate well above threshold ($J_m = J_s = 1.85J_{th}$, where $J_{th} = 14.7$ mA is the threshold current of the solitary laser) and the master laser is subjected to moderated optical feedback ($\gamma_m = 10$ ns⁻¹). For these parameters the master laser is in the coherence collapse (CC) regime (*cf.* §3.2.2.2), characterized by fast, chaotic intensity fluctuations (see Fig. 13).

In Fig. 14 (a) we show the synchronization region when the lasers are subject to the same feedback level ($\gamma_s = \gamma_m = 10$ ns⁻¹). The horizontal axis is the frequency detuning between the lasers, the vertical axis is the optical injection rate, and the gray levels represent the value of C_1 (the dark gray represents large correlation). The synchronization region is broad, allowing for frequency detunings up to tens of gigahertz, and is asymmetric. Figure 14 (b) displays the same correlation coefficient as Fig. 14 (a) (and for the same parameter values), but when the slave laser is subjected to CW optical injection. As was reported in Ref. [101] for the case of an open-loop scheme, we find that the shapes of the chaotic synchronization region [in Fig. 14 (a)] and the CW injection-locking region [in Fig 14 (b)] are similar. We can see that the chaotic synchronization region is broader than the CW injection-locking region. The similarity of the two regions suggests that isochronous synchronization is an

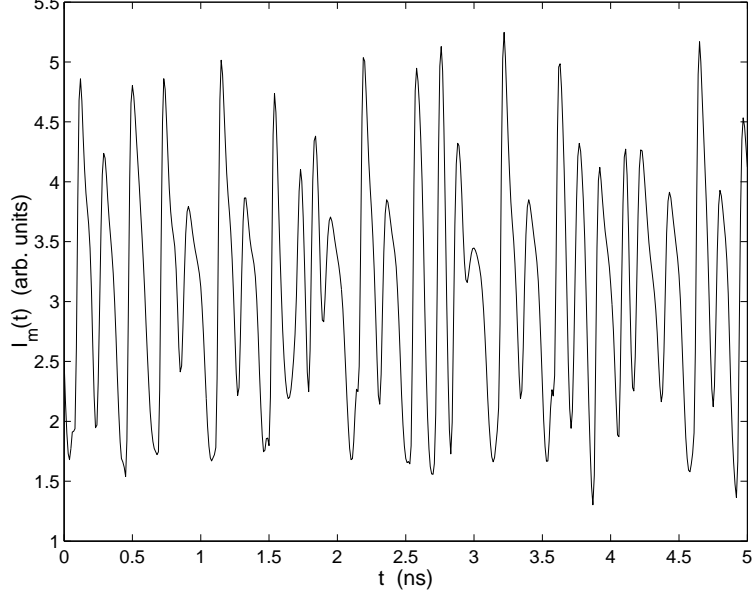


Figure 13: Intensity fluctuations of the ML operating on the coherence collapse regime. The parameters are: $\gamma_m = 10 \text{ ns}^{-1}$, $J_m = 1.85 \times J_{th} = 27.2 \text{ mA}$, $\tau = 1 \text{ ns}$, $\tau_p = 2 \text{ ps}$, $\tau_n = 2 \text{ ns}$, $\alpha = 5$, $G_n = 1.5 \times 10^4 \text{ s}^{-1}$, $N_0 = 1.5 \times 10^8$, $\epsilon = 5 \times 10^{-7}$, $\omega\tau = 0 \text{ rad}$.

injection-locking-type phenomenon.

Figures 15 (a) and (b) show the same quantities as Figs. 14 (a) and (b) but in the case of an open-loop scheme ($\gamma_s = 0$). Again we observe that there is a similarity between the chaotic synchronization region in Fig. 15 (a) and the CW injection-locking region in Fig. 15 (b). Comparing Figs. 14 (a) and 15 (a) (which are plotted with the same gray-scale), it is clear that the synchronization quality is in general lower when the slave laser does not have its own feedback. For example, for zero frequency detuning and for the maximum injection rate considered in Figs. 14 (a) and 15 (a) ($\eta = 50 \text{ ns}^{-1}$), $C_1 = 0.999$ for a close-loop scheme while $C_1 = 0.86$ for an open-loop scheme. Moreover, in order to obtain a correlation coefficient of 0.99 with an open-loop scheme, the injection rate has to be increased to as much as 170 ns^{-1} for our parameter values. The lower degree of correlation is a disadvantage when comparing open- and closed-loop schemes. Since the coupling strength has a maximum value in a real experiment, it will not always be possible to achieve a good degree of synchronization with an open-loop scheme. Similar results were experimentally obtained in Ref. [103]: the injected power had to be about one hundred

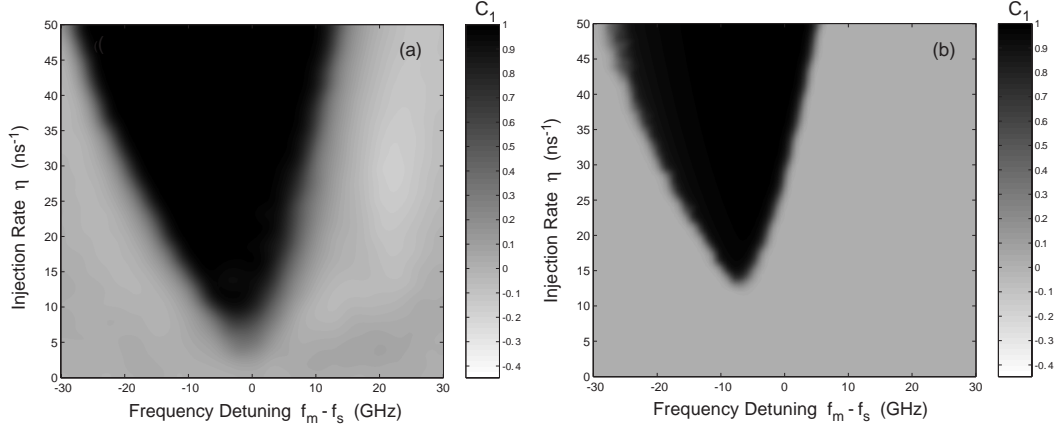


Figure 14: (a) Correlation coefficient C_1 as a function of the frequency detuning and the optical coupling strength, when the slave is an external cavity laser subjected to chaotic injection from the master laser. $\gamma_m = \gamma_s = 10 \text{ ns}^{-1}$. (b) Correlation coefficient C_1 as a function of the frequency detuning and the optical coupling strength, when the slave is an external cavity laser subjected to CW injection from the master laser. $\gamma_s = 10 \text{ ns}^{-1}$. All other parameters as Fig. 13.

times larger than the power fed back into the master laser cavity in order to observe good synchronization with an open-loop scheme.

The difference in synchronization quality for the cases of a SL with or without feedback at a lag time τ_c can be explained by the fact that when $\gamma_m = \gamma_s$, an analytical synchronized solution exists (63-64). On the contrary, as discussed in the previous section, when $\gamma_s = 0$ no such solution exists. Therefore, in the case of an open-loop scheme, chaotic synchronization with a lag time τ_c corresponds to a direct generalization of CW injection-locking, whereas in the case of a closed-loop scheme there is “true” synchronization in the sense that a synchronized solution exists. As a consequence the synchronization with a closed-loop scheme has advantages for applications where a high degree of synchronization is required; it has the disadvantage, however, that additional components have to be used in the experimental setup. In particular, the external mirror at the slave laser has to be very carefully positioned such that the phase accumulations in the external cavities verify $(\omega\tau)_m - (\omega\tau)_s = (\omega_m - \omega_s)\tau$.

This fact is shown in Fig. 16, where we assume that the lasers have identical frequencies but slightly different delay times. It is clear that small differences in the delay times strongly

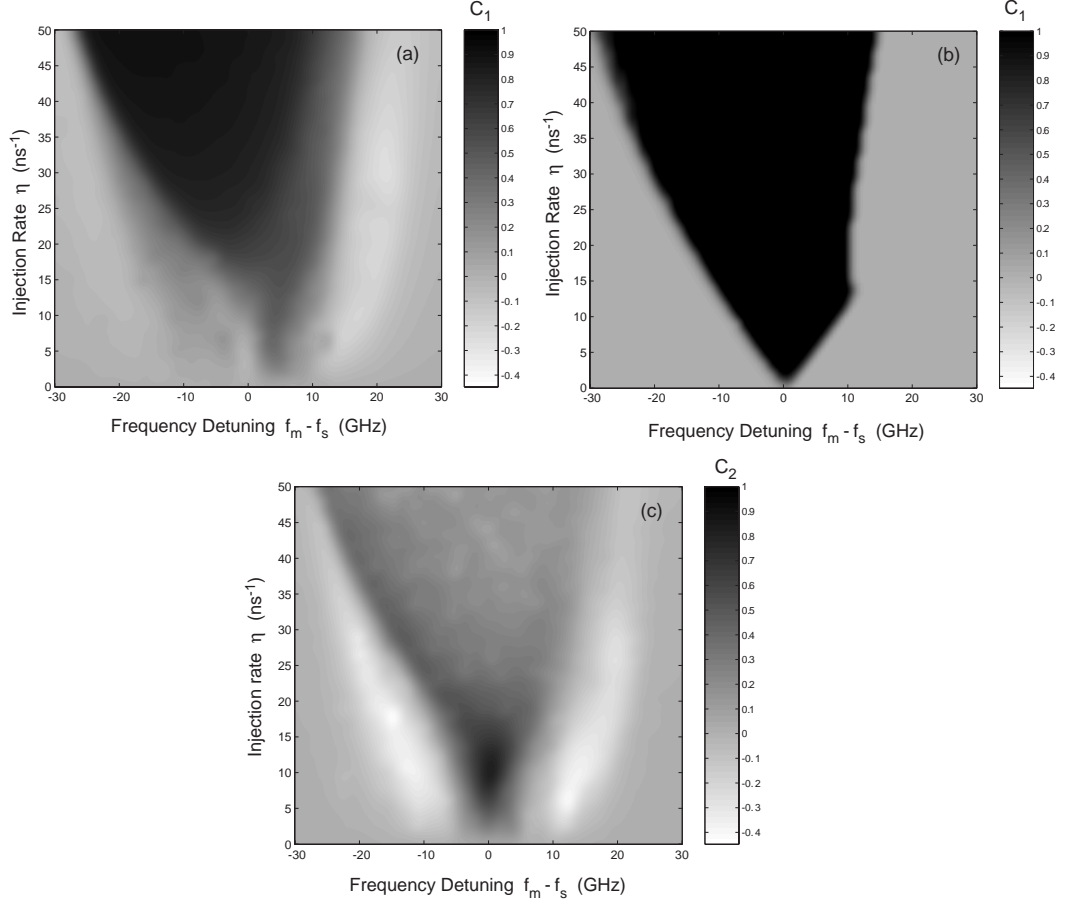


Figure 15: (a) Correlation coefficient C_1 as a function of the frequency detuning and the optical coupling strength, when the slave laser is subjected only to chaotic injection from the master laser. $\gamma_m = 10 \text{ ns}^{-1}$, $\gamma_s = 0$. (b) Correlation coefficient C_1 as a function of the frequency detuning and the optical coupling strength, when the slave laser is subjected only to CW injection from the master laser. $\gamma_s = 0 \text{ ns}^{-1}$. (c) Correlation coefficient C_2 as a function of the frequency detuning and the optical coupling strength, when the slave laser is subjected only to chaotic injection from the master laser. All other parameters as Fig. 13.

degrade the synchronization quality.

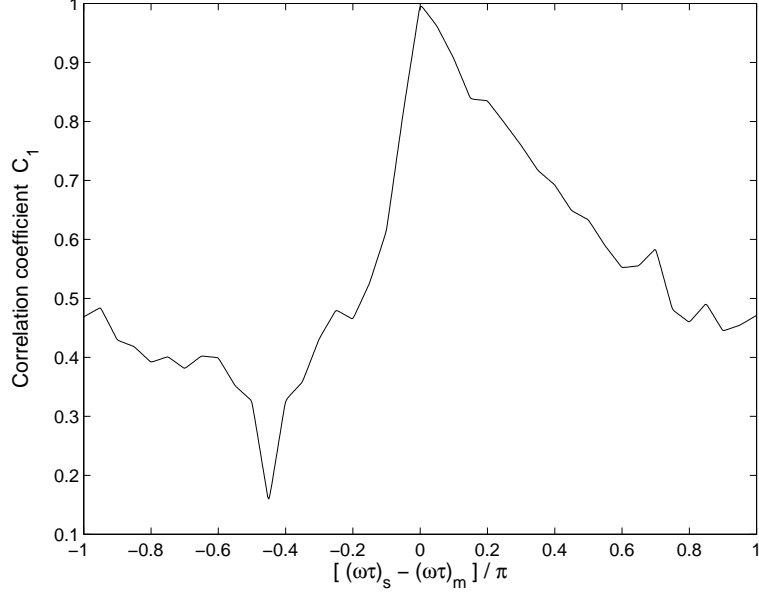


Figure 16: Correlation coefficient C_1 as a function of the difference between the phase accumulations in the external cavities of the slave laser, $(\omega\tau)_s$, and of the master laser, $(\omega\tau)_m$. $\Delta\omega=0$, $\eta = 25 \text{ ns}^{-1}$, all other parameters as Fig. 13.

Since in the case of an open-loop scheme synchronization with a lag-time $\tau_c - \tau$ is possible when $\eta = \gamma_m$ and $\Delta\omega = 0$, it is also interesting to study the value of C_2 , defined in Eq. (15), in the parameter space (detuning, injection rate). This is displayed in Fig. 15 (c), which shows C_2 on the same gray-scale as Figs. 14 (a) and 15 (a). Comparing Figs. 15 (a) and (c) it is clear that the correlation coefficient C_1 calculated with a lag time τ_c is usually larger than the correlation coefficient C_2 calculated with a lag time $\tau_c - \tau$. However, when $\eta \sim \gamma_m$ and for small detuning, $C_2 > C_1$. This is because when $\eta = \gamma_m$ and $\Delta\omega = 0$ an analytic solution exists for synchronization with a lag time $\tau_c - \tau$, as discussed in the previous section. We obtain a reasonable quality of synchronization for frequency detunings up to a few GHz. Notice that in the two white regions in Fig. 15 (c) a certain degree of antisynchronization occurs since the correlation coefficient is negative (the dynamics is not anticorrelated, however, since in these regions C_2 is at most -0.4).

Figure 17 shows the value of C_2 when the slave laser is an external-cavity laser and its feedback level is varied such that $\gamma_s = \gamma_m - \eta$. As mentioned before, this is a necessary

condition for the existence of a perfectly synchronized solution with a lag time $\tau_c - \tau$, in the absence of frequency detuning. Since γ_s cannot be negative, we are restricted in Fig. 17 to a maximum value of the injection rate η , which is the feedback rate of the master laser, $\gamma_m = 10 \text{ ns}^{-1}$. It can be seen that even when there is no frequency detuning (in this case a perfectly synchronized solution exists) synchronization does not occur for small injection rates. This means that the synchronized solution is stable only for large enough injection rates (and hence small enough slave feedback rates). Moreover, contrary to the two preceding cases, a reasonably good level of synchronization is preserved for detunings of only few GHz.

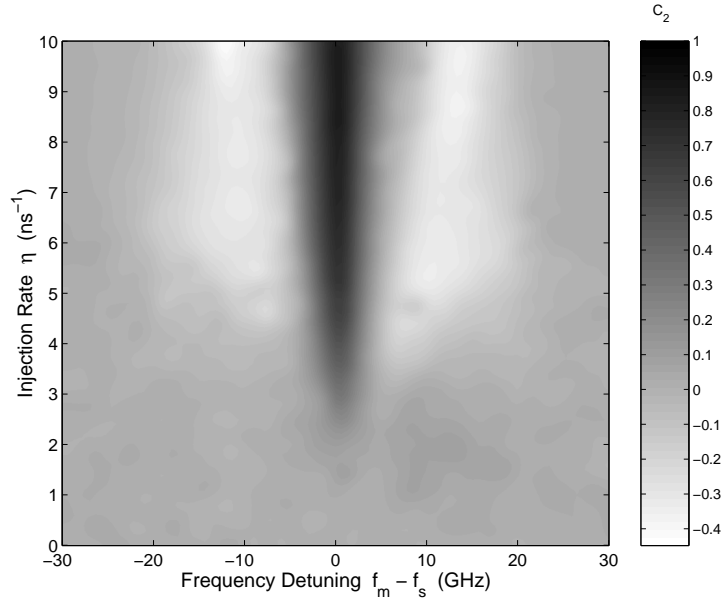


Figure 17: Correlation coefficient C_2 as a function of the frequency detuning and the optical coupling strength, when $\gamma_s = \gamma_m - \eta$. All other parameters as Fig. 15.

As mentioned before, from the mathematical point of view the phase space of the ML is infinite dimensional because of the delayed feedback. It is well accepted that the dimension of the chaotic attractor associated with the master-laser dynamics increases with the feedback rate γ_m (and with the delay time τ). It is therefore interesting to determine how the synchronization quality evolves when the master feedback rate is changed, and how the minimum injection rate above which synchronization occurs depends on the master feedback rate.

Figure 18 displays the synchronization regions in the parameter space (master feedback rate, injection rate) when there is no frequency detuning. In Fig. 18 (a) $\gamma_s = \gamma_m$, in Fig. 18 (b) $\gamma_s = 0$, and in Fig. 18(c) $\gamma_s = \gamma_m - \eta$. Since γ_s cannot be negative, in Fig. 18 (c) the maximum value of η is γ_m . As in the previous figures, Figs. 18 (a) and (b) display the value of C_1 , while Fig. 18 (c) displays the value of C_2 . It can be clearly seen that when γ_m increases, the injection rate has to be increased in order to maintain the synchronization quality. For example, when $\gamma_s = \gamma_m$ a correlation coefficient $C_1 > 0.999$ can be obtained for an injection rate $\eta > 20 \text{ ns}^{-1}$ for $\gamma_m = 10 \text{ ns}^{-1}$, while $\eta > 45 \text{ ns}^{-1}$ for $\gamma_m = 20 \text{ ns}^{-1}$. In the case of an open-loop scheme, an injection rate as high as 100 ns^{-1} leads to a correlation coefficient $C_1 = 0.95$ when $\gamma_m = 10 \text{ ns}^{-1}$ and $C_1 = 0.79$ when $\gamma_m = 20 \text{ ns}^{-1}$. Since in experiments the injection rate has a maximum value, it can be expected that there is a maximum value of the master feedback rate above which high quality synchronization with an open-loop scheme is not possible. Figure 18 (c) shows that in the case of anticipated synchronization there is also the need to increase the injection rate when the master feedback rate is increased. Moreover, one can notice that the larger the value of the feedback rate γ_m , the closer η must be to γ_m in order to ensure good synchronization.

As we have seen, with an open-loop scheme it is possible to observe synchronization with a lag time $\tau_c - \tau$ (if $\eta = \gamma_m$), and also synchronization with a lag time τ_c . Therefore, it might be that under adequate conditions the two regimes coexist (*i.e.* they occur for identical or close parameter values). This possibility is studied in the next section.

3.2.6 Transitions between synchronization regimes

As we have seen, with an open-loop scheme it is possible to observe synchronization with a lag time $\tau_c - \tau$ (if $\eta = \gamma_m$), and also synchronization with a lag time τ_c . Therefore, it might be that under adequate conditions the two regimes coexist (*i.e.* they occur for identical or close parameter values).

Koryukin and Mandel [96] have recently shown that a transition between synchronization with lag-time $\tau_c - \tau$ to synchronization with lag-time τ_c occurs when the injection rate η is slightly *increased* above γ_m or when the injection current J_s is slightly *decreased* below

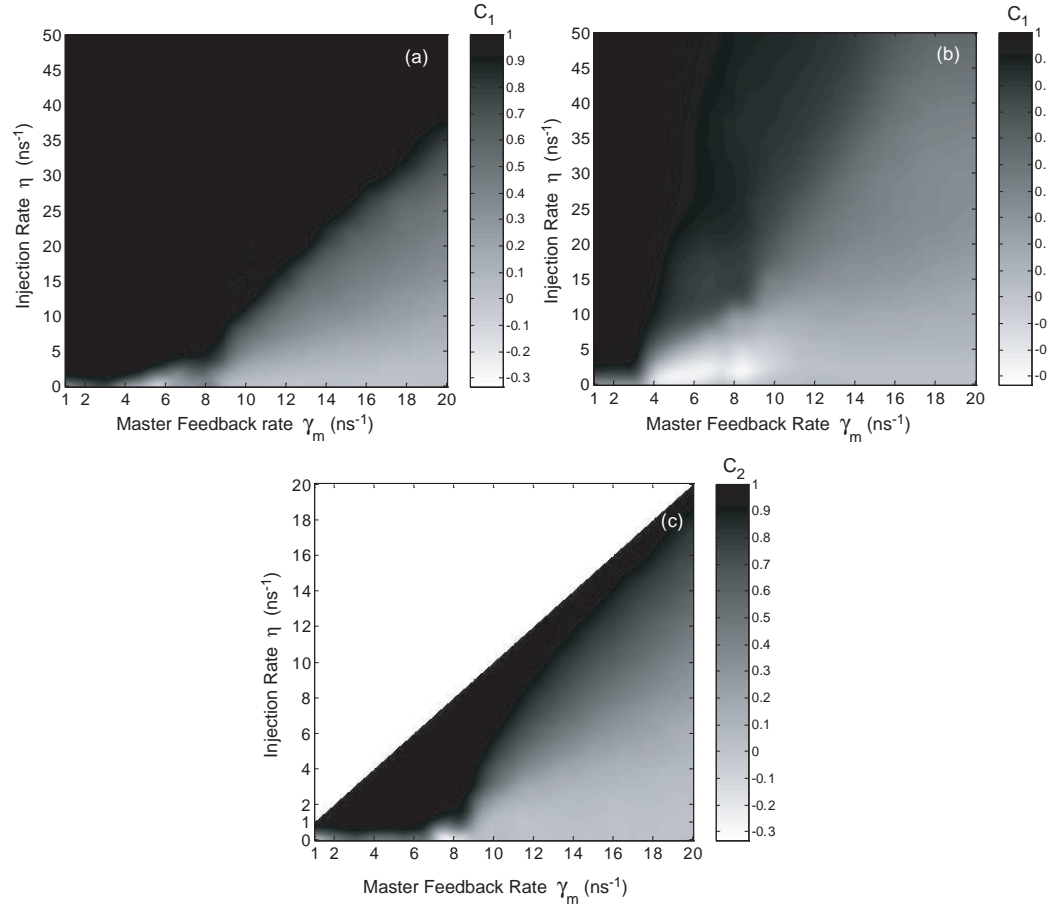


Figure 18: Synchronization regions in the parameter space (master feedback rate, optical coupling rate). (a) $\gamma_s = \gamma_m$, the value of C_1 is plotted. (b) $\gamma_s = 0$, the value of C_1 is plotted. (c) $\gamma_s = \gamma_m - \eta$, the value of C_2 is plotted. $\Delta\omega = 0$, all other parameters as Fig. 15.

J_m . The parameters considered in [96] correspond to a master laser operating in the low frequency fluctuations (LFF) regime (*cf.* §3.2.2.2). This regime occurs when the laser is biased close to the threshold and subjected to weak to moderate feedback, and is characterized by abrupt, random, intensity dropouts followed by deterministic, step-like recoveries.

In this section we analyze the possible transitions from one regime of synchronization to the other, in the case of an open-loop scheme, and considering an injection current close to threshold (such that the master laser operates in the LFF regime). Figures. 19 (a) and (b) display the correlation coefficients C_1 and C_2 , respectively, in the parameter space (frequency detuning, injection rate). All other parameters are the same as in Figs. 15 (a), (c) except that the injection current is lower ($J_m = J_s = 1.02J_{th}$).

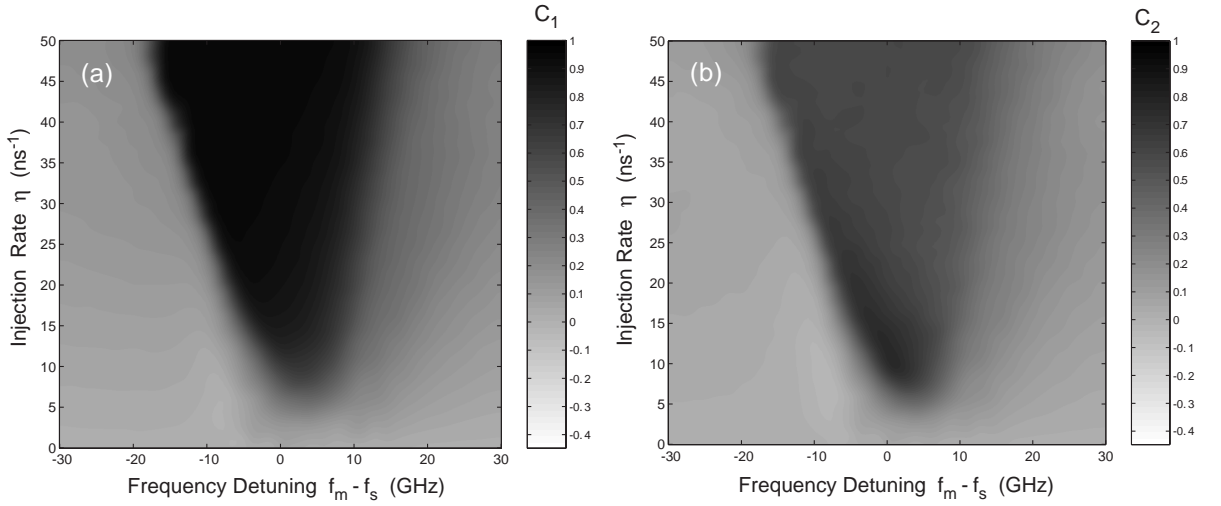


Figure 19: Correlation coefficients C_1 (a), C_2 (b) as a function of the frequency detuning and the optical coupling strength. $\gamma_m = 10 \text{ ns}^{-1}$, $\gamma_s = 0$, $J_m = J_s = 1.02 J_{th} = 15 \text{ mA}$. All other parameters as Fig. 15.

When comparing Fig. 19 (a) with Fig. 15 (a), it is clear that for lower current the synchronization region with lag-time τ_c *shifts down* towards lower values of η . As could be expected, Fig. 19 (b) shows that anticipated synchronization occurs when η is close to γ_m and the frequency detuning is small. Since the injection rate for synchronization with time-lag τ_c now is slightly larger than $\gamma_m (= 10 \text{ ns}^{-1})$, and the injection rate for synchronization with lag-time $\tau_c - \tau$ is still η equal or close to γ_m , a small increase of η above $\eta = \gamma_m$

will cause a transition from synchronization with lag-time $\tau_c - \tau$ to synchronization with time-lag τ_c . This is in agreement with the observations of Ref. [96].

This transition is illustrated in Fig. 20, which shows the ML and SL intensities, averaged in time to simulate the typical bandwidth of the detectors used in experiments. Fig. 20 (a) displays $I_m(t - \tau_c)$ for a feedback level $\gamma_m = 10 \text{ ns}^{-1}$, while Figs. 20 (b), (c) and (d) display $I_s(t)$ for different injection rates. Notice that in Fig. 20 (a) I_m is lagged τ_c in time. For $\eta = \gamma_m = 10 \text{ ns}^{-1}$ [Fig. 20 (b)] $I_s(t)$ is identical to $I_m(t - \tau_c + \tau)$, therefore $I_s(t)$ anticipates the injected intensity $I_m(t - \tau_c)$ by an anticipation time τ ($=1 \text{ ns}$). If η is increased to 12 ns^{-1} [Fig. 20 (c)] we observe a transition to synchronization with lag-time τ_c . Notice that the time traces shown in Figs. 20 (a) and 9 (c) are most of the time equal, the main difference being a less pronounced drop-out in the intensity of the slave laser. On the other hand, when η is decreased to 9 ns^{-1} [Fig. 20 (d)] synchronization with a lag time $\tau_c - \tau$ disappears (because the condition $\eta = \gamma_m$ is not met any more), and a transition to synchronization with a lag time τ_c does not occur (because the system is driven outside of the synchronization region). Notice that the time traces shown in Figs. 20 (a) and 20 (d) are completely different.

We also observe that, as previously reported in Ref. [96], when the injection current in the slave laser J_s is slightly decreased a transition to isochronous synchronization occurs, however, this transition does not happen if J_s is increased. In addition, we find that the transition occurs when the slave laser photon lifetime, $\tau_{p,s}$ or the carrier lifetime $\tau_{n,s}$ are *decreased* and when the slave carrier number at transparency $N_{0,s}$ is *increased*. The parameter changes that lead to a transition to synchronization with a lag time τ_c always correspond to a *decrease* of the solitary slave laser output power, I_s^{sol} . We have checked the generality of the above conclusion, by doing several parameter variations that compensated one another. It is remarkable that an increase of the injection rate (that causes a transition to synchronization with a lag time τ_c) and a decrease of the solitary slave laser power, I_s^{sol} , both correspond to an increase of the ratio between the injected power and the solitary slave power. A certain level of adequate parameter mismatch is needed to induce a transition between synchronization regions, but if the mismatches become too large, synchronization

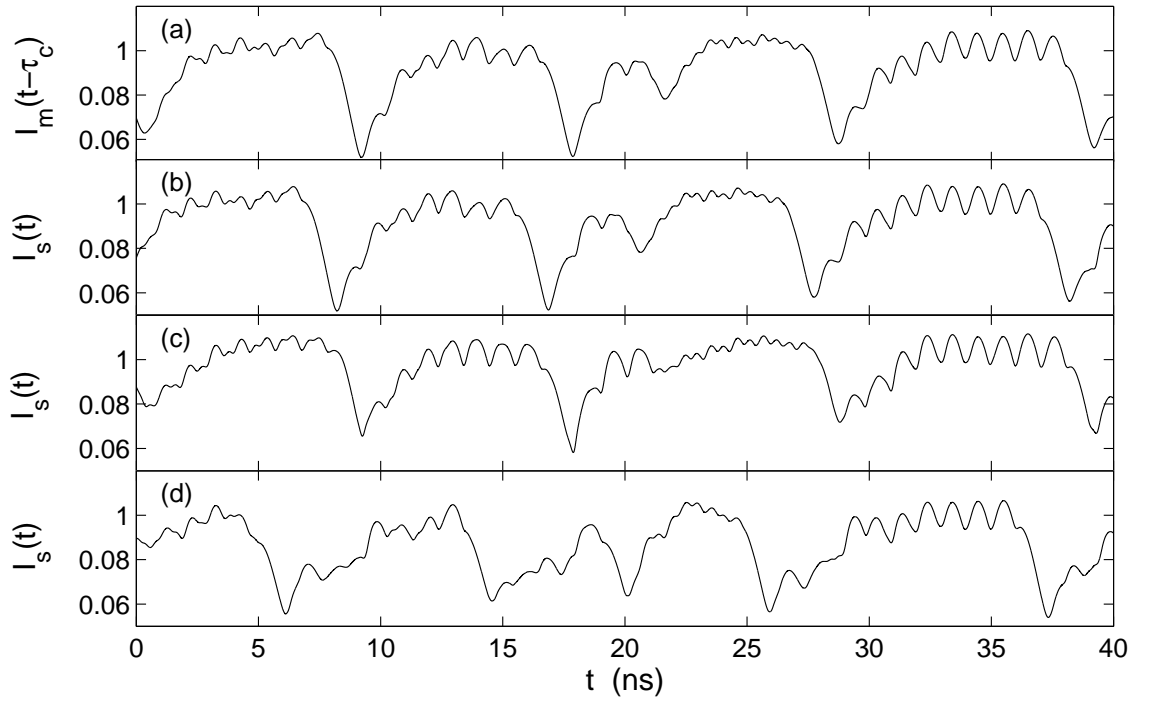


Figure 20: Time traces of the time-averaged intensities. (a) Intensity of the master laser (lagged τ_c in time) for $\gamma_m = 10 \text{ ns}^{-1}$. Intensity of the slave laser for (b) $\eta = \gamma_m$; (c) $\eta = 12 \text{ ns}^{-1}$; (d) $\eta = 9 \text{ ns}^{-1}$. $\Delta\omega = 0$, all other parameters as Fig. 15.

is lost. This is due to the fact that when the mismatch is too large, the chaotic attractors of the master and slave systems become too different to allow synchronized chaotic orbits [24]. We find that when $\tau_{p,s}$, $\tau_{n,s}$, J_s are increased (all these changes yield an increase of I_s^{sol}), neither type of synchronization occurs. If the injection rate η is increased (above γ_m), however, we find again isochronous synchronization. Therefore, synchronization with a lag time $\tau_c - \tau$ only occurs for almost identical parameters while small parameter mismatches either induce a transition to isochronous synchronization or destroy the synchronization. Since in an experimental setup the lasers will not have exactly identical parameters, our results suggest that it will be more likely to observe experimentally LFF synchronization with a lag time τ_c than with a lag $\tau_c - \tau$ where perfectly matched lasers and a strict observation of the synchronization condition $\eta = \gamma_m$ are needed.

Figure 21 shows as an example of these behaviors, the transitions that occur when a mismatch on τ_n is considered. Fig. 21 (a) displays the time-averaged master laser intensity, $I_m(t - \tau_c)$ for a feedback level $\gamma_m = 10 \text{ ns}^{-1}$ and a carrier lifetime $\tau_{n,m} = 2 \text{ ns}$, while Figs. 21 (b), (c), (d) and (e) display the slave laser time-averaged intensity, $I_s(t)$ for different injection rates and carrier lifetimes $\tau_{n,s}$. When $\tau_{n,s} = \tau_{n,m} = 2 \text{ ns}$ [Fig. 21 (b)], complete synchronization of $I_s(t)$ with $I_m(t - \tau_c)$ occurs with a lag-time τ . When $\tau_{n,s} = 1.99 \text{ ns}$, $I_s(t)$ [Fig. 21 (c)] synchronizes with $I_m(t - \tau_c)$ [Fig. 21 (a)] (notice that the dropouts occur nearly simultaneously, but the dropouts of the slave laser intensity are less pronounced). When $\tau_{n,s}$ is increased to 2.01 ns , Fig. 21 (d) confirms that none of the two synchronization regimes occur. In Fig. 21 (d) $\tau_{n,s} > \tau_{n,m}$ and $\eta = \gamma_m$; however, if η is increased to 12 ns^{-1} , synchronization of $I_s(t)$ [Fig. 21 (e)] with $I_m(t - \tau_c)$ [Fig. 21 (a)] occurs.

Figure 22 represents the correlation coefficient, $C(\tau^*)$, between the time-averaged $I_s(t)$ and $I_m(t - \tau_c + \tau^*)$, as a function of the variable τ^* , for the four cases considered above. When $\eta = \gamma_m = 10 \text{ ns}^{-1}$ and $\tau_{n,s} = \tau_{n,m} = 2 \text{ ns}$, the correlation coefficient exhibits a global maximum at $\tau^* = \tau$ [Fig. 22 (a)], while for $\tau_{n,s} = 1.99 \text{ ns}$ there is a very pronounced maximum located at $\tau^* = 0$ [Fig. 22 (b)]. When $\eta = \gamma_m$, $\tau_{n,s} = 2.01 \text{ ns}$ there is a much less pronounced maximum located at $\tau^* = \tau$ [Fig. 22 (c)]. In this case, neither type of synchronization occurs but there is still be a tendency to synchronization with a lag time

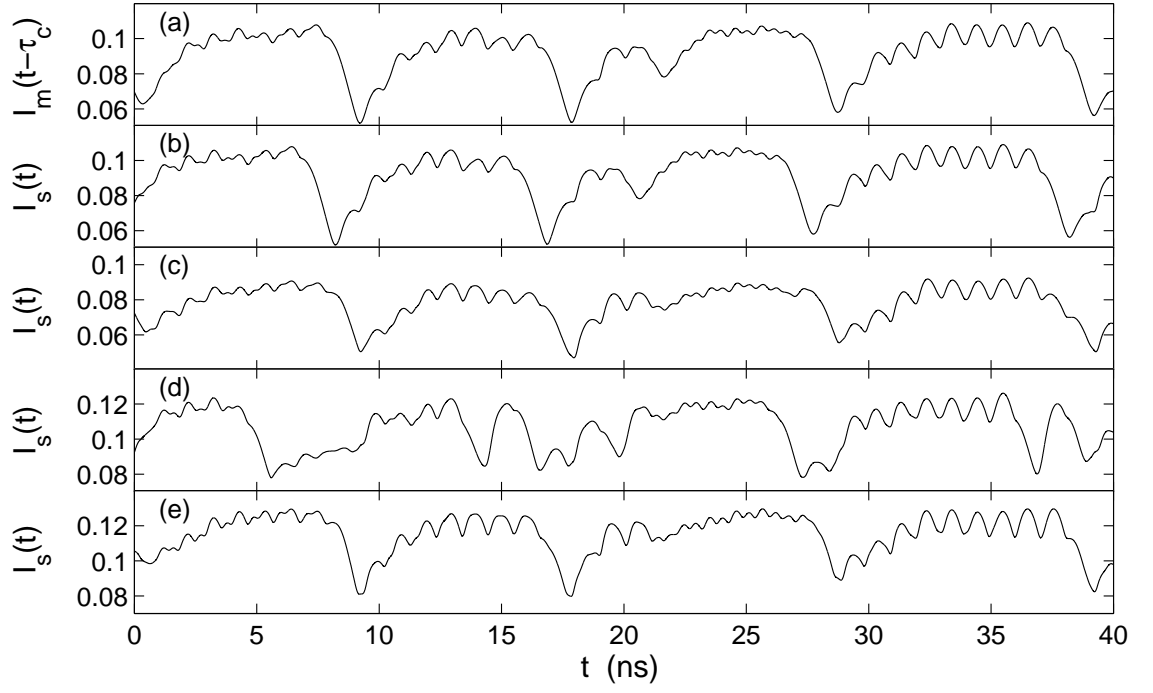


Figure 21: Time traces of the time-averaged intensities. (a) Intensity of the master laser (lagged τ_c in time) for $\gamma_m = 10 \text{ ns}^{-1}$ and $\tau_{n,m} = 2 \text{ ns}$. Intensity of the slave laser for (b) $\eta = \gamma_m$, $\tau_{n,s} = \tau_{n,m}$; (c) $\eta = \gamma_m$, $\tau_{n,s} = 1.99 \text{ ns}$; (d) $\eta = \gamma_m$, $\tau_{n,s} = 2.01 \text{ ns}$; (e) $\eta = 13 \text{ ns}^{-1}$, $\tau_{n,s} = 2.01 \text{ ns}$. $\Delta\omega = 0$, all other parameters as in Fig. 15.

$\tau_c - \tau$ during short intervals of time, explaining the maximum at $\tau^* = \tau$. If $\tau_{n,s}$ is further increased above $\tau_{n,m}$, this tendency is completely lost. Finally, when η is increased up to 13 ns^{-1} , maintaining $\gamma_m = 10 \text{ ns}^{-1}$, an increase of $\tau_{n,s}$ to 2.01 ns again a maximum located at zero is obtained. These results show that the function $C(\tau^*)$ can be a useful tool for analyzing synchronization regimes of coupled chaotic systems, and is also a good quantification of the synchronization error [104].

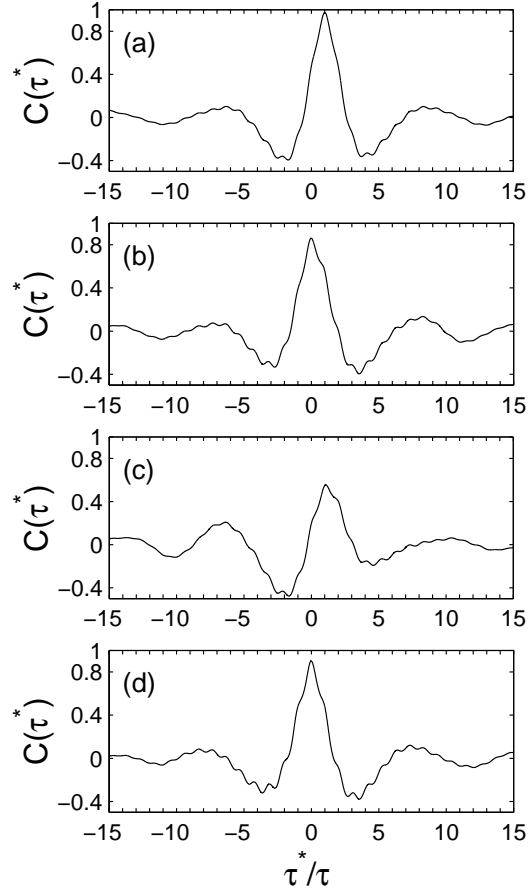


Figure 22: Correlation coefficient as a function of the lag-time (as explained in the text). Figs. (a), (b), (c), and (d) are for the same parameters as in Figs. 21 (b), (c), (d), and (e) respectively.

In this section, we have identified which parameter changes induce transitions between the two synchronization regimes, extending the results of Koryukin and Mandel [96]. As we have mentioned previously, numerical [103] and experimental [95] studies indicate that while synchronization with a lag time $\tau_c - \tau$ effectively occurs when $\eta = \gamma_m$, the injection

rate η must be much larger than γ_m in order to have synchronization with a lag time τ_c . For example, the experimental results of Ref. [103] show that, in order to observe synchronization with a lag time τ_c , the power that is optically injected into the slaver laser must be at least one hundred times larger than the power that is fed back into the master laser. Since the authors of Ref. [103] and [95] find that the two types of synchronization correspond to very different values of the injection rate, small injection rate or parameter changes cannot lead to transitions between the two types of synchronization.

This seems to contradict the results presented in this section. It is important to notice, however, that the dynamical regimes considered are different. In this section we considered a master laser operating in the LFF regime, while in Ref. [103], [95] the authors consider a master laser operating in the coherence collapse (CC) regime (as we have done in the previous section). In order to clearly show how the synchronization regions depend on the injected current, Fig. 23 displays the synchronization regions in the parameter space (injection current, injection rate). We consider an open-loop scheme, C_1 is represented in Fig. 23 (a) and C_2 in Fig. 23 (b). The white line displayed in Fig. 23 (a) corresponds to the injection rate above which C_1 is larger than 0.95. We see that for injection currents very close to threshold a good level of synchronization with lag-time τ_c can be obtained with small injection rates (η close to γ_m), but for larger injection currents, much larger injection rates are needed.

In Fig. 23 (b), good synchronization with lag-time $\tau_c - \tau$ occurs only when η is close to γ_m . Notice that for injection currents close to threshold, C_2 is relatively large even when η is much larger than γ_m . In the parameter region (low J , large η) both C_1 and C_2 are large, but $C_1 > C_2$ and it is isochronous and not anticipated synchronization that occurs. The large value of C_2 is due to the form of the chaotic intensity fluctuations in the LFF regime [the averaged intensity oscillates with a period nearly equal to τ in between dropouts, see Fig. 20 (a)]. Notice also that there is an interval of injection currents (roughly speaking, for $1.1 < J_m/J_{th} < 1.3$), in which anticipated synchronization is not stable.

Thus, we can conclude that only for injection currents close to threshold small parameter variations can lead to transitions between different synchronization regimes because the

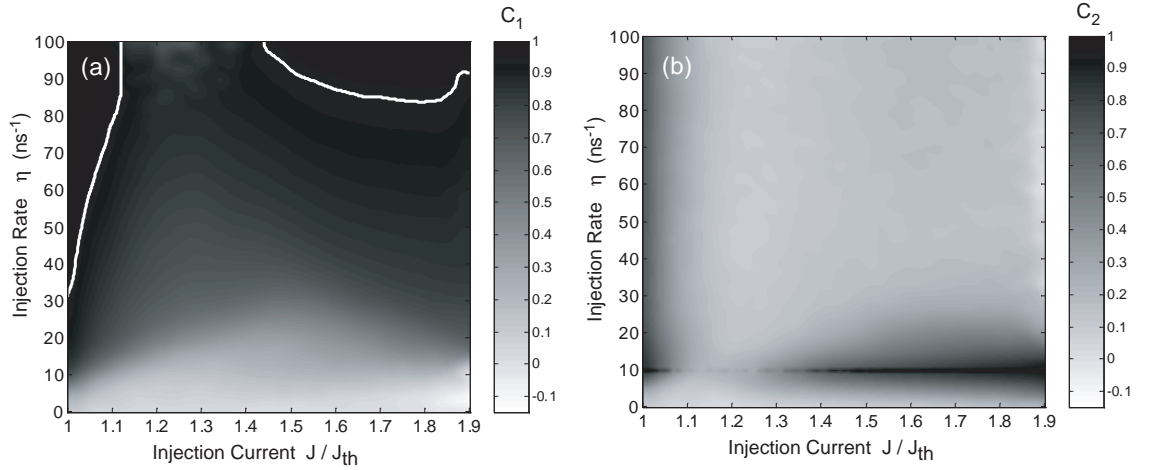


Figure 23: Synchronization regions in the parameter space (injection current, optical coupling rate). (a) The value of C_1 is plotted. The white line corresponds to the threshold injection rate above which C_1 is larger than 0.95. For $1.15j_{th} < j < 1.4j_{th}$ approximately, the threshold injection rate is larger than 10 ns^{-1} (b) The value of C_2 is plotted. $\Delta\omega = 0$, $\gamma_s = 0$, all other parameters as Fig. 15.

corresponding synchronization regions are close to each other in the parameter space. This is not possible with larger injection currents, since in that case the two types of synchronization occur in distant regions of the coupling strength.

3.2.7 Summary

We have studied numerically the synchronization of two unidirectionally coupled single-mode chaotic semiconductor lasers based on a Lang-Kobayashi-type model. The master laser is an external-cavity laser, while for the slave laser we considered two configurations: an external-cavity slave laser (closed-loop scheme), and a laser subjected only to optical injection from the master laser (open-loop scheme). Depending on the operating conditions two different types of synchronization are found: synchronization with a lag-time τ_c , which corresponds to the synchronization of the slave optical field with the injected field (isochronous synchronization), and synchronization with a lag-time $\tau_c - \tau$ (anticipated synchronization).

We have shown that chaotic synchronization with a lag-time τ_c occurs in a similar parameter region to the one in which stable CW injection-locking occurs. This form of

synchronization is much more robust than the anticipated synchronization, which occurs in a much narrower parameter region. Therefore it should be easier to implement in a real chaotic communications scheme. We have also observed that the synchronization quality is usually better in the closed-loop scheme than in the open-loop scheme; when the slave laser is an external-cavity laser, however, the external mirror has to be carefully positioned, since small differences in the delay times strongly degrade the synchronization quality.

We have analyzed the synchronization regions in the parameter space (master feedback rate, injection rate), finding that an increase of the master feedback rate requires an increase of the injection rate in order to obtain a good synchronization. In the case of the closed-loop scheme, very good synchronization can occur even for a large value of γ_m , while in the case of an open-loop scheme the chaotic intensity produced by large feedback levels is difficult to synchronize with feasible injection levels.

Finally, we have studied the transitions between the two synchronization regimes for an open-loop scheme, extending the results reported in Ref. [96]. We have shown that it is only for injection currents close to threshold, that small parameter variations can lead to transitions between the different synchronization regimes, because the synchronization regions are close to each other in parameter space. On the contrary, for large injection currents, transitions are not possible, since the two types of synchronization occur for very different coupling strengths. We have also shown that not all parameter variations lead to a transition from one synchronization regime to the other, but only the parameter variations that increase the ratio between the injected power and the solitary slave laser output power. When a parameter variation decreases this ratio, a transition to the other synchronization regime does not occur, and the synchronization is lost.

The existence of two synchronization regimes has now been proved experimentally [103] and is widely accepted. In addition, Kusumoto and Ohtsubo [105] have recently shown numerically that, in the case of an open-loop scheme, it is possible to observe an anticipating synchronization based on an injection-locking-type phenomenon.

3.3 *Synchronization of external-cavity vertical-cavity surface-emitting lasers*

3.3.1 Introduction

A vertical-cavity surface-emitting Laser (VCSEL) is a semiconductor microlaser diode that emits light in a cylindrical beam vertically from the surface of a fabricated wafer. It offers many advantages over edge-emitting lasers such as single-longitudinal-mode operation, low threshold current, low cost, easy integration in two-dimensional arrays, and a cylindrical beam. Contrary to edge-emitters, the polarization of the emitted light may switch between two linearly polarized light (LP) states (x and y). A rich polarization dynamics is encountered in these devices. In particular, VCSELs can exhibit *vectorial* chaos, *i.e.* involving both the intensity and the polarization of the electric field.

Very recent experimental results demonstrate the synchronization of unidirectionally coupled external-cavity VCSELs [106, 107]. In these experiments, only one of the two LP components is injected into the slave laser and it appears that one of the slave LP modes synchronizes with the injected field, while the other is antisynchronized. The only three published numerical studies of VCSEL synchronization [108, 109, 110] do not take into account the vectorial nature of the electric field and cannot be used to explain the recent experimental results. Therefore, it can be interesting to model coupled external-cavity VCSELs to interpret these experimental results, and to determine which role the polarization degree of freedom, which is specific to vertical-cavity surface-emitters, plays in the synchronization phenomena.

Scire *et al.* [111] have shown that the polarization dynamics of VCSELs can be exploited in an original chaos-shift keying scheme using two unidirectionally coupled VCSELs. The authors claim that with this scheme, very high bit rates (hundreds of GHz) can be reached. The VCSELs used in Ref. [111] are lasers with a saturable absorber surrounding the active region. We propose to study the same kind of encoding but with conventional VCSELs, with no saturable absorber, and subjected to an external-optical feedback. The advantages are of eliminating the requirement of an uncommon type of VCSEL and generating a much

higher-dimensional chaos than what can be achieved with a VCSEL with a saturable absorber. Moreover, we think that the synchronization technique used in Ref. [111], involving a feedback control, is probably unnecessarily complex, and we propose to study a scheme in which the slave is synchronized by optically injecting the master laser output into it.

In section 3.3.2, we present the main characteristics of vertical-cavity surface-emitting lasers. The model used to simulate the dynamical behavior of VCSELs is presented in section 3.3.3. It is the spin-flip model (SFM) developed by M. San Miguel, Q. Feng, and J. V. Moloney [112], which is a four-level model that has proved to give results in good agreement with the experimentally observed polarization dynamics of VCSELs. Section 3.3.4 presents the model used for external-cavity VCSELs and some of the dynamical instabilities induced by the optical feedback. Section 3.3.5 explains the synchronization phenomena between two unidirectionally coupled VCSELs, for three different coupling configurations, and, finally, section 3.3.6 presents some preliminary results on polarization encoding that uses the vectorial chaos produced by VCSELs.

3.3.2 Vertical-cavity surface-emitting lasers

A vertical-cavity surface-emitting laser has a different geometry than a conventional edge-emitting laser. A short resonator cavity is perpendicular to a thin quantum-well active layer (10-30 nm) and the optical beam is guided and emitted in the vertical direction (normal to the wafer) as shown in Fig. 24. Because of the short active region, VCSELs have low round-trip gains compared to edge-emitting lasers. The first VCSELs used metallic mirrors of low reflectivities and had very large threshold currents. In current VCSEL structures, the mirrors are distributed Bragg reflectors (DBR) formed by laying down alternating layers of semiconductor material with a difference in the refractive index. These mirrors have very high reflectivities ($> 99.9\%$) which allow for reasonable threshold currents despite the low round-trip gains. The cavity length is typically very short, about one to three wavelengths of the emitted light (a few μs), and a VCSEL is therefore inherently single-mode. To maximize the modal gain, the quantum-well structures are placed at the antinodes of the standing wave of the resonant longitudinal mode. Spacing layers are needed to make the

cavity length equal to an integer multiple of the emission wavelength. The geometry of the cavity is cylindrical, resulting in a narrow circular output beam, and reducing the coupling losses with optical fibers. This is a clear advantage over edge-emitters, which produce very divergent elliptical beams. Another advantage comes from the fact that the vertical structure makes the VCSELs compact and, allows for easy integration in two-dimensional arrays.

In an edge-emitting laser, the polarization of the electric field is determined by the structure. It is linearly polarized and the direction of the polarization is rigidly defined. The circular symmetry of the VCSEL cavity implies that its polarization is not as well stabilized. Due to cavity anisotropies, the polarization of a VCSEL is usually linearly polarized, but the polarization can switch between two orthogonal linearly polarized states (of directions x and y).

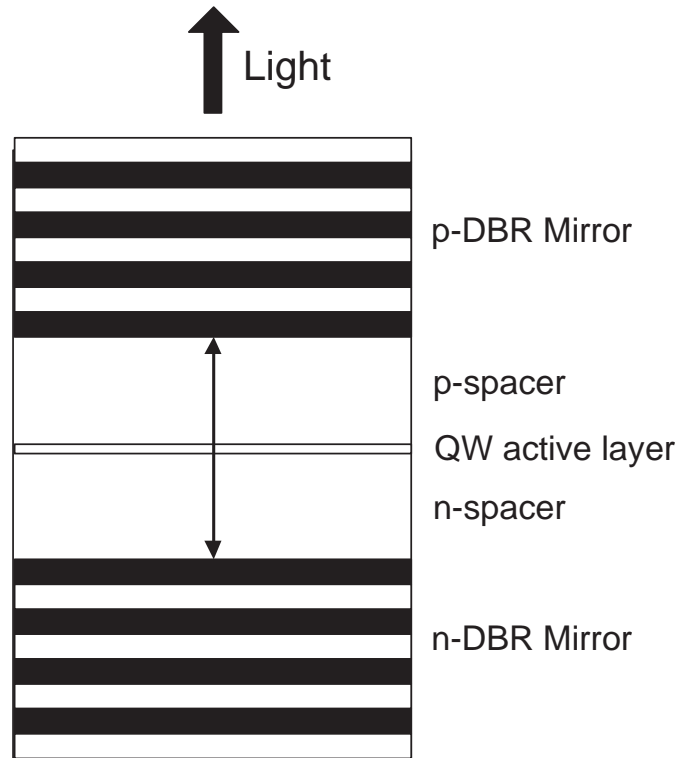


Figure 24: Vertical-cavity surface-emitting laser.

3.3.3 The Spin-Flip Model and polarization dynamics

One would expect that the polarization degree of freedom influences the dynamics significantly. We present briefly here the spin-flip model that describes the dynamical behavior of a VCSEL, including the polarization dynamics. Polarization selection can be due to the material dynamics of the different lasing transitions. When there is a transition that corresponds to a change of the projection of the total material angular momentum on the direction of propagation by $+1$ (-1), emission of a quantum of light with right (left) circular polarization occurs. The selection of a particular polarization state can also be due to the anisotropies, geometry, and waveguiding effects of the cavity.

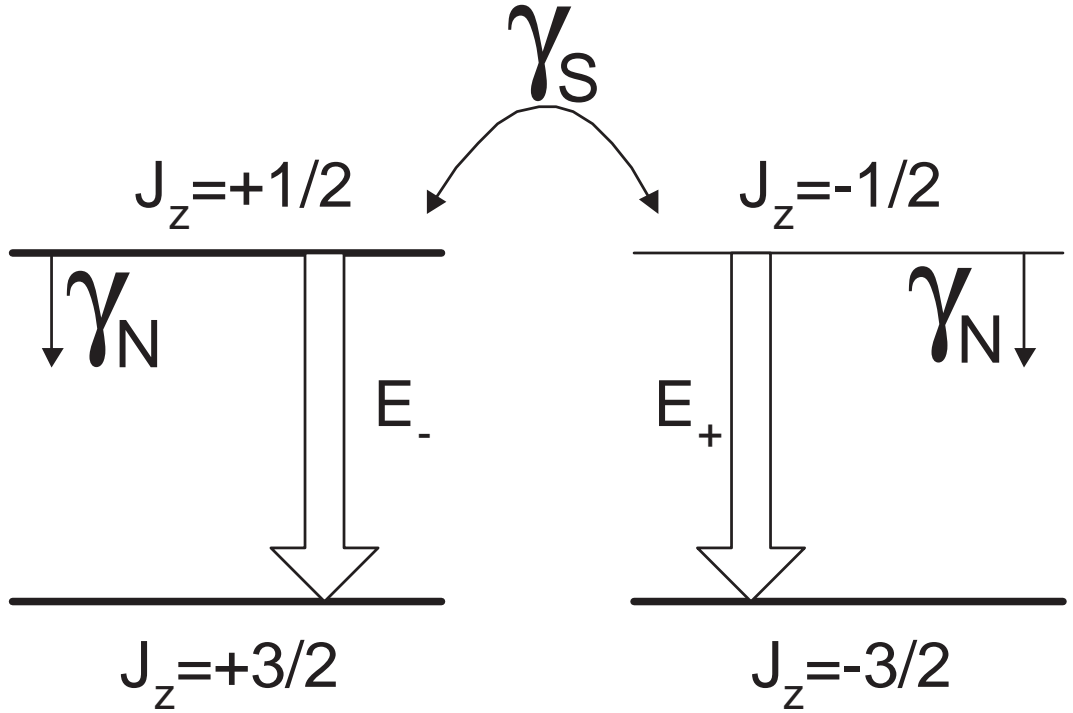


Figure 25: Sketch of a four-level model of a quantum-well VCSEL.

The spin-flip model, proposed by San Miguel, Feng, and Moloney [112], incorporates both the material and cavity properties. We recall that at the bottom of the conduction band, the quantum number for the total angular momentum of the electron states is $J = 1/2$ [113]. In bulk material, the upper valence bands known as the heavy- and light-hole

bands are degenerate at the center of the band gap and have a quantum number J for the total angular momentum equal to $3/2$, arising from considerations of spin-orbit coupling. In VCSELs, the active layer is made of quantum wells which remove the degeneracy and give the heavy-hole band, which is associated with projected angular momentum $J_z = \pm 3/2$, a higher energy. Since the only allowed transitions are those which meet the selection rule $\Delta J_z = \pm 1$, we are left with two allowed transitions between the conduction and heavy-hole band. One possible transition is from $J_z = 1/2$ to $J_z = 3/2$ and is associated to left circularly polarized light. The other possible transition is from $J_z = -1/2$ to $J_z = -3/2$, and is associated to right circularly polarized light. In a first approximation, these transitions can be described by a four level-model shown in Fig 25. The conduction band is replaced by two levels populated by electrons with opposite spin orientations and projected angular momentum $J_z = \pm 1/2$. The heavy-hole band is replaced by two levels populated by holes with opposite spin orientations and projected angular momentum $J_z = \pm 3/2$. It can be considered that a spin-up and a spin-down radiation channels exist and the carriers are split into spin-up and spin-down carrier reservoirs. Various microscopic processes, loosely named spin-flip relaxation processes, tend to mix the carriers of the two spin channels. The spin-flip processes tend to balance the populations of the two channels.

On the basis of the previous considerations, and of the standard semi-classical approach, including adiabatic elimination of the material polarization, San Miguel, Feng, and Moloney [112] have determined the following rate equation model for the VCSEL dynamics

$$\dot{E}_+ = \kappa(1 + i\alpha) [(N + n - 1)E_+] , \quad (65)$$

$$\dot{E}_- = \kappa(1 + i\alpha) [(N - n - 1)E_-] , \quad (66)$$

$$\dot{N} = -\gamma_N [N - \mu + (N + n)|E_+|^2 + (N - n)|E_-|^2] , \quad (67)$$

$$\dot{n} = -\gamma_S n - \gamma_N (N + n)|E_+|^2 + \gamma_N (N - n)|E_-|^2 . \quad (68)$$

In this model, E_+ is the slowly varying amplitude of the right circularly-polarized component of the electric field, E_- is the slowly-varying amplitude of the left circularly-polarized component of the electric field, N is a normalized value of the total population inversion

between the upper and lower states (*i.e.* of the total carrier number in excess of its value at transparency), and n is a normalized value of the difference in the population inversions of the spin-up and spin-down radiation channels. The parameters of the model are the decay rate κ of the electric field in the cavity ($1/(2\kappa)$ is the photon lifetime), the decay rate γ_N of the total carrier number, the spin-flip relaxation rate⁶ γ_S , the linewidth enhancement factor α , and the normalized injection current μ , which takes the value 1 at the lasing threshold.

This model can be rewritten in terms of the orthogonal linearly-polarized components E_x and E_y of the electric field

$$E_x = \frac{E_+ + E_-}{\sqrt{2}}, \quad (69)$$

$$E_y = (-i)\frac{E_+ - E_-}{\sqrt{2}}. \quad (70)$$

The model then becomes

$$\dot{E}_x = \kappa(1 + i\alpha) [(N - 1)E_x + inE_y] \quad (71)$$

$$\dot{E}_y = \kappa(1 + i\alpha) [(N - 1)E_y - inE_x] \quad (72)$$

$$\dot{N} = -\gamma_N [N - \mu + N(|E_x|^2 + |E_y|^2) + in(E_y E_x^* - E_x E_y^*)] , \quad (73)$$

$$\dot{n} = -\gamma_S n - \gamma_N [n(|E_x|^2 + |E_y|^2) + iN(E_y E_x^* - E_x E_y^*)] . \quad (74)$$

This original SFM model leads to stationary solutions that are linearly polarized modes. The orientation of the modes, however, is undetermined by this model of field-matter interaction. This is not consistent with the experimental observation that VCSELs often exhibit two preferred orthogonal modes of linear polarization that coincide with crystal axis. These preferred orientations are due to anisotropies of the laser cavity which have to be taken into account. The two linearly polarized modes in VCSELs have a frequency splitting, which is due to the birefringence of the medium, *i.e.* to the fact that the two modes “see” two different indexes of refraction.⁷ This can be modeled by a linear phase anisotropy, given by parameter γ_p . Moreover, the two modes have a slightly different gain-to-loss ratio, which is modeled by the amplitude anisotropy parameter γ_a . When these anisotropies are included,

⁶It is the excess of γ_S over γ_N which accounts for the mixing of carriers with opposite value of J_z .

⁷The birefringence is usually due to the crystal structure, but can also be stress-induced.

the rate equations of the x - and y -polarized components of the electric field become:

$$\begin{aligned}\dot{E}_x &= \kappa(1+i\alpha)[(N-1)E_x + inE_y] - (\gamma_a + i\gamma_p)E_x \\ &= -(\kappa + \gamma_a)E_x - i(\kappa\alpha + \gamma_p)E_x + \kappa(1+i\alpha)[NE_x + inE_y]\end{aligned}\quad (75)$$

$$\begin{aligned}\dot{E}_y &= \kappa(1+i\alpha)[(N-1)E_y - inE_x] + (\gamma_a + i\gamma_p)E_y \\ &= -(\kappa - \gamma_a)E_y - i(\kappa\alpha - \gamma_p)E_y + \kappa(1+i\alpha)[NE_y - inE_x]\end{aligned}\quad (76)$$

The phase anisotropy γ_p leads to a frequency difference of $2\gamma_p$ between the x - and y -polarized solutions. The amplitude anisotropy leads to different thresholds for these two modes.

As mentioned previously, it is typical to observe polarization instability in solitary VCSELs. It is often observed experimentally that when the VCSELs begins to lase, one linear polarization mode dominates, but when the injection current is increased, the emission switches to an orthogonal linearly polarized state [114]. Elliptically polarized light has also been observed [115]. The spin-flip model, with anisotropies, reproduces most of the experimentally observed behaviors. A linear stability analysis of the SFM model [116] shows regions in parameter space of monostability of either of the modes, of bistability, and of instability of the two modes which explain why polarization switching can occur when the injection current is increased. Numerical simulations of the model have confirmed the results and it appears, as could be expected, that the parameters whose interplay determines the polarization dynamics are the spin-flip relaxation rate and the amplitude and phase anisotropies.

Figure 26 represents the behavior of a solitary VCSEL when its injection current μ is increased, determined by simulating the SFM model. We see that the laser emits a y -polarized light when it is biased above threshold, and it switches to x polarization rather abruptly when the injection current reaches about 1.25 times its value at threshold. There is a small interval of values of μ , around 1.25, for which neither the x -polarized nor the y -polarized component of the electric field is equal to zero. In that interval, states of elliptical polarization, and of mixed polarization (partial polarization⁸), have been observed. When

⁸*i.e.* for which the fractional polarization [117] is smaller than 1.

the injection current is larger than 1.5 approximately, we observe that again both linearly polarized components are different from zero. In that region, for increasing values of μ , we observe first states of elliptically polarized light, then states of partially unpolarized light in which the polarization state varies periodically, with a period increasing with μ , until a chaotically fluctuating state of polarization is reached for $\mu = 1.8$ approximately. This type of transition toward a chaotic regime corresponds to a period-doubling route to chaos (*cf.* § 2.2).

A useful graphical tool to represent the polarization state is the Poincaré sphere [117]. From the slowly varying electric field, three parameters, called the normalized Stokes parameters S_1 , S_2 , and S_3 [117], can be computed and are the Cartesian coordinates of the polarization state on a sphere of unitary radius called the Poincaré sphere. In case of polarized light, the Stokes parameters are constant in time and a fixed point on the Poincaré sphere is associated to each state of polarization. Points that lie on the equator correspond to linear polarization, those lying on the poles to circular polarizations, and points lying anywhere else on the sphere correspond to the general case of elliptical polarization. For incompletely polarized light, the Stokes parameters vary in time because the amplitudes of E_x and E_y and their relative phases vary in time.

Figure 27 represents the intensities (which are proportional to the squares of the amplitudes of the electric fields) of the x - and y -polarized components of the electric field, for four different values of the injection current μ , and Fig. 28 represents the corresponding states of polarization on the Poincaré sphere. Case (a) corresponds to elliptical polarization, cases (b) and (c) to a periodic variation of the polarization state, and case (d) to chaotic variation of the polarization state. In the case of elliptically polarized light, the x and y components have constant amplitude and there is a constant difference between their linearly-varying phases. The state of polarization is represented by a point on the Poincaré sphere. In cases (b) and (c), the intensities associated to the two x and y components of the electric field vary periodically, and the state of polarization varies on a closed curve on the sphere, corresponding to a periodic variation of the polarization characteristics. In case

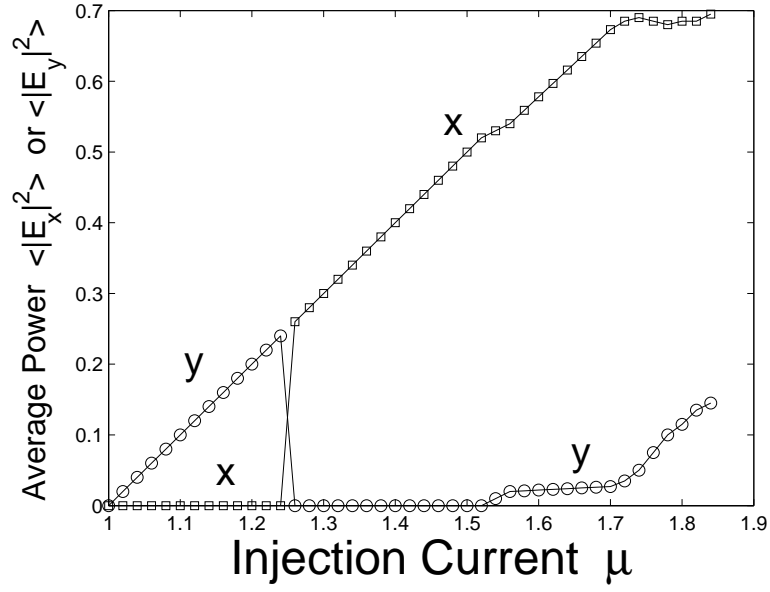


Figure 26: Light-current characteristics of each linearly-polarized component of the electric field (circles: y-polarized, squares: x-polarized). The powers are averaged over 20 ns. The parameters are: $\kappa = 300 \text{ ns}^{-1}$, $\gamma_N = 1 \text{ ns}^{-1}$, $\alpha = 3$, $\gamma_S = 50 \text{ ns}^{-1}$, $\gamma_p = 10 \text{ ns}^{-1}$, and $\gamma_a = 0.1 \text{ ns}^{-1}$.

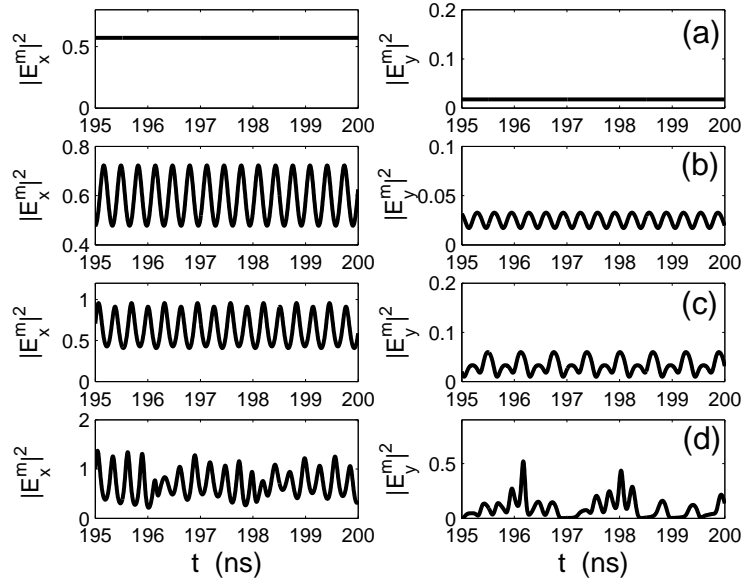


Figure 27: Intensities of the x - and y -polarized components of the electric field. (a) $\mu = 1.6$, (b) $\mu = 1.64$, (c) $\mu = 1.68$, (d) $\mu = 1.8$. All the other parameters are the same as in Fig. 26.

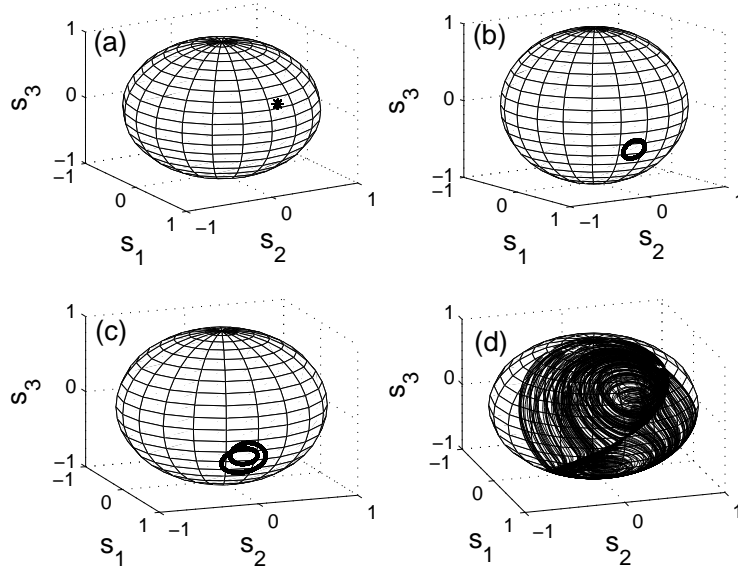


Figure 28: Poincaré sphere representation of the polarization state of light. (a) $\mu = 6$, (b) $\mu = 1.64$, (c) $\mu = 1.68$, (d) $\mu = 1.8$. All the other parameters are the same as in Fig. 26.

(d), the x - and y - polarized components of the electric field have chaotically-varying amplitudes, their phase difference is time-dependent, and the polarization states wanders on a big portion of the Poincaré sphere⁹, corresponding to a chaotic variation of the polarization state. The light emitted by the laser is almost unpolarized¹⁰.

Semiconductors lasers subjected to optical injection and feedback have attracted considerable attention. This is true for edge-emitters as well as for surface-emitters. In the case of VCSELs, there is an additional degree of freedom created by the possible existence of two linearly polarized modes. Several schemes have been considered in which the optical injection or feedback is either isotropic (the two polarizations are injected or fed back) or selective (only one polarization is injected or fed back). Additionally, in case of polarization-selective injection, the injected field can be either parallel or orthogonal to the polarization of the solitary slave laser.¹¹ Depending on the configuration, the laser can be stabilized or destabilized by the injected field, and polarization instabilities can also be either reinforced

⁹It does not move on a closed curve.

¹⁰*i.e.* the fractional polarization is close to 0.

¹¹Assuming that we are in a case in which only one polarization is emitted.

or suppressed by the injection (see [118, 119] and references therein).

We consider in the next section the case of a laser subjected to isotropic (or polarization-preserving) optical feedback, which is the configuration used in the experimental results on synchronization of VCSELs [106] and on chaotic communications with VCSELs [107].

3.3.4 External-cavity vertical-cavity surface-emitting lasers

It was initially thought that VCSELs should be almost immune to external feedback in reason of the large reflectivities of their facets. The VCSELs have, however, much smaller intracavity round-trip times τ_{in} compared to edge-emitters, which lead to similar feedback rates [$\gamma = \kappa/\tau_{in}$ in Eq. (38)], even if the feedback parameters κ are lower. This means that the sensitivity of VCSELs to optical feedback is similar to that of edge-emitting lasers. The five dynamical regimes described in (3.2.2.2) have been identified in VCSELs [120], but some behaviors specific to VCSELs, linked to polarization instabilities, have also been observed (see Ref. [119] and references therein).

The external optical feedback is taken into account in the rate equations of the laser in the same way as for edge-emitters (Lang-Kobayashi model, *cf.* §3.2.2.1). The rate equations describing the dynamical behavior of an external-cavity semiconductor laser subjected to external optical feedback are

$$\begin{aligned}\dot{E}_x &= \kappa(1 + i\alpha) [(N - 1)E_x + inE_y] - (\gamma_a + i\gamma_p)E_x \\ &\quad + f_x E_x(t - \tau) \exp(-i\omega\tau) ,\end{aligned}\tag{77}$$

$$\begin{aligned}\dot{E}_y &= \kappa(1 + i\alpha) [(N - 1)E_y - inE_x] + (\gamma_a + i\gamma_p)E_y \\ &\quad + f_y E_y(t - \tau) \exp(-i\omega\tau) ,\end{aligned}\tag{78}$$

$$\dot{N} = -\gamma_N [N - \mu + N(|E_x|^2 + |E_y|^2) + in(E_y E_x^* - E_x E_y^*)] ,\tag{79}$$

$$\dot{n} = -\gamma_S n - \gamma_N [n(|E_x|^2 + |E_y|^2) + iN(E_y E_x^* - E_x E_y^*)] ,\tag{80}$$

where τ is the optical delay, ω is the angular frequency of the laser in the absence of anisotropies and feedback, $\omega\tau$ is the feedback phase, and f_x and f_y are the feedback rates of

the x - and y -polarized components of the electric field¹². In the case of isotropic feedback considered in this work, we have $f_x = f_y = f$.

We use the following values for the parameters of the SFM model: $\kappa = 300 \text{ ns}^{-1}$, $\gamma_N = 1 \text{ ns}^{-1}$, $\alpha = 3$, $\gamma_S = 50 \text{ ns}^{-1}$, $\gamma_p = 30 \text{ ns}^{-1}$, $\gamma_a = 0.5 \text{ ns}^{-1}$. For this set of parameters, the VCSEL exhibits polarization switching, from y -polarized to x -polarized light, when the injection current is increased, for a value of the current of 1.2 approximately. We use, in the remainder of this work, and unless stated otherwise, an injection current $\mu = 1.5$, corresponding to a solitary VCSEL emitting linearly x -polarized light of constant intensity and linearly varying phase (CW regime). This is confirmed by Fig. 29 which represents the intensities of the two linearly polarized components of the electric field of the solitary laser. The carrier numbers N and n are also stationary.

The parameters of the external cavity are the external-cavity round-trip time $\tau = 3 \text{ ns}$, the feedback phase $\omega\tau = 6$ radians, and the feedback rate f . In the following, we present briefly the feedback-induced instabilities that occur when the feedback rate f is increased. The effect of a modification of the delay τ is not presented in this manuscript. When an isotropic feedback is introduced, the x - polarized mode is destabilized and undergoes a route to chaos through quasi-periodicity (*cf.* §2.2) for increasing feedback rates.

Chaos appears for a feedback rate f of 1.3 GHz approximately. Figure 30 represents a chaotic solution for a feedback rate $f = 1.4 \text{ GHz}$. We see that the intensity of the x -polarized mode fluctuates in an aperiodic way while the y -polarized mode is inactive, and the light emitted by the laser is therefore linearly polarized along the x direction. It should be noted that the y -polarized component does emit some light transiently, just after the laser is switched on, but its intensity goes rapidly to zero. We also find that in this regime the phase of the electric field does not vary linearly anymore. We have represented in Fig. 31 the corresponding carrier numbers N and n . We observe that the total population inversion N varies chaotically, similarly to the intensity, while the population difference between the two spin channels n is equal to zero (except in transient regimes, not represented here).

¹²The letter f is used here for the feedback rate instead of the letter γ that was used in edge-emitters, to avoid any confusion with the parameters that represent the anisotropies.

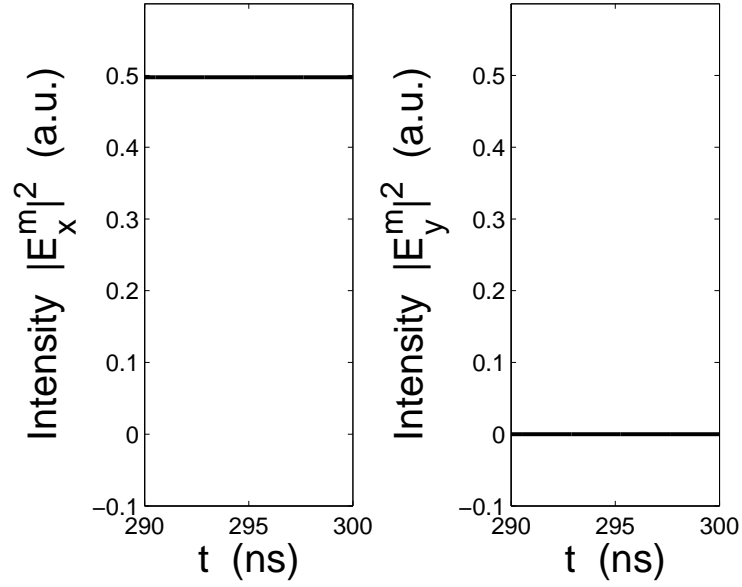


Figure 29: Intensities of the x - and y -polarized components of the electric field of the solitary VCSEL. The parameters of the SFM model are $\mu = 1.5$, $\kappa = 300 \text{ ns}^{-1}$, $\gamma_N = 1 \text{ ns}^{-1}$, $\alpha = 3$, $\gamma_S = 50 \text{ ns}^{-1}$, $\gamma_p = 30 \text{ ns}^{-1}$, and $\gamma_a = 0.5 \text{ ns}^{-1}$.

When the feedback rate is further increased, the x -polarized components exhibits more developed chaos, and the y -polarized mode is still equal to zero at steady state, though the switch-on transients tend to become longer.

Figure 32 represents the intensities of the linearly-polarized modes for a feedback rate $f = 5 \text{ GHz}$. While for a feedback of 1.4 GHz (Fig. 30), the chaotic intensity looks like a perturbed stationary solution in which the quasiperiodic route to chaos is still visible, for a feedback rate of 5 GHz there is no trace of the bifurcations route as we observe that the intensity has a *pulse-like* appearance. The transient emission in the y -polarized component takes the form of a series of short pulses, separated by periods during which no light is emitted along this component. Further increases of f lead to similar (and increasingly obvious) pulse-like chaotic emission in the x -polarized mode and transient emission of short pulses in the y -polarized component.

It is not until the feedback rate reaches a value of 30 GHz that some qualitative changes appears. The x -polarized component still has a chaotic pulse-like intensity, and the y -polarized components still emits pulses of light in a transient way only. But additionally,

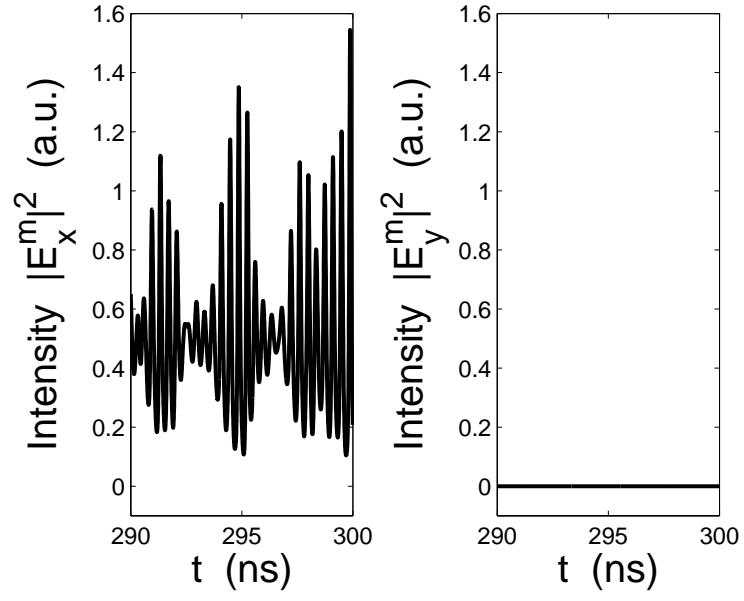


Figure 30: Intensities of the x - and y -polarized components of the electric field of the external-cavity VCSEL, for a feedback rate $f = 1.4$ GHz, a delay $\tau = 3$ ns, and a feedback phase $\omega\tau = 6$ rad. All other parameters are as in Fig 29.

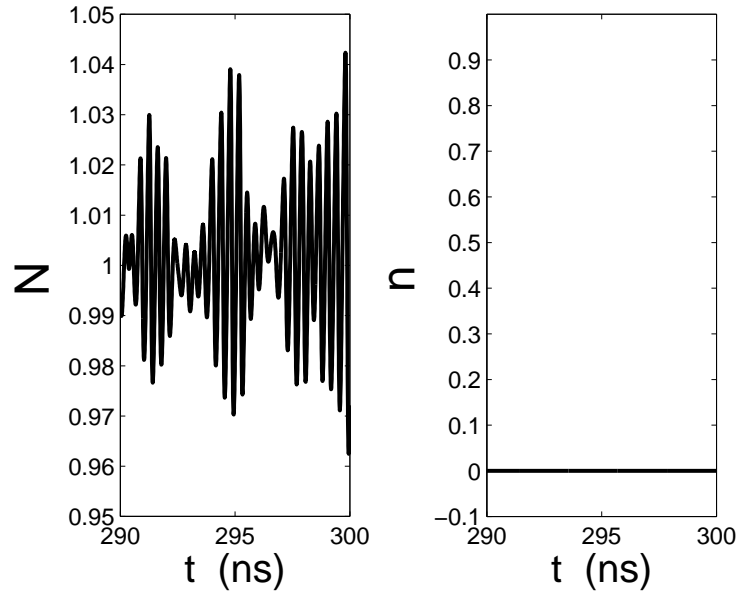


Figure 31: Carrier number N and n for a feedback rate $f = 1.4$ GHz. All parameters are as in Fig 29.

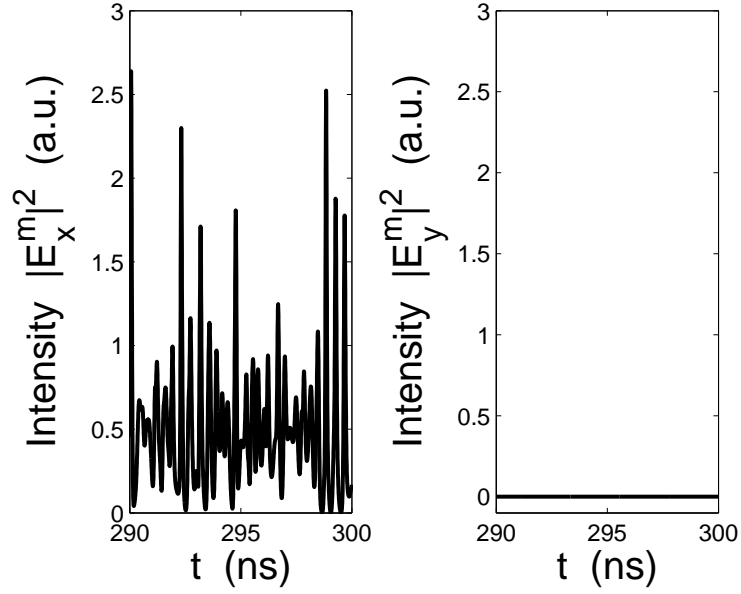


Figure 32: Intensities of the x - and y -polarized components of the electric field of the external-cavity VCSEL, for a feedback rate $f = 5$ GHz. All parameters are as in Fig 29.

when the intensity of the x component is filtered by a low pass filter of cutoff frequency of a few hundreds of MHz, to simulate the filtering effect of a slowly responding photodiode, sudden dropouts of the intensity followed by progressive build-ups appear. This behavior of the filtered intensity and the underlying pulse-like behavior is characteristic of the LFF regime described in section 3.2.2.2. Figure 33 represents the (unfiltered) intensities of the x and y -polarized components for a feedback rate $f = 30$ GHz. The pulse-like emission is obvious, and the pulses have width of several tens of picoseconds, again similarly to what has been found in the LFF regime. The filtered intensity of the y -polarized mode is represented in Fig. 34 and shows the characteristics of LFF emission. The amplitudes of the dropouts, which are relatively small for $f = 30$ GHz, increase with the feedback rate.

When the feedback rate reaches the value of 40 GHz, the y -polarized component of the electric field emits light in the steady-state regime (and not only transiently), though the x -polarized mode is still clearly dominant. Both components exhibit the emission of short pulses as shown in Fig. 35. The total intensity, $|E_x(t)|^2 + |E_y(t)|^2$, represented in Fig. 36 exhibits a similar pulsating behavior. In this regime in which both components

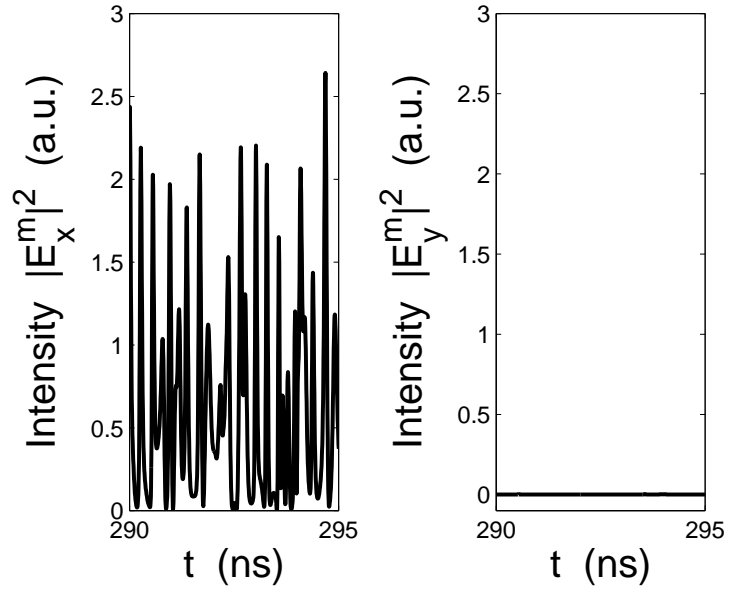


Figure 33: Intensities of the x - and y -polarized components of the electric field of the external-cavity VCSEL, for a feedback rate $f = 30$ GHz. All parameters are as in Fig 29.

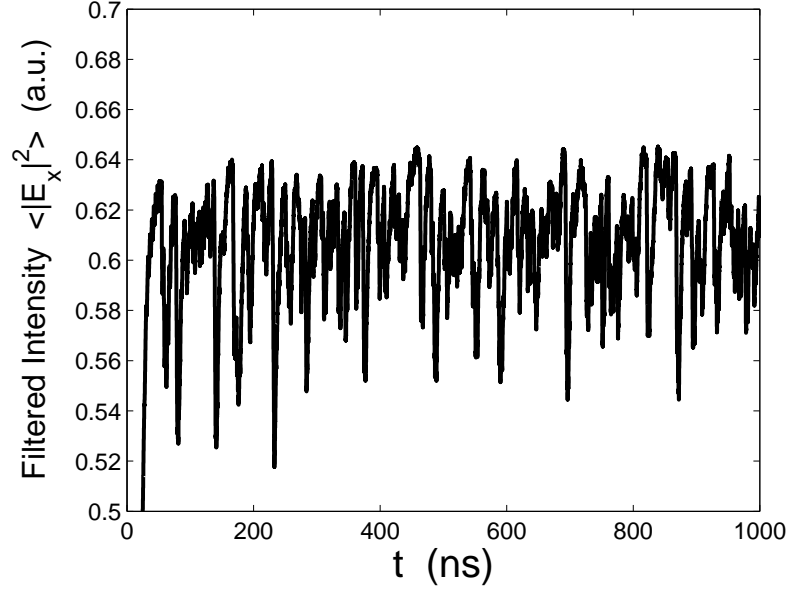


Figure 34: Filtered intensities of the x - and y -polarized components of the electric field of the external-cavity VCSEL, for a feedback rate $f = 30$ GHz. All parameters are as in Fig 29. A second-order Butterworth filter of 0.1 GHz cutoff frequency is used.

have nonzero amplitude, the carrier number n varies in time, expressing a (fluctuating) unbalance between the populations of the spin channels. The filtered intensity of the x component shown in Fig. 37 exhibits the build-ups and dropouts characteristic of the LFF regime, while the y component shows a sort of *anti*-LFF, in which the dropouts are replaced by sudden increases of the filtered power. It is interesting to note that the buildup periods of the x component usually coincide with periods in which the intensity of the y component decreases, a behavior which reflects a an *antiphase* behavior of the two components, which occurs frequently in VCSELs [121, 122]. It should be noted that the antiphase is observed here on the time scale of the filtered signals and not on the time scale of the unfiltered (fast-pulsating) dynamics. Since both components have nonzero amplitude, the polarization of

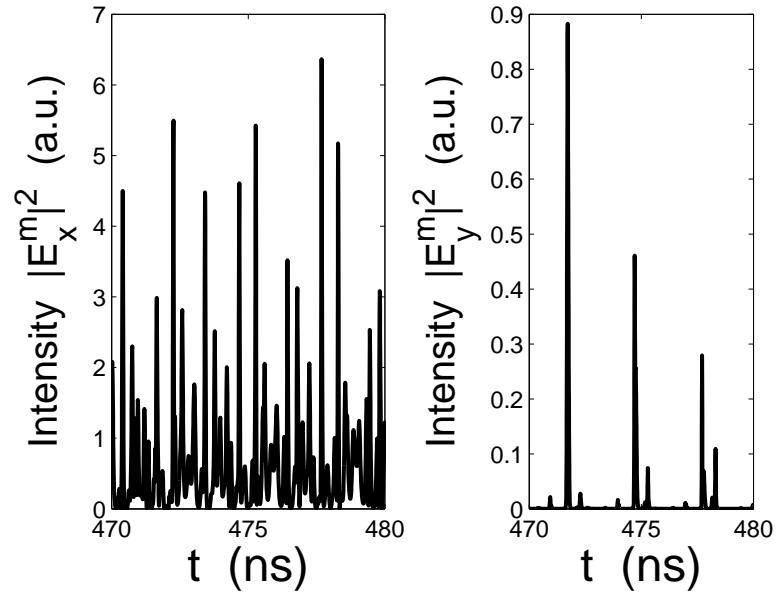


Figure 35: Intensities of the x - and y -polarized components of the electric field of the external-cavity VCSEL, for a feedback rate $f = 40$ GHz. All parameters are as in Fig. 29.

light is not linear anymore. We checked that the state of polarization evolves chaotically on the Poincaré sphere.

We end this section by emphasizing that the feedback-induced instabilities presented in this section are fundamentally different from the ones described in the previous section, which are intrinsic VCSEL instabilities enhanced by large injection currents.

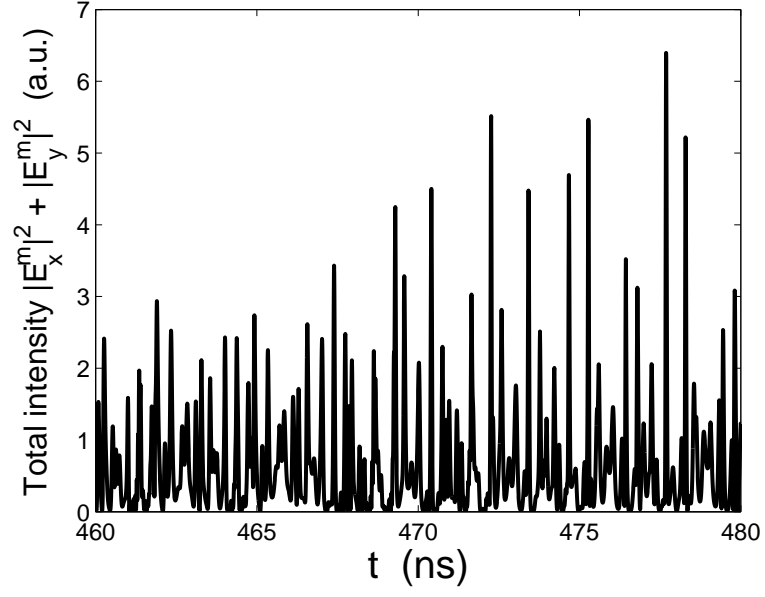


Figure 36: Total intensity emitted by the external-cavity VCSEL, for a feedback rate $f = 40$ GHz. All parameters are as in Fig. 29.

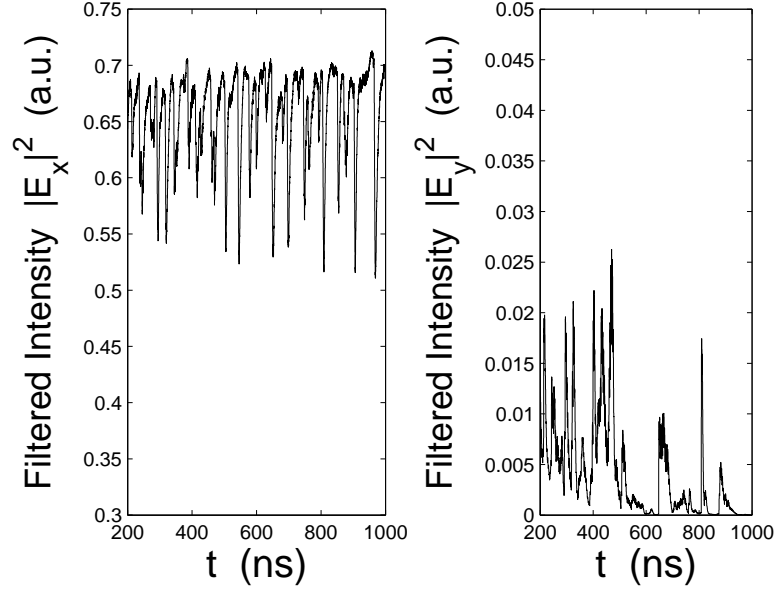


Figure 37: Filtered intensities of the x - and y -polarized components of the electric field of the external-cavity VCSEL, for a feedback rate $f = 40$ GHz. All parameters are as in Fig 29. A second-order Butterworth filter of 0.1 GHz cutoff frequency is used.

3.3.5 Synchronization regimes

We consider VCSELS subjected to *isotropic* optical feedback, coupled in a unidirectional way. We also assume that the two lasers have the same parameters. The additional degrees of freedom introduced by the presence of two competing linearly-polarized modes also mean that there are more ways to couple the lasers than in the case of edge-emitting lasers. We consider here three configurations.

1. *First configuration.* In the first configuration, the two linearly-polarized components of the electric field are optically injected into the slave laser, with the same injection rate (isotropic or polarization-preserving injection). Since both the feedback and the optical injection are isotropic, no polarization component is favored by the setup. The setup is the same as the one represented in Fig 12 in the case of edge-emitters. The optical injection into the slave laser is taken into account in a similar way to what has been done in the case of edge-emitters. The rate equations for master laser (superscript m) are

$$\begin{aligned} \dot{E}_x^m &= \kappa(1 + i\alpha) [(N^m - 1)E_x^m + in^m E_y^m] - (\gamma_a + i\gamma_p)E_x^m \\ &\quad + f_x^m E_x^m(t - \tau) \exp(-i\omega_m \tau) , \end{aligned} \quad (81)$$

$$\begin{aligned} \dot{E}_y^m &= \kappa(1 + i\alpha) [(N^m - 1)E_y^m - in^m E_x^m] + (\gamma_a + i\gamma_p)E_y^m \\ &\quad + f_y^m E_y^m(t - \tau) \exp(-i\omega_m \tau) , \end{aligned} \quad (82)$$

$$\dot{N}^m = -\gamma_N [N^m - \mu + N^m(|E_x^m|^2 + |E_y^m|^2) + in^m(E_y^m E_x^{m*} - E_x^m E_y^{m*})] , \quad (83)$$

$$\dot{n}^m = -\gamma_S n^m - \gamma_N [n^m(|E_x^m|^2 + |E_y^m|^2) + iN^m(E_y^m E_x^{m*} - E_x^m E_y^{m*})] . \quad (84)$$

and for the slave laser (superscript s):

$$\begin{aligned}\dot{E}_x^s &= \kappa(1+i\alpha) [(N^s-1)E_x^s + in^s E_y^s] - (\gamma_a + i\gamma_p)E_x^s \\ &\quad + f_x^s E_x^s(t-\tau) \exp(-i\omega_s\tau) \\ &\quad + \eta_x E_x^m(t-\tau_c) \exp[i(\omega_m - \omega_s)t] \exp(-i\omega_m\tau_c),\end{aligned}\tag{85}$$

$$\begin{aligned}\dot{E}_y^s &= \kappa(1+i\alpha) [(N^s-1)E_y^s - in^s E_x^s] + (\gamma_a + i\gamma_p)E_y^s \\ &\quad + f_y^s E_y^s(t-\tau) \exp(-i\omega_s\tau) \\ &\quad + \eta_y E_y^m(t-\tau_c) \exp[i(\omega_m - \omega_s)t] \exp(-i\omega_m\tau_c),\end{aligned}\tag{86}$$

$$\dot{N}^s = -\gamma_N [N^s - \mu + N^s(|E_x^s|^2 + |E_y^s|^2) + in^s(E_y^s E_x^{s*} - E_x^s E_y^{s*})],\tag{87}$$

$$\dot{n}^s = -\gamma_S n^s - \gamma_N [n^s(|E_x^s|^2 + |E_y^s|^2) + iN^s(E_y^s E_x^{s*} - E_x^s E_y^{s*})],\tag{88}$$

where η_y is the injection rate, τ_c is the propagation time of light between the two lasers, and $\omega_m - \omega_s$ is the frequency detuning between the master and the slave lasers. The condition of isotropic feedback means that $f_x^m = f_y^m$ and $f_x^s = f_y^s$.

2. *Second configuration.* In the second configuration, only one of the two linearly polarized components of the electric field is optically injected into the slave laser. One polarization component is clearly favored in this setup. To model this system, in equations (81), (82), (85), (86), either the injection rate in the x component, η_x , or the injection rate in the y component, η_y , has to be set to zero.
3. *Third configuration.* In the third configuration, similarly to what has been done in the experimental setup used to demonstrate the synchronization of VCSELs [106], one of the linearly polarized components of the electric field is selected, rotated by 90 degrees, and injected into the open-loop slave ($f^s = 0$). This can be realized by half-wave plates placed between the master and the slave lasers. In this case, the

equations of the linearly-polarized components of the electric field are

$$\begin{aligned}\dot{E}_x^s &= \kappa(1 + i\alpha) [(N^s - 1)E_x^s + in^s E_y^s] - (\gamma_a + i\gamma_p)E_x^s \\ &\quad + \eta_x E_y^m(t - \tau_c) \exp[i(\omega_m - \omega_s)t] \exp(-i\omega_m \tau_c) ,\end{aligned}\quad (89)$$

$$\begin{aligned}\dot{E}_y^s &= \kappa(1 + i\alpha) [(N^s - 1)E_y^s - in^s E_x^s] + (\gamma_a + i\gamma_p)E_y^s \\ &\quad + \eta_y E_x^m(t - \tau_c) \exp[i(\omega_m - \omega_s)t] \exp(-i\omega_m \tau_c) ,\end{aligned}\quad (90)$$

where $\eta_x = 0$, when the x -polarized component is selected, rotated, and injected into the slave, and $\eta_y = 0$, when it is the y -polarized component which is injected into the slave, after being rotated. In these equations, η_x represents the injection rate of the y -polarized component and η_y represents the injection rate of the x -polarized component.

In the following, we describe the different synchronization regimes that can occur, depending on the type of configuration used.

3.3.5.1 First coupling configuration

Similarly to what has been done in the case of edge-emitting lasers (*cf.* §3.2.4), we can look for synchronized solutions of anticipating and isochronous type.

It is easy to show that in the absence of frequency detuning between the lasers ($\omega_m = \omega_s = \omega$), the following anticipating synchronization can occur between the complex electric fields $F(t) = E(t) \exp^{i\omega t}$ and the carrier numbers:

$$F_x^m(t - \tau_c) = F_x^s(t - \tau) \Rightarrow E_x^m(t - \tau_c) \exp(-i\omega \tau_c) = E_x^s(t - \tau) \exp(-i\omega \tau) , \quad (91)$$

$$F_y^m(t - \tau_c) = F_y^s(t - \tau) \Rightarrow E_y^m(t - \tau_c) \exp(-i\omega \tau_c) = E_y^s(t - \tau) \exp(-i\omega \tau) , \quad (92)$$

$$N^m(t - \tau_c) = N^s(t - \tau) , \quad (93)$$

$$n^m(t - \tau_c) = n^s(t - \tau) , \quad (94)$$

if the following conditions are met:

$$\begin{aligned}f_x^m &= f_x^s + \eta_x , \\ f_y^m &= f_y^s + \eta_y .\end{aligned}\quad (95)$$

The synchronization conditions are similar to those found in the case of edge-emitting lasers modeled by the Lang and Kobayashi model. They express that the master feedback rates of the x and y components must be equal to the sum of the slave feedback rates and the injection rates of the corresponding components. It is important to understand that these conditions only ensure the *existence*, but not the stability, of a synchronized solution¹³. The synchronization of the complex electric fields ($F(t) = A(t) \exp i(\omega t + \phi(t))$) corresponds to a synchronization of the amplitudes $A(t)$ and of the phases $\Omega(t) = \omega t + \phi(t)$ of the electric field:

$$A_x^m(t - \tau_c) = A_x^s(t - \tau) , \quad (96)$$

$$\Omega_x^m(t - \tau_c) = \Omega_x^s(t - \tau) \Rightarrow \phi_x^m(t - \tau_c) = \phi_x^s(t - \tau) + \omega\tau_c - \omega\tau , \quad (97)$$

$$A_y^m(t - \tau_c) = A_y^s(t - \tau) , \quad (98)$$

$$\Omega_y^m(t - \tau_c) = \Omega_y^s(t - \tau) \Rightarrow \phi_y^m(t - \tau_c) = \phi_y^s(t - \tau) + \omega\tau_c - \omega\tau . \quad (99)$$

The preceding identities mean that the electric field produced by the slave, at a given time t , synchronizes identically with the electric field that will be injected into it τ units of time later, and the synchronization is therefore clearly a form of anticipating synchronization. Figures 38 and 39 represent the synchronization of the master and slave laser intensities, in a regime of feedback-induced instabilities in which both linearly polarized components of the electric field are active, in the case of an open-loop slave ($f^s = 0$). We observe that the two components of the electric field synchronize perfectly, in an anticipating way. The same is obviously true for the total master and slave intensities. Figure 40 shows that the carrier densities n^m and n^s exhibit aperiodic behavior and evolve in a synchronous way.

Numerical simulations indicate that, similarly to the case of edge-emitting lasers, when the slave isochronous feedback rate is equal to the master isochronous feedback rate ($f^m = f^s$), an approximate isochronous solution of the following form exists, in the absence of

¹³It is also interesting to note this solution exists even if the master is subjected to anisotropic feedback, if the injection rates are chosen correctly.

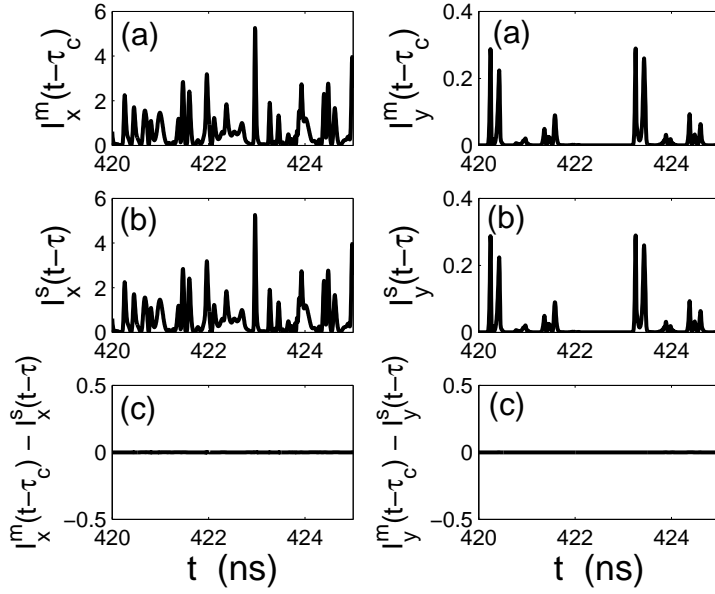


Figure 38: (a) Intensities of the x - and y -polarized components of the master electric field. (b) Intensities of the x - and y -polarized components of the slave. (c) Difference between the synchronized intensities showing anticipating synchronization. Master isotropic feedback rate $f^m = 40$ GHz, slave feedback rate $f^s = 0$ (open-loop), injection rate $\eta = 40$ GHz. All other parameters are as in Fig. 29.

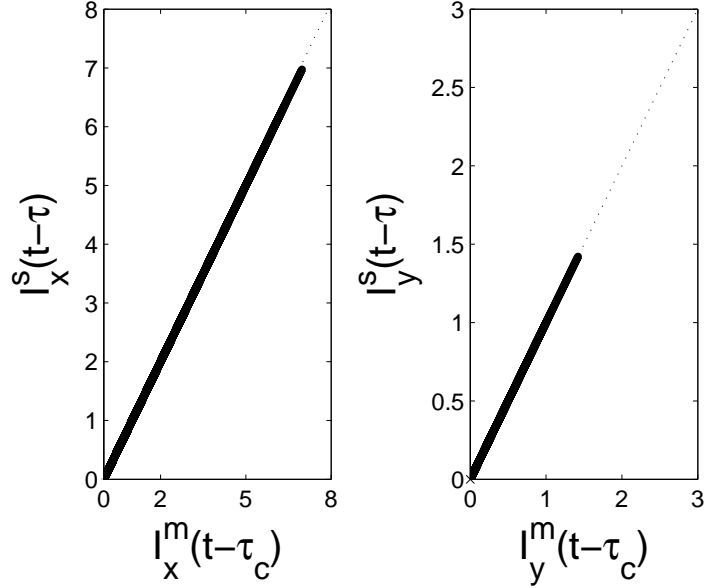


Figure 39: Synchronization diagrams for the intensities of the x - and y - polarized components of the electric field, revealing anticipating synchronization. Master isotropic feedback rate $f^m = 40$ GHz, slave feedback rate $f^s = 0$ (open-loop), injection rate $\eta = 40$ GHz. All other parameters are as in Fig. 29.

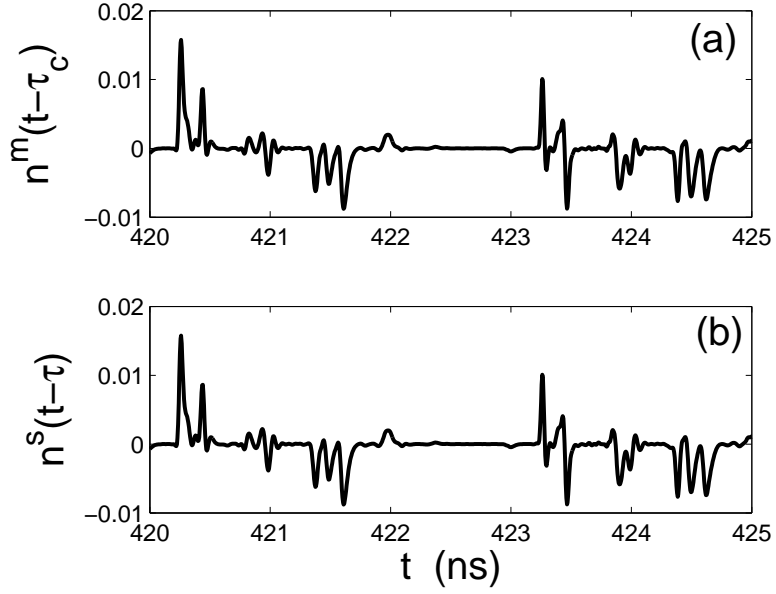


Figure 40: (a) Master carrier number n and (b) synchronized slave carrier number. Master isotropic feedback rate $f^m = 40$ GHz, slave feedback rate $f^s = 0$ (open-loop), injection rate $\eta = 40$ GHz. All other parameters are as in Fig. 29.

frequency detuning¹⁴:

$$\begin{aligned}
A_x^m(t - \tau_c) &= a_x A_x^s(t) , \\
\phi_x^m(t - \tau_c) &= \phi_x^s(t) + \Delta_\phi , \\
A_y^m(t - \tau_c) &= a_y A_y^s(t) , \\
\phi_y^m(t - \tau_c) &= \phi_y^s(t) + \Delta_\phi . \\
N^m(t - \tau_c) &= N^s(t) + \Delta_N , \\
n^m(t - \tau_c) &= n^s(t) ,
\end{aligned} \tag{100}$$

where a_x , a_y , Δ_ϕ , and Δ_N are constants. Figure 41 represents the synchronization diagrams for the intensities of the master and slave lasers, when the feedback rates are $f^m = f^s = 40$ GHz, and the (large) injection rates are $\eta_x = \eta_y = 200$ GHz. We observe good, though not perfect, synchronization, and a linear fit of the data allows us to estimate the constants $a_x = a_y = 1.5$.

¹⁴We have not checked the influence of frequency detuning on isochronous synchronization, but we expect that a synchronized solutions also exists in presence of detuning.

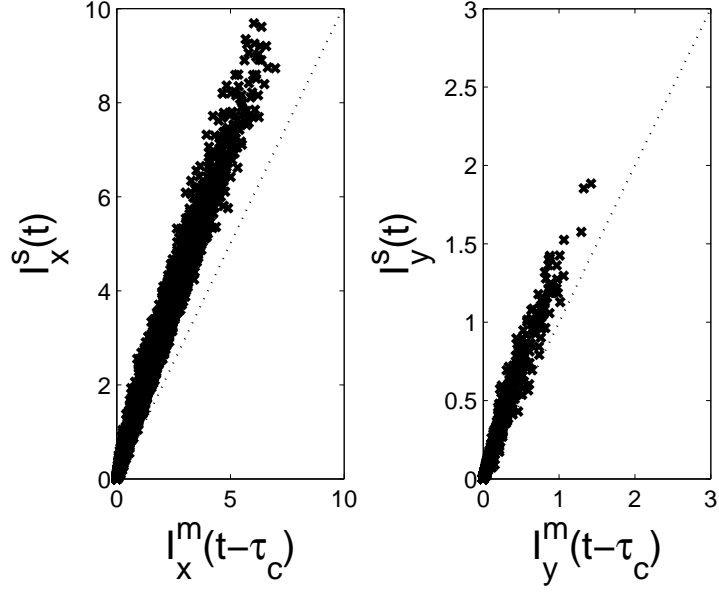


Figure 41: Synchronization diagrams for the intensities of the x and y polarized components of the electric field, revealing isochronous synchronization. The correlation coefficients are $C_{1x} = 0.994$ and $C_{1y} = 0.988$. Master isotropic feedback rate $f^m = 40$ GHz, slave feedback rate $f^s = 40$ GHz, injection rate $\eta = 200$ GHz. All other parameters are as in Fig. 29.

The quality of the synchronization of the intensities of the master x - and y - polarized components, with the corresponding intensities emitted by the slave, can be characterized by the following correlation coefficients

$$C_{1x} = \frac{\langle [I_x^m(t - \tau_c) - \langle I_x^m \rangle][I_x^s(t) - \langle I_x^s \rangle] \rangle}{[\langle (I_x^m(t) - \langle I_x^m \rangle)^2 \rangle \langle (I_x^s(t) - \langle I_x^s \rangle)^2 \rangle]^{1/2}}, \quad (101)$$

$$C_{1y} = \frac{\langle [I_y^m(t - \tau_c) - \langle I_y^m \rangle][I_y^s(t) - \langle I_y^s \rangle] \rangle}{[\langle (I_y^m(t) - \langle I_y^m \rangle)^2 \rangle \langle (I_y^s(t) - \langle I_y^s \rangle)^2 \rangle]^{1/2}}, \quad (102)$$

$$C_{2x} = \frac{\langle [I_x^m(t - \tau_c + \tau) - \langle I_x^m \rangle][I_x^s(t) - \langle I_x^s \rangle] \rangle}{[\langle (I_x^m(t) - \langle I_x^m \rangle)^2 \rangle \langle (I_x^s(t) - \langle I_x^s \rangle)^2 \rangle]^{1/2}}, \quad (103)$$

$$C_{2y} = \frac{\langle [I_y^m(t - \tau_c + \tau) - \langle I_y^m \rangle][I_y^s(t) - \langle I_y^s \rangle] \rangle}{[\langle (I_y^m(t) - \langle I_y^m \rangle)^2 \rangle \langle (I_y^s(t) - \langle I_y^s \rangle)^2 \rangle]^{1/2}}. \quad (104)$$

Large values of C_{1x} and C_{1y} correspond to high-quality isochronous synchronization, while large values of C_{2x} and C_{2y} are the signature of good anticipating synchronization.

Though we have shown the existence of anticipating synchronization in the system, this does not mean that it will be observed, since it can be unstable. We have studied if this

synchronization regime can be observed numerically for the different regimes of feedback-induced instabilities described in section 3.3.4. We have considered first a configuration in which the slave is not subjected to optical feedback ($f^s = 0$), and therefore the injection rates are $\eta_x = \eta_y = f^m$, in order to verify the conditions for anticipating synchronization (95). Figure 42 represents the correlation coefficients for the x -polarized mode, C_{1x} and C_{2x} , when the injection rate $\eta_x = \eta_y$ is varied from 0.5 GHz to 50 GHz. We observe that for very small feedback rates (< 1.5 GHz approximately), perfect anticipating synchronization occurs (since $C_{2x} = 1$)¹⁵. For these values of the feedback rate, the intensity emitted by the master is not chaotic (*i.e.* it is stationary, periodic, or quasi-periodic), or it corresponds to very low-developed chaos. When the feedback rate is larger than 1.5 GHz, the chaos develops and the anticipating solution becomes unstable as the correlation coefficient C_{2x} drops sharply. Depending on the feedback rate, either complete desynchronization, or intervals of anticipating synchronization, interrupted by bursts of desynchronization, occur. The coefficient C_{2x} starts to increase again for feedback values larger than 5 GHz approximately. This increase in the anticipating correlation coefficient seems to be concomitant, and perhaps linked, to the appearance of a pulse-like behavior in the intensity. It is not until the feedback rate reaches a value of 17 GHz, approximately, that stable anticipating synchronization occurs again, as the correlation coefficient remains equal to 1 from 17 GHz to 50 GHz. The awakening of the y -polarized mode, that occurs around $f^m = 40$ GHz, does not seem to influence the quality of the synchronization, which is perfect, *both* for the x and the y -polarized modes (not shown here for the y mode).

It is interesting to notice that for large master feedback rates, the value of the correlation coefficient C_{1x} for isochronous synchronization takes relatively large values. In the configuration considered here though, it is fundamentally anticipating synchronization that occurs, and the value of the coefficient C_{1x} actually gives information on the shape of the chaotic signal, rather than on the synchronization process. It is important to understand that the only difference between the coefficients C_1 and C_2 is that in the master intensity

¹⁵Additionally, we have checked that anticipating synchronization does not only occur for exactly identical master and slave parameters, but is reasonably robust to mismatches which would be inevitable in a real experiment.

used in the calculation of C_2 is shifted by τ units of time with respect to the intensity used in the computation of C_1 . To illustrate this, Fig. 43 which represents the injected x -polarized intensity in the slave laser at a time t , $I_x^m(t - \tau_c)$, the intensity that *will* be injected τ units of time later $I_x^m(t - \tau_c + \tau)$, and the x -polarized intensity emitted by the slave at the same time t . The master feedback rate is $f^m = 30$ GHz and the conditions for anticipating synchronization are met. We see that the slave intensity synchronizes perfectly with the intensity that will be injected into it τ units of time later, therefore perfect anticipating synchronization occurs and $C_{2x} = 1$. We also see, however, that the slave intensity $I_x^s(t)$ is very similar to the intensity that is injected into it $I_x^m(t - \tau_c)$, leading to a large value of C_{1x} also. This large value of C_{1x} does not indicate true isochronous synchronization, but rather the fact that a pseudo-period τ exists in the chaotic intensity, so that even if it is fundamentally $I_x^s(t)$ and $I_x^m(t - \tau_c + \tau)$ that synchronize, $I_x^s(t)$ and $I_x^m(t - \tau_c)$ also look similar because $I_x^m(t - \tau_c + \tau)$ and $I_x^m(t - \tau_c)$ are similar to each other.

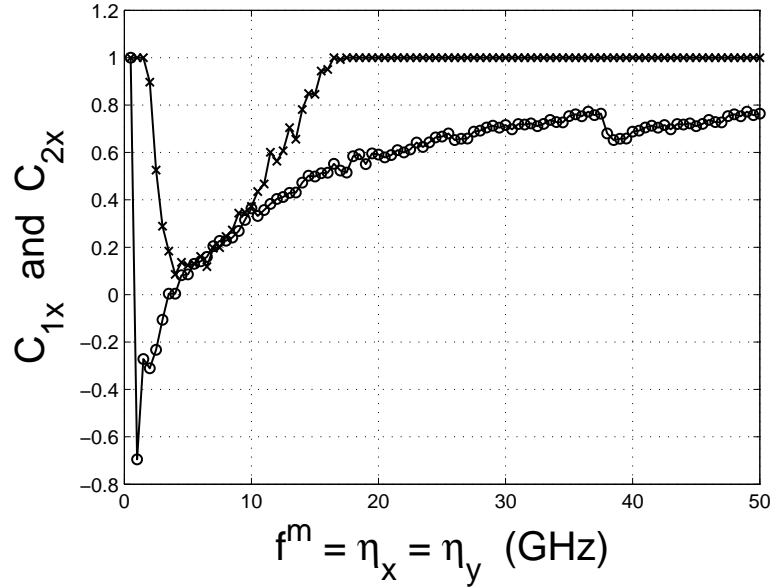


Figure 42: Correlations coefficients C_{1x} (circles) and C_{2x} (crosses) for the synchronization of the x -polarized components of the electric field. Slave feedback rate $f^s = 0$ GHz, injection rate $\eta_x = \eta_y = f^m$. All other parameters are as in Fig. 29.

Many of the characteristics of this anticipating synchronization in VCSELs are similar to those of anticipating synchronization in edge-emitting lasers, even when the two polarization

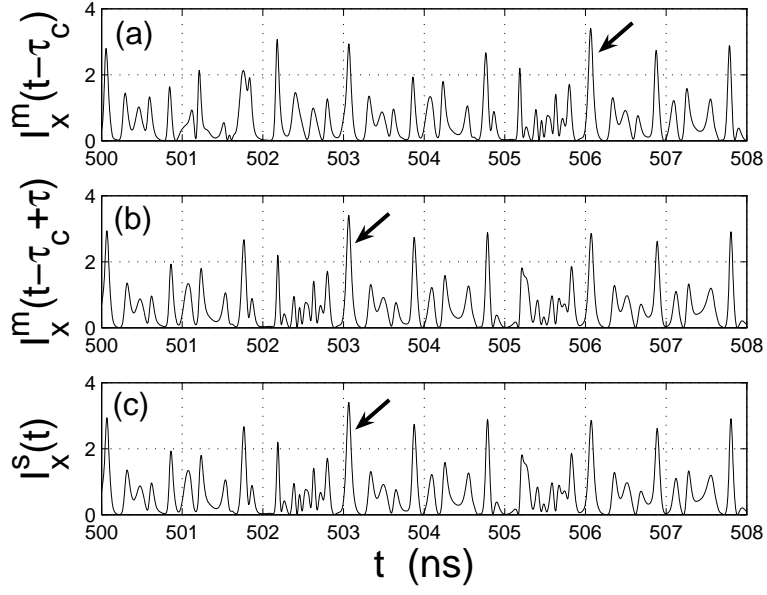


Figure 43: (a) Intensity of the x -polarized component of the electric field injected into the slave laser at a time t . (b) Intensity of the x -polarized component of the electric field that will be injected into the slave laser at a time $t + \tau$. (c) Intensity emitted by the x -polarized component of the electric field emitted by the slave at time t . Master isotropic feedback rate $f^m = 30$ GHz, slave feedback rate $f^s = 0$ GHz, injection rate $\eta = 30$ GHz. All other parameters are as in Fig. 29.

components are active. For example, we find that the open-loop slave gives rise to the most stable anticipating synchronization, as explained in the following. If we imagine that, starting from a regime of stable anticipating synchronization with an open-loop slave ($f^s = 0$), we introduce a feedback at the slave and increase the feedback rate (while decreasing the injection rate so that $\eta_x = \eta_y = f^m - f^s$), bursts of desynchronization usually occur, the frequency of the bursts increases with f^m , and finally for a certain limit feedback rate the anticipating synchronization becomes completely unstable. This same type of behavior occurs in the anticipating synchronization of edge-emitting lasers.

The regime of isochronous synchronization also displays many characteristics that resemble those observed in edge-emitting lasers. We have verified that the proportionality factors a_x and a_y for the synchronization of the intensities, and the proportionality term Δ_N for the synchronization of the carrier numbers (100), varies with the injection rate ($\eta_x = \eta_y = \eta$), even in the absence of frequency detuning, while the proportionality term Δ_ϕ does not. Similar behaviors occur in the case of isochronously synchronized edge-emitters [101].

As in the case of anticipating synchronization, we have studied the influence of a change in the feedback rate ($f^m = f^s$) on the synchronization process. It appears that it is always possible to find an injection rate that leads to isochronous synchronization. When the feedback rates are low, the injection rate must be significantly larger than the feedback rate to ensure synchronization, while for larger feedback rates, comparatively smaller injection rates are necessary (*i.e.* the ratio η_S/f^m , where η_S is the injection rate ensuring a given level of synchronization, decreases with f^m .) This can be due to the fact that since η measures the *fraction* of the master output power injected into the slave, and that this output power increases with f^m , the effective coupling between the two lasers increases with f^m , for a given η . For large feedback rates ($f^m = f^s$), even if it is isochronous synchronization that occurs, we observe a large value of the correlation coefficient that measures anticipating synchronization (C_{2i}) in reason of the presence of a pseudo-periodicity in the intensity, as explained above. Additionally, we observe that for large feedback rates, it is possible that a good synchronization of the amplitudes occurs (large correlation coefficient), while the phases exhibit bursts of desynchronization. It is important to note that the excitation of

the y -polarized component of the electric field for large feedback rates does not seem to affect qualitatively the synchronization process.

Finally, we mention that similarly to the case of edge-emitters, it is possible to observe a certain degree of isochronous synchronization even when the slave is not subjected to feedback ($f^s = 0$), but the injection rate needed to obtain a given synchronization quality is significantly larger than in the case of an external-cavity slave.

3.3.5.2 Second coupling configuration

In this configuration, the symmetry between the two linearly-polarized components is broken since only one of the two components is optically injected into the slave laser. This can be considered a first step toward the modeling of the experimental setup described in Refs. [106, 107], with which synchronization of chaotic VCSELs has been observed. We consider here the case in which the x -polarized component only is injected ($\eta_y = 0$).

It is obvious that in the regimes in which only the x -polarized component of the master electric field is active, setting the injection rate η_y for the y -polarized component to zero does not have any physical effect and the synchronization regimes that can be observed are those described in the previous section, for the first coupling configuration. The interesting cases are therefore those for which the two components are active, and only the x -polarized component is injected. The injection current of the slave laser is chosen here such that, in the absence of optical feedback and injection, it emits x -polarized CW light.

It is clear that, in this configuration, *perfect* anticipating synchronization cannot occur because the conditions (95) cannot be met since $\eta_y = 0$. This is shown in Fig. 44, which represents the intensities produced by the two lasers, when the master laser is subjected to a feedback rate $f = 40$ GHz, and the open-loop slave is subjected to optical injection with a rate $\eta_x = 40$ GHz. In this condition, the anticipating synchronization condition is met for the x component, but not for the y component. We see that, contrary to the case in which $\eta_x = \eta_y = 40$ GHz (*cf.* Fig. 38), only the x -polarized component is active at the slave laser, and perfect anticipating synchronization does not occur between the x -polarized components. Since the y -polarized component of the electric field produced

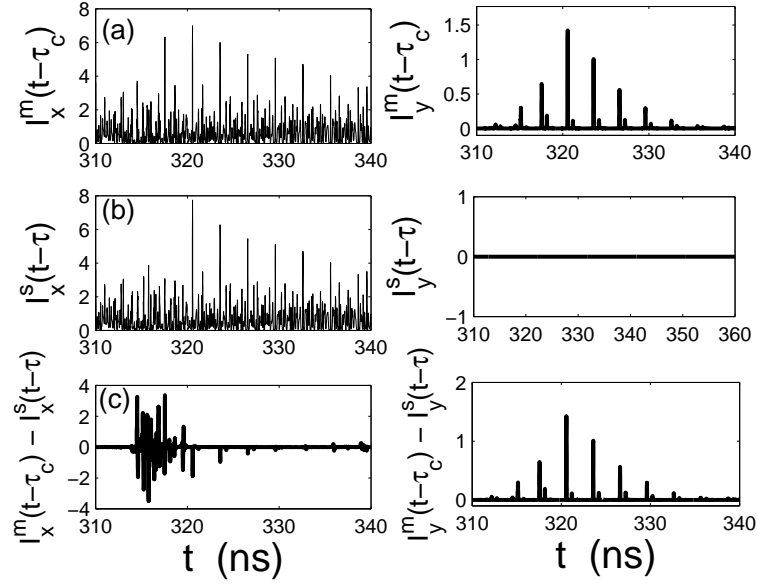


Figure 44: (a) Intensities of the x - and y -polarized components of the master electric field. (b) Intensities of the x - and y -polarized components of the slave. (c) Difference between the intensities. Master isotropic feedback rate $f^m = 40$ GHz, slave feedback rate $f^s = 0$ (open-loop), injection rates $\eta_x = 40$ GHz and $\eta_y = 0$. All other parameters are as in Fig. 29.

by the master is significantly smaller than the x -polarized component and consists of a series of pulses, we still observe a tendency to anticipating synchronization between the x components, especially during the periods of inactivity of the y component (between two pulses). It is easy to understand that for regimes in which the y -polarized component has a larger amplitude, anticipating synchronization between the x -polarized components does not occur at all.

Isochronous synchronization seems to be due to the fact that a strong optical injection in the slave forces this laser to synchronize (or lock) with the injected signal. It can be interesting to determine if this also happens when only one of the components of the electric field is injected into the laser, either open-loop or closed-loop, as is the case in the configuration studied here. We observe that for sufficiently large injection rates η_x , the x -polarized component of the slave electric field synchronizes in an isochronous way with the injected optical field. When this happens, the y -polarized component of the slave field is inactive, whether the slave is subjected to feedback or not. When the slave is not subjected

to feedback, it emits x -polarized light, and it remains x polarized when subjected to x -polarized optical injection. When the laser is subjected to a feedback such that it activates the y -polarized component, the injection of x -polarized light *kills* the y -polarized component, while the x -polarized component synchronizes with the injected field. The quality of the synchronization, between the x -polarized components of the electric field, when the x -polarized component (only) is injected, is only slightly lower than the quality when both components are injected, even if the x and y components have similar amplitudes.

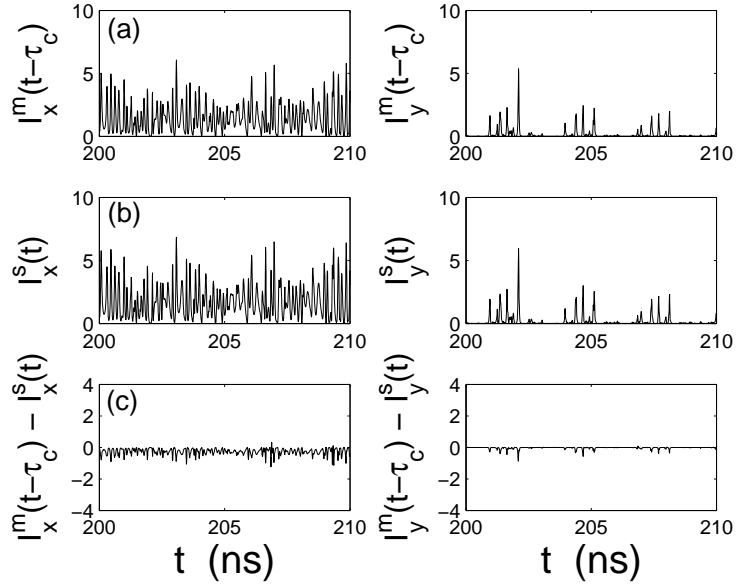


Figure 45: (a) Intensities of the x - and y -polarized components of the master electric field. (b) Intensities of the x - and y -polarized components of the slave. (c) Difference between the intensities. The correlation coefficient between the x -polarized components is 0.996. Injection currents $\mu^m = \mu^s = 2.5$, master isotropic feedback rate $f^m = 25$ GHz, slave feedback rate $f^s = 25$ GHz (open-loop), injection rates $\eta_x = 100$ GHz and $\eta_y = 100$ GHz. All other parameters are as in Fig. 29.

Figures 45 and 46 represent the intensities of the master and slave lasers when both components, or only the x -polarized components, of the master field are injected respectively. The two lasers have a normalized injection current $\mu^m = \mu^s = 2.5$ and an isotropic feedback rate $f^m = f^s = 25$ GHz, leading to feedback-induced instabilities in which both components of the electric field are active. We see that the optical injection of the two components, with an injection rate $\eta_x = \eta_y = 100$ GHz, leads to good synchronization of

the x and y components of the slave with the corresponding components of the injected field ($C_{1x} = 0.996$ and $C_{1y} = 0.997$). When the x -polarized component only is injected, with an injection rate $\eta_x = 100$ GHz, the y -polarized component stops being active, and the x -polarized component exhibits good isochronous synchronization with the injected light. The synchronization quality is, however, slightly lower than in the case of isotropic injection ($C_{1x} = 0.980$). This suggests that isotropic optical injection leads to a situation of coexistence of the two linearly-polarized modes at the slave laser, which mimics better the dynamics of the master laser, in which the two modes also coexist. This also means that the coexistence, and competition, between the two modes, is not detrimental to the quality of the synchronization.

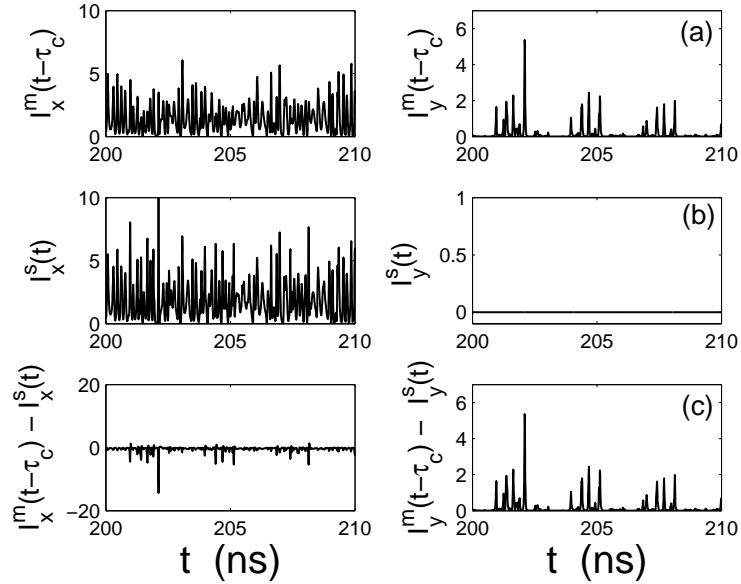


Figure 46: (a) Intensities of the x - and y -polarized components of the master electric field. (b) Intensities of the x - and y -polarized components of the slave. (c) Difference between the intensities. The correlation coefficient between the x -polarized components is 0.980. Injection currents $\mu^m = \mu^s = 2.5$, master isotropic feedback rate $f^m = 25$ GHz, slave feedback rate $f^s = 25$ GHz (open-loop), injection rates $\eta_x = 100$ GHz and $\eta_y = 0$. All other parameters are as in Fig. 29.

In summary, it is not possible to observe perfect anticipating synchronization when only one of two active linearly-polarized component is injected into the slave. A strong injection of one component induces, however, isochronous synchronization of the corresponding

component of the slave electric field and kills the orthogonal component.

3.3.5.3 Third coupling configuration

This configuration reproduces the main characteristics of the experimental observation of synchronization of chaotic VCSELs described in Refs. [106, 107]. In these experiments, the master laser is subjected to isotropic feedback, and the x -polarized component of its electric field is selected, rotated to the y polarization, and injected into an open-loop slave, which, in the absence of optical injection, emits CW x -polarized light. This type of injection is sometimes termed *orthogonal* optical injection, while the type of injection considered in the second configuration is termed *parallel* injection.

The configuration considered here, like the one described in the previous section, clearly favors one of the components of the electric field and it is easy to understand that perfect anticipating synchronization cannot exist here in the general case.

Our simulations of the model (81)-(84), (87), (88), (89), (90), show that for large injection rates η_y , the polarization emitted by the laser switches from the x direction to the y direction, following the polarization of the injected field. Moreover, the fluctuations of the intensity of the light emitted by the slave synchronizes isochronously with the fluctuations of the injected optical field. Figure 47 represents the intensities of the x - and y -polarized components of the slave laser, when it is free-running (a), and when it is subjected to strong orthogonal optical injection (b), as well as the injected intensity (c), for an isotropic master feedback rate $f^m = 1.3$ GHz, and an injection rate $\eta_y = 50$ GHz. We see that the free-running slave emits x -polarized light and is in a CW regime, while under strong injection of y -polarized light, the x -polarized component of the slave field stops lasing and the y -polarized component is activated. Moreover, the y -polarized field emitted by the slave synchronizes with the injected field. In particular, we find that the intensity of the y -polarized component of the slave field, $I_s(t)$, synchronizes with the injected intensity, $I_{inj}(t) = I_x^m(t - \tau_c)$, up to a proportionality factor. The synchronization observed in this case is therefore a form of isochronous synchronization, which is consistent with the experimental observations reported in Ref. [107]. The synchronization is of good quality, as is

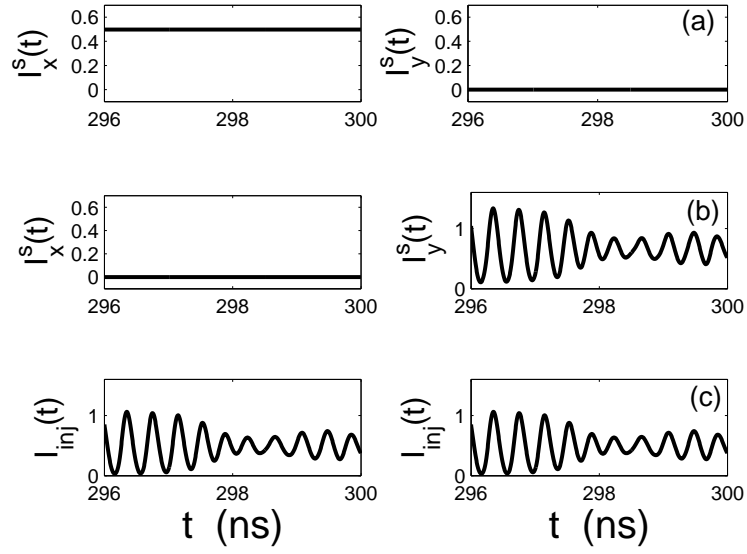


Figure 47: (a) Intensities of the x - and y -polarized components of the electric field of the solitary slave ($\eta_y = 0$). (b) Intensities of the x - and y -polarized components of the slave when subjected to strong orthogonal injection ($\eta_y = 50$ GHz). (c) Intensity of the injected field, $I_{inj}(t)$, which is the x -polarized output of the master, rotated to y -polarization. The correlation coefficient between $I_y^s(t)$ and $I_{inj}(t)$ is 0.984. Master isotropic feedback rate $f^m = 1.3$ GHz, slave feedback rate $f^s = 0$ GHz (open-loop), injection rates $\eta_y = 0$ GHz (a) or 50 GHz (b), and $\eta_x = 0$. All other parameters are as in Fig. 29.

shown by the correlation coefficient between the synchronized intensities, which is equal to 0.993.

This correlation coefficient is even larger than the one obtained for parallel optical injection. Indeed, when the x -polarized output of the master laser is injected into the open-loop slave, *without* being rotated, the correlation coefficient between the x -polarized component of the slave and the injected field is of 0.958 only. In Fig. 48, we have compared the quality of the synchronization of the slave with the injected field, under orthogonal and parallel injection, for a given injection rate of 50 GHz, and for various master feedback rates f^m . We observe that for feedback rates smaller than 28 GHz, approximately, the synchronization is better under orthogonal injection, even though a switching of polarization is involved. For higher master feedback rates, the synchronization quality under orthogonal injection drops sharply. In reference [107], it is suggested that synchronization should be achieved at lower injection powers with orthogonal polarization. Our model allows us to confirm these suggestions for an (upper limited) range of master feedback rates only¹⁶.

Hong *et al.* [106] have observed in their experiments that the y -polarized component of the slave electric field synchronizes with the injected field, and that the x -polarized component exhibits inverse synchronization (or antisynchronization) with this injected field. Two variables are said to be antisynchronized when they tend to vary in opposite ways, for example when one variable increases, the other decreases. This is characterized by a negative value of the correlation coefficient between the two variables. We have shown above, that under *strong* injection, the polarization of the light emitted by the slave switches to the polarization of the injected field. We consider now weaker injections, for which the x -polarized component has not been yet suppressed, and observe the behavior of the two components of the slave field. Figure 49 represents the x and y components of the slave field, and the injected field, for a feedback rate $f^m = 1.3$ GHz, and an injection rate $\eta_y = 5$ GHz. It is clear that the y -polarized component synchronizes with the injected field, with a correlation coefficient of 0.71, while there is inverse synchronization between the

¹⁶It is important to remember that we consider here lasers that do not exhibit any frequency detuning.

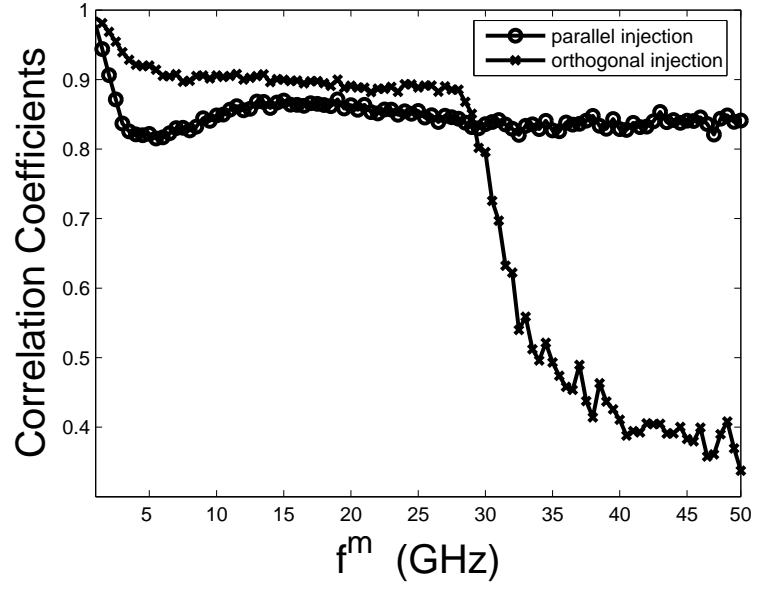


Figure 48: Correlation coefficient between the intensity of the injected field and the intensity of the x -polarized component of the slave field (parallel injection) or of the y -polarized component of the slave field (orthogonal injection). The master feedback rate f^m is varied from 0.5 GHz to 50 GHz. The injection rate is of 50 GHz, and the slave feedback rate is $f^s = 0$ GHz (open-loop). All other parameters are as in Fig. 29.

x -polarized component and the injected field, characterized by a correlation coefficient of -0.59. The x - and y -polarized modes clearly exhibit antiphase dynamics, which is common in VCSELS, as mentioned before, and is probably due to the competition for carriers between the two modes. What probably occurs is a synchronization of the y -polarized mode with the injected field, and the antiphase dynamics between the x - and y -polarized components creates mechanically an inverse synchronization between the x -polarized component and the injected field. It is important to notice, however, that although the fluctuations in the x -

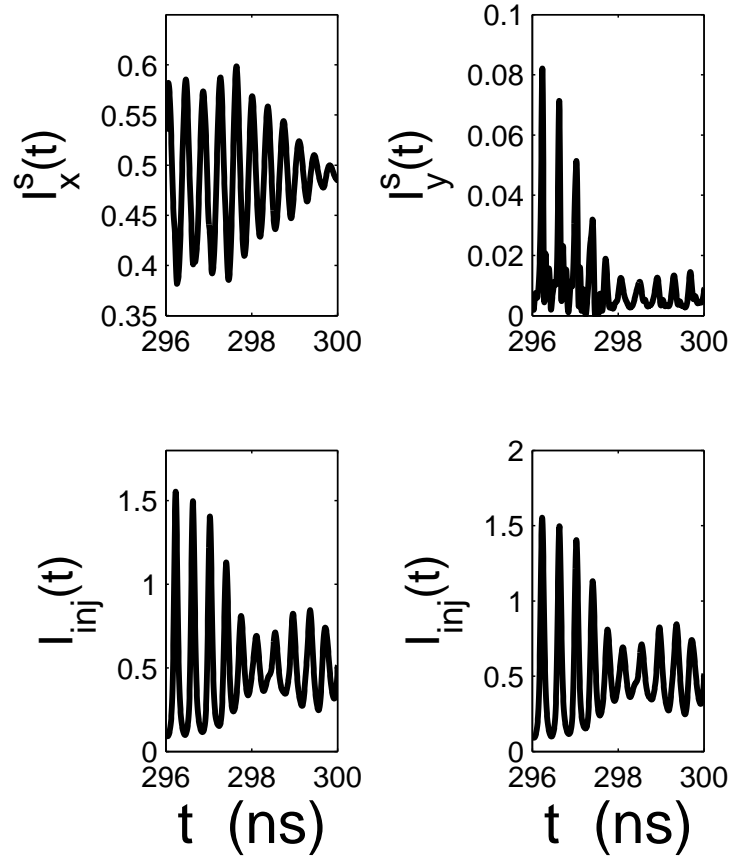


Figure 49: (a) Intensities of the x - and y -polarized components of the electric field of the slave when subjected to orthogonal injection ($\eta_y = 5$ GHz). (b) Intensity of the injected field, $I_{inj}(t)$, which is the x -polarized output of the master, rotated to y -polarization. The correlation coefficient between $I_y^s(t)$ and $I_{inj}(t)$ is 0.70 and the correlation coefficient between $I_x^s(t)$ and $I_{inj}(t)$ is -0.59. Master isotropic feedback rate $f^m = 1.3$ GHz, slave feedback rate $f^s = 0$ GHz (open-loop), injection rates $\eta_y = 5$ GHz and $\eta_x = 0$. All other parameters are as in Fig. 29.

and y -polarized components of the slave field are clearly synchronized (or antisynchronized) with the fluctuations of the injected field, their amplitude is much smaller than those of the injected field. For larger injection rates, the amplitude of the fluctuations of the y -polarized component becomes comparable to that of the injected field, and these fluctuations are isochronously synchronized, but the x -polarised component stops lasing, and therefore no inverse synchronization can be observed. In the experimental results of Hong *et al.* [106], the amplitudes of the fluctuations of the injected intensity, and of the synchronized and antisynchronized intensities of the slave are comparable; therefore, the results of Fig. 49 only show tendencies to a behavior similar to the experimental results, but do not reproduce them. We have tried to find results that are closer to the experimental ones, by investigating different values of the feedback rate, of the injection rate, and of the injection current. We find consistently a competition between the two linearly-polarized components of the slave, resulting in antiphase dynamics or alternate emissions in the two components. In the regime of alternate emission, one of the linearly polarized components is active while the other one is inactive or strongly suppressed, and *vice versa*. This regime is usually observed when the injected intensity has a *pulse-like* appearance, *i.e.* for large values of the master feedback rate. For the large injection rates that ensure a good synchronization quality, however, the x -polarized component is usually completely inactive, and no antiphase dynamics, and therefore no inverse synchronization, can be observed. Therefore, we only find relatively low qualities of (concomitant) inverse and direct synchronization.

The experimental results of Hong *et al.* show relatively good quality of synchronization and antisynchronization, with a slave experiencing fluctuations of similar amplitudes to those of the injected field. We have not been able to reproduce completely these results. We think, however, that there is a good chance that it should be possible to observe these phenomena in the framework of the SFM model used here. We should try, for example, to play with the parameters of the model to put the slave laser in a regime in which both linearly-polarized components have a strong tendency to lase, hoping that this will still be the case when the injection rate is such that good isochronous synchronization occurs. Frequency detuning between the two lasers should also be considered since it usually plays

an important role in the dynamics of optically injected lasers. For example, a frequency-detuned y -polarized injection could have a lower tendency to make the laser switch and to suppress the x -polarized component. Noise, and particularly spontaneous emission noise, can play an important role in the competition between the components of the electric field, especially for low feedback level, and should be considered. Since in an experimental setup, it is difficult to suppress completely one of the linearly polarized components, we could consider in the model that the injection of y -polarized light is accompanied by a low level of optical injection of the x -polarized component also. Finally, it could be necessary to include the presence of several transverse modes in the model, if large injection currents are used, since these transverse modes can play an important role in this case.

3.3.6 Polarization encoding

Based on the experimental setup used for the demonstration of synchronization of chaotic VCSELs [106], Won Lee *et al.* have shown experimentally that a 200 MHz sine waveform could be transmitted to the receiver. The message is encoded in a standard way by modulating the injection current. This type of setup does not exploit the polarization dynamics which is a specificity of VCSELs, and the results of Won Lee *et al.* can be considered as a transposition, in the context of VCSELs, of a technique used for chaotic communications using edge-emitters. Scire *et al.* [111] have proposed to exploit the polarization dynamics of VCSELs in an original chaos-shift keying scheme using two unidirectionally coupled VCSELs. In their theoretical setup, the phase relation between the two orthogonal linearly-polarized components of the electric field is changed by a polarization modulator, depending on the value taken by a binary information-bearing signal. The authors suggest that this leaves unaffected the total emitted intensity. As is typical in a CSK scheme (*cf.* §2.8), the x - and y -polarized components of the master and slave lasers desynchronize and resynchronize at the rhythm of the information-bearing signal. According to the authors the total intensities of the two lasers, however, remain synchronized all the time, and because of this the resynchronization should happen on a ps time scale and not on a ns time scale, as would be typical in a CSK technique using semiconductor lasers, since the relaxation

oscillations¹⁷ are not involved any more in the resynchronization process.

Unfortunately, there are some shortcomings associated with this scheme. First of all, the VCSELs used in Ref. [111] are lasers with a saturable absorber surrounding the active region, which are an uncommon type of laser. Additionally, chaos is produced in this scheme by the interplay of the (few) dynamical variables of the VCSEL itself, and therefore it can only be low-dimensional. Finally, the synchronization scheme is relatively complex since it involves a feedback mechanism that optically reinjects, in the slave, the difference between the master and slave electric fields. We have examined if it is possible to realize a similar setup, but using standard VCSELs, subjected to feedback, and synchronized by direct optical injection of the master field in the slave. The advantage of using a master laser subjected to feedback is that the chaos generated can be much higher dimensional than the chaos generated by a solitary laser with a saturable absorber. Additionally, synchronization by direct optical injection is easier to realize experimentally and a good synchronization quality should be possible to obtain, as was shown above. Therefore we do not think it is necessary to use the complex synchronization scheme that Scire *et al.* propose.

We use here the setup of the first coupling configuration described in section 3.3.5, in which the slave laser is not subjected to feedback ($f^s = 0$). We change the phase relation between the x - and y -polarized components of the electric field, and therefore the polarization state, at the rhythm of an information-bearing digital pseudo-random message $m(t)$, of period T . Every T units of time, the message has a probability 1/2 of taking the value 0 or H , and the phase of the x -polarized component of the slave field is either unaffected, or H radians are added to it for the duration of the bit. The setup can be modeled by the system of equations of the first coupling scheme considered in section 3.3.5, except that the equation for the x -polarized component of the electric field has to be modified in the following way to take into account the modulation:

¹⁷The relaxation oscillations in the photon and electron populations are a manifestation of an intrinsic resonance in which energy oscillates back and forth between these two populations.

$$\begin{aligned}
\dot{E}_x^s = & \kappa(1 + i\alpha) [(N^s - 1)E_x^s + in^s E_y^s] - (\gamma_a + i\gamma_p)E_x^s \\
& + f_x^s E_x^s(t - \tau) \exp(-i\omega_s \tau) \\
& + \eta_x E_x^m(t - \tau_c) \exp[i(\omega_m - \omega_s)t] \exp(-i\omega_m \tau_c) \exp[im(t)] .
\end{aligned} \tag{105}$$

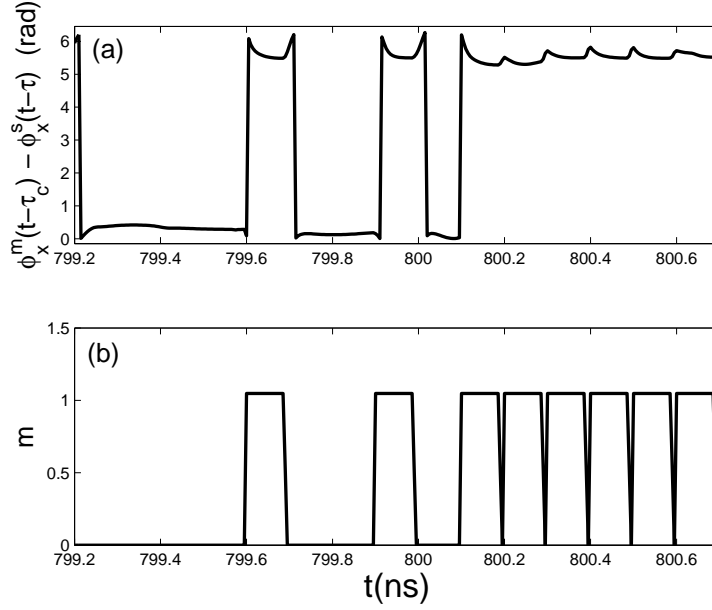


Figure 50: (a) Difference between the phases of the x - polarized components of the master and slave electric fields. (b) Information bearing signal m . Master isotropic feedback rate $f^m = 55$ GHz, slave feedback rate $f^s = 0$ GHz (open-loop), injection rates $\eta_x = 55$ GHz and $\eta_y = 55$ GHz. All other parameters are as in Fig. 29.

Preliminary results suggest that it is possible to transmit an information-bearing signal using this technique. We consider here a master laser subjected to an isotropic feedback rate $f^m = 55$ GHz, which leads to the concomitant emission of the two linearly-polarized components and to a chaotic evolution of the polarization state on the Poincaré sphere. We use anticipating synchronization, as the injection rates are chosen to be $\eta_x = \eta_y = 55$ GHz. In the absence of the message m , perfect anticipating synchronization occurs between the intensities of master and slave fields. The presence of a message m changes the evolution of the state of polarization on the Poincaré sphere, but is undetectable on the intensity of the electric field transmitted to the slave. Our simulations indicate that it seems to be possible

to transmit a 10 Gbit/s message, of amplitude $H = \pi/3$, using this technique¹⁸. Figure 50 shows that the phases of the x -polarized component of the master and slave lasers experience synchronization and desynchronization at the rhythm of the message m . This property can therefore be used to recover the message, though an experimental realization would be non-trivial. The intensities of the x -polarized components remain relatively well synchronized, and they cannot be used to recover the message, as shown in Fig. 51. We also find, however,

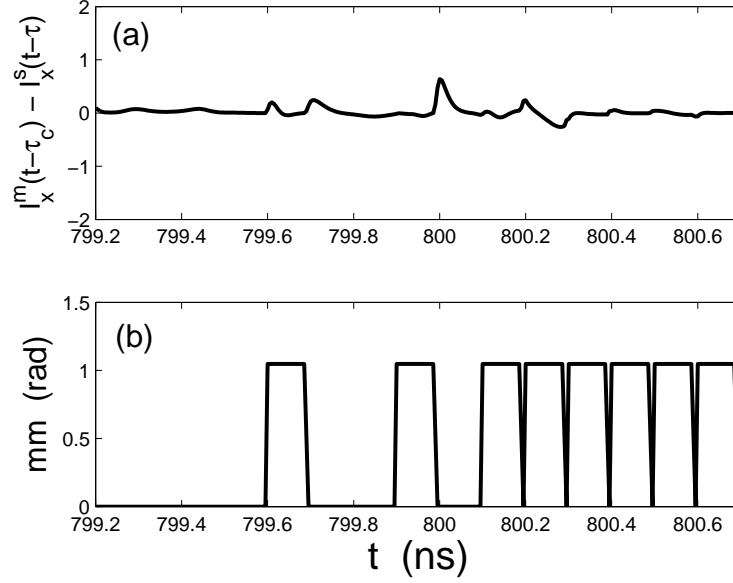


Figure 51: (a) Difference between the intensities of the x - polarized components of the master and slave electric fields. (b) Information bearing signal m . Master isotropic feedback rate $f^m = 55$ GHz, slave feedback rate $f^s = 0$ GHz (open-loop), injection rates $\eta_x = 55$ GHz and $\eta_y = 55$ GHz. All other parameters are as in Fig. 29.

that some periods of desynchronization occur during which it is impossible to recover the information bearing signal. During these bursts of desynchronization, not only the phases, but also the amplitudes and the carrier numbers desynchronize. Figure 52 represents the evolution of the master and slave carrier and shows that a period of desynchronization starts around $t = 827$ ns.¹⁹ These periods of desynchronization occur more frequently for

¹⁸Our simulations also indicate that it does not seem to be possible to transmit a message with such a high bit rate using the technique based on a direct modulation of the injection current.

¹⁹It should be noticed that Figs. 50 and 51 correspond to an interval of time that precedes the burst of desynchronization.

high bit rates than for low bit rates. A bit rate of 10 Gbit/s seems to be the approximate limit above which it becomes impossible to recover the message m , because of the absence of synchronization. These preliminary results need to be confirmed by a more detailed

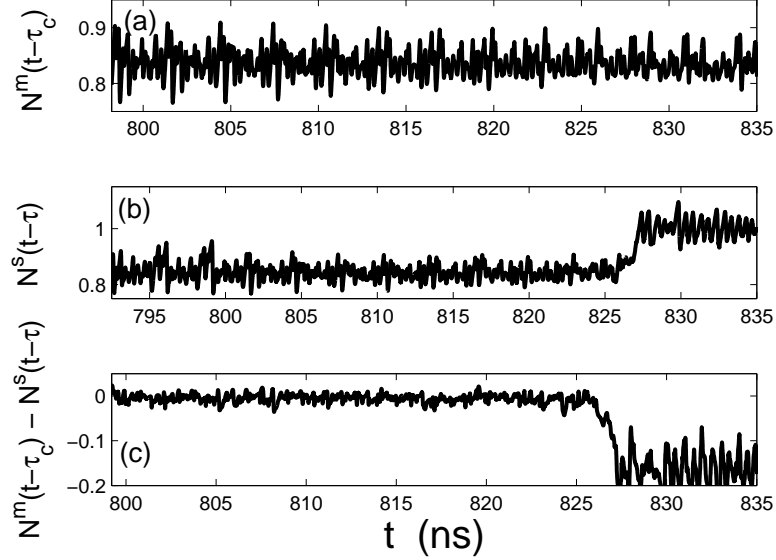


Figure 52: (a) Master carrier number N . (b) Slave carrier number N . (c) Difference between the master and laser carrier numbers showing a period of desynchronization starting after 827 ns approximately. Master isotropic feedback rate $f^m = 55$ GHz, slave feedback rate $f^s = 0$ GHz (open-loop), injection rates $\eta_x = 55$ GHz and $\eta_y = 55$ GHz. All other parameters are as in Fig. 29.

study of the synchronization/desynchronization mechanisms under the effect of polarization modulation.

3.3.7 Summary

We have studied the synchronization of external-cavity VCSELs on the basis of the spin-flip model. We have considered a master laser subjected to isotropic optical feedback, while different types of optical injection in the slave have been studied.

In the case of isotropic injection, we observe regimes of anticipating and isochronous synchronization of the two linearly-polarized components of the electric field. The characteristics of these synchronization regimes are similar to the characteristics of the anticipating and isochronous regimes identified in edge-emitting lasers.

The optical injection of only one of the linearly-polarized components of the electric field clearly favors the corresponding component at the slave laser. For sufficiently large injection levels, the component parallel to the injection synchronizes isochronously with the injected field. If this component is inactive at the slave laser, the polarized optical injection activates it, and if the orthogonal component is active, the optical injection kills it. In the case of orthogonal injection, and for intermediate injection levels, the two linearly-polarized components of the slave electric field can be active contemporaneously, and antiphase dynamics between the two components is often observed. In this case, the component parallel to the direction of the polarized injection tends to synchronize with the injected field, while the other component experiences antisynchronization with the injected field. The component of the electric field perpendicular to the injection is usually killed, however, before good synchronization (and antisynchronization) occurs. We are confident that some modifications of the operating conditions, and especially the inclusion of frequency detuning between the lasers, should lead to the observation of good synchronization and antisynchronization, consistently with the experimental results of Hong *et al.* [106, 107].

Finally, preliminary results indicate that it should be possible to realize chaotic communications, between external-cavity VCSELs, in which the information-bearing signal is coded on the polarization state of the master laser.

CHAPTER IV

ANALYSIS OF TIME SERIES PRODUCED BY CHAOTIC DELAY SYSTEMS

4.1 Introduction

It is well known that since delay systems have an infinite-dimensional phase space, they can produce high-dimensional chaos, because of the infinite number of directions of evolutions of the system in phase space. It is believed that the use of a complex chaos is useful in chaotic communications because it leads to a better masking of the information-bearing signal than when lowly-developed chaos is used. We are interested in analyzing the delay cryptosystems used at the GTL-CNRS Telecom Laboratory, in verifying that they can indeed produce complex chaos, and in determining the conditions under which complex chaos occurs. This will help the experimentalist determine the operating conditions that lead to better encryption.

In the case of delay systems however, the standard techniques of time series analysis, and of computation of the Lyapunov spectrum from the dynamical model, described in sections 4.2 and 4.3, fail because of the high dimensionality of the attractors. Special techniques for delay systems have been developed by Farmer [123] in the case of a known model, and by Hegger *et al.* [79, 124] when only time series are known. These techniques are quite involved and we refer the reader to the aforementioned references for more details. We will just give a flavor of the technique that uses time series analysis, because part of it will also be useful for a delay time identification technique studied in the next section.

Section 4.2 describes the principles of specific techniques that can be used to analyze time series produced by delay systems, while section 4.3 explains how these techniques can be used to estimate the Lyapunov spectrum, and how this spectrum can be computed when the dynamical model is known. Section 4.4 is devoted to the identification of the delay of

a series of experimental chaotic delay emitters, which is the first step in the analysis of a delay system. Section 4.5 shows briefly how the specific time series analysis techniques can be used to identify, in certain cases, the nonlinear function. Finally, section 4.6 is devoted to the estimation of the Lyapunov spectrum of the Mackey-Glass system, and of the generator of wavelength chaos, from time series and from the dynamical model.

4.2 Principles of the analysis of time series produced by delay systems

We have seen in section 2.6 that the first step in time series analysis is an embedding of the attractor in a phase space reconstructed by the method of delays. Since we want to characterize high-dimensional delay systems, this is not a practical thing to do¹. It has been shown indeed that the number of points of the time series necessary to determine deterministic quantities by statistical methods increases exponentially with the attractor dimension [125, 126]. This is due to the fact that the number of variables that have to be used in the method of delays increases with the attractor dimension. High-dimensional attractors mean, therefore, that it is necessary to work in high-dimensional reconstructed spaces. It is easy to understand that the number of elements of the time series must be very important in order to find a sufficient number of neighbors of a point in such high-dimensional reconstructed spaces and thus to obtain statistically significant results. Practically, for dimensions larger than 5, it becomes very difficult to determine the deterministic properties of a system and thus to make the difference between high-dimensional chaos and colored noise.

This section shows that it is nevertheless possible to determine deterministic quantities of delay systems by exploiting their peculiar structure. Techniques that are tailored to delay systems have to be used. We have been greatly inspired by the references [127, 128, 129, 79, 130, 131] for the presentation we give here. We consider first the simple case of a scalar delay-differential system.

¹Even if from a theoretical point of view, it would be possible to apply the Takens embedding theorem to high-dimensional data coming from a delay system

4.2.1 Scalar delay systems

A continuous-time scalar delay system can be described by a scalar delay-differential equation

$$\dot{x}(t) = F[x, x(t - \tau)] , \quad (106)$$

where τ is the delay, F is a real nonlinear function, and $x \in \mathbb{R}$ the dynamical variable. As we have noted in section 2.3, the phase space is here the infinite-dimensional space of functions defined on an interval of length τ .

In this delay system, the derivative of $x(t)$ depends not only on the value of the dynamical variable x at time t but also on its value at the time $t - \tau$. This means that correlations exist that are nonlocal in time. These nonlocal correlations allow for complex evolutions of the system dynamics. It should be noted that these correlations are not easily detectable by a visual analysis of the time series.

It is essential to notice that Eq. (106) is a constraint in the space spanned by $\dot{x}(t)$, $x(t)$, and $x(t - \tau)$ and therefore the equation $\dot{x}(t) - F[x, x(t - \tau)] = 0$ defines a two-dimensional manifold, \mathcal{S} , on which the system evolves. Equivalently, it can be said that the projection of a trajectory of the system in the infinite-dimensional phase space on the three-dimensional space $(\dot{x}(t), x(t), x(t - \tau))$ is confined on a surface \mathcal{S} . It is important to understand that in the general case the projection of a high-dimensional attractor on a space of dimension three does *not* lead to a two-dimensional manifold. It is a specific property of delay systems.

The main idea behind the analysis techniques for delay systems is to work in the three-dimensional space spanned by $\dot{x}(t)$, $x(t)$, and $x(t - \tau)$ instead of the infinite-dimensional phase space. In particular, we show in this work that it is possible to identify the delay (§ 4.2, § 4.3), to perform local linear approximations of the dynamics (§ 4.2), to identify the nonlinear function (§ 4.5), to compute the Lyapunov spectrum, dimension, and entropy (§ 4.3, § 4.6) by working in such a low-dimensional space. In the remainder of this section, we explain how local linear approximations can be performed and how the delay can be identified.

The presence of a delay in the dynamical system can be detected and its value can be

identified by detecting the presence of the surface \mathcal{S} in the three-dimensional space. There are several ways to test the existence of this surface [128, 129, 79], but they are all based on the study of the behavior of the system in a space $(\dot{x}(t), x(t), x(t - \tau^*))$, where τ^* is an arbitrary delay. As discussed above, the surface only exists when $\tau^* = \tau$ since only in this case does Eq. (106) define a constraint. In Ref. [128], the space $(\dot{x}(t), x(t), x(t - \tau^*))$ is divided in a large number of cubes and a filling factor is defined as the number of cubes that are visited by the projection of the trajectory. When $\tau^* = \tau$, a relatively small number of cubes are visited given that the trajectory is confined to a surface, whereas when $\tau^* \neq \tau$, a larger number of cubes are visited. A maximal value of the filling factor is therefore expected for the correct value of τ^* . We will use in this chapter another technique that employs local linear approximations of the dynamics and that corresponds to the construction of a series of planes tangent to the surface \mathcal{S} . Since these approximations only make sense if a surface is effectively spanned, a minimum of the approximation error is expected for $\tau^* = \tau$.

Of course, one does not have the variable x in the form of a continuous function of time, but as a set of N values x_n of x taken at discrete times, separated by a time interval h . This time interval can be a sampling period or an integration step. This discretization implies that the phase space is also discretized: instead of an infinite-dimensional function space, a vector space of dimension P is used. It is constituted by the vectors $(x_n, x_{n-1}, x_{n-2}, \dots, x_{n-(P-1)})$, where $P - 1 = \tau/h$ is the number of samples corresponding to the delay τ of the system. To simplify notations, and without loss of generality, we will assume that $h = 1$, which means that $P - 1 = \tau$. The preceding considerations are still valid in this discretized phase space, even if a loss of information can result from the discretization. In particular, it can be considered that the space $(\dot{x}_n, x_n, x_{n-\tau})$ is the discretized version of $(\dot{x}(t), x(t), x(t - \tau^*))$. In this space, \mathcal{S} can be modeled by

$$\hat{x}_n = g_1[\vec{v}_n(\tau)], \quad (107)$$

where \hat{x}_n is an estimation of the derivative obtained from the time series, g_1 is a map from \mathbb{R}^2 to \mathbb{R} and $\vec{v}_n(\tau)$ is a vector defined by $\vec{v}_n(\tau) = (x_n, x_{n-\tau})$. The system dynamics can be

modeled by the iteration

$$x_{n+1} = g_2[\vec{v}_n(\tau)], \quad (108)$$

where g_2 is a map from \mathbb{R}^2 to \mathbb{R} . It is important to note that this does not correspond to a model of the attractor in phase space but to a reconstruction of the dynamical rule of the scalar delay system.

It is possible to make a local linear approximation of the dynamics of the system in a neighborhood of $\vec{v}_n(\tau^*)$:

$$x_{n+1} = a_n + b_n x_n + c_n x_{n-\tau^*}, \quad (109)$$

where a_n , b_n , and c_n are the coefficients of the approximation and τ^* is a delay expressed as a number of samples². A least squares method is used to determine the coefficients of the approximation by minimizing the following quantity

$$e_n^2(\tau^*) = \frac{1}{\text{Card}(\mathcal{U}_n)} \sum_{i \in \mathcal{U}_n} (x_{i+1} - a_n - b_n x_i - c_n x_{i-\tau^*})^2 \quad (110)$$

with respect to the coefficients in the approximation, in a small neighborhood $\mathcal{U}_n(\epsilon) = \{i : \|\vec{v}_i - \vec{v}_n\| < \epsilon\}$ of $\vec{v}_n = (x_n, x_{n-\tau})$. The quantity $\text{Card}(\mathcal{U}_n)$ represents the number of elements of the set \mathcal{U}_n . The choice of the neighborhood size faces the same issues as those described in section 2.6.2 and the search for neighbors itself is a nontrivial problem described in the appendix A. The quantity $e_n^2(\tau^*)$ is obviously the error of the local linear approximation in the neighborhood of the vector \vec{v}_n . An average approximation error can be defined as

$$E^2(\tau^*) = \langle e_n^2(\tau^*) \rangle_n, \quad (111)$$

where $\langle \dots \rangle_n$ is an average taken on the whole time series. This quantity therefore represents the average error of the local linear approximations all along the trajectory under consideration. A global minimum of the function $E^2(\tau^*)$ is expected for $\tau^* = \tau$ since

²It is better to approximate (108) rather than (107) because in this way we will avoid the problem of estimating derivatives, which can be a difficult task in the presence of noise, and because the approximations (108) will be useful to determine the Lyapunov spectrum.

it is only in this case that x_{n+1} , x_n , and $x_{n-\tau^*}$ are linked by a constraint and thus that the approximations make sense.

We will present numerous applications of this identification method in section 4.4. It is useful to notice that first, contrary to the standard embedding techniques, it is not necessary that the trajectory has settled on the attractor (thus time series corresponding to transient periods can be used) and second, that the techniques described hereabove are independent of the dimension of the attractor. We end this section by noting that this type of local linear approximations has been used by Zhou and Lai [80] to break a cryptosystem based on a Mackey-Glass delay system.

4.2.2 Vectorial delay systems

We consider now the more general case of a system with d dynamical variables in which one of its variables is involved in a delayed feedback. This type of system can be described by an equation

$$\frac{d\vec{x}(t)}{dt} = \vec{F}(\vec{x}, x^{(l)}(t - \tau)) , \quad (112)$$

where $\vec{x} \in \mathbb{R}^k$ is the vector of dynamical variables and $x^{(l)}$ is the component of $\vec{x} \in \mathbb{R}^k$ that is involved in the feedback. We assume that we only have a scalar time series, (x_n) , which corresponds to the measure of a component of \vec{x} .

The fact that only one variable of a vectorial system is measured must be taken into account in some way. Hegger *et al.* [79] have proposed to analyze these systems by combining the technique for scalar delay systems described in the preceding section with a reconstruction of the unmeasured variables by the method of delays. More precisely, they propose to work in a neighborhood of the vector

$$\vec{v}_n = (x_n, x_{n-1}, x_{n-2}, \dots, x_{n-m+1}, x_{n-\tau}, x_{n-\tau-1}, x_{n-\tau-2}, \dots, x_{n-\tau-m+1}) .$$

If we compare the scalar case to the vectorial case, we notice that delayed variables of the form x_{n-j} and $x_{n-\tau-j}$ have been added to reconstruct the variables that have not been measured. It should be noticed that delayed variables have been introduced for $x_{n-\tau}$ as

well as for x_n . This is based on an analogy between delay systems and input/output systems [$x(t - \tau)$ is considered as an input of the system which is dealt with, as shown in [132], by introducing it, with its delayed values, in the vector \vec{v}_n]. Hegger *et al.* suggest that $m = 2k$ should be sufficient to reconstruct the unobserved variables³. In a similar way to the case of a scalar system, the following local linear approximation is performed

$$x_{n+1} = a_n + \langle \vec{b}_n, \vec{v}_n \rangle = a_n + \sum_{j=1}^m b_n^{(j)} x_{n-j+1} + \sum_{j=1}^m c_n^{(j)} x_{n-\tau^*-j+1}, \quad (113)$$

where a_n , $b_n^{(j)}$ and $c_n^{(j)}$ are the coefficients of the local linear approximation. They can be determined by a least squares method in a neighborhood of the vector \vec{v}_n . The search for neighbors must thus be performed in this case in a space of dimension $2m$. This non-trivial problem is described in appendix A. It is possible to use these approximations to identify the delay τ in a similar way to what has been done for scalar systems (§106).

It is important to understand that the additional delayed variables are used only to reconstruct the unobserved variables and not to reconstruct the full dynamics on the attractor in the phase space. In particular, we work with vectors \vec{v}_n that evolve in a space whose dimension, $2m$, is independent of the attractor dimension. The attractor dimension can be greatly superior to $2m$ and the application of the Takens' embedding theorem to reconstruct the dynamics on the attractor could require a number of delayed variables greatly superior to $2m$. In the case of a vectorial delay system, the time series analyst will have to work in a space of larger dimension than in the case of a scalar delay system, but this dimension is still much lower than the dimension of the reconstructed space that would have resulted from the application of an embedding of the high-dimensional attractor.

As a conclusion, the peculiar structure of delay equations, in which only a small number of variables is involved (only one variable in the case of a scalar system), can be used to model locally the dynamical rule in a low-dimensional space, independently of the dimension of the attractor. We have shown that these approximations can be used to identify the delay. We show in the next section (4.3.1) that they can also be used to estimate the Lyapunov

³the reader should notice the analogy with condition on the number of variables of Takens embedding theorem.

spectrum.

4.3 Estimation of the Lyapunov spectrum of a delay system

We show here how the Lyapunov spectrum can be estimated in the case of delay systems. Section 4.3.1 studies the case in which only a time series is known and section 4.3.2 considers the case in which the dynamical model is known. In both cases, the techniques presented in sections 2.5.2 and 2.6.2 cannot be used directly and thus specific techniques have to be developed.

4.3.1 From the time series

We have explained in section 2.6.2 that the standard techniques used to estimate the spectrum involves making local linear approximations in a reconstructed phase space. We have shown above (§4.2) that this procedure is not practicable in the case of high-dimensional attractors.

The solution is to use the results of the preceding section and to work in the projection of the phase space onto a low dimensional space instead of working in the (high-dimensional) phase space itself. In this way, it is possible to find a sufficiently high number of neighbors to determine statistically significant coefficients in the approximations. The computation technique of the Lyapunov spectrum is due to Hegger *et al.* [124].

We consider here scalar delay systems (106). As explained in section 2.5.2, it is necessary to determine the jacobian matrices of the time- h map that associates to the state of the system in phase space at time t , the state of this system h units of time later. In the case of delay systems of course, the phase space *stricto sensu* is not accessible directly since it is infinite-dimensional: it is therefore necessary to work in a discretized phase space (which is finite-dimensional). This space of dimension P (*cf.* 4.2.1) is spanned by the vectors of the form $\vec{x}_n = (x_n, x_{n-1}, x_{n-2}, \dots, x_{n-\tau})$. Once again, to make things simple, we use the same variable (τ) to designate the delay and the number of samples contained in the delay.

Our aim is thus to determine the jacobians of the map

$$\vec{\phi}_h : \mathbb{R}^P \rightarrow \mathbb{R}^P; \vec{x}_n = (x_n, x_{n-1}, x_{n-2}, \dots, x_{n-\tau}) \mapsto \vec{x}_{n+1} = (x_{n+1}, x_n, x_{n-1}, \dots, x_{n-\tau+1}) \quad (114)$$

along the trajectory that corresponds to the analyzed time series. It is fundamental to notice that it is only the first component $x_{n+1} = \vec{\phi}_h^{(1)}(x_n, x_{n-1}, \dots, x_{n-\tau})$ of $\vec{\phi}_h$ that corresponds to nontrivial dynamics. Its linearized behavior is of the form $x_{n+1} = a_n + b_n x_n + c_n x_{n-\tau}$ and can be determined in the way indicated in section 4.2.1 (in a three-dimensional space). The other components of $\vec{\phi}_h$ simply select one of the components of \vec{x}_n (*e.g.* $x_n = \vec{\phi}_h^{(2)}(x_n, x_{n-1}, \dots, x_{n-\tau})$) and correspond globally to a time shift of h units of time.

On the basis of the previous considerations, it is easily found that the jacobian matrix of $\vec{\phi}_h$ (in the discretized phase space) takes the following form

$$J_n = \begin{pmatrix} b_n & 0 & \cdots & 0 & c_n \\ 1 & 0 & \cdots & 0 & 0 \\ 0 & 1 & \cdots & 0 & 0 \\ \vdots & \vdots & \ddots & \vdots & \vdots \\ 0 & 0 & \cdots & 1 & 0 \end{pmatrix} \quad (115)$$

The elements of the first line can be obtained from the local linear approximation (109). The local linear approximations described in section 4.2.1 can thus be used to determine the jacobian matrices all along the trajectory. The computation of the Lyapunov spectrum from these matrices then follows the procedure described in section 2.5.2.

In principle, we are now able to compute the Lyapunov spectrum of a system from its time series. It is also necessary, however, to choose the values of a series of critical parameters which influence the quality of the results. One of these parameters is the time step h that discretizes the continuous-time system. The delay system is time-continuous and its phase space is infinite dimensional, but with a finite time step h , the dimension shrinks to τ/h . It is easily understood that h must be chosen small enough to reproduce the full dynamics of the continuous-time system. Practically, this can be done by checking the convergence of certain characteristic quantities when the value of h is decreased. Another

critical parameter is the neighborhood size. If it is too small, the results can be statistically ill-determined; if it is too large, the linear approximations lose their meaning. Moreover, in the case of noisy time series, the neighborhoods must be large enough to ensure that it is the deterministic dynamics, and not the noise, that is fitted.

The case of vectorial delay systems can be treated in a similar way by exploiting the local linear approximations of the form (113).

4.3.2 From the model – Farmer’s method

In this section, we show how the Lyapunov spectrum can be determined when the dynamical model (106) of a scalar delay system is known. We have shown in section 2.5.2 that in the case of a system described by ordinary differential equations, this can be done by integrating in parallel the dynamical model and the variational equation. In particular, the variational equation was used to determine the Jacobians of the time- h map.

In the case of delay systems, a state of the system is no longer determined by the collection of the values of a finite set of variables, at a given time, but by a function of an interval of length τ . Therefore the calculation procedure of the case of systems of ordinary differential equations cannot be applied directly. The first step is once again to discretize the phase space by observing the system at instants separated by a time interval h . This leads to a space of dimension P whose elements are of the form $(x(t), x(t - h), x(t - 2h), \dots, x(t - \tau))$. The Lyapunov spectrum can then be computed by using the Jacobian matrices of the time- h map. We could derive the rate equations of the Jacobians, but to keep things simple, we present Farmer’s approach [123] to compute the Lyapunov spectrum. Farmer uses the standard procedure for computing the spectrum described in §2.5.2 and applies it to the case of scalar delay systems discretized as explained above. As in section 2.5.2, we start from an orthonormal basis of the discretized phase space, that we call here $(\vec{\delta x}_1, \vec{\delta x}_2, \dots, \vec{\delta x}_p)$. Farmer calls these vectors “separation functions”: it can be considered indeed that these vectors are P discretized versions of functions defined on an interval of length τ . As in the case of the standard procedure, the evolution of these separation functions under the linear

part of the time- h map must be computed. Before the transformed vectors become degenerate, they must be orthonormalized by a Gram-Schmidt-like procedure. The accumulation of these normalization factors gives the Lyapunov exponents as shown in formula (21)⁴.

Specifically, the evolution of the separation functions can be determined by linearizing the dynamical equation (106) of the system. This linearization leads to the linear non-autonomous delay-differential equation

$$\frac{d\delta x(t)}{dt} = \frac{\partial F[x(t), x(t-\tau)]}{\partial x(t)}\delta x(t) + \frac{\partial F[x(t), x(t-\tau)]}{\partial x(t-\tau)}\delta x(t-\tau). \quad (116)$$

The integration of this equation using as initial conditions the values of the different components of a separation function allows us to compute the evolution of the separation function. If the evolution of all the separation functions is computed in this way and an orthonormalization procedure is applied, the Lyapunov spectrum can be determined as described above. Further details can be found in Refs. [123, 133].

In the remainder of this chapter, we use the concepts presented so far on the analysis of delay systems to determine important characteristics of several delay systems, and in particular of several chaotic emitters used in chaotic cryptosystems. Section 4.4 is devoted to the identification of the delay, section 4.5 to the identification of the nonlinearity, and finally section 4.6 studies the estimation of the Lyapunov spectrum, of dimension, and of entropy.

4.4 Delay identification

The delay is obviously the most important parameter of a delay system and its identification is of fundamental importance for a time series analyst. Moreover, as we have mentioned before, its identification can lead to breaking a chaotic delay cryptosystem. In addition to the specific techniques based on local linear fits and filling factors presented in section 4.2, some other standard techniques can be used to identify the delay. Section 4.4 is devoted to the presentation of these techniques. The different identification methods are then applied

⁴We should consider that in formula (21), the vector $\vec{y}_k^{(i)}$ represents here the transformed k^{th} separation function, orthogonalized but not normalized, at the i^{th} iteration.

to several delay systems. Section 4.4.2 studies the case of the Mackey-Glass system, section 4.4.3 the case of an optoelectronic system generating wavelength chaos, section 4.4.4 the case of an optoelectronic generator of chaos in intensity, and finally section 4.4.5 examines the case of an electronic system generating frequency chaos.

4.4.1 Identification Techniques

In the following, we present several quantities that can be used to identify a delay, namely the autocorrelation, the autocovariance, and the mutual information.

4.4.1.1 Autocorrelation

The autocorrelation of a real random signal $X(t)$ is the real function R_X of two real variables t_1 and t_2

$$R_X(t_1, t_2) = E [X(t_1)X(t_2)] , \quad (117)$$

where E represents the expected value. When a random process is stationary, its probability laws are invariant with respect to a shift of the time origin. Direct consequences are that the mean value m_X of the process does not depend on time and the autocorrelation depends only on the difference $t_1 - t_2 = \tau$. The autocorrelation is therefore a function of a single variable

$$R_X(\tau) = E [X(t)X(t - \tau)] . \quad (118)$$

If we assume additionally that the process is ergodic, the ensemble average performed by the expectation operator can be replaced by a time average

$$R_X(\tau) = \lim_{T \rightarrow +\infty} \frac{1}{2T} \int_{-T}^T x(t)x(t - \tau)dt , \quad (119)$$

where $x(t)$ is a realization of the random process $X(t)$. We will mainly use the notion of autocovariance defined in the general case by

$$C_X(t_1, t_2) = E \{ [X(t_1) - m_X(t_1)] [X(t_2) - m_X(t_2)] \} . \quad (120)$$

The difference between autocovariance and autocorrelation lies in the fact that the former is centered with respect to the mean value. When the process is stationary and ergodic, the

autocovariance can be written as

$$C_X(\tau) = E \{ [X(t) - m_X] [X(t - \tau) - m_X] \} = R_X(\tau) - m_X^2 . \quad (121)$$

The autocovariance measures, for a given value of τ , the tendency of the cloud of points $(x(t), x(t - \tau))$ to align along an oblique straight line. It measures therefore a *linear* link between $x(t)$ and a delayed version, $x(t - \tau)$, of $x(t)$.

4.4.1.2 Mutual Information

The notion of mutual information comes from information theory. Consider a discrete random variable X and call \mathcal{X} the set of all possible realizations of X . We define first the entropy $H(X)$ of X :

$$H(X) = \sum_{x \in \mathcal{X}} p(X = x) \log p(X = x) , \quad (122)$$

where x is a realization of the random variable X . This quantity corresponds intuitively to a measure of the quantity of information necessary to the description of X . If the logarithm is in base 2, this quantity is measured in bits. Consider now two random variables X and Y . \mathcal{X} and \mathcal{Y} represent the set of all possible realizations of X and Y respectively. The relative entropy of X knowing Y , $H(Y | X)$, is given by

$$H(Y | X) = \sum_{x \in \mathcal{X}} \sum_{y \in \mathcal{Y}} p(X = x, Y = y) \log p(Y = y | X = x) . \quad (123)$$

The relative entropy corresponds to the quantity of information necessary to the description of X knowing Y . From these two notions, the mutual information $I(X, Y)$ of two random variables can be defined as

$$I(X; Y) = H(X) - H(X | Y) = \sum_{x \in \mathcal{X}} \sum_{y \in \mathcal{Y}} p(X = x, Y = y) \log \frac{p(X = x, Y = y)}{p(X = x)p(Y = y)} . \quad (124)$$

We understand easily that this quantity corresponds to the reduction of the quantity of information necessary to the description of X due to the knowledge of Y . The larger the value of $I(X; Y)$, the more information Y contains on X .

The dynamical systems studied in this thesis produce chaotic signals $x(t)$, that can be considered as realizations of a random process $X(t)$. When the time is discretized (corresponding to numerical integration or sampling), and when ergodicity is assumed, it can be considered that the values $x(t_i)$, where t_i is a time of observation of the system, correspond to the different realizations of a random variable. Moreover, a discrete random variable is obtained when the continuous-time density function is approximated by an histogram (discrete distribution function). The interested reader can find further details on these information theoretical concepts in the book by Thomas M. Cover and Joy A. Thomas [134].

The mutual information between $x(t)$ and $x(t - \tau)$, where τ is an arbitrary delay, can be used to identify nonlinear nonlocal links in time due to the presence of a delay in the system under consideration. It is useful to know that the mutual information computed between $x(t)$ and $x(t - \tau)$ is sometimes called “delayed mutual information”.

4.4.2 Mackey-Glass system

We consider here the famous Mackey-Glass system [8]. This system models the production of blood cells in the human body. The generation of these cells is greatly influenced by the delay that exists between the initiation of the cell production process and the liberation of mature cells in the blood flow. The dynamical model that describes this system is a first order differential equation

$$\tau^R \dot{x}(t) = \frac{cx(t - \tau)}{1 + x(t - \tau)^{10}} - x(t). \quad (125)$$

This system is among the delay systems that have received the greatest attention from the scientific community and is often considered as an archetype of delay systems. Figure 53 represents the nonlinearity of the Mackey-Glass system as well as a chaotic signal produces by this system.

The reader should note that this nonlinearity has only one extremum and that, on the contrary, systems used for chaotic encryption always use more complex nonlinearities which have several extrema. The Mackey-Glass system is not a good candidate to perform chaotic encryption. We use this system, that has been largely studied in the literature, to test all

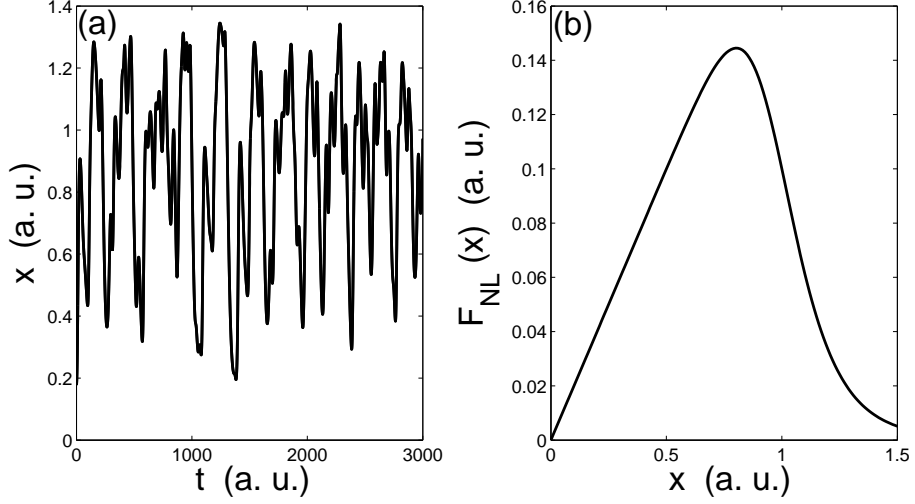


Figure 53: (a) Chaotic signal and (b) nonlinear function of the Mackey-Glass system. $\tau = 46$, $\tau^R = 10$, $c = 2$.

the time series analysis techniques for delay systems. It is therefore used mainly to validate our algorithms of time series analysis. Since we do not have a physical system that behaves like the Mackey-Glass model, we analyze numerically generated time series.

We begin by studying the efficiency of the various delay identification techniques described in section 4.4.1. Figure 54 represents the autocovariance of $x(t)$. As could have been expected, a global maximum is reached for $\tau^* = 0$. The global minima are reached for a value of $|\tau^*|$ equal to 52, which is close, but larger, than the delay τ . This overestimation is typical in the autocovariance technique. The autocovariance measures a link between $x(t)$ and a delayed version, $x(t - \tau^*)$, of $x(t)$. If we imagine a pulse x_i produced by the system at time t , this pulse comes back into the system after a time τ due to the feedback, and the system will only respond to that pulse after an additional time τ^R which is the response time of the system. This illustrates why identifying the delay with the autocorrelation leads to an overestimation caused by the system response time.

The mutual information technique has been applied in Fig. 55. In addition to the global maximum reached for $\tau^* = 0$, a series of local maxima are observed for values of τ^* that are integer multiples of themselves. The deepest local maximum is reached for a value of τ^* equal to 51.5. The mutual information also leads to an overestimation of the delay, for

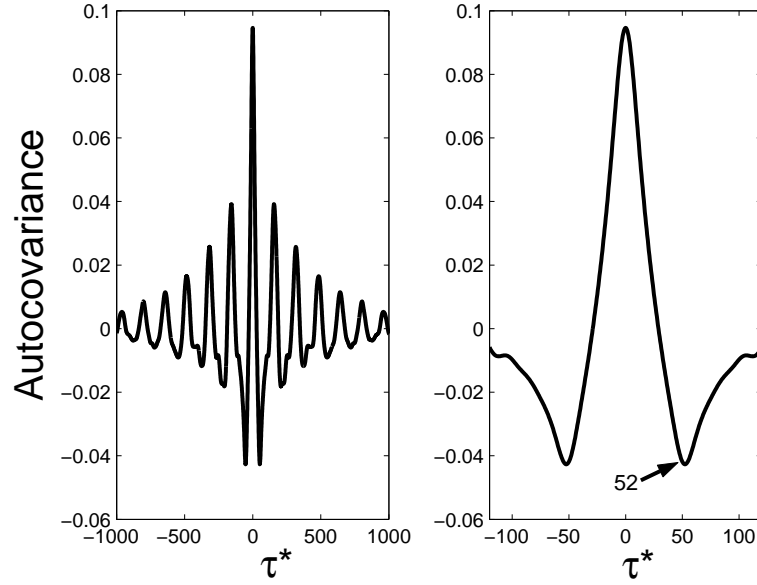


Figure 54: Autocovariance of $x(t)$. $\tau = 46$, $\tau^R = 10$, $c = 2$, $h = 0.5$.

the same reasons explained for the case of the autocovariance technique.

Finally, Fig. 56 represents the approximation error coming from local linear fits, defined by formula (111), as a function of an arbitrary delay τ^* . The number N of samples is 41500 (corresponding to 450 intervals of length τ), and the neighborhood size ϵ is 1 percent of the amplitude of the variations of $x(t)$ [footnote⁵]. The global minimum is reached for a value of τ^* equal to 46, which corresponds exactly to the value of the delay τ [footnote⁶]. We see that this method does not lead to an overestimation of the system delay τ . This is because it does not measure a link between $x(t)$ and a delayed version of $x(t)$, but it uses the structure of the delay equation by performing, loosely speaking, an approximation of the nonlinear function as a collection of linear functions of $x(t)$ and $x(t - \tau^*)$.

We have checked on the Mackey Glass system that the technique based on an approximation error leads to a more accurate estimation of the delay time τ than the autocovariance and the mutual information. It should be pointed out, however, that it requires, for a given number of samples N , a much longer computation time.

⁵In the following, ϵ will always be expressed in this way.

⁶It is worth noticing that there is also a local minimum for a value of τ^* slightly larger than τ , and function of the response time τ^R of the system.

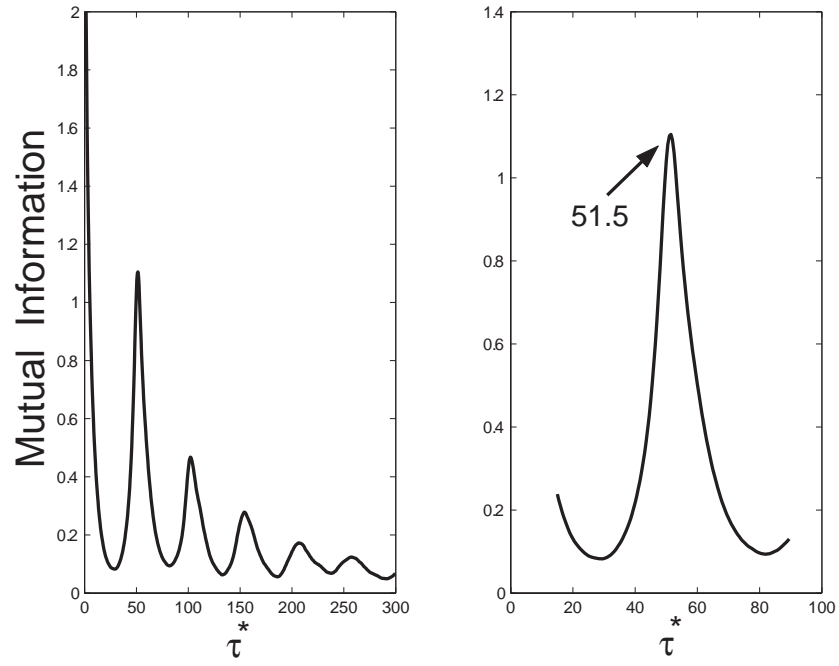


Figure 55: Mutual information between $x(t)$ and $x(t-\tau^*)$. $\tau = 46$, $\tau^R = 10$, $c = 2$, $h = 0.5$.

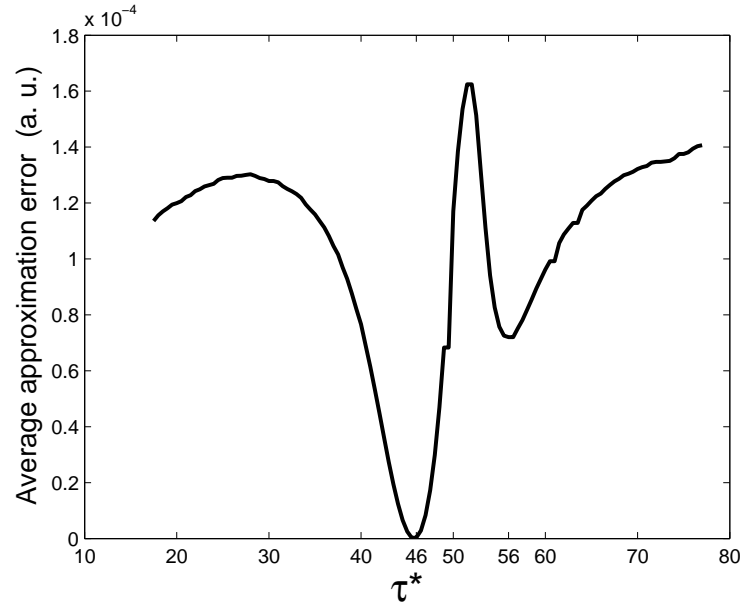


Figure 56: Average approximation error. $\tau = 46$, $\tau^R = 10$, $c = 2$, $h = 0.5$, $\epsilon = 1\%$, $N = 41400$ samples.

4.4.2.1 Influence of the parameters N , ϵ , and h of the identification procedure

The average approximation error represented in Fig. 56 has been drawn for a given value of the number of samples N , of the neighborhood size ϵ , and of the sampling period h . A good choice of these values can be critical to a good estimation of the delay. This is why we study in this section how the choice of these parameter values influences the identification of the delay.

The first parameter that we study is the number N of samples in the time series. Figure 57 represents the mean approximation error for different values of N . We notice that the larger the number of samples is, the more pronounced the minimum is, but at the same time even a relatively small number of samples (*e.g.* 5000) allows the identification of the delay. It should be noted at this point that even if the estimation of the Lyapunov spectrum uses the same local linear fits as the delay identification technique does, the number of samples N that will be needed to ensure the convergence of the Lyapunov spectrum will be much larger than the number needed to identify the delay.

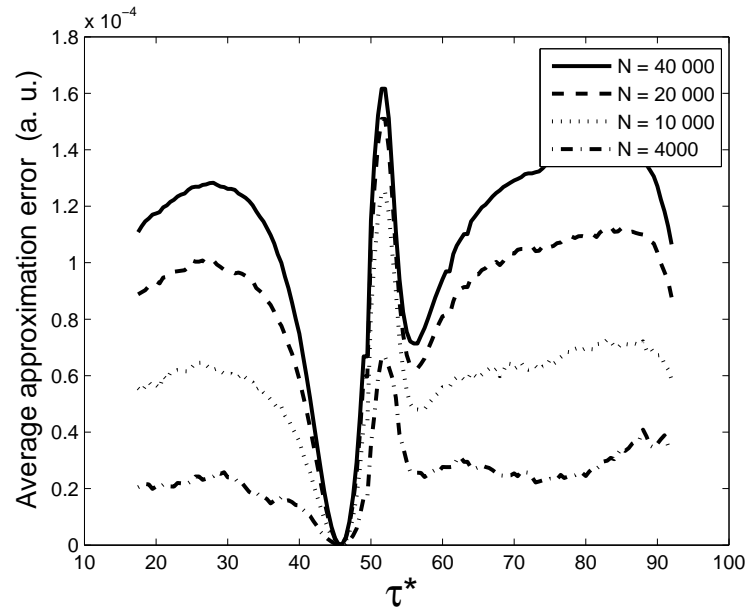


Figure 57: Influence of the number of samples N . $\tau = 46$, $\tau^R = 10$, $c = 2$, $h = 0.5$, $\epsilon = 1\%$.

Figure 58 represents the approximation error for a large range of values of the neighborhood size ϵ , going from 0.5% to 20%. We notice that for all the values of ϵ considered, the

delay τ can be identified. We also notice that large neighborhoods lead to more pronounced maxima, but it should be pointed out at the same time that bigger neighborhoods means larger numbers of neighbors to consider and larger computation times ⁷.

The last parameter in the delay identification procedure is the sampling time h . Figure 59 shows that when h increases, the minimum of the approximation error becomes more pronounced and tends to become narrower also. This is because when τ^* is different from τ , an approximation of the form $x_{i+1} = a_i + b_i x_i + c_i x_{i-\tau^*}$ is better when the sampling step is small. When τ^* is different from τ , the linear expression given is not a good approximation, which leads to a high values of the approximation error when $\tau^* \neq \tau$. But there will always be a correlation between the terms x_{i+1} and x_i and this correlation is weaker when the corresponding time interval h is larger. This explains larger values of the approximation error when h is bigger and thus the more pronounced maxima.

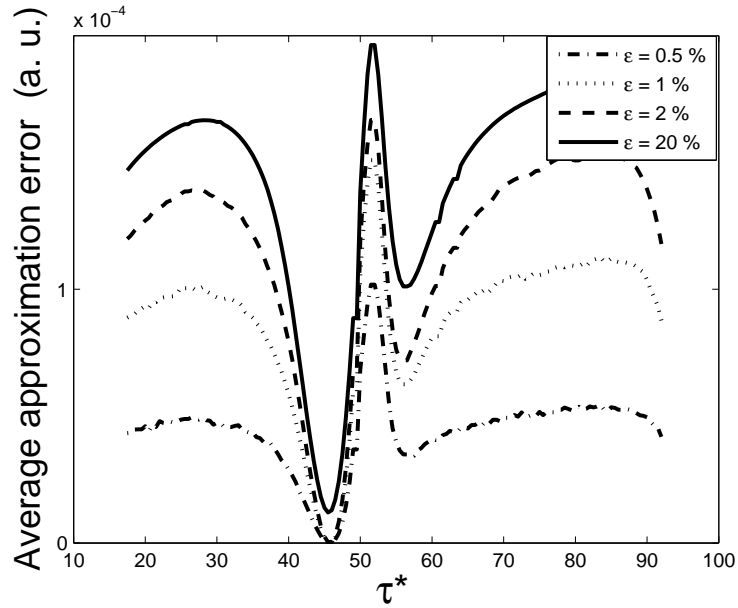


Figure 58: Influence of the neighborhood size ϵ . $\tau = 46$, $\tau^R = 10$, $c = 2$, $h = 0.5$, $N = 20000$.

Finally, it can be interesting to determine the precision with which the delay τ can be obtained by the local fits technique. The preceding study on the influence of h can give us

⁷Bigger neighborhoods mean bigger “boxes” in the neighbor search algorithm (*cf.* appendix A).

some indications in this matter. We know that obviously the minimal difference between two successive values of the τ^* is necessarily equal to the sampling period h , but two values of the delay that differ by h do not lead necessarily to significantly different values of the approximation error. Figure 59(b) shows that for $h = 0.25$, several values of τ^* around τ lead to almost identical values of the approximation error. This means that the error in the determination of τ must be larger than 0.25. A closer look at Fig. 59 tells us that we can only hope for an absolute error in the order of 0.5.

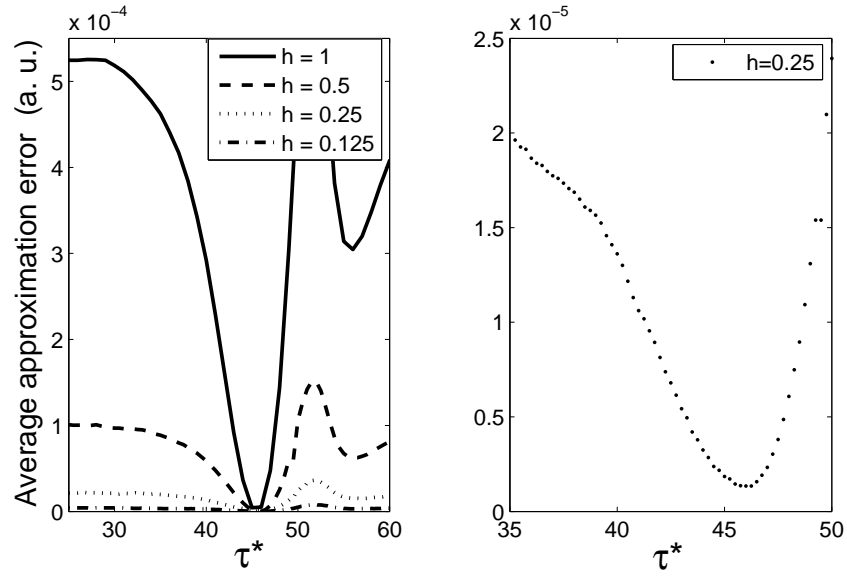


Figure 59: Influence of the sampling period h . $\tau = 46$, $\tau^R = 10$, $c = 2$, $\epsilon = 0.01$, $N = 20000$.

4.4.3 Optoelectronic system producing wavelength chaos

We consider here the optoelectronic emitter producing a chaos in wavelength described in section 2.4.3. We recall that this system is described by the equation

$$\tau^R \dot{x}(t) = \beta \sin^2[x(t - \tau) + \phi] - x(t) , \quad (126)$$

where τ^R is the response time, β the feedback strength, and ϕ an optical phase shift. This system has been used to perform chaotic encryption [135] - [137] and has been our main source of experimental data for time series analysis in reason mainly of the easiness with which its experimental parameters can be tuned. We give in the next section a flavor of

the dynamical behavior of the system, which will be useful to interpret the results on the complexity of the system presented in section 4.6.2.

4.4.3.1 Influence of the parameters β and τ on the dynamics

We focus here on the influence of the feedback strength β and the delay τ on the dynamics. Both parameters are easily tunable experimentally and have an important influence on the system dynamics, which will also be studied in section 4.6.2 in terms of Lyapunov spectrum, dimension, and entropy.

Figure 60 represents the bifurcation diagram when the feedback strength is varied from 1 to 30. The values of the system parameters correspond to typical experimental conditions. This diagram represents the probability density function of the chaotic signal, in gray levels, for the different values of β . The darker the gray, the higher the value of the probability density is. It is seen that the transitions toward a fully developed chaos take place for values of β smaller than 3. To better understand the bifurcation mechanisms, we have represented in Fig. 61 the bifurcation diagram for values of β ranging from 1 to 3. In this figure, however, it is the extrema of the chaotic signal, for each value of β , that are represented. We see that, when β increases, the solution is first stationary, then periodic, with period 2τ , then the period doubles and reaches 4τ , followed by an inverse transition toward a periodic solution of period 2τ . Close to $\beta = 2.7$, a chaotic solution appears that still bears a periodic component, of period 2τ (T_2 chaos [29]), and a fully-developed chaos appears when β is larger than 3 approximatively. We also notice that when β increases, both the mean value of the chaotic signal and the amplitude of the chaotic fluctuations increase.

It is important to know that the nature and localization of the bifurcations toward a fully-developed chaos depend on the values of the other parameters of the system (such as τ , ϕ , and τ^R) and on the initial conditions⁸. Whatever the route toward chaos is, however, a regime a fully-developed chaos always appears when β is sufficiently large (around 5). It is this chaotic regime, which is also the most complex, that is the most interesting for encryption purposes.

⁸Refer to [29, 30] for more details

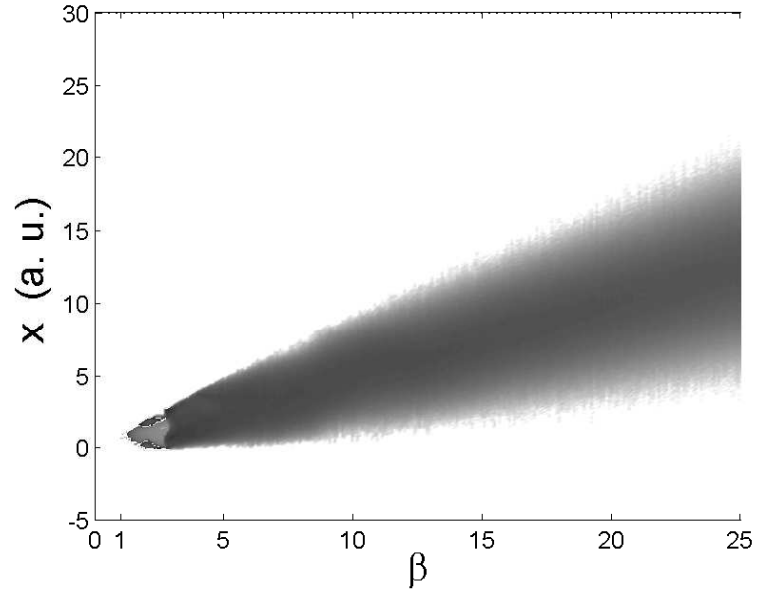


Figure 60: Bifurcation diagram when β is varied. $\tau^R = 8.4 \mu\text{s}$, $\phi = \pi/3$, $\tau = 523 \mu\text{s}$.

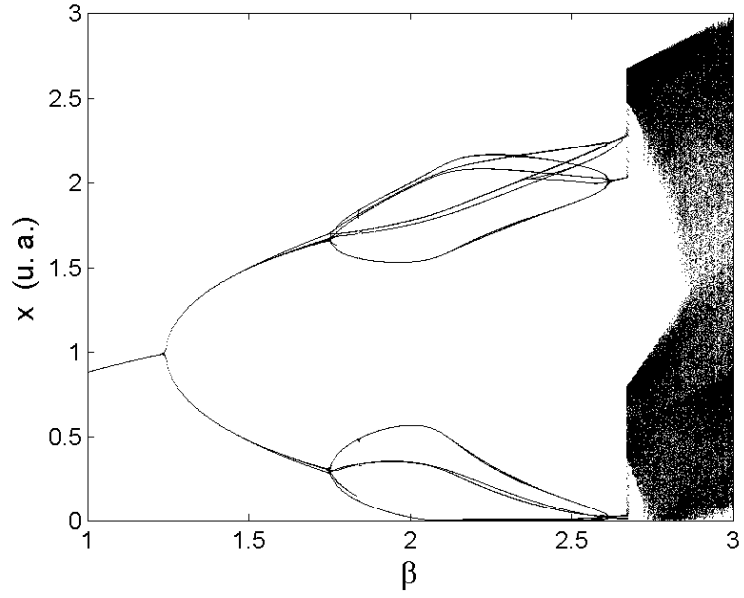


Figure 61: Bifurcation diagram when β is varied. $\tau^R = 8.4 \mu\text{s}$, $\phi = \pi/3$, $\tau = 523 \mu\text{s}$.

Figure 62 shows the bifurcation diagram, in terms of the pdf, when the delay τ is increased, for a given (relatively high) value of the strength of the nonlinearity ($\beta = 8$)⁹. For such a large value of β , x remains chaotic on the whole span of values of τ (in the diagram, τ varies between 100 and 1000 μs). We also notice that contrary to the case of a variation of β , the probability density function does not seem to be significantly influenced by a variation of τ .

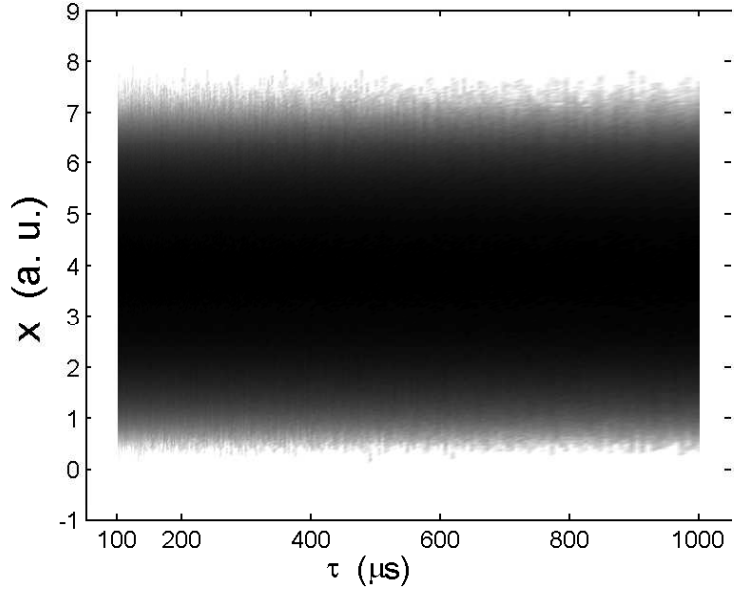


Figure 62: Bifurcation diagram when τ is varied. $\tau^R = 8.4 \mu\text{s}$, $\phi = \pi/3$, $\beta = 8$.

A bifurcation diagram is not the only way to characterize the dynamical behavior of a system. The temporal evolution of the signal x , the probability density function, the portion of the nonlinear function effectively visited, and the power spectral density of x can all give some useful information. These quantities are represented in Figs. 63, 64, 65, and 66 for values of β equal to 2.8, 3, 10, and 25, respectively. The reader should remember that the power spectral density corresponds to the Fourier transform of the autocorrelation function. The spectral estimation is performed by averaging several tens of simple spectral estimations (Welch's method). The portion of the nonlinear function that is represented is the one that

⁹This corresponds to the chosen value of β in section 4.6.2 for the study of the influence of the delay on the Lyapunov spectrum. This relatively large value of β leads to a chaotic behavior of the system even when the delay τ is quite small.

is effectively visited by the signal x during a time span of several times the delay τ . The case $\beta = 2.8$ corresponds to a " T_2 chaos", whilst the other cases correspond to a "fully developed chaos", as can be seen from the bifurcation diagram of Fig. 60. The comparison of the different figures shows immediately that the number of extrema of the nonlinear function increases with the value of β . Figure 63 reveals some distinctive features of the chaos generated for $\beta = 2.8$. It is seen from the time series x that a periodic component exists in the signal (of period 2τ), and this component is also found, with its harmonics, in the spectrum. The probability density function is also peculiar since it is concentrated mainly in two disjoint intervals of values of x , which is easily understood by looking at the time series x . Increasing β to 3 leads to a significant change in the type of chaos produced

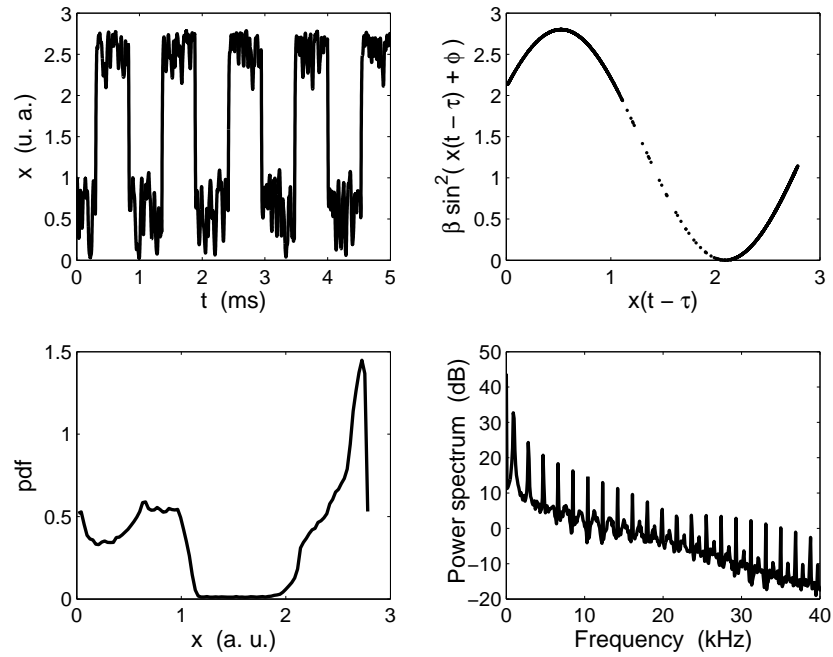


Figure 63: T_2 chaos for $\beta = 2.8$. $\tau = 523 \mu\text{s}$, $\tau^R = 8.4 \mu\text{s}$, $\phi = \pi/3$.

by the system. A periodic component can no longer be seen, in an obvious way, neither in the time series nor in the spectrum. The probability density function still shows similarities with the case $\beta = 2.8$, but it should be expected that a further increase of the value of β leads to the loss of the signature of the bifurcations that have lead to chaos. This can be seen in the cases when $\beta = 10$ and $\beta = 25$: a periodicity can no longer be found neither

in the time series nor in the spectrum. Increasing β leads to faster chaotic fluctuations, a pdf that tends towards a gaussian law, and an increase of the number of active extrema of the nonlinearity. The spectrum gets closer to that of a white noise, although it is seen that it tends to decrease for increasing frequencies, due in part to the filtering effect of the low-pass filter, whose cutoff frequency is $1/(2\pi\tau) = 18.9$ kHz.

It thus appears that the chaotic regimes that correspond to a high value of β have characteristics that resemble those of a white gaussian noise. These regimes are those that interest us the most for applications in secure communications.

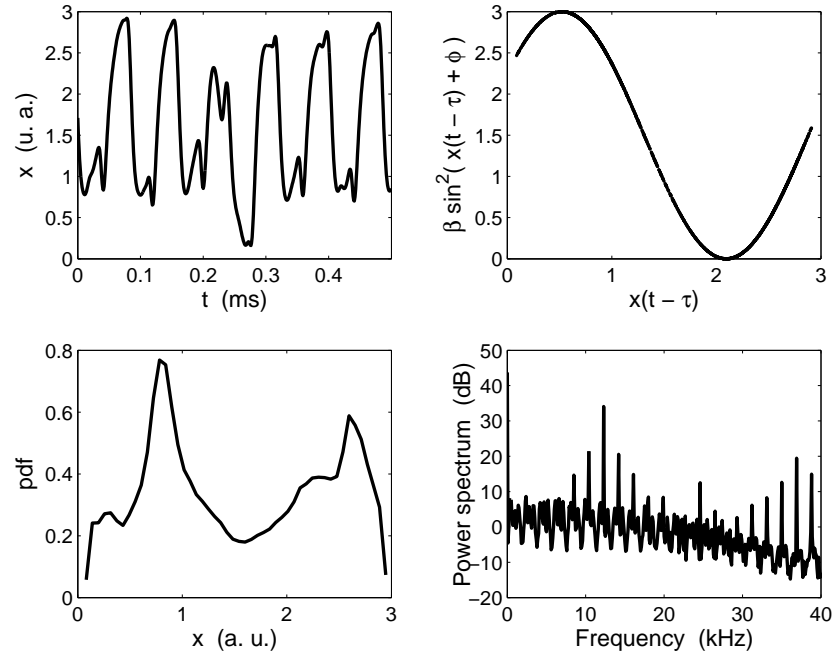


Figure 64: Chaotic signal for $\beta = 3$. $\tau = 523 \mu\text{s}$, $\tau^R = 8.4 \mu\text{s}$, $\phi = \pi/3$.

The influence of τ is represented in Figs. 67, 68, and 69, that correspond to values of the delay equal to 100, 523, and 1000 μs , respectively. As could be expected from an observation of the corresponding bifurcation diagram (Fig. 62), the dynamical behavior is very similar for all the values of the delay considered here. In every case, the behavior of the system resembles that of a white gaussian noise.

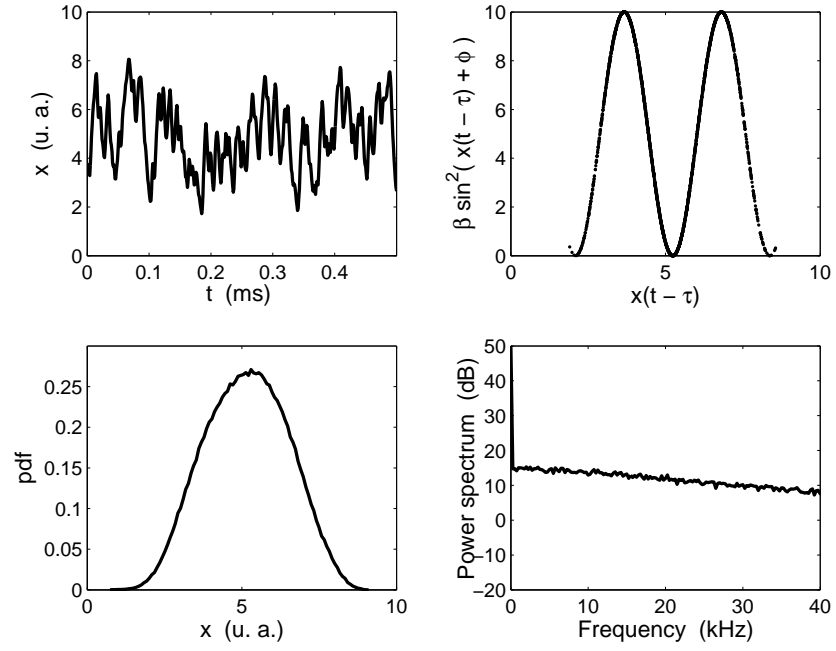


Figure 65: Fully-developed chaos for $\beta = 10$. $\tau = 523 \mu\text{s}$, $\tau^R = 8.4 \mu\text{s}$, $\phi = \pi/3$.

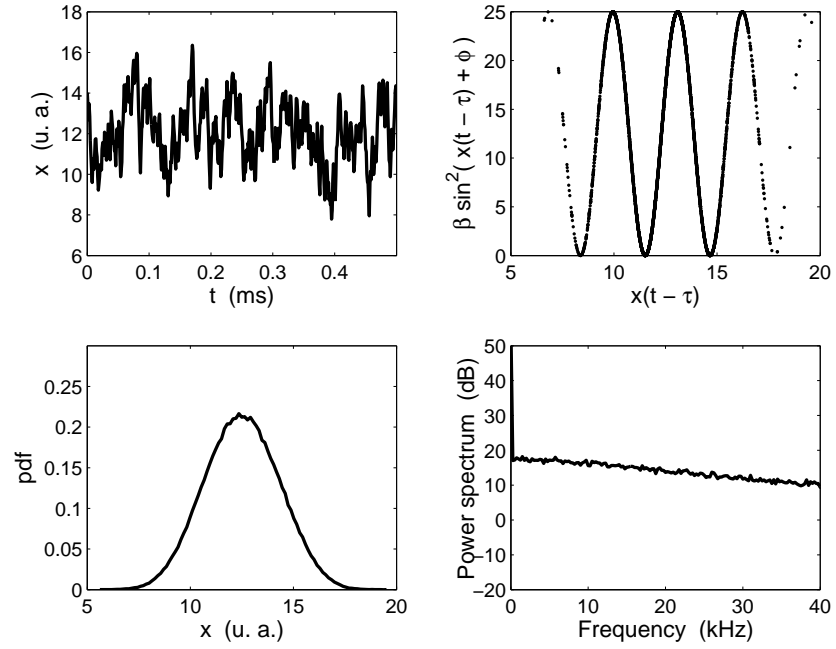


Figure 66: Fully-developed chaos for $\beta = 25$. $\tau = 523 \mu\text{s}$, $\tau^R = 8.4 \mu\text{s}$, $\phi = \pi/3$.

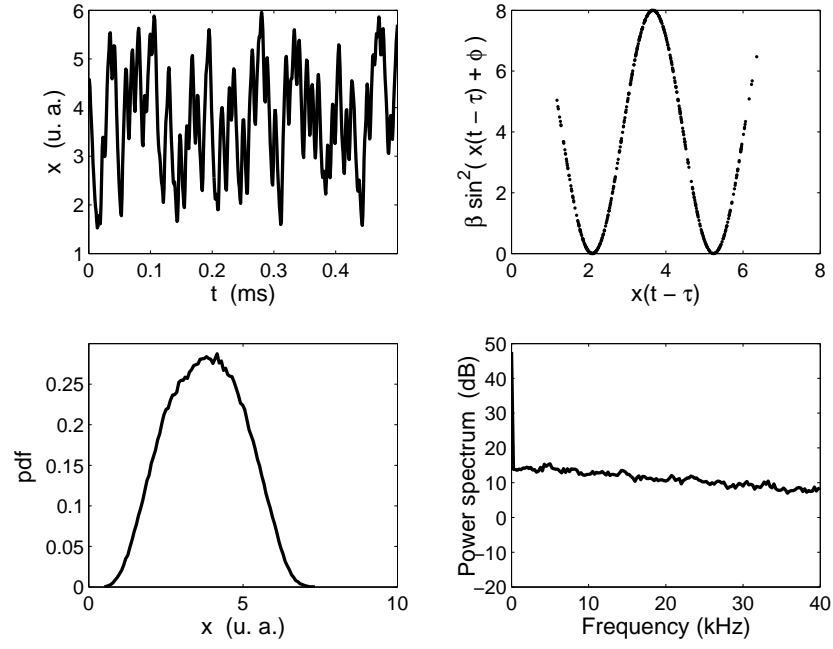


Figure 67: Fully-developed chaos for $\tau = 100 \mu\text{s}$. $\beta = 8$, $\tau^R = 8.4 \mu\text{s}$, $\phi = \pi/3$.

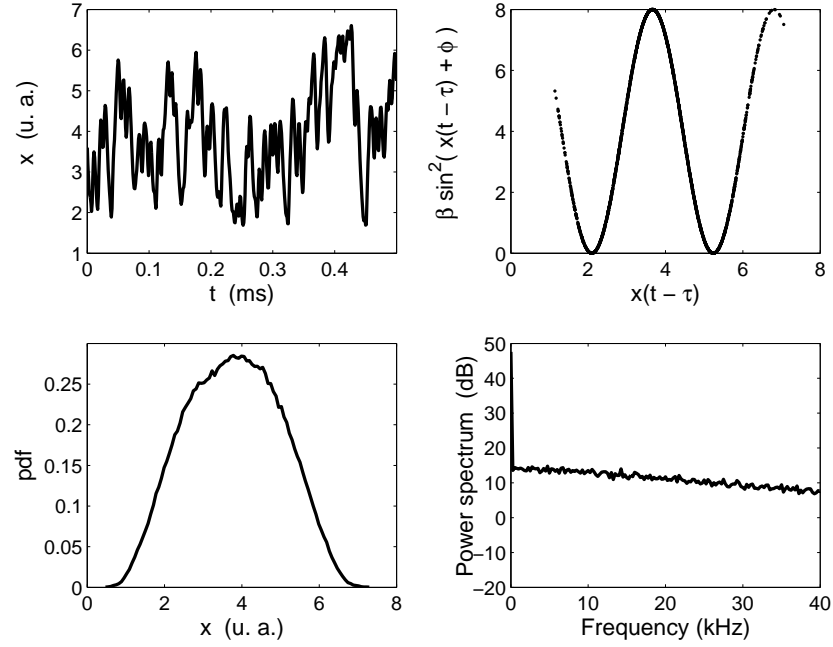


Figure 68: Fully-developed chaos for $\tau = 523 \mu\text{s}$. $\beta = 8$, $\tau^R = 8.4 \mu\text{s}$, $\phi = \pi/3$.

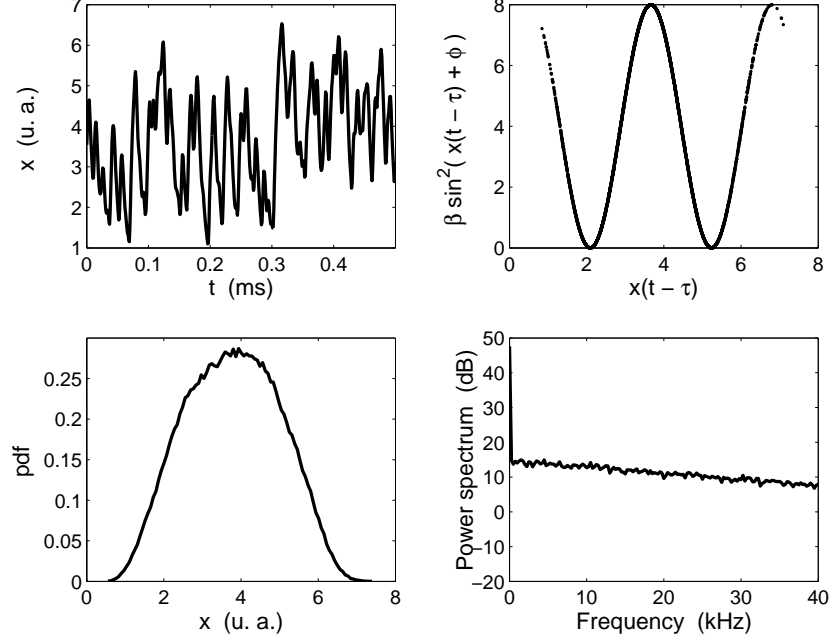


Figure 69: Fully-developed chaos for $\tau = 1000 \mu\text{s}$. $\beta = 8$, $\tau^R = 8.4 \mu\text{s}$, $\phi = \pi/3$.

4.4.3.2 Local linear fits

In this section, we study the delay identification problem by using the method based on local linear fits. Similarly to what has been shown in section 4.4.2 for the Mackey-Glass system, the autocovariance and autocorrelation would lead to an overestimation of the delay. More details will be found in chapter 5. We examine the influence of the parameters N , h , and ϵ on the identification process as well as the influence of the presence of an information-bearing signal in the time series. We consider here the case in which the optoelectronic system is in a regime of fully-developed chaos ($\beta = 7$, $\tau = 523 \mu\text{s}$, $\tau^R = 8.4 \mu\text{s}$, $\phi = \pi/3$).

The influence of the number of samples N and of the neighborhood size ϵ is represented in Figs. 70 and 71, respectively. We see that the identification is possible for all the choices of parameters considered here. More specifically, we notice that the bottom of the "valley" in the approximation error curve is composed of two very close values of the approximation error, corresponding to two successive values of τ^* ($522 \mu\text{s}$ and $523 \mu\text{s}$). This technique is therefore shown to lead to the identification of the delay with an uncertainty in the order of one microsecond. The influences of N and ϵ are similar to those observed in the

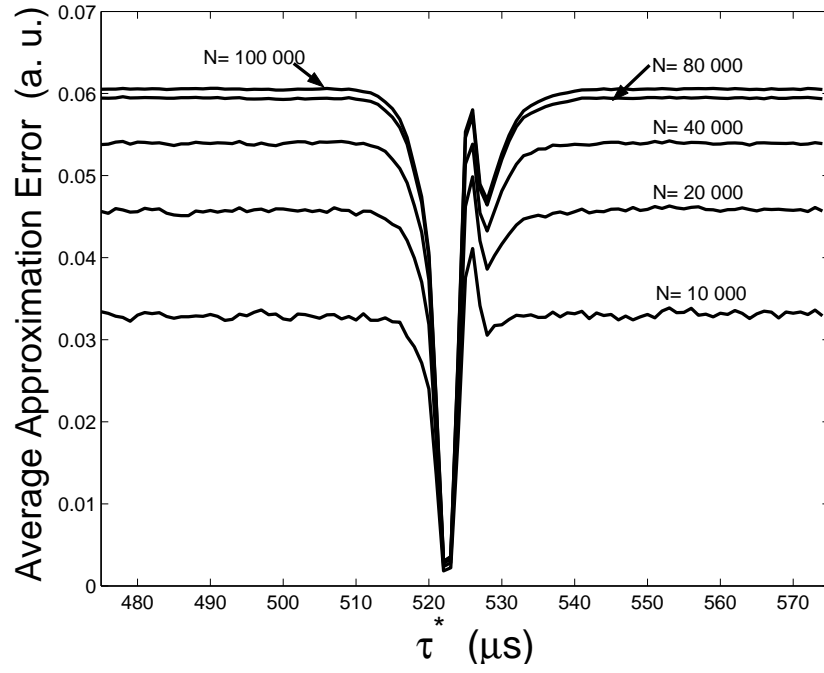


Figure 70: Influence of the number of samples N . $\beta = 7$, $\tau = 523 \mu s$, $\tau^R = 8.4 \mu s$, $\phi = \pi/3$, $h = 1 \mu s$, $\epsilon = 1\%$.

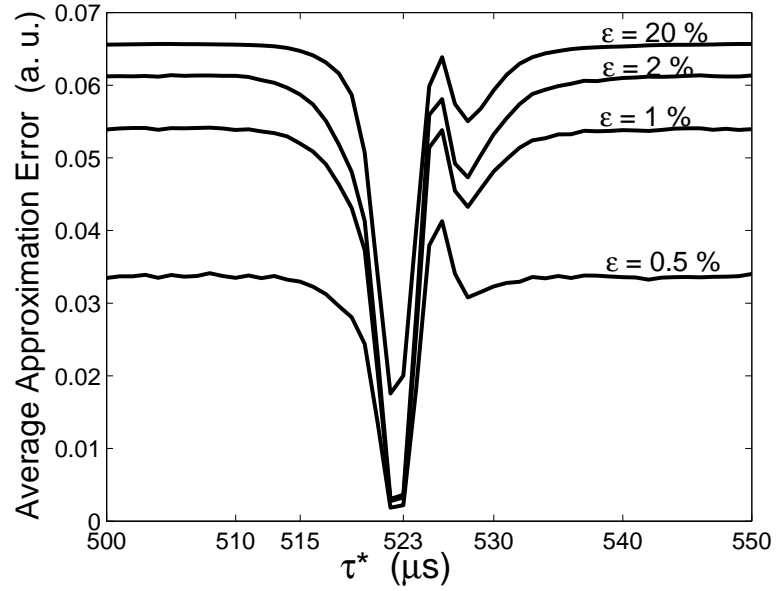


Figure 71: Influence of the neighborhood size ϵ . $\beta = 7$, $\tau = 523 \mu s$, $\tau^R = 8.4 \mu s$, $\phi = \pi/3$, $h = 1 \mu s$, $N = 40000$.

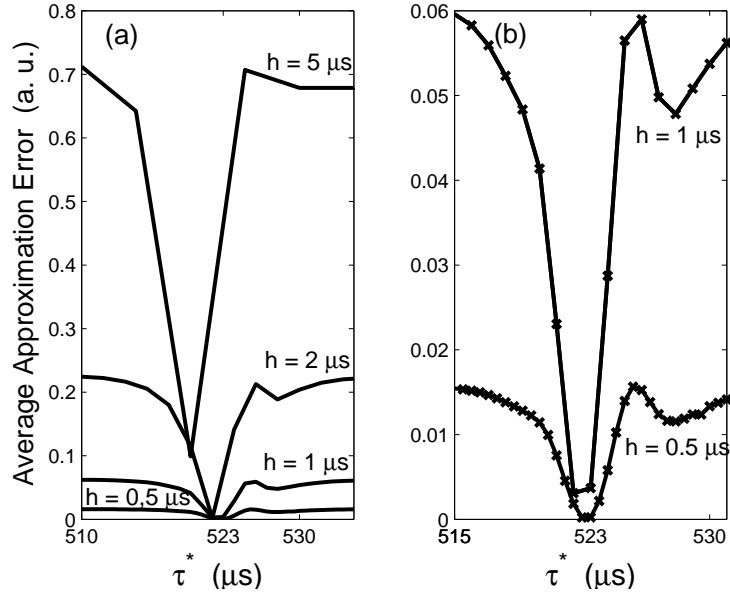


Figure 72: Influence of the sampling period h . $\beta = 7$, $\tau = 523 \mu\text{s}$, $\tau^R = 8.4 \mu\text{s}$, $\phi = \pi/3$, $N = 80000$, $\epsilon = 2\%$.

case of the Mackey-Glass system. An increase of the number N of samples and of the size ϵ of the neighborhoods leads to more pronounced maxima in reason of an increase of the approximation error when τ^* is different from τ . On the contrary, the value of the approximation error when $\tau^* = \tau$ seems to be almost independent of N and ϵ . When $\tau^* = \tau$, the system trajectory lies on a surface \mathcal{S} in the space $(x_{i+1}, x_i, x_{i-\tau})$ and an increase of N or ϵ leads to an increase in the number of neighbors taken into account in the determination of local tangent planes through local linear approximations. The invariance of the approximation error as a function of N and ϵ can be interpreted by the fact that even when the smallest values of these parameters are considered, the tangent planes are determined correctly and an increase of these parameters does not change the quality of the local approximations. We notice, however, that if very large neighborhoods are used ($\epsilon = 20\%$), the quality of the approximations decreases when $\tau^* = \tau$. This is due to the fact that with big neighborhoods, the curvature of the the \mathcal{S} is revealed and a linear approximation loses of its meaning, leading to higher approximation errors.

The influence of the sampling period h is represented in Figs. 72(a) and 72(b). Once

again, the results confirm the conclusions drawn from the study of the Mackey-Glass system. An increase of h leads to more pronounced and narrower valleys. Of course, since the difference between two consecutive values of τ is equal to h , large values of h can lead to large errors in the determination of the delay, as can be seen from Fig. 72. In Fig. 72(b), we study more specifically the cases $h = 1 \mu\text{s}$ and $0.5 \mu\text{s}$. We observe that for these two values of h , the bottom of the valley is constituted by two successive values of τ , spaced by an interval of time equal to h . These two values correspond to two very close values of the approximation error, meaning that the uncertainty in the determination of the delay is in the order of h . For example, when h is equal to 1 microsecond, it is not clear whether the delay is equal to 522 or 523 μs , and when h is equal to 0.5, there can be a hesitation between 522.5 and 523 μs .

We have used so far a time series that corresponds exactly to the chaotic carrier x produced by the dynamical equation (126). What an eavesdropper will usually have is a mix of the chaotic carrier and the message $m(t)$, as explained in section 2.8.3. Figure 73 shows the result of the identification technique when a message $m(t)$ is included in the time series analyzed. The regime used is fully-developed chaos and the message is a binary pseudo-random bipolar signal whose amplitude is 5% of the maximal amplitude of the chaotic carrier that would have been generated in the absence of a message. We observe that the approximation error is almost uninfluenced by the presence of the information-bearing signal, and therefore that the identification of the delay is possible even when $m(t)$ is present in the time series.

We have checked that all the conclusions of this section hold independently of the dynamical regime considered¹⁰ and that the influence of ϵ , N , and h is similar to the case when no message is included. We conclude by emphasizing the fact that the identification technique using local linear approximations is very "robust". By this we mean that a wide range of the parameters (N, h, ϵ) can be used to identify the delay, independently of the presence of a message.

¹⁰*i.e.* mainly when other values of β and τ are considered. Further details on this will be found in section 5.2.

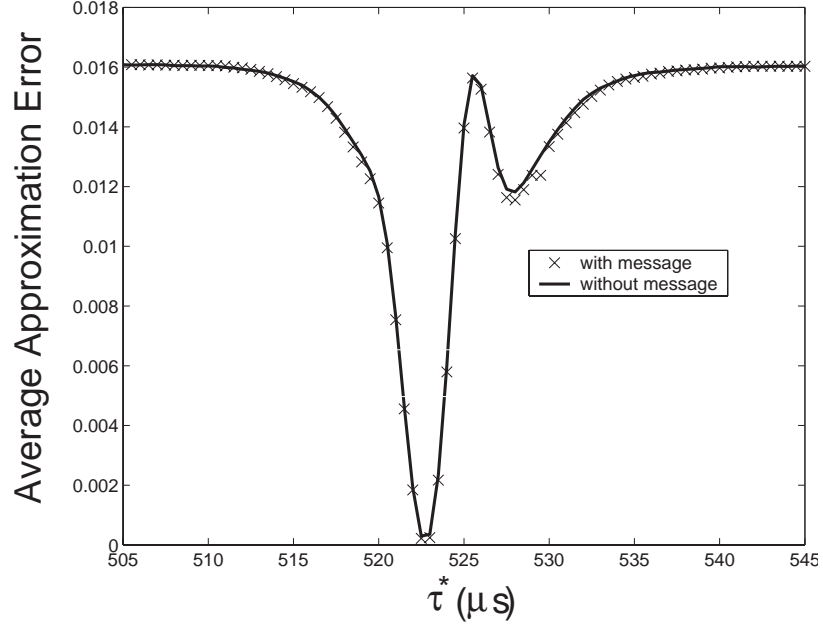


Figure 73: Delay identification with and without a message. $\beta = 7$, $\tau = 523 \mu\text{s}$, $\tau^R = 8.4 \mu\text{s}$, $\phi = \pi/3$, $h = 0.5 \mu\text{s}$, $N = 80000$, $\epsilon = 2\%$.

The two following sections investigate the identification of the delay of two other experimental setups that are being used at the GTL-CNRS Telecom laboratory for chaotic encryption.

4.4.4 Optoelectronic system producing chaos in intensity

The chaos generator considered here is described in the publications [24, 138, 25] and represented in Fig. 74. It uses an intensity electro-optic modulator subject to delayed feedback on its control electrode. It is the output power of the modulator that is fed back to this electrode, after having been detected by a photodiode. A continuous voltage V_b is also applied to the control electrode of course and is used to determine the working point of the modulator. The delay τ can be varied by changing the length of the optical fiber in the feedback loop. The transfer function of the intensity modulator, which gives the evolution of the output power I as a function of the voltage V applied to the control electrode, is of the form $I(t) = \cos^2[SV(t) + \phi]$, where S is a proportionality factor characteristic of the electro-optic efficiency of the modulator and ϕ is a phase shift that depends on the

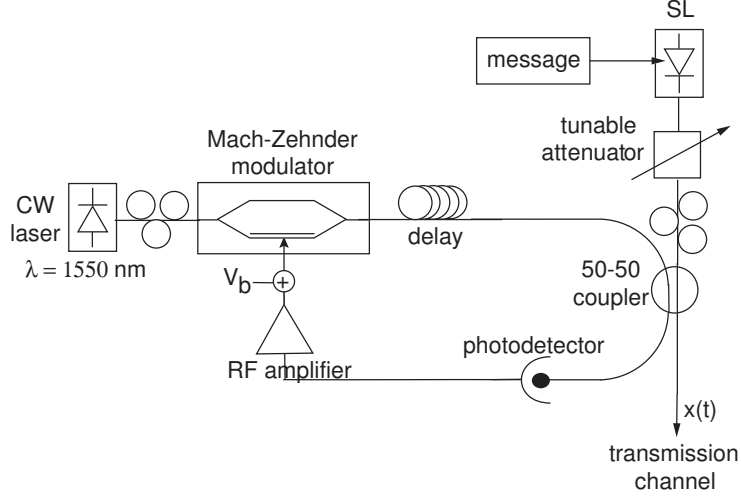


Figure 74: Chaos oscillator in intensity.

value of the voltage V_b . It is easy experimentally to make sure that a large number of extrema of the nonlinear function are spanned by choosing a sufficiently large amplitude of the signal applied to the control electrode. The resulting filtering effect of the different elements composing this generator is modeled by a band-pass filter constituted by a first order high-pass filter (whose time constant is τ_1^R) and of a first order low-pass filter (with an associated time constant τ_2^R) in series.

This system is described by the integro-differential delay equation

$$x(t) + \frac{\tau_1^R \tau_2^R}{\tau_1^R + \tau_2^R} \dot{x}(t) + \frac{1}{\tau_1^R + \tau_2^R} \int_{-\infty}^t x(\tau) d\tau = \beta \cos^2[x(t - \tau) + \phi] , \quad (127)$$

where x is proportional to the output power of the modulator, and β in an experimentally tunable factor that measures the strength of the feedback.

The introduction of the additional variable

$$y(t) = \dot{x}(t) , \quad (128)$$

allows us to transform the integro-differential delay equation (127) into a system of two

delay differential equations

$$\dot{x}(t) = y(t) \quad (129)$$

$$\frac{\tau_1^R \tau_2^R}{\tau_1^R + \tau_2^R} \dot{y}(t) = -\beta \sin \{2[x(t - \tau) + \phi]\} - \frac{1}{\tau_1^R + \tau_2^R} x(t) - y(t). \quad (130)$$

We can therefore consider that we are facing the case, described in section 4.2, of a system of differential equations in which only one variable (x) is subjected to feedback and in which only one variable (x) is measured. It is thus natural to use local linear approximations of the form

$$x_{i+1} = a_i + \sum_{j=1}^m b_i^{(j)} x_{i-j+1} + \sum_{j=1}^m c_i^{(j)} x_{i-\tau^*-j+1}. \quad (131)$$

The notations are the same as in section 4.2.

We have represented in Fig. (75) the approximation error, for different values of the number $2m$ of variables in the linear approximations, and the delayed mutual information. The experimental time series used correspond to a regime of fully-developed chaos. The

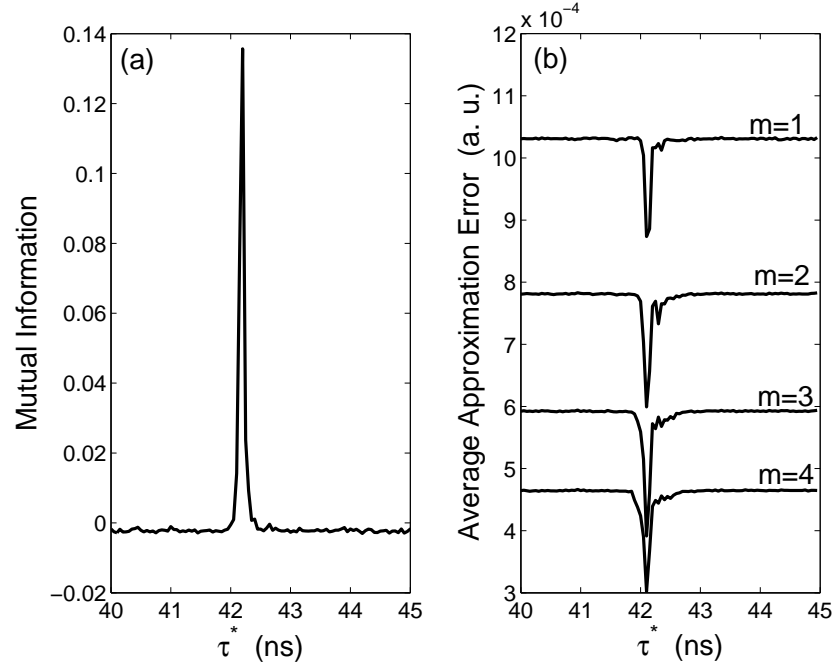


Figure 75: Delay identification. (a) Mutual information. (b) Local linear fits. $N = 80000$ samples, $\epsilon = 1\%$, $h = 50$ ps.

mutual information presents a very sharp maximum for a value of the delay equal to 42.2 ns.

The approximation error has a very pronounced minimum, for a value of the delay equal to 42.1 ns, for all values of the number $2m$ of additional variables in the local approximations. An experimental measure of the delay of the system leads to a value of 42.15 ns [139]. We notice once again that the mutual information leads to a (slight) overestimation. The value obtained by the method based on local approximations seems to be slightly under estimated. It is important to know, however, that a lower bound of the error in the experimental determination of the delay is of 40 ps and that the determination by the local approximations could be closer to the real value than the experimental measure. We also notice that the average approximation error is smaller when the number of additional variables is larger. This can be explained by the increased quality of the approximations when more variables are used.

It is important to notice that local linear approximations with $m = 1$, *i.e.* of the form $x_{i+1} = a_i + b_i x_i + c_i x_{i-\tau}$, work to identify the delay even if these approximations have been devised for a system modeled by a first order delay-differential equation, which is not the case of the system considered in this section. The use of additional variables is therefore not essential to identify the delay.

We end this section by mentioning that the experimentally measured time series are significantly distorted since the 3 dB spectral width of the modulator is of the order of 6,5 GHz¹¹ while the bandwidth of the oscilloscope used to take the measurements is of 5 GHz only. Moreover, since the maximum sampling frequency is of 20 GHz, the spectral aliasing is significant, which also leads to a distortion of the measured time series x . Despite this, the identification method based on local approximations still works very well, proving once again the robustness of the method.

4.4.5 Electronic system producing frequency chaos

We consider here another chaotic emitter that has been realized at the GTL-CNRS Telecom laboratory for chaotic encryption. It is a purely electronic system that produces chaos in the frequency domain and that has been described in the references [140, 141, 142, 143]. The

¹¹Cette valeur a t mesure par un analyseur de spectre RF

frequency chaos (FM-type signal) is produced by a voltage controlled oscillator (VCO). This oscillator is subjected to a nonlinear delayed feedback that leads to the generation of chaos. The nonlinearity is realized by three RLC filters in parallel that have three different resonance frequencies. The dynamics is limited in the spectral domain by a low-pass [140, 141] or a band-pass [142, 143] filter.

In the case in which a first-order low-pass filter is used, the system can be modeled by the following delay differential equation

$$x(t) + \tau^R \dot{x}(t) = \beta F[x(t - \tau)] , \quad (132)$$

where τ^R is the time constant of the filter, β is a multiplicative factor of the nonlinearity and $x(t)$ is a quantity proportional to the input voltage of the VCO. The nonlinear function F has the following form

$$F(x) = \left| \sum_{j=1}^3 \frac{G_j Q_j}{1 - i Q_j \left(\frac{f_0 + S_x x(t)}{f_j} + \frac{f_j}{f_0 + S_x x(t)} \right)} \right| , \quad (133)$$

where G_j and Q_j represent the gain and the quality factor of the j^{th} RLC filter, f_0 is the output frequency of the VCO in the absence of an input signal, and S_x is the conversion factor between the normalized voltage x and the output frequency of the oscillator. This nonlinear function is represented in Fig. 76 as a function of the output frequency f of the VCO. It is highly nonlinear and has five extrema.

Another experimental realization uses a band-pass filter constituted by first-order low-pass and high-pass filters in series. In this case, the following integro-differential equation can describe the dynamical behavior of the system

$$x(t) + \frac{\tau_1^R \tau_2^R}{\tau_1^R + \tau_2^R} \dot{x}(t) + \frac{1}{\tau_1^R + \tau_2^R} \int_{-\infty}^t x(\tau) d\tau = \beta F[x(t - \tau)] , \quad (134)$$

where τ_1^R is the time constant of the high-pass filter and τ_2^R is the time constant of the low-pass filter.

The local approximations method has been applied to experimental time series and the result is shown in Fig. 77. Figure 77 (a) is for a low-pass filter and Fig. 77 (b) is for a band-pass filter, when $m = 1$ (cf. 131). We observe in both cases a very sharp minimum for

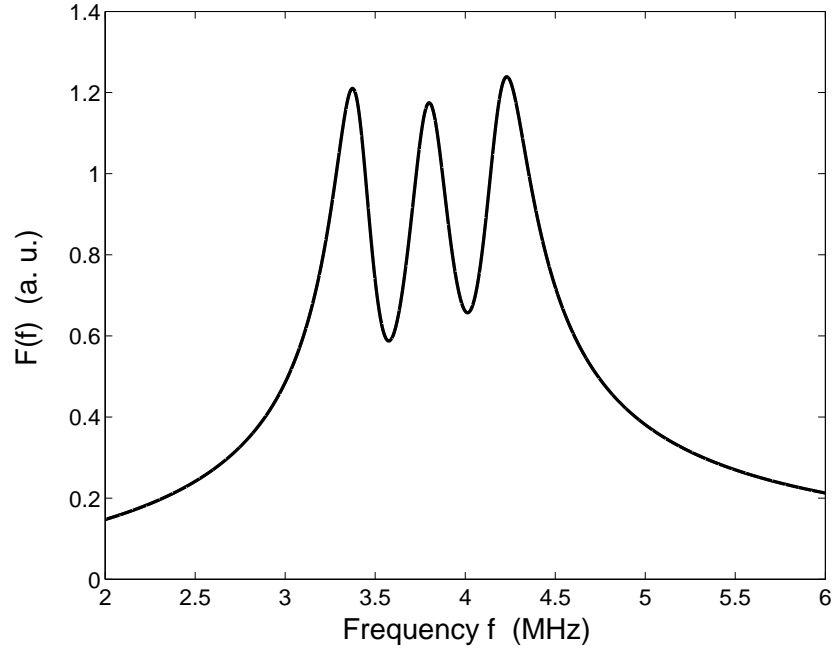


Figure 76: Nonlinear function realized by three RLC filters in parallel

$\tau = 518 \mu\text{s}$, corresponding to the correct value of the delay. We notice once again that the identification technique devised for first-order delay systems (*i.e.* when $m = 1$) works also to identify system that are described by an integro-differential delay equation. We have checked that the identification works for all possible chaotic regimes, in the low-pass as well as in the band-pass case.

All the chaotic emitters we have tested have helped us prove that the local linear approximations provide an accurate and robust method to identify the delay from time series produced by chaotic scalar or vectorial delay systems.

4.5 Identification of the nonlinear function

Our aim here is not to make an exhaustive presentation of all the techniques that can be used to reconstruct accurately the nonlinear function; we will limit ourselves to a simple technique, described in Ref. [127], that is closely linked to the technique of analysis of a delay system presented in section 4.2.1.

We restrict ourselves to the special case of a system responding to a delay-differential

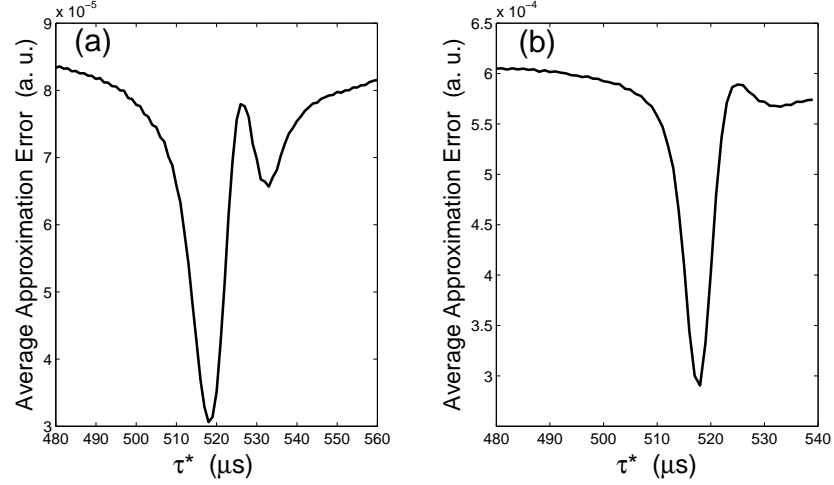


Figure 77: Delay identification by the local linear approximations method. $\epsilon = 1\%$ (a) low pass filter (b) band pass filter. $m = 1$.

equation of the form

$$\tau^R \dot{x}(t) = F[x(t - \tau)] - x(t), \quad (135)$$

If t_{extr} represent a time at which $x(t)$ reaches an extremum, the preceding equation can be written, at that time t_{extr} , as

$$x(t_{extr}) = F[x(t_{extr} - \tau)] . \quad (136)$$

The nonlinear function can therefore be identified by finding a large number of different times t_{extr} at which the time series reaches an extremum and then plotting $x(t_{extr})$ as a function of $x(t_{extr} - \tau)$. It can be considered that the procedure described above corresponds to the projection, on the plane spanned by $x(t)$ and $x(t - \tau)$, of an extremal section of the object described in the phase space. It is necessary of course to know the value of the delay τ , which could be identified by one of the techniques described in section 4.4. Moreover, the number of samples N must be sufficient to span the entire nonlinear function, or should be sufficient to at least reveal its shape. It is also important to understand that the above reasoning and conclusions, as in the case of the local linear approximations described in section 4.2, are independent of the dimension of the chaotic attractor and do not require the trajectory in the phase space to have settled on the attractor. It could even be thought that it is preferable to have a high-dimensional attractor. A higher dimensional attractor

means that larger portions of the phase space are visited and the reconstruction of the nonlinearity is more complete. Similarly, the use of time series that correspond to transient phases allows to take into account regions of the phase space that are not visited in a steady-state regime.¹²

The identification technique has been applied to a time series obtained by numerically integrating the Mackey-Glass system. The result is represented in Fig. 78. We observe that the nonlinearity is well identified except for the fact that certain portions of it are not reproduced. This is due to the fact that there are certain intervals of values of x in which extrema rarely lie, and it is therefore difficult to determine the corresponding portion of the nonlinear function. We see for example that there is not a single extremum that lies on the "top" of the nonlinearity even though 500 intervals of length τ are used.

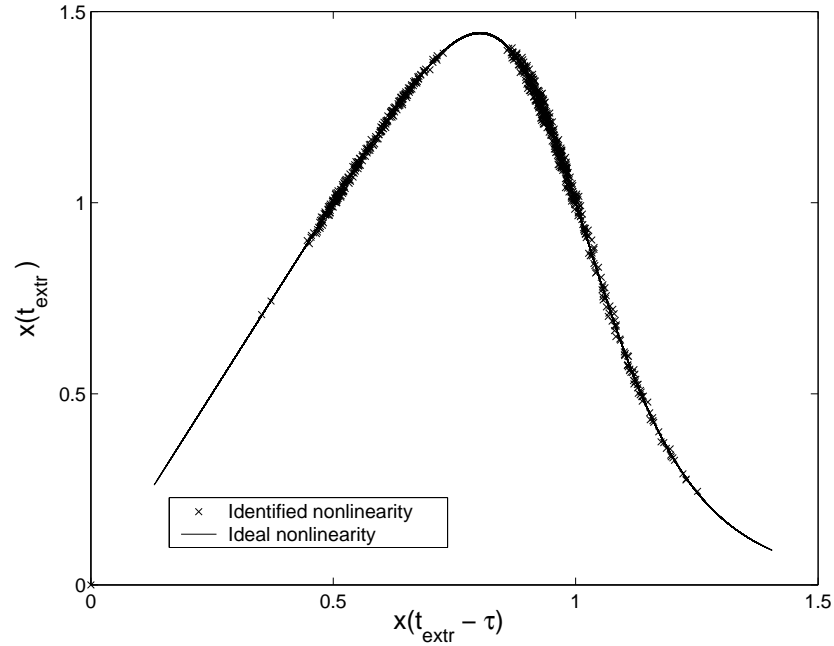


Figure 78: Identification of the nonlinear function of a Mackey-Glass system. $\tau = 46$, $\tau^R = 10$, $c = 2$, $h = 0.5$, $N = 46000$.

We have also applied the identification procedure to experimental time series produced by the optoelectronic generator of chaos in wavelength and the electronic generator of

¹²*i.e.* when the trajectory has settled on the attractor.

frequency chaos. The results are represented in Figs. 79 and 80. We observe that the shape of the function can be identified but also that the results are very noisy. The presence of noise on experimental time series is of course inevitable.

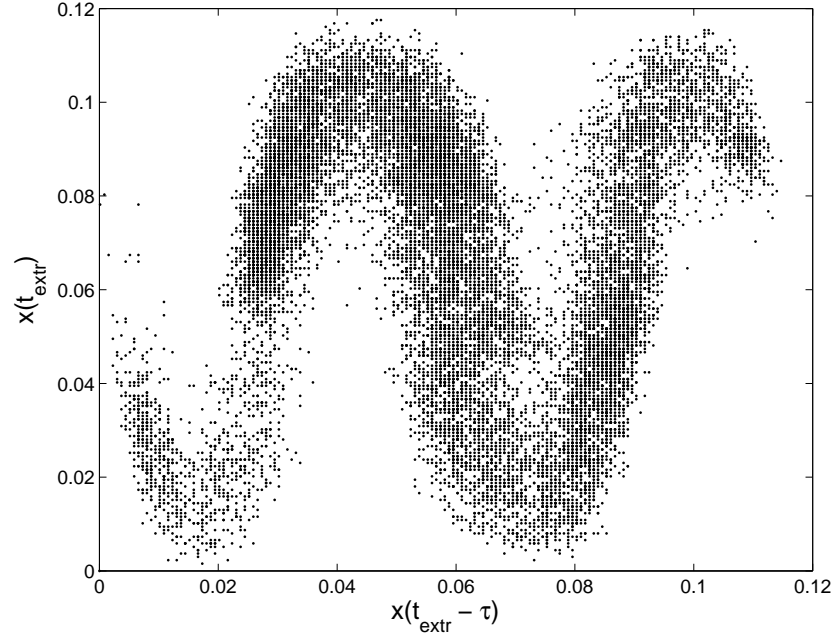


Figure 79: Identification of the nonlinear function of the optoelectronic generator of wavelength chaos. $h = 1 \mu\text{s}$. Experimental estimation of the parameter values: $\beta = 7.2$, $\tau = 523 \mu\text{s}$, $\tau^R = 8.4 \mu\text{s}$, $\phi = \pi/3$.

As a conclusion, the identification technique presented here, even if very simple, gives an idea of the shape of the nonlinear function. Approximation techniques can of course be used subsequently to determine the nonlinear function more accurately.

4.6 *Computation of the Lyapunov spectrum, of dimension, and of entropy*

As we have explained before, it is useful to use high-dimensional chaos to ensure the secrecy of chaotic communications. We study here two quantities that are traditionally used to characterize a chaotic regime: the attractor dimension and the entropy of the chaotic process. Large attractor dimensions make traditional time series analysis techniques difficult to apply to break the system and large entropies make the chaotic process more difficult to predict, which also complicates the task for an eavesdropper. We are particularly interested

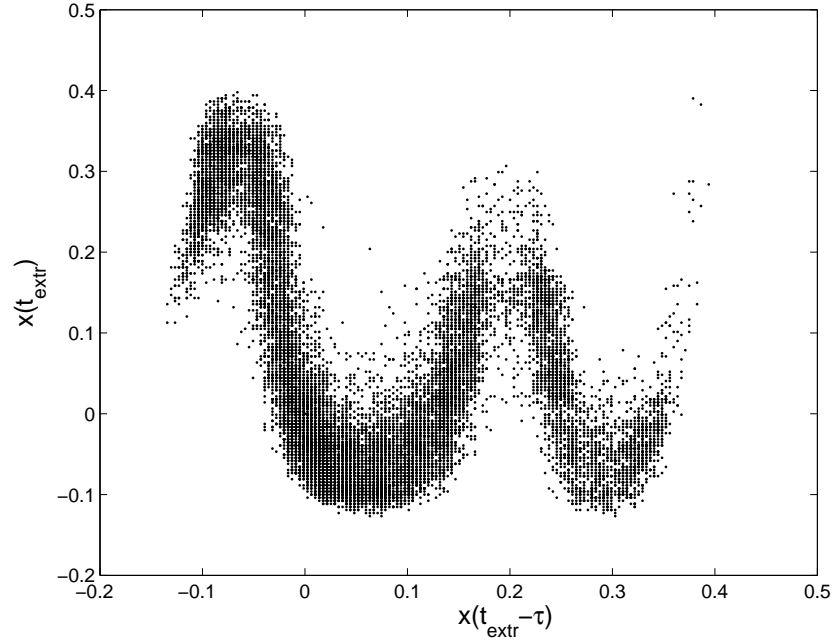


Figure 80: Identification of the nonlinear function of the electronic generator of wavelength chaos.

in determining the evolution of dimension and entropy when the delay and the feedback strength are varied. Both of these parameters can be easily modified in the experimental cryptosystems and knowing how the chaos characteristics evolve helps the experimentalist determine the operating conditions to use for efficient chaotic communications. A few theoretical studies have shown that for certain delay systems, the dimension varies linearly with the delay [123, 144, 145], whereas the entropy tends to saturate [123, 145] for large values of the delay. Leberre *et al.* have even conjectured that this is a general property of delay systems. Additionally, some theoretical results show that the dimension increases linearly also with the feedback strength [144], in the specific case of the "Ikeda system" [146]. We wish to verify these tendencies and determine some other ones on the Mackey-Glass system and on the optoelectronic system producing wavelength chaos. We will determine the Lyapunov spectrum both theoretically from the dynamical model, using Farmer's method, and from time series. The estimation from time series uses the specific time series analysis techniques for delay systems presented previously in this chapter. Finally, we should mention that the fact that delay systems used in chaotic cryptosystems really produce high-dimensional chaos

has been a controversial issue. The estimation of dimension and entropy from experimental times series of the wavelength chaos generator helps prove that chaos used in chaotic delay cryptosystems is indeed high dimensional.

4.6.1 Mackey-Glass system

In this section, we consider again the Mackey-Glass system (125) and we choose initially the same parameters as those used in section 4.4.2 for the delay identification problem (*i.e.* $\tau^R = 10$, $c = 2$, $\tau = 46$). Figure 81 represents the first 20 Lyapunov exponents, computed from the model by Farmer's method and from a times series generated by numerically integrating the Mackey-Glass equation (125).¹³ We have used a time series of $N = 500000$ samples, a neighborhood size $\epsilon = 1\%$, and a sampling period $h = 0.5$. Choosing a sampling period $h = 0.5$ implies that the maximum number of exponents that can be computed is $\tau/h = 92$. We observe that the Lyapunov spectra computed from the model and from a time series are almost identical. We are therefore confident in the accurateness of the computation technique of the Lyapunov spectrum from a time series. As has been shown in section 2.5.3, the Lyapunov dimension D_L and the Kolmogorov-Sinai entropy H_{KS} can be found from the Lyapunov spectrum¹⁴. Figures 82 and 83 represent the evolution of dimension and entropy, computed from a time series, as a function of the number n of iterations (*i.e.* of the number of Jacobian matrices taken into account). We observe a relatively quick convergence of dimension and entropy, though small oscillations remain even for a large number of iterations (500000). We can tell from the figures that $D_L \approx 5.1$ and $S_{KS} \approx 0.01$. Since the dimension is of the order of 5, an analysis of the time series using an embedding of the phase space would have imposed to work in a space of dimension at least ten (*cf.* § 2.6.1). Thanks to the specific technique described in section 4.3.1 and used here, the Lyapunov spectrum has been estimated by working in a space of dimension 2 only.

¹³We thank Laurent Larger, Min Won Lee, and Eric Genin for some programs implementing Farmer's method.

¹⁴We assume in this section that the Kolmogorov-Sinai entropy is *equal* to the sum of the positive Lyapunov exponents.

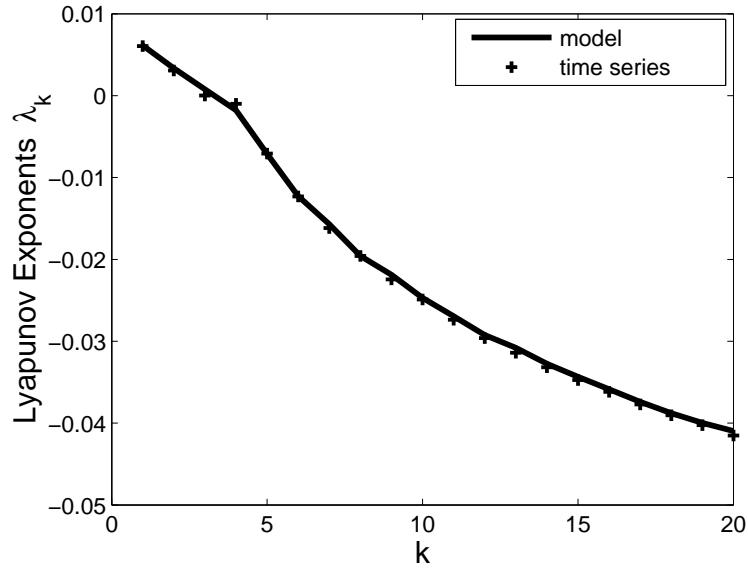


Figure 81: The twenty largest Lyapunov exponents, computed from the dynamical equations and from a numerically generated time series. $\tau = 46$, $\tau^R = 10$, $c = 2$. $N = 500000$, $\epsilon = 1\%$, $h = 0.5$.

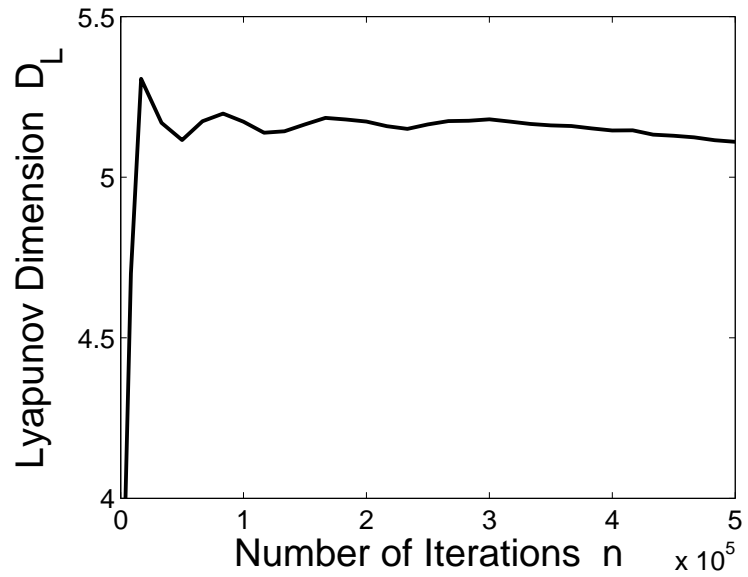


Figure 82: Lyapunov dimension as a function of the number of iterates. The results are obtained by time series analysis. The parameters are the same as in Fig. 81.

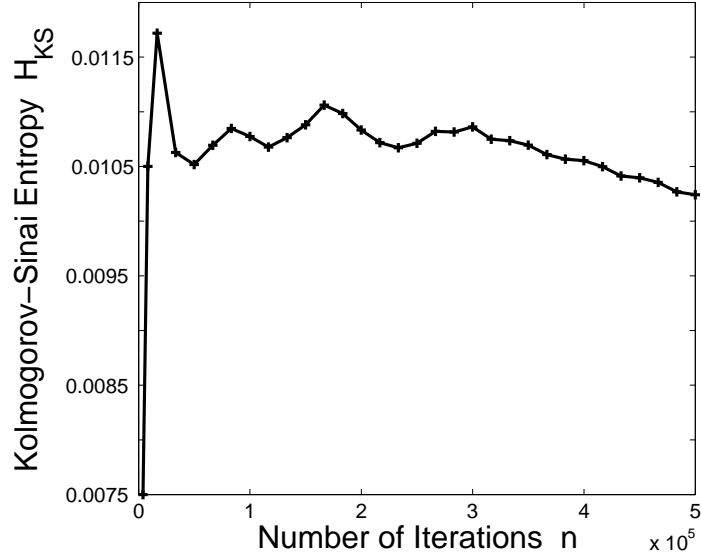


Figure 83: Kolmogorov-Sinai entropy as a function of the number of iterates. The results are obtained by time series analysis. The parameters are the same as in Fig. 81.

It is important to understand that the results presented in the preceding figures correspond to a choice of values of the parameters of the computation procedure. These parameters are the neighborhood size ϵ , the number N of samples of the time series, the sampling period h , and the frequency at which the re-orthonormalizations occur. It can be difficult to determine the parameter values to use. The ultimate way to determine if the estimated spectrum is correct is to compare it with the spectrum calculated from the dynamical model. This is obviously not always possible. In the case of the Mackey-Glass system, it appears that the spectral estimation is relatively robust with respect to variations of the parameters of the procedure. By this we mean that even significantly different (but reasonable) values of the parameters N , ϵ , and h lead to very similar spectra.

In general, the value of N is considered to be good if it is sufficiently large to ensure the convergence of the Lyapunov spectrum. This means that all the exponents must be arranged in decreasing order and that a further increase of N does not change the spectrum significantly. Of course, this is not a proof of the exactness of the estimated spectrum since we can imagine that the convergence occurs towards an incorrect set of exponents. For the Mackey-Glass system, a number of samples N in the order of 10^5 is sufficient to ensure

convergence. We have also observed that the computed spectrum is not very sensitive to neighborhood size. We have chosen to take $\epsilon = 1\%$ to draw Fig. 81 but significantly smaller or larger values of the neighborhood size lead to similar spectra. It is not surprising that small values of the neighborhood size lead to a good determination of the spectrum since the numerically generated time series are noiseless. The only thing that has to be taken into account is that when small neighborhoods are used, the number of samples N has to be increased to find sufficient numbers of neighbors to have statistically significant results. The tendency to invariance of the spectrum with respect to an increase of the neighborhood size is more surprising. It is probably due to the fact that the Mackey-Glass system is relatively weakly nonlinear (in the sense that the nonlinear function has only one extremum) and therefore large portions of surface \mathcal{S} (defined in section 4.2.1) are close to planar¹⁵. Finally, another important parameter, for Farmer's method as well as for the estimation from time series, is the integration step or the sampling period h , that sets the degree of discretization of the phase space. The parameter h must be smaller than the time scale of the fastest fluctuations of x . If h is too big, the discretization of phase space is too coarse and some information on the system dynamics is lost. We have computed the Lyapunov spectrum for different values of h and have observed indeed a convergence of the estimated spectra when h decreases, and that large values of h lead to incorrect estimations. The value used to draw the figures of this section ($h = 0.5$) has obviously been determined to be sufficiently small to lead to a good estimation of the Lyapunov spectrum.

As explained in the introduction to this section, we are interested in determining the evolution of the Lyapunov spectrum, of dimension, and entropy when the delay and the feedback strength are varied. In the case of the Mackey-Glass system, we study the influence of the delay only, since an increase of the parameter c , which can be considered as a feedback strength, tends to stabilize the laser which leaves chaotic regimes. Figure 84 represents the Lyapunov spectrum for four different values of the delay. The spectra have been estimated from time series but we have checked that a computation based on the knowledge of the

¹⁵The reader should notice the nonlinear function of the Mackey Glass system has only one extremum while the nonlinear functions of the systems used for secure communications often have several extrema

dynamical model leads to the same results. We observe that an increase of the delay leads to an increase of the number of positive exponents, leading inevitably to an increase of the dimension. But a delay increase also leads to a decrease of the amplitude of all the Lyapunov exponents. Figures 85 and 86 represent the evolution of the dimension and of the entropy as a function of τ . We observe that the dimension varies linearly with the delay while the entropy is almost unaffected by a change in the delay. Even if the number of positive exponents increases with the delay, the amplitude of the exponents (positive and negative) decreases, leading globally to an entropy that is almost constant as a function of the delay. An increase of the delay "activates" new direction of the phase space in which perturbations are amplified but at the same time the rate of change of the perturbations decreases in all directions.

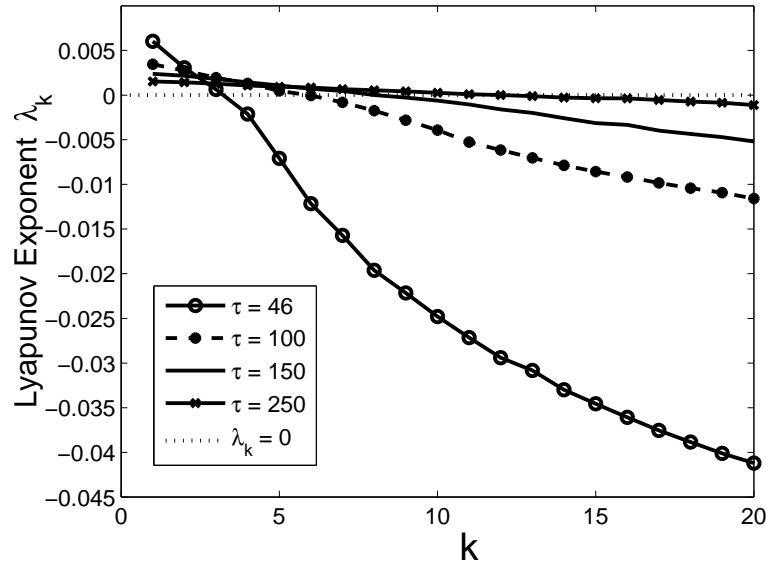


Figure 84: The twenty largest Lyapunov exponents, estimated from time series, for four different delay values. $\tau^R = 10$, $c = 2$. $N = 250000$, $\epsilon = 1\%$, $h = 0.5$.

4.6.2 Optoelectronic system producing wavelength chaos

We consider in this section the optoelectronic system described in sections 2.4 and 4.4.3 and modeled by Eq. (126)

$$\tau^R \dot{x}(t) = \beta \sin^2[x(t - \tau) + \phi] - x(t) .$$

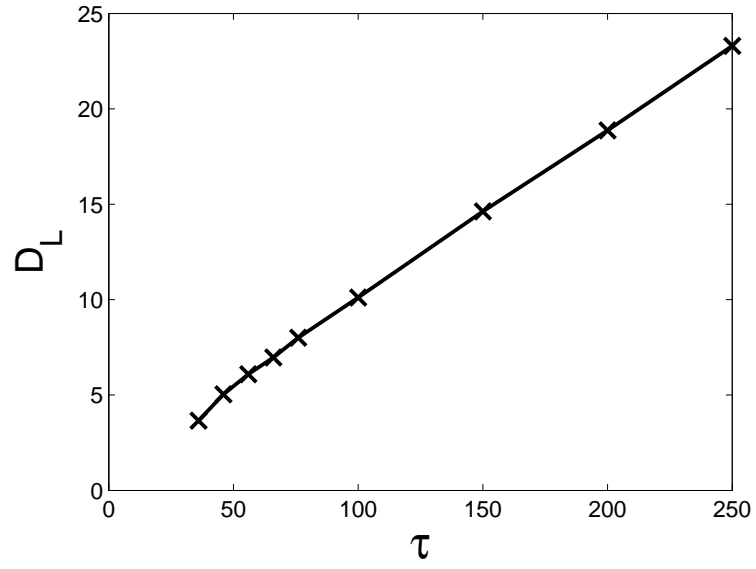


Figure 85: Lyapunov dimension as a function of the delay τ . The parameters are the same as in Fig. 84.

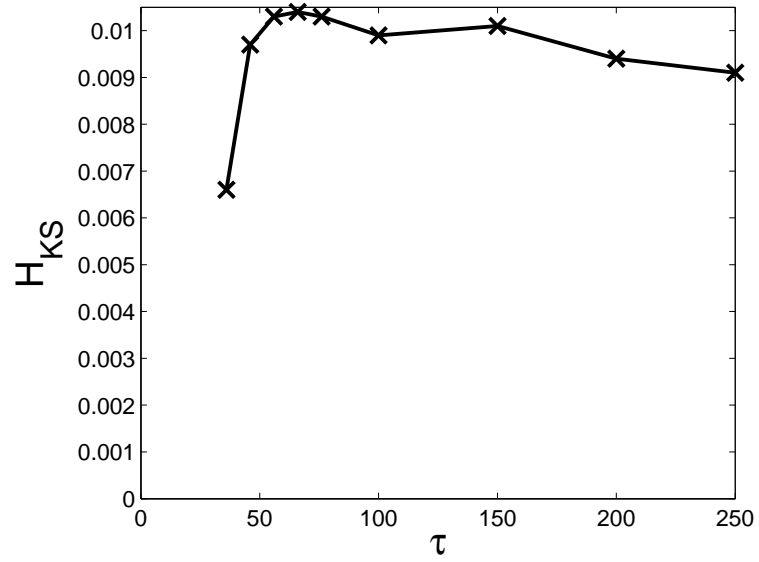


Figure 86: Kolmogorov-Sinai entropy as a function of the delay τ . The parameters of the analysis are the same as in Fig. 84.

We are especially interested in studying the influence of the delay τ and the feedback strength β on the Lyapunov spectrum. Both of these parameters are easily tunable experimentally and their influence on the system dynamics has been studied in section 4.4.3.1.

We assume first that the dynamical model is known and that the spectrum can be estimated by Farmer's method. Figure 87 represents the Lyapunov spectrum for four different values of the delay τ and Fig. 88 represents the dimension and entropy as a function of delay. The parameters are the same as those considered in section 4.4.3. The observations are similar to the case of a Mackey-Glass system. When the delay is increased, the number of positive exponents increases, but at the same time, the amplitude of all the exponents decreases. The attractor dimension evolves linearly with the delay, while the entropy is almost constant. The influence of the feedback strength β on the Lyapunov spectrum

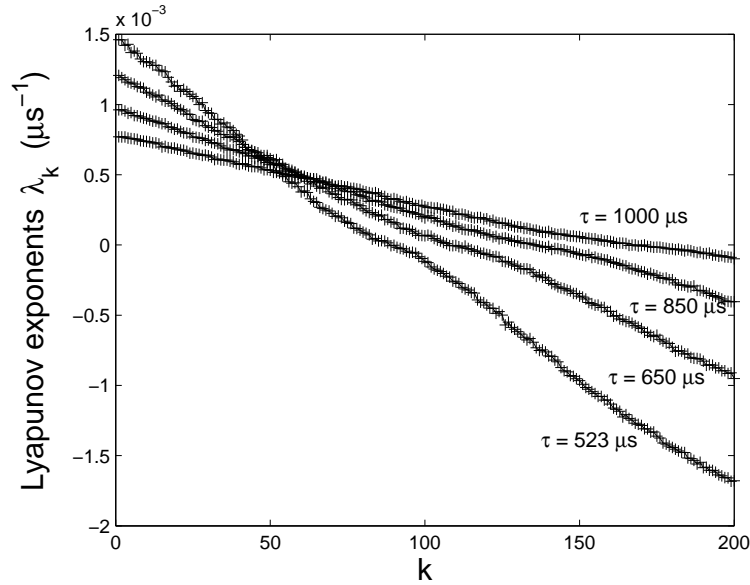


Figure 87: The 200 largest Lyapunov exponents, computed by Farmer's method, for four different values of the delay. $h = 0.42 \mu s$, $\beta = 8$, $\tau^R = 8.4 \mu s$, $\phi = \pi/3$.

is represented in Fig. 89 and its influence on the dimension and entropy is represented in Fig. 90. An increase of the feedback strength influences the Lyapunov spectrum differently than an increase of the delay. If in both cases, the number of Lyapunov exponents and thus the dimension increases (linearly), the entropy also increases with β while it remains constant as a function of τ . We observe that when the feedback strength is increased,

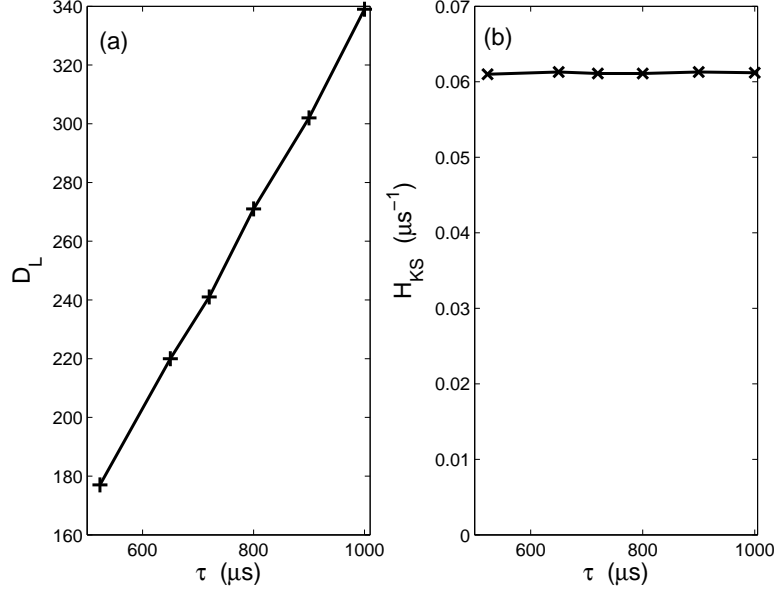


Figure 88: (a) Dimension as a function of delay. (b) Entropy as a function of delay. $h = 0.42 \mu\text{s}$, $\beta = 8$, $\tau^R = 8.4 \mu\text{s}$, $\phi = \pi/3$.

the number of positive exponents increases, and the amplitude of all the exponents also increases. This explains that the entropy increases with the feedback strength, and it increases linearly as can be seen from Fig. 90. We have shown hereabove that the attractor dimension increases linearly with both the feedback strength and the delay. It is possible to express these two tendencies by the following empirical formula

$$D_L \approx 0.35\beta \frac{\tau}{\tau^R} . \quad (137)$$

This formula has a similar form to the one found by Dorizzi *et al.* in the case of an Ikeda system [144].

Before considering the estimation of the spectrum from time series, we will try to interpret the evolution of the entropy as function of β and τ using the results (presented in section 4.4.3) on the influence of β and τ on the pdf of x . We had observed that for a fully-developed chaos, which is what we consider here, the pdf is close to gaussian. Moreover, Figs. 64 to 69 show that the (gaussian) pdf is invariant with respect to a change in the delay τ while an increase of β leads to an increase of the mean and the variance of the gaussian distribution. Similarly, the bifurcation diagrams 60 and 62 show significant changes in the

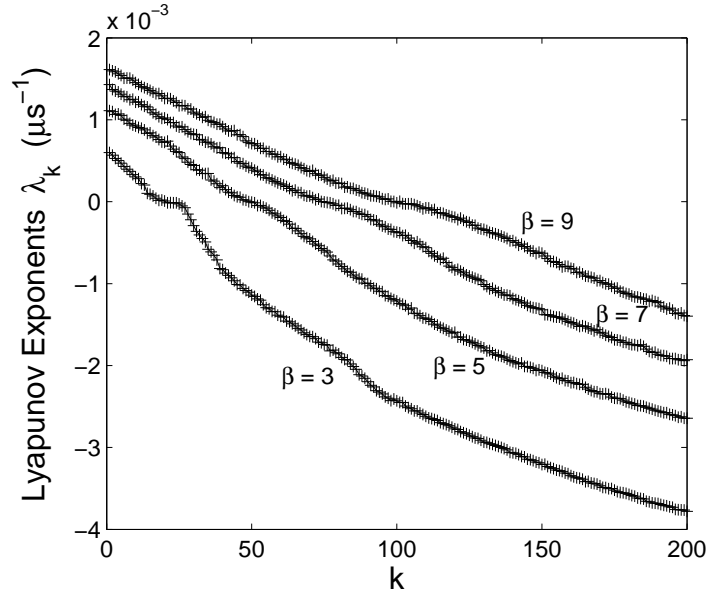


Figure 89: The 200 largest Lyapunov exponents, computed by Farmer's method, for four different values of the delays. $h = 0.42 \mu s$, $\tau = 523 \mu s$, $\tau^R = 8.4 \mu s$, $\phi = \pi/3$.

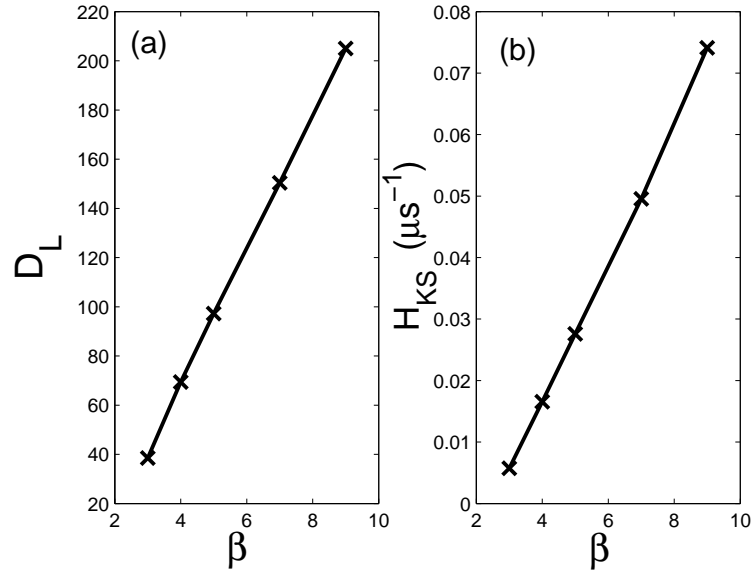


Figure 90: (a) Dimension as a function of the feedback strength β . (b) Entropy as a function of the feedback strength. $h = 0.42 \mu s$, $\tau = 523 \mu s$, $\tau^R = 8.4 \mu s$, $\phi = \pi/3$.

chaotic regime when β is increased but not when τ is increased. Information theory tells us that the entropy,¹⁶ in the Shannon sense, of a continuous gaussian random variable of variance σ^2 is given by $H = (1/2) \log(2\pi e \sigma^2)$ [134]. The observation of the probability density functions can give us an idea of the evolution of the entropy. When τ is modified, the pdf does not change and so the entropy does not either; when β is increased, the variance of the probability distribution increases, and so does the entropy. Of course, this reasoning is limited by the fact that the entropy considered here is the Shannon entropy of information theory and is not the same entropy as the one that is found from the Lyapunov spectrum. Nevertheless, the observation of the pdf seems to give a good idea of the evolution of the Kolmogorov-Sinai entropy with the feedback strength and the delay.

We consider now the estimation of the Lyapunov spectrum from experimental time series. The experimental setup used is the one described in section 2.4 and represented in Fig. 4. The parameter β can be easily tuned experimentally by changing the gain of an amplifier of the feedback loop and the delay τ can also be tuned easily by changing the frequency of the oscillator that drives the delay line.

The first step in the time series analysis is of course the identification of delay τ . We use for this the technique based on local linear approximations. Figure 91 represents the average approximation error as a function of the arbitrary delay τ^* for three different values of the neighborhood size ϵ . This technique leads once again to a sharp minimum in the average approximation error and to the identification of the delay, which is $\tau = 523 \mu s$. We have checked that the identification works in all the possible dynamical regimes of the system and that the influence of parameters ϵ , h , and N on the identification is the same as what as been described in section 4.4.

The second step is the estimation of the Jacobian matrices from experimental time series. We observe that the estimated spectrum is much more sensitive to the values of the parameters of the estimation procedure than in the case of the Mackey-Glass system. This sensitivity is probably due to a series of factors: the chaos is higher dimensional, the nonlinearity is more “complex” (in particular it has several extrema while there is only

¹⁶or more precisely the *differential* entropy

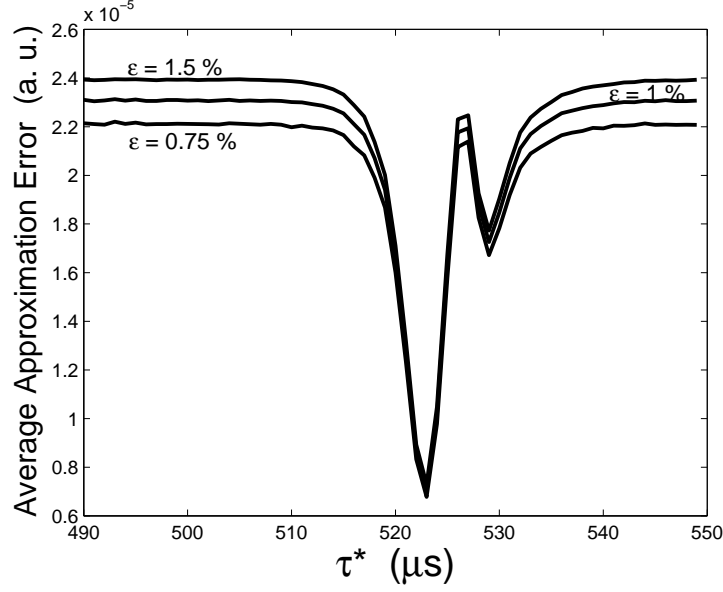


Figure 91: Delay identification from experimental time series. $h = 1 \mu\text{s}$. *Experimental* estimation of the parameter values: $\beta = 8.1$, $\tau = 523 \mu\text{s}$, $\tau^R = 8,4 \mu\text{s}$, $\phi = \pi/3$.

extremum in the Mackey-Glass case), and finally noise is present on the experimentally generated time series considered in this section.

The sampling period h is one of the critical parameters of the procedure. It must be sufficiently small with respect to the delay to allow the evaluation of the several hundreds of positive Lyapunov exponents¹⁷ we anticipate in the case of the chaos in wavelength. The discretization of the phase space cannot be too fine-grained, however, since the presence of noise limits the useful information that can be extracted from successive samples, since they correspond to variations that are in the order of the noise level. Moreover, the number of elements of the Jacobian matrices of the time- h map, in the discretized phase space (*cf.* section 4.3.1), increases as the inverse of the square of the sampling period h . We understand that we will also be limited by computation time constraints. In the measurement made on the chaos in wavelength system, we have considered a minimal sampling step of $1 \mu\text{s}$, which leads to Jacobians that have 523^2 elements. Smaller sampling steps lead to unreasonably long computations.

¹⁷The reader should recall that the dimension of the discretized phase space, and thus the number of exponents that can be evaluated, is τ/h

Another especially critical parameter is the neighborhood size ϵ . In the presence of noise, small neighborhoods can give results that are more influenced by the noise than the deterministic dynamics. Large neighborhoods, on the other hand, do not allow to reconstruct all the details of the dynamics. We have observed that the spectrum and therefore also the estimated values of the dimension and entropy are strongly influenced by the neighborhood size. Figures 92 and 93 represent the evolution of the Lyapunov dimension, estimated from experimental time series, as a function of ϵ , for two different values of the feedback strength β . Additionally, the dotted line corresponds to the value of the dimension computed by Farmer's method, assuming that the model is given by Eq. (126), and using experimentally estimated values of the parameters β , τ^R , ϕ , and τ . The dimension takes a high value for small neighborhoods, then decreases rapidly with ϵ and finally it keeps an approximately constant value for even larger neighborhoods. When ϵ is very small, the influence of noise is very strong and it is not surprising to find large values of the dimension. When large neighborhoods are used, the effect of noise is decreased but at the same time certain details of the dynamics are lost. This is why we observe that for large values of ϵ , the dimension is almost independent of ϵ , but at the same time it is underestimated. Large neighborhoods create an averaging of the phenomena that contributes to decrease the influence of noise but at the same time it cancels some of the details of the dynamics. This is particularly critical for the high-dimensional system we examine. The nonlinearity presents numerous extrema and therefore the surface \mathcal{S} (cf.4.2.1) must be very "curved" and large neighborhoods lead to approximation by tangent planes that make little sense and mask the subtleties of the dynamics. We have represented in Fig. 94 the Lyapunov spectrum estimated from experimental time series, for two values ($\epsilon = 0.75\%$ and $\epsilon = 2\%$) of the neighborhood size, as well as the spectrum found by Farmer's method. In the case in which $\epsilon = 0.8\%$, the effect of noise is significant and a large number of exponents are overestimated. When $\epsilon = 2\%$, the effect of noise is not as critical but the exponent values are underestimated, leading to an underestimation of the dimension.

The last parameter of the estimation procedure is the number N of samples of the time

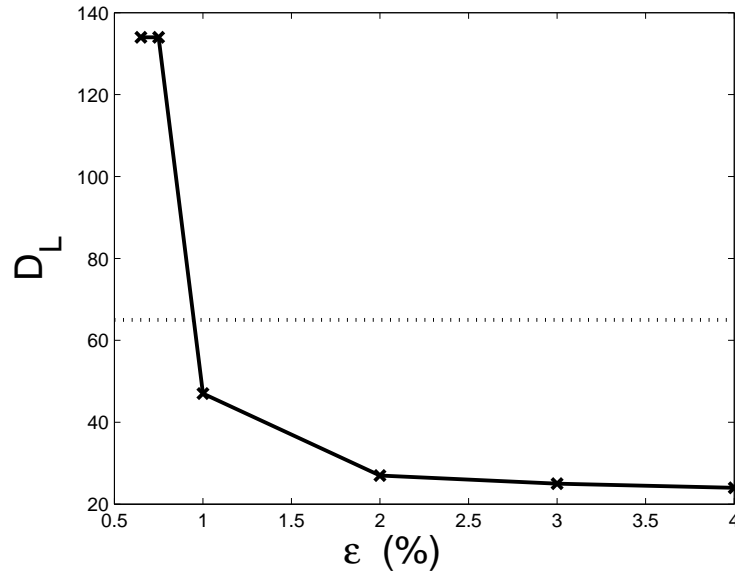


Figure 92: Dimension estimated from experimental time series as a function of the neighborhood size ϵ (solid line). The dotted line corresponds to the dimension computed by Farmer's method. Parameters of the estimation procedure: $N = 300000$, $h = 1 \mu s$. Experimentally estimated values of the system parameters: $\beta = 3.6$, $\tau = 523 \mu s$, $\tau^R = 8.4 \mu s$, $\phi = \pi/3$.

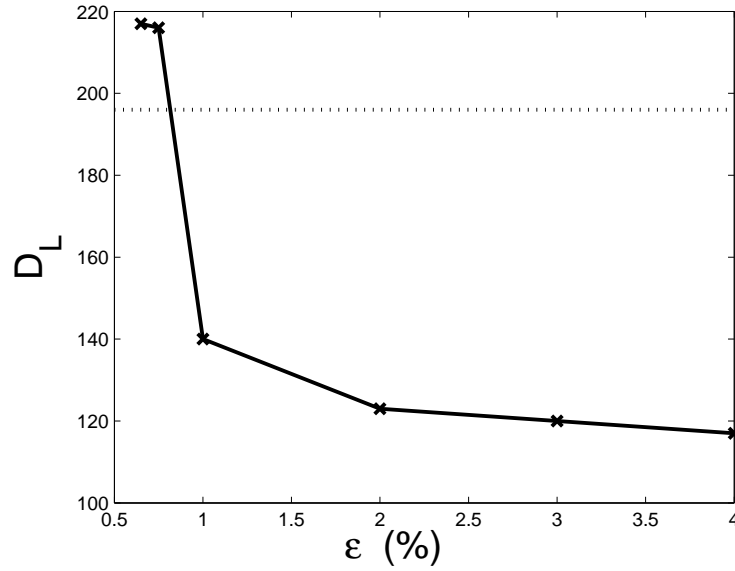


Figure 93: Dimension estimated from experimental time series as a function of the neighborhood size ϵ . The dotted line corresponds to the dimension represented by Farmer's method. Parameters of the estimation procedure $N = 300000$, $h = 1 \mu s$. Experimentally estimated values of the system parameters: $\beta = 9$, $\tau = 523 \mu s$, $\tau^R = 8.4 \mu s$, $\phi = \pi/3$.

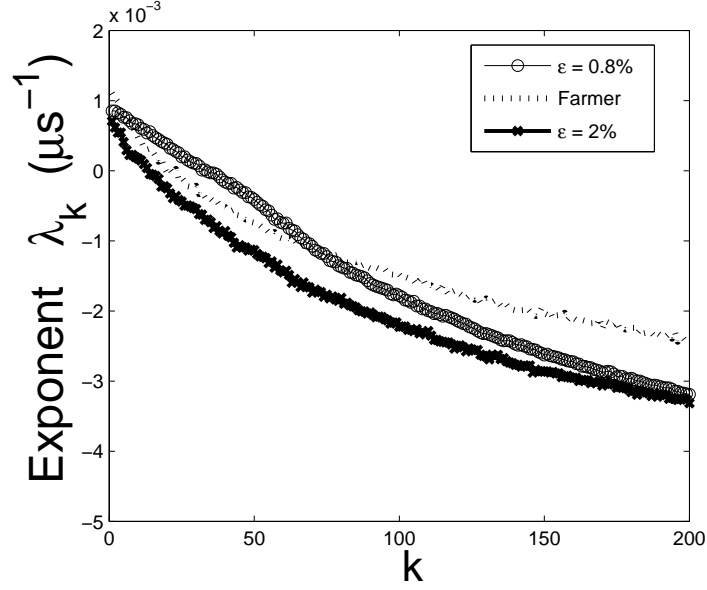


Figure 94: Lyapunov spectrum estimated from experimental time series and by Farmer's method. Parameters of the estimation procedure $N = 300000$, $h = 1 \mu s$. Experimentally estimated values of the systems parameters: $\beta = 3.6$, $\tau = 523 \mu s$, $\tau^R = 8.4 \mu s$, $\phi = \pi/3$.

series. It must be sufficiently large to ensure statistically significant approximations and a convergence of the spectrum. We find that we typically need several hundreds of thousands of samples to observe convergence. It is worthwhile to notice that this is significantly more than the number of samples necessary to identify the delay of the system (*cf.* § 4.4.3).

Even though we have shown that the estimation of the Lyapunov spectrum from time series is arduous, we have tried to determine the evolutions of the dimension and entropy with β and τ . We have chosen a neighborhood size of (2 %) which is the smallest value of ϵ that lies in the zone for which the dimension D_L is constant as a function of ϵ . Figures 95 and 96 represent the effect of a variation of β on the estimation of the dimension and entropy respectively. We observe that even though the dimension and entropy are underestimated, the tendencies to a linear variation of these quantities with β , predicted by Farmer's method, is also found from a time series analysis of experimental data.

The study of the influence of the delay has proved to be more problematic. We have observed that the estimated spectrum tends to be invariant as a function of the delay.¹⁸ This

¹⁸for the minimal neighborhood size ϵ corresponding to the region in which the dimension is a constant

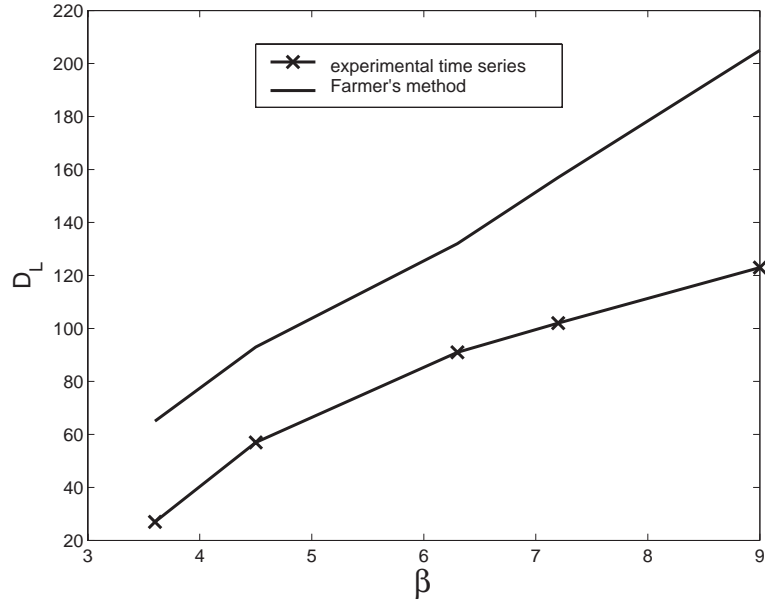


Figure 95: Lyapunov dimension as a function of β . Parameters of the estimation procedure: $N = 300000$, $h = 1 \mu s$. Experimentally estimated values of the system parameters: $\tau = 523 \mu s$, $\tau^R = 8.4 \mu s$, $\phi = \pi/3$.

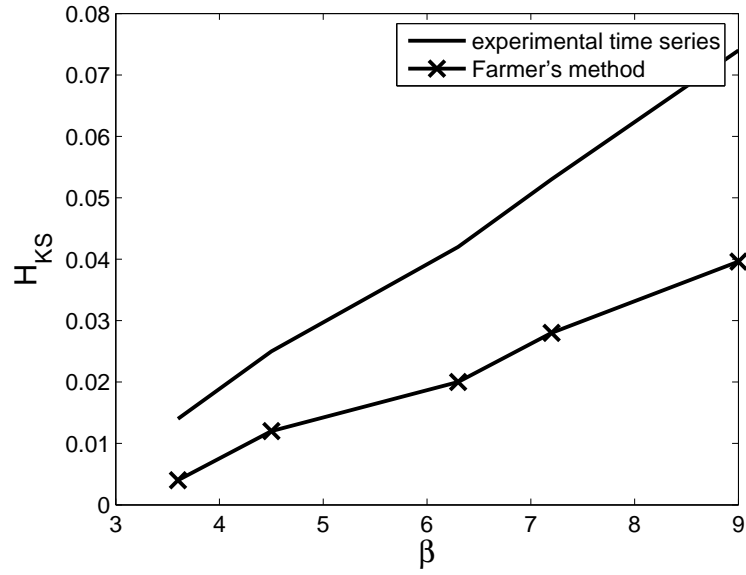


Figure 96: Entropy as a function of β . Parameters of the estimation procedure: $N = 300000$, $h = 1 \mu s$. Experimentally estimated values of the system parameters: $\tau = 523 \mu s$, $\tau^R = 8.4 \mu s$, $\phi = \pi/3$.

is probably due to the fact that the time series that we have measured to study the influence of the delay all correspond to extremely high chaos dimensions (at least 200, according to Farmer's method). Such dimensions probably imply that it is absolutely necessary to choose small neighborhoods to reveal the system dynamics, but this is impossible because of the noise present in the measurements. In addition to the phenomena described hereabove, the differences between the spectra estimated by Farmer's method and from experimental time series might be due in part to differences between the actual and the experimentally estimated values of the system parameters and to the quantization of the measured time series.

We end this section by emphasizing that one must be careful with the conclusions that can be drawn from the estimation of the Lyapunov spectrum from experimental time series. As we have seen above, the results are very sensitive to the choice of the parameters of the estimation procedure. Moreover, for a given set of parameter values, it is possible to observe a convergence of the spectrum, as a function of the number of samples, to an incorrect set of values. This fallacious behavior can easily lead to hasty and incorrect conclusions. It seems difficult to draw conclusions on the dimension and entropy of this high-dimensional chaotic system based on time series analysis only. The results obtained from the dynamical model constitute a very important, and probably indispensable, benchmark.

4.7 *Conclusion*

In this chapter, we have used specific techniques for delay systems, based on local linear models of the dynamics, to analyze experimental and numerically-generated time series of different chaotic delay systems.

We have shown that the identification of the delay is possible for systems that can be modeled by a scalar delay-differential equation (Mackey-Glass system, optoelectronic generator of wavelength chaos, and electronic system producing frequency chaos, when a low-pass filter is used), as well as for vectorial systems modeled by an integro-differential delay equation (electronic generator of frequency chaos using a band-pass filter, optoelectronic

function of ϵ .

system producing chaos in intensity). We have observed that, contrary to the identification techniques based on autocorrelation and mutual information, the technique based on local linear approximations leads to the exact (non-overestimated) delay value. We have also found that this technique is very robust. In particular, we have observed that the identification is possible for a large range of values of the internal parameters of the identification procedure, and in presence of an information-bearing signal. It has also been possible to estimate, from time series, the nonlinear function of the Mackey-Glass system and of the generator of wavelength chaos.

Finally, we have estimated the Lyapunov spectrum, the chaos dimension, and entropy, from numerically-generated time series of a Mackey-Glass system, and from experimental time series produced by the generator of wavelength chaos. In both case, we have compared the spectrum estimated from time series with the spectrum estimated from the dynamical model. In the case of the Mackey-Glass system, we have observed a very good correspondence between the two spectra. We have verified that the dimension increases linearly with the delay, while the entropy is independent of the value of the delay. In the case of wavelength chaos, the computation of the spectrum from the dynamical model shows that the dimension increases linearly with the delay and the feedback strength, while the entropy also increases linearly with the feedback strength, but does not increase with the delay. The estimation of the Lyapunov spectrum from experimental time series has proved to be more problematic. We have not been able to find a satisfactory agreement between the spectrum calculated from the time series and from the model. We believe the disagreement is due to the presence of noise on the time series, and to the concomitant fact that we try to estimate the spectrum of a very hyperchaotic system, whose nonlinear function has many active extrema. We have nevertheless been able to confirm that the dimension and entropy tend to vary linearly with the feedback strength.

CHAPTER V

IDENTIFICATION OF THE DELAY TIMES IN SINGLE- AND MULTIPLE-DELAY SYSTEMS

5.1 *Motivations*

Even though delay systems can experience very high-dimensional dynamics, if the value of the delay is known, these systems can be analyzed in a low-dimensional space, as was shown in chapter 4. Several studies have demonstrated that certain chaotic delay systems could be broken. Zhou and Lai [80] and Ortin *et al.* [147] have shown that a Mackey-Glass cryptosystem could be broken. Udaltsov *et al.* [81] and Ortin *et al.* [148] have demonstrated that, under certain conditions, the nonlinear dynamics of the cryptosystem based on the optoelectronic generator of chaos in wavelength could be extracted, and that the information-bearing signal could be found by analyzing the time series produced by this system. The common feature of the analysis techniques used by these different authors is that the first step of the analysis is to identify the delay time. Once the value of the delay is known, it is possible to analyze the delay cryptosystem without the need to reconstruct the full (potentially very high-dimensional) dynamics. This has to be avoided in order to ensure the confidentiality of a chaotic communication and therefore it is crucial to be able to hide the delay.

One of the possible ways to increase the difficulty of the delay identification problem is to modify the architecture of the delay system to include several feedback loops. In section 5.2, we examine the delay identification problem in the case of chaotic systems subjected to one delayed feedback, and in section 5.3 we analyze different types of systems with two delays. Section 5.4 presents our conclusions and perspectives for future work.

5.2 One-delay cryptosystems

We have described in section 4.4.1 different techniques that can be used to identify the delay of a scalar or vectorial delay system, from a times series (x_n) . These include the autocorrelation of (x_n) , the delayed mutual information between (x_n) and $(x_{n-\tau^*})$, where τ^* is an arbitrary delay, and the average approximation error of a series of local linear fits performed in the low-dimensional space $(x_{n+1}, x_n, x_{n-1}, \dots, x_{n-m+1}, x_{n-\tau^*}, x_{n-\tau^*-1}, \dots, x_{n-\tau^*-m+1})$. Other techniques exist; for example¹, Ortin *et al.* [147, 148] have proposed to use *global* discrete *nonlinear* models of the form:

$$x_{n+1} = M_{NL}(x_n, x_{n-1}, \dots, x_{n-m+1}, x_{n-\tau^*}, x_{n-\tau^*-1}, \dots, x_{n-\tau^*-m+1}), \quad (138)$$

where M_{NL} is a nonlinear function obtained by a neural network divided in two modules, one for the non-feedback part, and one for the feedback part. In the case of scalar systems, we can take $m = -1$ for the global nonlinear model, as well as for the local linear models. The common point of these different techniques is that they analyze the system in a low-dimensional projection of the (infinite-dimensional) phase space, as is explained in the following.

We consider, for the sake of clarity, a system described by a scalar delay-differential equation

$$\dot{x}(t) = F[x, x(t - \tau)], \quad (139)$$

but similar considerations apply in the case of vectorial delay systems. Because the preceding equation defines a constraint in the three-dimensional space $(\dot{x}(t), x(t), x(t - \tau))$, it is inevitable that a projection of a trajectory in the phase space, on this three-dimensional space, lies on a surface \mathcal{S} . If we had access to the space $(\dot{x}(t), x(t), x(t - \tau^*))$, where τ^* is an arbitrary delay, we could detect, with adequate methods, the presence of the surface \mathcal{S} , when $\tau^* = \tau$, and therefore identify the delay. We do not have access to this space, however, but only to a discretized version of it, $(\hat{x}_n, x_n, x_{n-\tau})$, where \hat{x}_n is an estimation of the derivative, or similarly to $(x_{n+1}, x_n, x_{n-\tau})$. If the discretization is good enough to reproduce the characteristics of the continuous-time system, it should also be possible to detect the

¹A list of possible techniques can be found in Ref. [149] and in references therein.

presence of the surface in a discretized version of the three-dimensional space. Additionally, if a structure is present in the space $(x_{n+1}, x_n, x_{n-\tau})$, its projection on the plane $(x_n, x_{n-\tau^*})$, for example, could also be detected by appropriate techniques, when $\tau^* = \tau$, and therefore lead to the identification of the delay. It is to be noted that the projection we consider here is not the projection of the *complete* surface \mathcal{S} , but the projection of the structure which is described by a trajectory of the system on the surface \mathcal{S} . It is also to be noted that there is no guarantee that this type of projection leads necessarily, in the general case, to an identifiable structure. Both the autocorrelation and the mutual information technique measure a relationship between x_n and $x_{n-\tau^*}$. The autocorrelation measures a linear link, and is therefore not the most adequate when highly nonlinear systems are studied. The mutual information measures a nonlinear link and is a statistical quantity. Therefore it takes into account the *probability* that a given region of the discretized projected phase space $(x_n, x_{n-\tau})$ is visited by the projection of the trajectory, and can therefore reveal structures that are not purely geometric. This technique should work if the discretization is good enough, and if there is a detectable structure in the projection of the infinite-dimensional phase space on the two-dimensional space $(x_n, x_{n-\tau})$, *i.e.* if the set defined by $(x_n, x_{n-\tau})$ is measurably different from the set defined by $(x_n, x_{n-\tau^*})$, when τ^* is different from τ . The techniques based on a series of local linear fits of the form

$$x_{n+1} = a_n + b_n x_n + c_n x_{n-\tau^*} , \quad (140)$$

and on the global nonlinear model use the discretized three-dimensional space $(x_{n+1}, x_n, x_{n-\tau})$. Both of these techniques should work to identify the delay of a scalar delay system, if the discretization were good enough. In the case of the local linear models, even though the models are linear, since they are local and not global, they can be used to identify a nonlinear system.

In the following, we consider the case of the generator of wavelength chaos described in sections 2.4.3 and 4.4.3, which is described by the scalar delay-differential equation

$$x(t) + \tau^R \dot{x}(t) = \beta \sin^2[x(t - \tau) + \phi] . \quad (141)$$

In Figs. 97 and 98, we have represented the autocovariance of the time series (x_n) , the

delayed mutual information, the average approximation error of a series of local linear fits (140), and the projection of a trajectory on the $(x_n, x_{n-\tau})$ plane. We have considered two different values of the feedback strength β ($\beta = 5$ and 25), for a sampling time $h = 1 \mu s$. It is to be noted that a value of β of 25 , as considered in Fig. 98, corresponds to the upper limit of what can be done experimentally, and corresponds to a very high dimension and entropy ($D_L \approx 500$). We observe that, in every case, there is an identifiable structure in the plane $(x_n, x_{n-\tau})$, and it is possible to identify the delay of the system. The only method that fails is the autocovariance, in the case in which $\beta=25$. The autocovariance measures, for each value of τ^* , the tendency of the cloud of points $(x(t), x(t - \tau))$ to align along an oblique straight line. There is such a tendency for small values of β (see Fig. 97), when the system is only slightly nonlinear. For large values of the feedback rate, there is no tendency to align along an oblique straight line, as the cloud of points has a vertical axis of symmetry, and the delay cannot be identified from the autocovariance (see Fig. 98). Both the mutual information and the method based on local linear fits lead to the identification of the delay, even though the peak in the mutual information, and the valley in the average fitting error, become sharper with increasing β . As noted in section 4.4, the mutual information leads to an overestimation of the delay in the system, due to the influence of the response time of the system. One advantage of the mutual information over the average approximation error coming from local models, however, is that it involves a much shorter computation time. We have checked, with our collaborators Silvia Ortin and Luis Pesquera, that the technique based on a global nonlinear model also leads to the identification of the delay.

When the feedback strength β is increased, we observe that the fluctuations of x tend to become faster and the amplitude of these fluctuations increases. Figure 99 represents the delayed mutual information, around $\tau^* = 0$, computed from a time series (x_n) , for $\beta = 3.5$ and $\beta = 25$. We observe that the mutual information decreases more rapidly for large values of β . This means that the statistical link that exists between, for example, two successive samples of $x(t)$, decreases with increasing β . Thus it might be necessary to choose smaller sampling times, for increasing β , to ensure that the discretization reproduces faithfully the characteristics of the continuous-time system and to help identify the delay. Therefore, it is

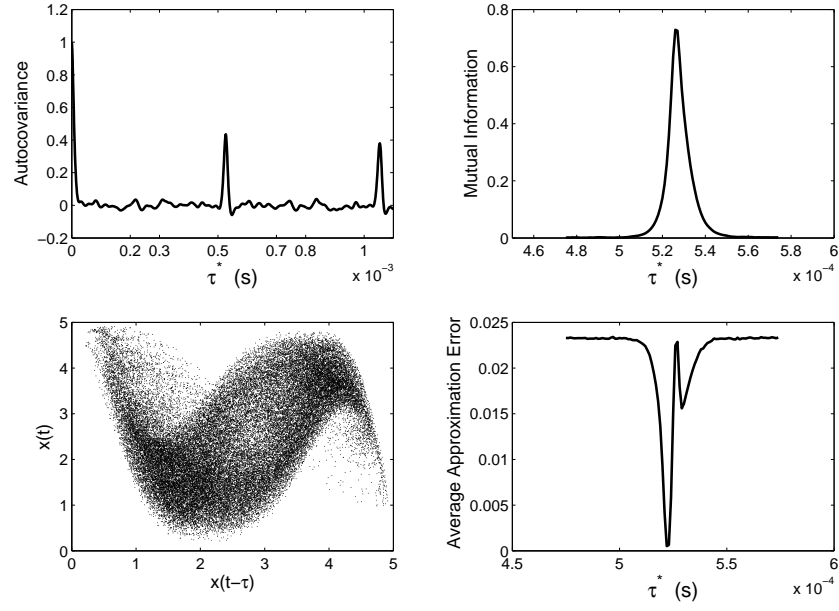


Figure 97: Identification of the delay produced by the optoelectronic emitter of chaos in wavelength. The parameters are: $\beta = 5$, $\tau = 523 \mu\text{s}$, $\tau^R = 8,4 \mu\text{s}$, $\phi = \pi/3$. The sampling time is $h = 1 \mu\text{s}$.

not surprising that the value of the delayed mutual information for $\tau^* = \tau$ decreases with increasing β , while the average approximation error, for $\tau^* = \tau$, increases with increasing β (see Figs. 97 and 98). Similarly, it is also logic that peak in the mutual information, and the valley in the average approximation error, tend to become sharper with increasing β since, for example, the link between $x(t - \tau)$ and $x(t - \tau + h)$ tends to decrease for increasing values of β . And the flat portion of the average approximation error curve corresponds to error values that increase with increasing β , since the (linear) link between x_{n+1} and x_n decreases. We can conclude that, in the case of the one-delay system described by Eq.(141), an increase of β may lead to the need to use smaller sampling times, leading to longer computation times, but we find that the identification of the delay is always possible, even for extremely large values of β (which lead to a chaos of large dimension and entropy).

We have seen that an increase of the feedback strength β leads to a decrease of the link that exists between two successive samples, leading to a more difficult identification of the delay, for a given sampling time. This phenomenon is not observed when the delay

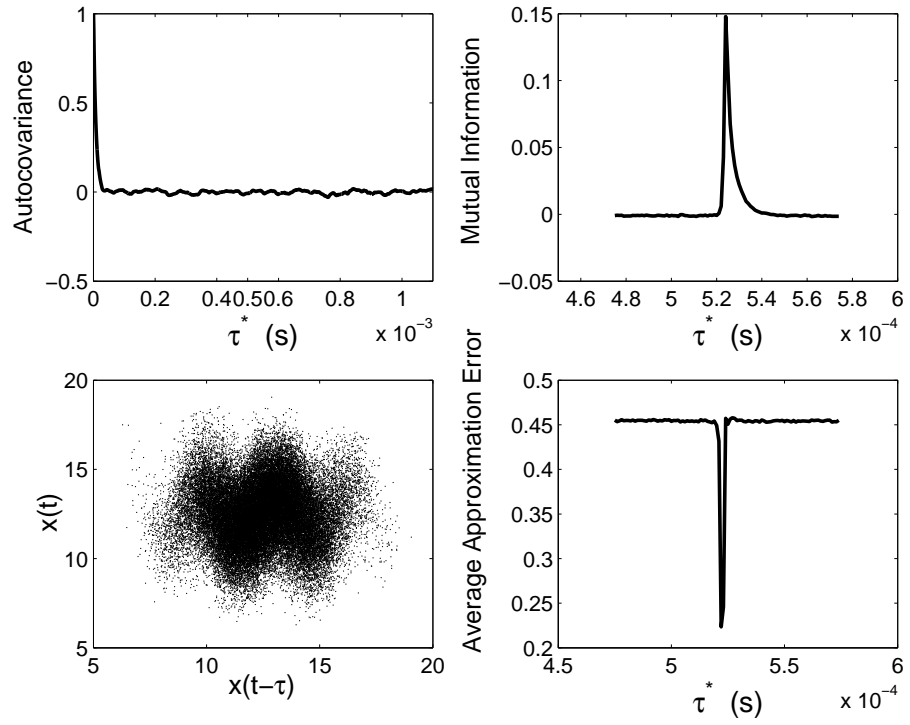


Figure 98: Identification of the delay produced by the optoelectronic emitter of chaos in wavelength. The parameters are: $\beta = 25$, $\tau = 523 \mu s$, $\tau^R = 8,4 \mu s$, $\phi = \pi/3$. The sampling time is $h = 1 \mu s$.

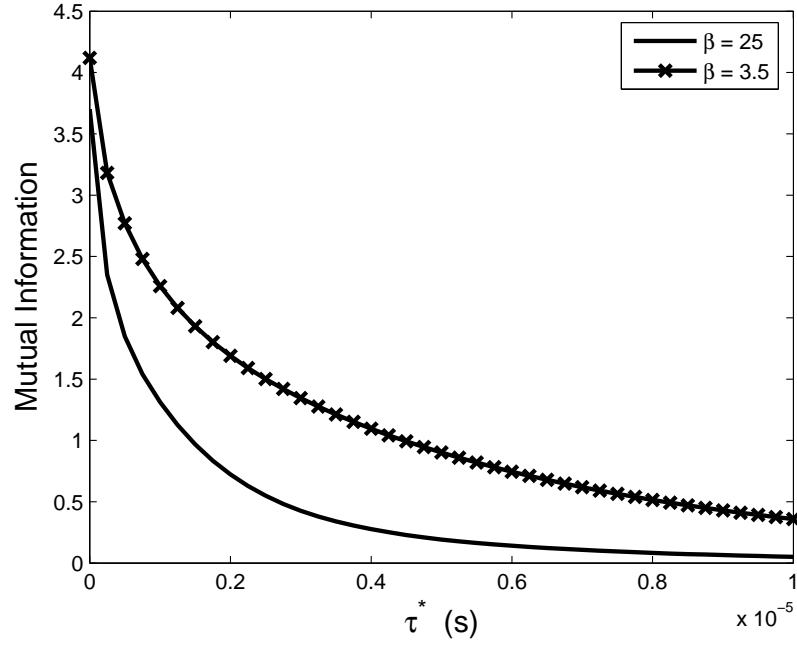


Figure 99: Delayed mutual information for two different values of the feedback strength β . The parameters are: $\tau = 523 \mu\text{s}$, $\tau^R = 8,4 \mu\text{s}$, $\phi = \pi/3$.

parameter τ is increased. This also means that we do not expect any change in the difficulty to identify the delay, when the delay itself is increased. This is represented in Figs. 100 and 101, which correspond to delay values of 500 and 1000 μs , respectively. The figures confirm that doubling the value of the delay itself does not lead to any significant change in the difficulty to identify the value of the delay.

The previous observations indicate that it is *always* possible to identify the delay of the optoelectronic generator of chaos in wavelength, using techniques such as the mutual information or the approximation error coming from a series of local linear fits. We have found that this is also true for all the delay systems presented in section 4.4, and for external-cavity lasers (described in chapter 3), even though these systems use other types of nonlinearities than the one involved in the emitter of wavelength chaos, and some of them are vectorial. It is interesting to note that the techniques used here for the scalar emitter of wavelength chaos also work for vectorial systems. For example, simple local linear approximations of the form $x_{n+1} = a_n + b_n x_n + c_n x_{n-\tau^*}$ are sufficient to find the delay of

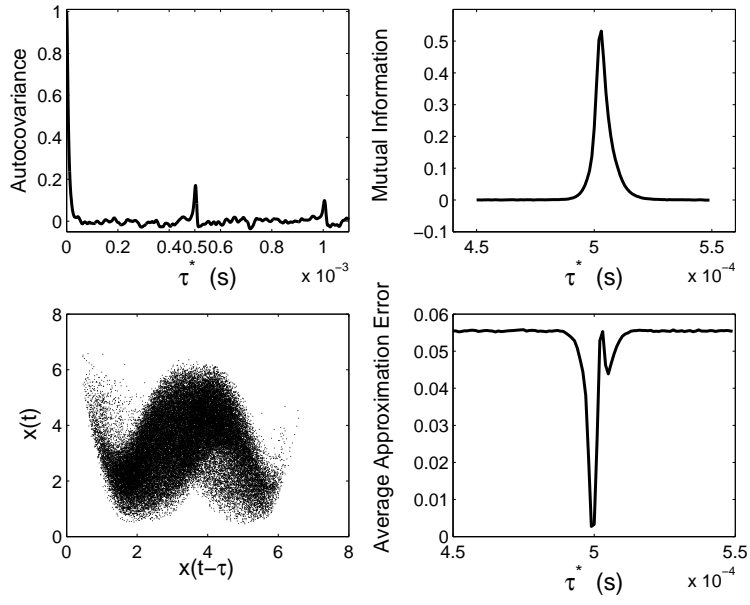


Figure 100: Identification of the delay from a time series of the optoelectronic generator of chaos in wavelength. The parameters are: $\tau = 500 \mu s$, $\beta = 7$, $\tau^R = 8,4 \mu s$, $\phi = \pi/3$. The sampling time is $h = 1 \mu s$.

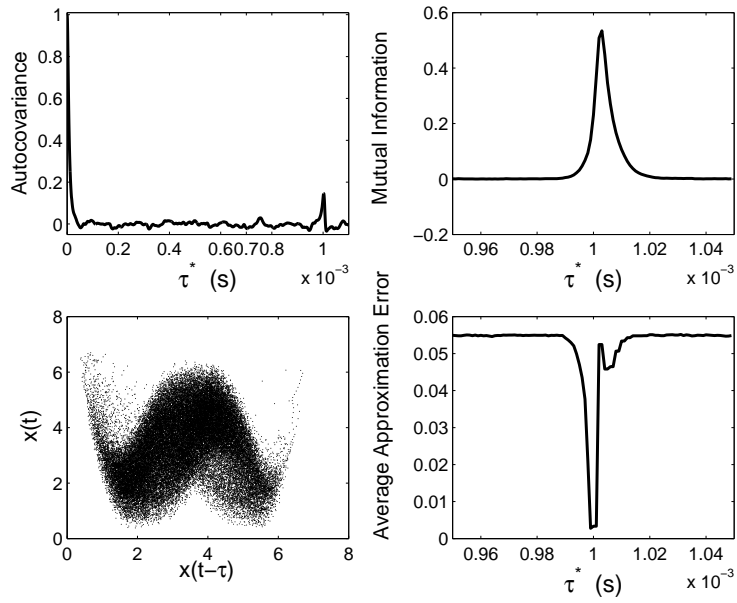


Figure 101: Identification of the delay from a time series of the optoelectronic generator of chaos in wavelength. The parameters are: $\tau = 1000 \mu s$, $\beta = 7$, $\tau^R = 8,4 \mu s$, $\phi = \pi/3$. The sampling time is $h = 1 \mu s$.

a vectorial system. The use of additional delayed variables, as described in section 4.2.2, leads to lower values of the approximation error, but is not indispensable to identify the delay. In conclusion, cryptosystems based on single-delay systems do not seem to provide a sufficient security level, despite the fact that they can produce chaotic signals of large dimension and entropy. In the next section, we try to determine if multiple-delay systems can provide a better security level.

5.3 *Two-delay cryptosystems*

Very recently, two chaotic emitters with two delayed feedback loops have been realized experimentally [150, 151], and the authors have suggested that their use might increase the security level of chaotic communications. Additionally, the numerical simulation of a chaotic system with three delays [152] has also suggested that systems with multiple feedback loops might lead to an increased security. It is in this context that we have decided to study the delay identification problem in the case of systems with multiple delays. It is interesting to determine if some architectures of multiple delay systems can lead to a better security in terms of the concealment of the values of the delays. We consider here three different systems subjected to two delayed feedback loops. The systems studied in sections 5.3.1 and 5.3.3 can be considered as generalizations of the generator of wavelength chaos in which a second feedback loop has been added. The system under consideration in section 5.3.2 is a semiconductor laser diode subjected to two optical feedbacks.

5.3.1 Delay system subjected to two delays: first configuration

The block-diagram of the system under consideration here is represented in Fig. 102. The basic elements of this diagram are the same as the basic elements of the diagram of Fig. 1, which represents typical chaotic emitters used at the GTL-CNRS Telecom laboratory. The arrangement of the elements is different, however, as two feedback loops are present. Each feedback loop comprises a delay τ_i and a nonlinear element NL_i . If we assume that the filter is a low-pass filter, the scalar delay-differential equation describing the dynamics of the system is

$$x(t) + \tau^R \dot{x}(t) = \beta_1 NL_1 [x(t - \tau_1)] + \beta_2 NL_2 [x(t - \tau_2)] , \quad (142)$$

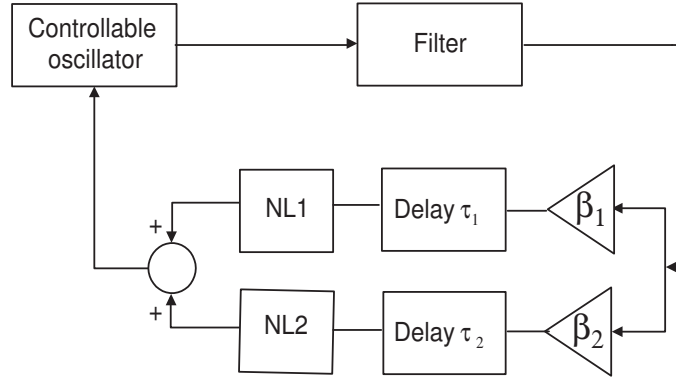


Figure 102: Block diagram of the first configuration of chaotic emitter with two feedback loops.

where τ_1 , NL_1 , β_1 and τ_2 , NL_2 , β_2 are the delays, nonlinear functions, and feedback strengths, respectively, of two feedback loops. If we consider that the two nonlinear functions are of the form $\beta_i \sin^2(\dots + \phi_i)$, the equation becomes

$$x(t) + \tau^R \dot{x}(t) = \beta_1 \sin^2[x(t - \tau_1) + \phi_1] + \beta_2 \sin^2[x(t - \tau_2) + \phi_2] . \quad (143)$$

This equation could correspond to a generator of chaos in wavelength, to which a second feedback loop has been added in the way represented in Fig. 102. It is also essentially the same equation as the one describing the dynamics of the experimental system used in Ref. [150], that has been proposed to increase the security level of chaotic communications using delay systems. We find that, unfortunately, it is easy to identify the delay values using the same techniques as the ones employed for single-delay systems in the preceding section. Figure 103 represents the delayed mutual information for the system described by Eq.(143), for very large feedback strengths $\beta_1 = \beta_2 = 50$. We observe that even for such strong feedbacks, it is possible to identify clearly the two delays. The application of the technique based on local linear fits and on a global nonlinear model lead to the same conclusions. We have checked that these results hold irrespective of the values of the delays and of the feedback strengths. Strong feedbacks may require to use smaller sampling times, but it is still always possible to identify the delays with the same techniques that work for single-delay systems. Additionally, we have also used different types of nonlinear functions in the feedback loops and, even in this case, the delays can be identified.

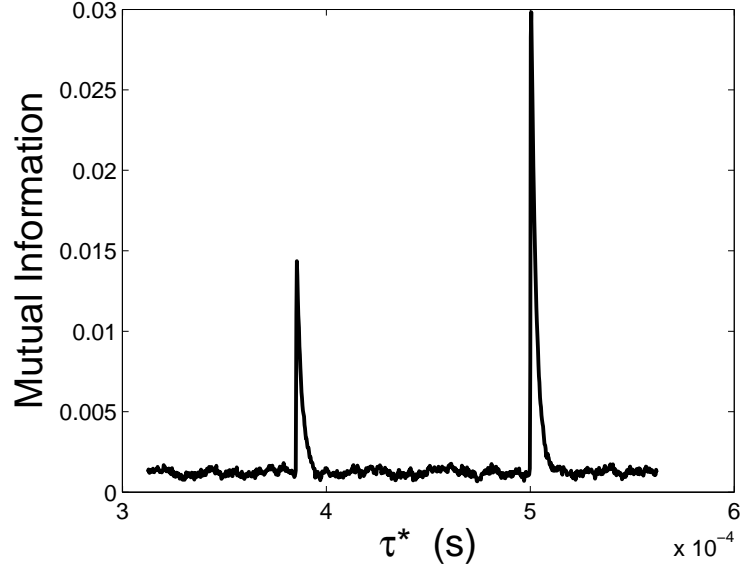


Figure 103: Identification of the delays from a time series of the system with two feedback loops given by Eq. (143). The parameters are: $\beta_1 = \beta_2 = 50$, $\tau_1 = 500 \mu s$, $\tau_2 = 385 \mu s$, $\phi_1 = \phi_2 = 0.74\pi$, $\tau^R = 5 \mu s$. The sampling time is $h = 0.25 \mu s$.

When the values of the two delays are identified, it is certainly possible to analyze and break a cryptosystem using techniques such as those described in chapter 4. We can thus conclude that this type of system with two feedback loops, and in particular the system proposed in Ref. [150], does not lead to a significant increase in the security level of chaotic communications, because the delays can be identified using the same techniques as for systems with a single delayed feedback loop. The authors of Ref. [150] argue that the increased security comes from the higher dimensionality created by the presence of a second delay. We find that, for the approach considered here, the dimension is not the most relevant factor to characterize the security. This is because an increase of the delay values leads to an increase of the dimension of chaos, but not of the difficulty to identify the delays, as was also found in the case of single-delay systems (*cf.* section 5.2).

5.3.2 Semiconductor laser subjected to two optical feedbacks

Semiconductor lasers with two optical feedbacks have been the subject of several studies which show that depending on the conditions, the second feedback can lead to the stabilization of the semiconductor laser [153, 154, 155], or to the production of high-dimensional chaotic dynamics [156]. We consider here conditions such that the intensity produced by the laser exhibits fully-developed chaos. In Ref. [151], it is suggested that the use of hyper-chaotic laser diodes subjected to delayed feedback from two external mirrors could lead to better security in chaotic communications. In this section, we examine this problem from the point of view of the identification of the delay times.

A semiconductor edge-emitting laser subjected to two optical feedbacks can be modeled by a generalization of the Lang and Kobayashi (*cf.* § 3.2.2.1) equations:

$$\begin{aligned} \frac{d[A(t)e^{i\phi(t)}]}{dt} = & \left\{ \frac{1}{2}(1 + i\alpha) \left[G(N, A^2) - \frac{1}{\tau_p} \right] \right\} A(t)e^{i\phi(t)} \\ & + \gamma_1 A(t - \tau_1) e^{i\phi(t-\tau_1)} e^{-i\omega\tau_1} \\ & + \gamma_2 A(t - \tau_2) e^{i\phi(t-\tau_2)} e^{-i\omega\tau_2}, \end{aligned} \quad (144)$$

$$\frac{dN(t)}{dt} = \frac{J}{e} - \frac{N(t)}{\tau_n} - G(N, A^2)A^2(t), \quad (145)$$

where γ_1, γ_2 are the feedback rates of the two feedbacks, and τ_1, τ_2 are the round-trip times of light in the external cavities. The other parameters have been described in sections 3.2.1 and 3.2.2.

We find that for this system too, it is possible to identify the two delays with the same identification techniques as those used in the case of a single-delay system. Figure 104 represents the delayed mutual information², applied to a time series of the intensity $A^2(t)$ of the laser, for two very different values of the feedback rates, $\gamma_1 = \gamma_2 = 10$ GHz, and $\gamma_1 = \gamma_2 = 100$ GHz (strong feedback), and for delay values of 1 ns and 0.77 ns. We observe that, for the two feedback levels, it is possible to identify the delays. It even seems that the stronger feedback leads to a more clear identification of the delays, because the main peaks in the mutual information, corresponding to the delay values, are not accompanied by side

²Other methods, like the local linear models, lead to the same conclusion.

peaks that can make the identification more difficult. The width of the peaks is smaller, however, for stronger feedback.

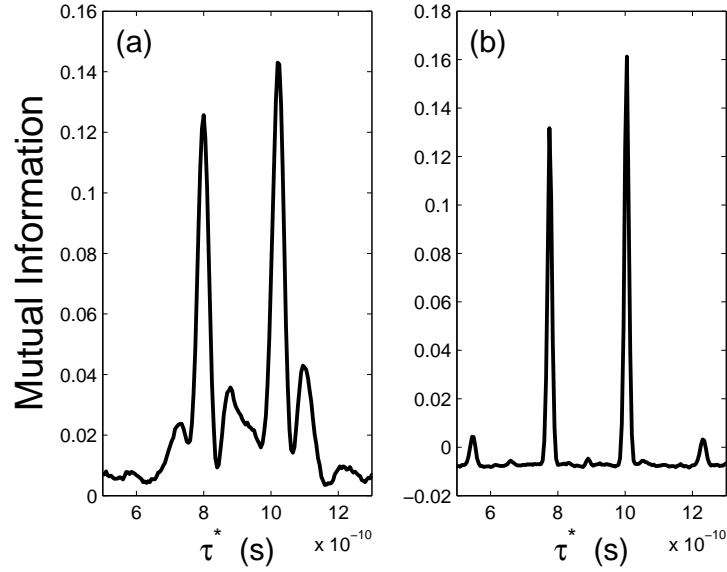


Figure 104: Delayed mutual information in the case of an edge-emitter laser diode subjected to two delayed optical feedbacks. The feedback rates are: (a) $\gamma_1 = \gamma_2 = 10$ GHz, (b) $\gamma_1 = \gamma_2 = 100$ GHz, and the delays are $\tau_1 = 1$ ns and $\tau_2 = 0.77$ ns. The other parameters are as in Fig. 13. The sampling time is $h = 5$ ps.

We have tried a wide range of parameter values and find consistently that the two delay values can be identified. The only case in which the identification is problematic, occurs when the feedback rates are small, and the two delay values are very close. In this case, the concomitant effect of the side peaks and of the (relatively large) width of the main peaks, can make the identification of the two delay values relatively difficult. Since the delay values are very close to each other, however, the system might behave like a single-delay system and it might not be necessary to find the values of the two delays to analyze the system.

The two configurations of systems with two delays considered so far do not increase significantly the security level of chaotic cryptosystems, since the two delay values can be determined by the same techniques that are used to identify single-delay cryptosystems. It is to be noted that the two types of systems considered so far have in common that in their model, the nonlinear functions are applied to each delayed term $x(t - \tau_i)$ separately, and

then added. In the next section, we consider a system in which the nonlinear function is applied to the sum, $x(t - \tau_1) + x(t - \tau_2)$, of the delayed terms.

5.3.3 Delay system subjected to two delays: second configuration

We consider here a system based on the block diagram represented in Fig. 105. In this case, the two delay elements are put in parallel to create two feedback loops. The two feedback loops use the same filter, nonlinearity, and amplifier. In the case of a low-pass filter, this

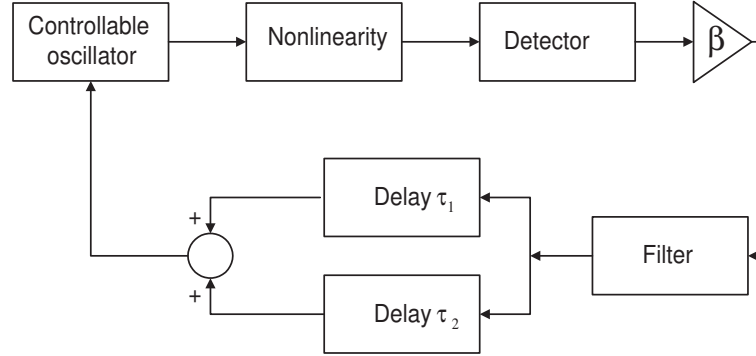


Figure 105: Block diagram of the second configuration of chaotic emitter with two feedback loops.

system can be modeled by the following equation

$$x(t) + \tau^R \dot{x}(t) = \beta \text{NL}_1 [x(t - \tau_1) + x(t - \tau_2)] . \quad (146)$$

In the case in which the nonlinearity is of the form $\sin^2(\cdots + \phi_i)$, the model becomes

$$x(t) + \tau^R \dot{x}(t) = \beta \sin^2 [x(t - \tau_1) + x(t - \tau_2) + \phi] . \quad (147)$$

This equation can be that of a generator of chaos in wavelength to which a second delay line has been added. Such a system is currently being realized [157] at the laboratoire d'optique P.-M. Duffieux of the Institut Femto-ST.

The dynamical behavior of this system has some apparent common features with that of a single-delay system. It is particularly interesting to note that a large feedback strength β leads to rapid fluctuations of the dynamical variable x , to a Gaussian probability density function, and to a spectrum that looks like that of a white noise³, as in the case of a

³Therefore, no frequency in relation with the delay times appears in the spectrum.

single feedback (*cf.* section 4.4.3). This is shown in Figs. 106 and 107, which represent the variable x , its pdf, and its power spectrum, for a feedback strength $\beta = 25$, in the case of a single feedback loop, and of two feedback loops, respectively. This means that for an

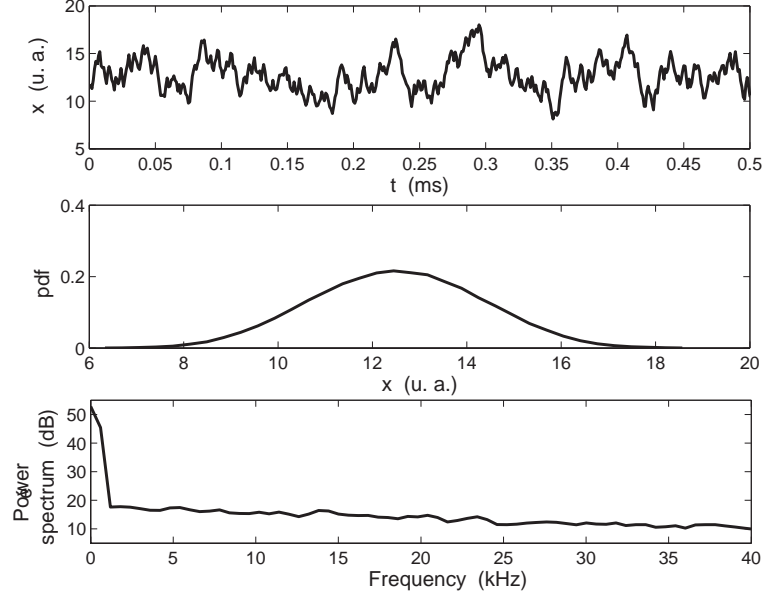


Figure 106: System with one feedback loop. $\beta = 25$, $\tau = 500 \mu\text{s}$, $\tau^R = 5 \mu\text{s}$, $\phi = 0.74\pi$.

eavesdropper, there is no obvious sign of the presence of a second delay.

Despite these characteristics, we find that the delay identification problem has become more difficult. When the feedback strength is large, so that several extrema of the nonlinear function are involved in the dynamics, it becomes impossible to find the delay values using the techniques that have been successful for single-delay systems. Figure 108 represents the result of the application of the identification techniques that make the use of delayed mutual information and of local linear fits, to the case of the two-delay system, for a feedback parameter $\beta = 25$, and for two delays values $\tau_1 = 500 \mu\text{s}$ and $\tau_2 = 385 \mu\text{s}$. We observe that none of the techniques gives any sign of the presence of the delays, while the single-delay chaotic emitter described by Eq. (141) can be identified, for the same feedback strength ($\beta = 25$), and even for much larger feedback strengths. The first configuration of system with two delays, described in section 5.3.1, can also be identified for larger feedback strengths (*cf.* Fig. 103). All the other identification techniques that have been devised for

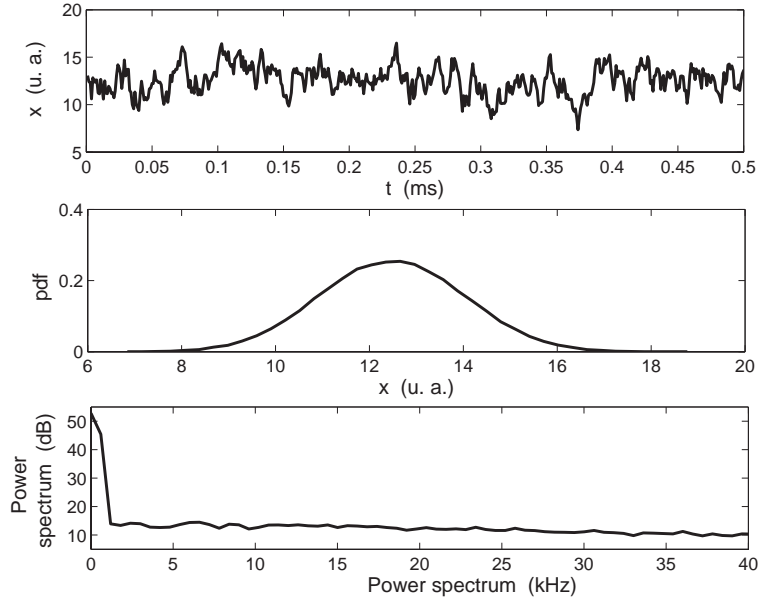


Figure 107: System with two feedback loops. $\beta = 25$, $\tau_1 = 500 \mu s$, $\tau_2 = 385 \mu s$, $\tau^R = 5 \mu s$, $\phi = 0.74\pi$.

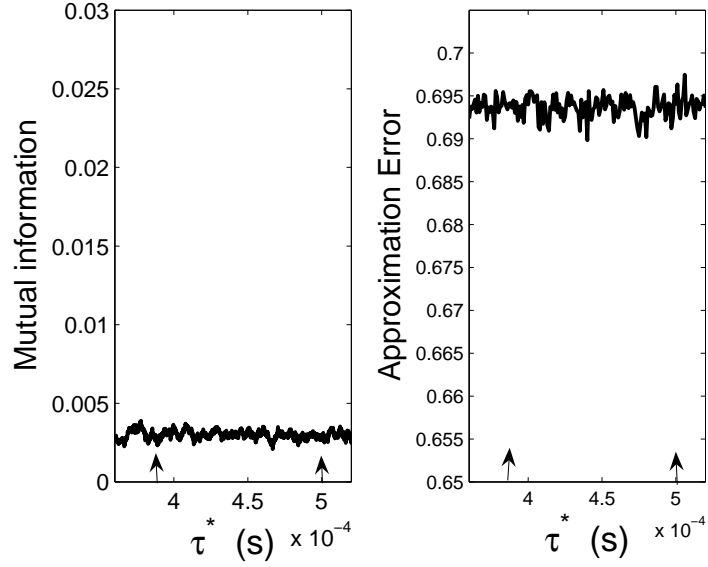


Figure 108: Mutual information and local linear fits applied to the system with two feedback loops given by Eq. (147). The parameters are $\beta = 25$, $\tau_1 = 500 \mu s$, $\tau_2 = 385 \mu s$, $\tau^R = 5 \mu s$, $\phi = 0.74\pi$. The sampling time is $h=1 \mu s$. The arrows indicate graphically the delay values.

single-delay systems, including the one based on a global nonlinear model of the form (138), or on local linear approximations of the form (113), also fail [149, 158, 159, 160]. Decreasing greatly the sampling time does *not* help either, *contrary* to what happens in the case of systems with a single delay. Additionally, these results hold when the difference between the delay values is varied. We should mention, however, that for small feedback strengths β , it is possible to identify the two delays using techniques such as the delayed mutual information. This is probably because for small feedback strengths, only a small portion of the nonlinearity is exploited, and the system is not very nonlinear. In this context, the approximation $\sin^2[x(t - \tau_1) + x(t - \tau_2)] \approx \sin^2[x(t - \tau_1)] + \sin^2[x(t - \tau_2)]$ can be made, and we thus go back to the configuration studied in section 5.3.1.

We should remember that the techniques used in Fig. 108 to identify the delays try to measure, in some way, the presence of a *structure* in the plane $(x_n, x_{n-\tau^*})$, in the case of the mutual information, and in the space $(x_{n+1}, x_n, x_{n-\tau^*})$, in the case of the local linear fits. The equations (143) and (147) of the systems with two delays define, however, a constraint in the four-dimensional space $(\dot{x}(t), x(t), x(t - \tau_1), x(t - \tau_2))$, which guarantees the existence of a structure in this space only. If we assume that we perform a sufficiently good discretization of the system, the projection of a trajectory of the phase space, on the space $(x_{n+1}, x_n, x_{n-\tau_1}, x_{n-\tau_2})$ should reveal the presence of a structure. It is not guaranteed, however, that a projection on a lower-dimensional space, like $(x_n, x_{n-\tau_i})$ or $(x_{n+1}, x_n, x_{n-\tau_i})$ leads to an identifiable object, even for a very good discretization. This depends on the system considered.

We have represented in Figs. 109 and 110 the projection of a trajectory on the spaces $(x_{n+1}, x_n, x_{n-\tau_1})$ and $(x_n, x_{n-\tau_1})$, respectively, in the case of the system subjected to two delayed feedbacks described by Eq.(143) (first configuration). We observe that a structure is detectable in these spaces. The same is true in the spaces $(x_{n+1}, x_n, x_{n-\tau_2})$ and $(x_n, x_{n-\tau_2})$. This explains why, in the case of the first configuration of multiple-delay systems considered in section 5.3.1, it is possible to identify the delays using techniques such as the mutual information and local linear fits of the form (140), which have been devised for single-delay systems.

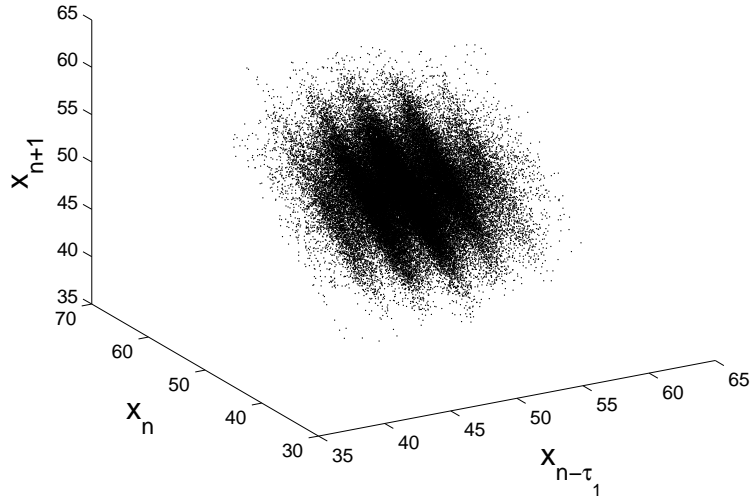


Figure 109: Representation of the system described by Eq. (143) in the space $(x_{n+1}, x_n, x_{n-\tau_1})$. The parameters are $\beta_1 = \beta_2 = 25$, $\tau_1 = 500 \mu s$, $\tau_2 = 385 \mu s$, $\tau^R = 5 \mu s$, $\phi = 0.74\pi$. The sampling time is $h=0.25 \mu s$.

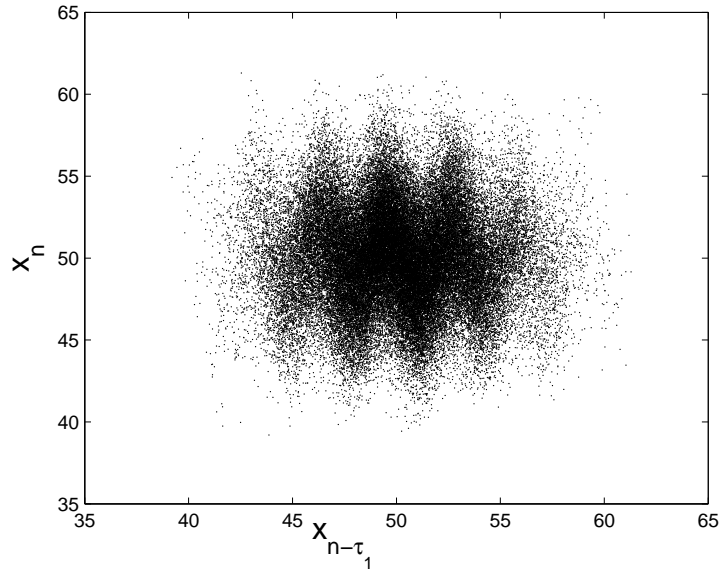


Figure 110: Representation of the system described by Eq. (143) in the plane $(x_n, x_{n-\tau_1})$. The parameters are $\beta_1 = \beta_2 = 25$, $\tau_1 = 500 \mu s$, $\tau_2 = 385 \mu s$, $\tau^R = 5 \mu s$, $\phi = 0.74\pi$. The sampling time is $h=0.25 \mu s$.

Figures. 111 and 112 represent the projection of a trajectory on the spaces $(x_{n+1}, x_n, x_{n-\tau_1})$ and $(x_{n+1}, x_n, x_{n-\tau_2})$, respectively⁴, in the case of the system subjected to two delayed feedbacks described by Eq.(147). We observe that no structure can be seen in these spaces, even though the sampling period is very small. The same is true in the spaces $(x_{n+1}, x_n, x_{n-\tau_2})$ and $(x_{n+1}, x_n, x_{n-\tau_1})$. Decreasing even further the sampling period does not help. This is why in the case of the first configuration of multiple-delay systems considered in section 5.3.1, it is impossible to identify the delays using techniques such as the mutual information and local linear fits of the form (140).

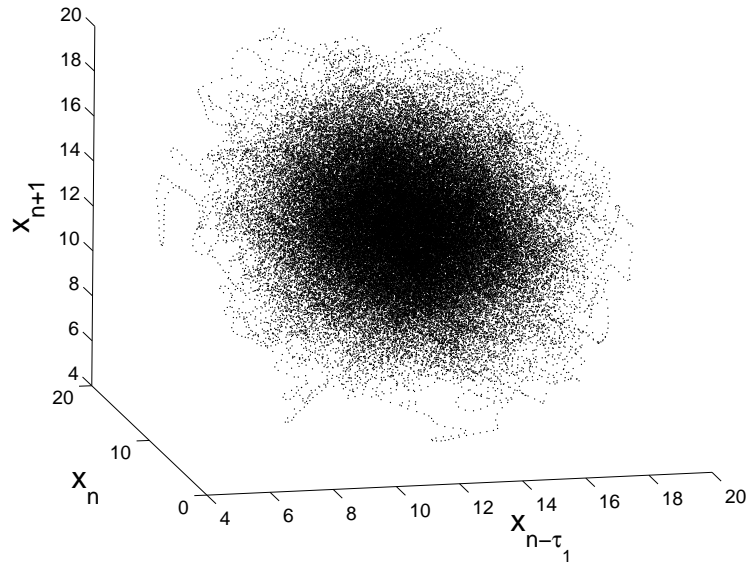


Figure 111: Representation of the system described by Eq. (147) in the space $(x_{n+1}, x_n, x_{n-\tau_1})$. The parameters are $\beta = 25$, $\tau_1 = 500 \mu s$, $\tau_2 = 385 \mu s$, $\tau^R = 5 \mu s$, $\phi = 0.74\pi$. The sampling time is $h=0.1 \mu s$.

The fact that decreasing the sampling period does not help identify the delays means that the reason why the identification fails is not a bad discretization of the continuous-time system. The reason is that the identification is not being performed in the correct space. In the case of Eq. (147), the dynamics is such that no structure can be revealed in the subspace $(x_{n+1}, x_n, x_{n-\tau_i})$, contrary to Eq. (143). It is therefore necessary, in this

⁴We have chosen to observe the projection of the attractor in the plane $(x_{n+1}, x_{n-\tau})$ instead of in $(x_n, x_{n-\tau})$, because it is usually easier to identify a structure (if it is present), in the former plane than in the latter one.

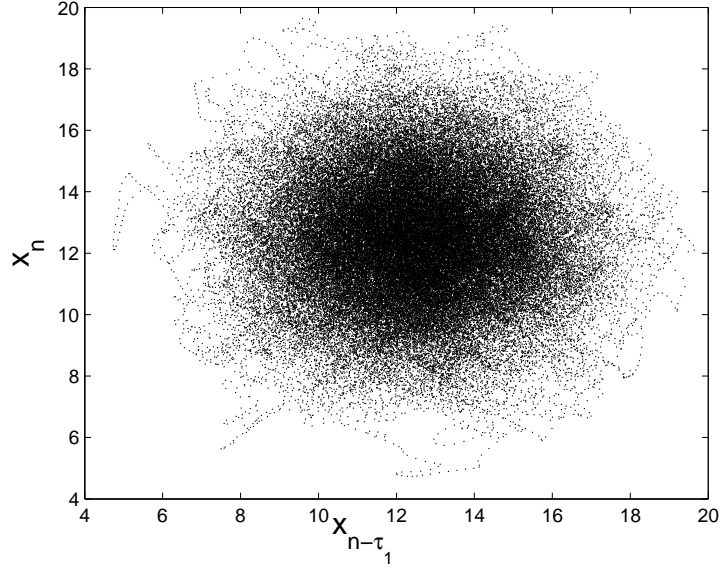


Figure 112: Representation of the system described by Eq. (147) in the plane $(x_{n+1}, x_{n-\tau_1})$. The parameters are $\beta = 25$, $\tau_1 = 500 \mu s$, $\tau_2 = 385 \mu s$, $\tau^R = 5 \mu s$, $\phi = 0.74\pi$. The sampling time is $h=0.1 \mu s$.

case, to work in the “full” space $(x_{n+1}, x_n, x_{n-\tau_1}, x_{n-\tau_2})$, in which Eq. (147) defines a constraint if the discretization is good enough. It is not possible to represent graphically the structure described in this four-dimensional space, but we find that its projection onto the three-dimensional space $(x_{n+1}, x_{n-\tau_1}, x_{n-\tau_2})$ also leads to an identifiable structure, which is represented in Fig 113.

On the basis of the previous observations, we can conclude that it is necessary to work in the space $(x_{n+1}, x_n, x_{n-\tau_1}, x_{n-\tau_2})$, or in the space $(x_{n+1}, x_{n-\tau_1}, x_{n-\tau_2})$, to identify the delay values.

We propose to generalize the technique of local linear models to the case of systems with two delays, by working in the space $(x_{n+1}, x_n, x_{n-\tau_1^*}, x_{n-\tau_2^*})$. In this space, the following local linear approximations can be performed:

$$x_{n+1} = a_n + b_n x_n + c_n x_{n-\tau_1^*} + d_n x_{n-\tau_2^*}, \quad (148)$$

where a_n , b_n , c_n , and d_n are the coefficients of the local approximations, and τ_1^* , τ_2^* are arbitrary delay values. We expect that a minimization of the average fitting error, of the entire time series considered, as a function of the two variables τ_1^* and τ_2^* , should lead to

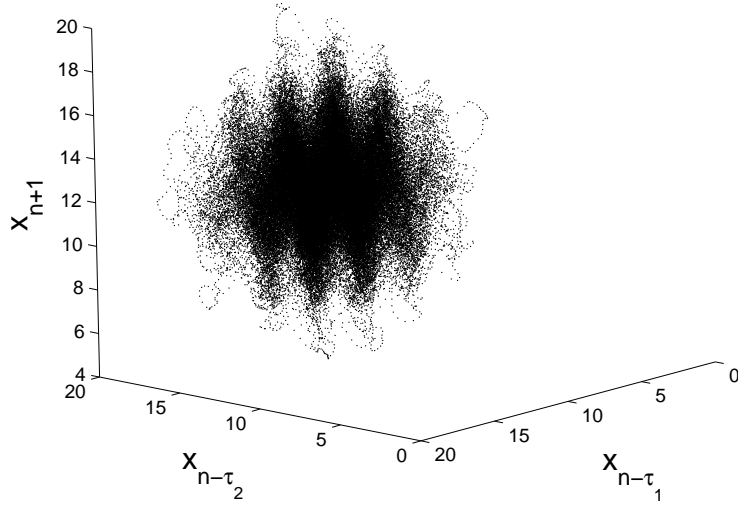


Figure 113: Representation of the system described by Eq. (147) in the space $(x_{n+1}, x_{n-\tau_1}, x_{n-\tau_2})$. The parameters are $\beta = 25$, $\tau_1 = 500 \mu s$, $\tau_2 = 385 \mu s$, $\tau^R = 5 \mu s$, $\phi = 0.74\pi$. The sampling time is $h=0.1 \mu s$.

an identification of the two delays, if the discretization is sufficiently fine. It is also possible to generalize the global nonlinear model (138) by adding a series of variables to take into account the second delay. This model takes the form

$$x_{n+1} = M_{NL}(x_n, x_{n-1}, x_{n-\tau_1^*}, x_{n-\tau_2^*}). \quad (149)$$

The nonlinear function M_{NL} can be realized, for example, using a neural network divided in three modules, one for the non-feedback part, and one for each feedback.

Figure 114 represents the average approximation error of a series of local linear fits of the form (148), in a rectangular area of values of τ_1^* and τ_2^* , for a strong feedback strength ($\beta = 15$). We observe a steep valley in the approximation error around the correct values of the delays. This valley corresponds to the detection of the presence of a 3-dimensional manifold in the four-dimensional space $(x_{n+1}, x_n, x_{n-\tau_1}, x_{n-\tau_2})$. This is because the local linear approximations (148) define hyperplanes tangent to the manifold, and these approximations only make sense if an underlying manifold exists, *i.e.* if the correct delay values are used.

We can therefore identify the two delays from a time series produced by the system

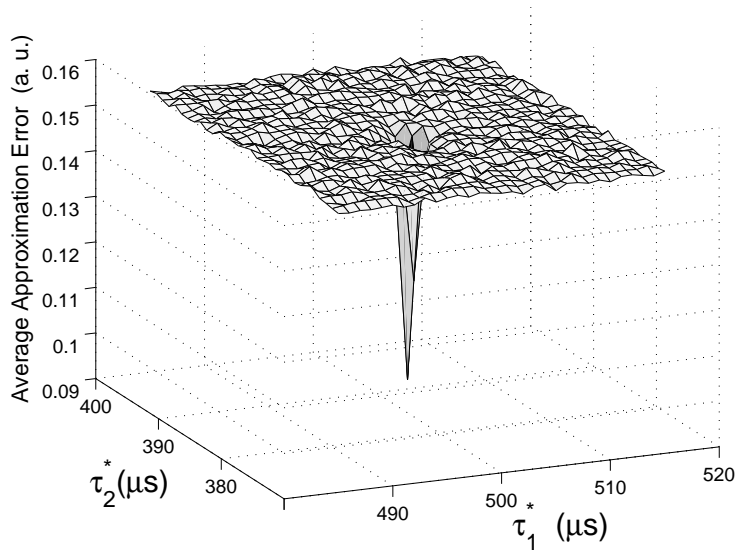


Figure 114: Approximation error as a function of the two unknown delay values τ_1^* , and τ_2^* , in the case of the system with two feedback loops given by Eq. (147). The parameters are $\beta = 15$, $\tau_1 = 500 \mu s$, $\tau_2 = 385 \mu s$, $\tau^R = 5 \mu s$, $\phi = 0.74\pi$.

described by Eq. (147), with no overestimation. These results hold even for very large values of the feedback strength, when the difference between the values of the delays is varied, and if a band-pass filter is used in place of the low-pass filter⁵.

It should be noted, however, that the computation time is much larger than when local linear approximations with a single delay [of the form given by Eq. (140)] are used. This is the mechanical consequence of the fact that the two delay values are searched for in an area, instead of in an interval. Since for given values of the delays, the approximations (140) and (148) necessitate similar computation times, if it takes a time T to compute the approximation error in an interval of values of τ^* of length L , it will take a time T^2 , approximately, to compute the approximation error in a region of values of τ_1^* and τ_2^* of area L^2 .

We also notice that the width of the valleys in the approximation error decreases with increasing feedback strength β . Figures 115, 116, and 117 represent the average approximation error for feedback strengths β of 5, 10, and 25, respectively. Similarly to the case

⁵leading to an integro-differential equation with two delays.

of single-delay systems, the decrease in the width of the valleys observed in these figures is due to the rapid decrease of the link existing between $x(t)$ and $x(t+h)$, for increasing β . For large values of β (for example $\beta = 25$), the valley is extremely thin, which means that an eavesdropper which tests values of the delays close to the correct ones, will have no indication of the fact that he is close to the correct values. Therefore, he will have to perform a systematic “blind” search for the correct delay values. While for lower feedback strengths, larger valleys mean that an eavesdropper knows when he is close to the delay values. In this sense, we can consider that increasing the feedback strength β leads to an increase of the security, because the computation time to identify the delays will be greater, on average.

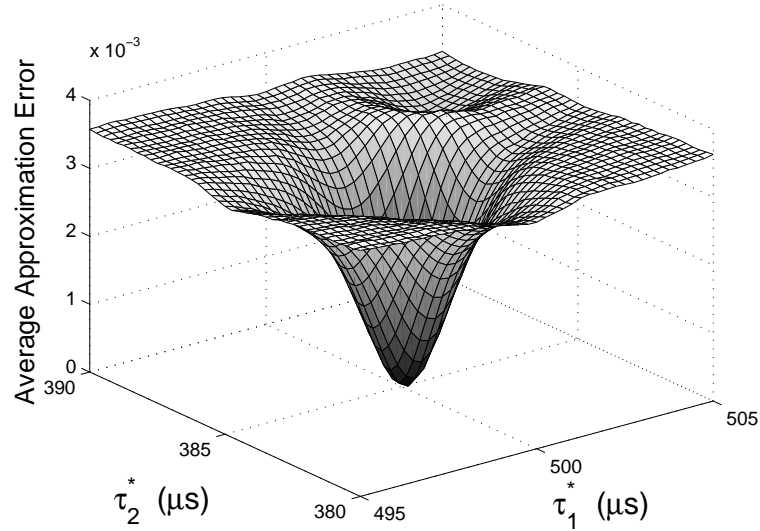


Figure 115: Approximation error as a function of the two unknown delay values τ_1^* , and τ_2^* , in the case of the system with two feedback loops given by Eq. (147), for a feedback strength $\beta = 5$. The other parameters are $\tau_1 = 500 \mu s$, $\tau_2 = 385 \mu s$, $\tau^R = 5 \mu s$, $\phi = 0.74\pi$.

Finally, we mention that preliminary results show that the approximation error of a global nonlinear model of the form given by Eq. (149) leads to similar results. We are confident that it should also be possible to identify the delays using information theoretic concepts, adapted to the presence of a second delay.

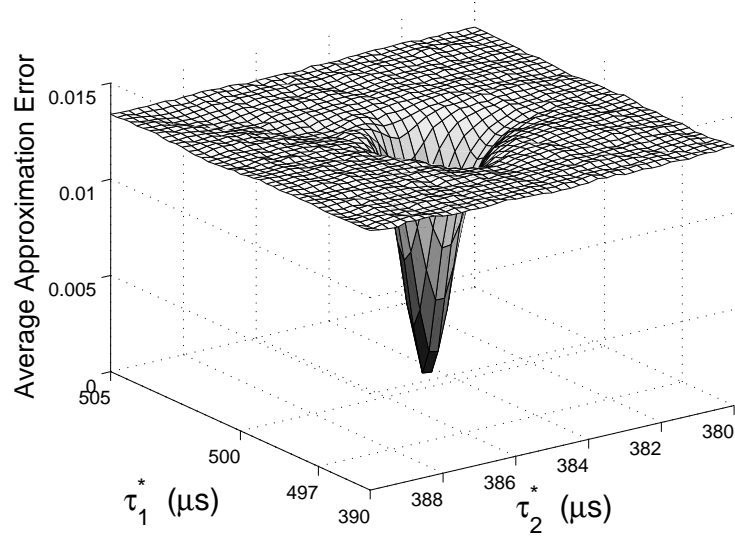


Figure 116: Approximation error as a function of the two unknown delay values τ_1^* , and τ_2^* , in the case of the system with two feedback loops given by Eq. (147), for a feedback strength $\beta = 10$. The other parameters are $\tau_1 = 500 \mu\text{s}$, $\tau_2 = 385 \mu\text{s}$, $\tau^R = 5 \mu\text{s}$, $\phi = 0.74\pi$.

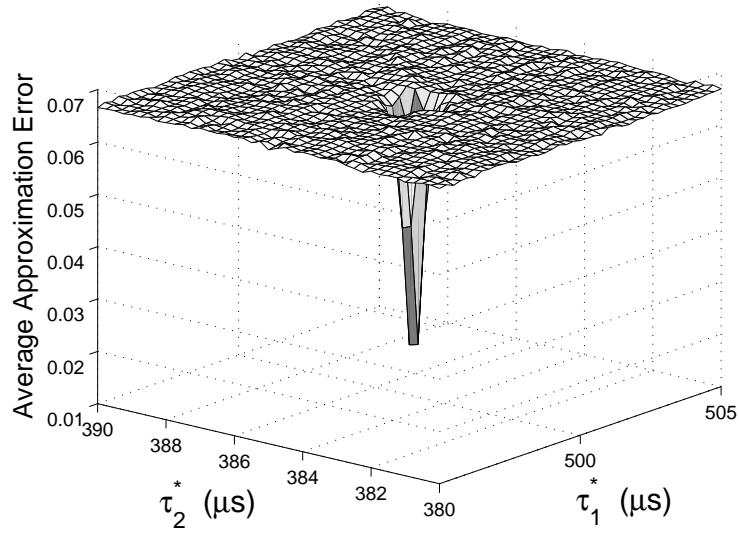


Figure 117: Approximation error as a function of the two unknown delay values τ_1^* , and τ_2^* , in the case of the system with two feedback loops given by Eq. (147), for a feedback strength $\beta = 25$. The other parameters are $\tau_1 = 500 \mu\text{s}$, $\tau_2 = 385 \mu\text{s}$, $\tau^R = 5 \mu\text{s}$, $\phi = 0.74\pi$.

5.4 *Conclusion and perspectives*

Cryptosystems with a single delayed feedback loop do not appear to be secure because several techniques exist to identify the value of the delay. Once the delay is known, the cryptosystem can usually be broken. Cryptosystems that use several delayed feedback loops have been suggested to be more secure. We have examined three different types of chaotic cryptosystems subjected to two delayed feedbacks. We have shown that in the case of the generalization of the generator of wavelength chaos in which a nonlinear function is applied to each delayed term separately, and in the case of a semiconductor laser subjected to two optical feedbacks, it is possible to identify the delays using the same techniques that work for single-delay systems. In the case of the generalization of the generator of wavelength chaos in which a nonlinear function is applied to the sum of the delayed terms, however, these techniques fail. We have proposed some adapted techniques that have enabled us to identify this latter type of system too. An eavesdropper will have more difficulty in identifying the delays, however, since these adapted techniques involve longer computation times. Additionally, we have found that it is interesting to use strong feedbacks, since this makes the identification of the delays more difficult. Finally, we mention that adaptations of the identification techniques, performed in the spirit of the work presented here, should lead to the identification of the three delays of the cryptosystem recently proposed in Ref. [152].

Preliminary results show that when two different, and suitably chosen, filtering elements are used in two delayed feedback loops, only one of the delays can be identified, even when the specific techniques for systems with two delays are used. This type of configuration could be interesting for cryptographic purposes. Another way to hide the delay value of a chaotic cryptosystem is to modulate it at the emitter. It has been shown [161, 162] that, under certain circumstances, the modulation makes the identification of the delay impossible with standard techniques, while it is still possible to synchronize the receiver and decode the message. Using the techniques described in this chapter, we have been unable so far to identify the delay in this kind of system, and it would be particularly interesting to determine some techniques to do so.

CHAPTER VI

CONCLUSION

This work was devoted to the numerical study of several topics lying in the field of chaotic communications.

In chapter 3, we have studied numerically the synchronization of two unidirectionally coupled single-mode chaotic edge-emitting semiconductor lasers based on a Lang-Kobayashi-type model. The master laser is an external-cavity laser, while for the slave laser we considered two configurations: an external-cavity slave laser (closed-loop scheme), and a laser subjected only to optical injection from the master laser (open-loop scheme). Depending on the operating conditions two different types of synchronization are found: synchronization with a lag-time τ_c , which corresponds to the synchronization of the slave optical field with the injected field (isochronous synchronization), and synchronization with a lag-time $\tau_c - \tau$ (anticipating synchronization).

We have shown that chaotic synchronization with a lag-time τ_c occurs in a similar parameter region to the one in which stable CW injection-locking occurs. This form of synchronization is much more robust than the anticipated synchronization, which occurs in a much narrower parameter region. Therefore it should be easier to implement in a real chaotic communications scheme. We have also observed that the synchronization quality is usually better in the closed-loop scheme than in the open-loop scheme; when the slave laser is an external-cavity laser, however, the external mirror has to be carefully positioned, since small differences in the delay times strongly degrade the synchronization quality.

We have analyzed the synchronization regions in the parameter space (master feedback rate, injection rate), finding that an increase of the master feedback rate requires an increase of the injection rate in order to obtain a good synchronization. In the case of the closed-loop scheme, very good synchronization can occur even for a large value of γ_m , while in the case of an open-loop scheme the chaotic intensity produced by large feedback levels is difficult

to synchronize with feasible injection levels.

Finally, we have studied the transitions between the two synchronization regimes for an open-loop scheme, extending the results reported in Ref. [96]. We have shown that it is only for injection currents close to threshold, that small parameter variations can lead to transitions between the different synchronization regimes, because the synchronization regions are close to each other in parameter space. On the contrary, for large injection currents, transitions are not possible, since the two types of synchronization occur for very different coupling strengths. We have also shown that not all parameter variations lead to a transition from one synchronization regime to the other, but only the parameter variations that increase the ratio between the injected power and the solitary slave laser output power. When a parameter variation decreases this ratio, a transition to the other synchronization regime does not occur, and the synchronization is lost.

The existence of two synchronization regimes has now been proved experimentally [103] and is widely accepted.

We have also studied, in chapter 3, the synchronization of external-cavity vertical-cavity surface-emitting lasers on the basis of the spin-flip model. We have considered a master laser subjected to isotropic optical feedback, while different types of optical injection in the slave have been studied.

In the case of isotropic injection, we observe regimes of anticipating and isochronous synchronization of the two linearly-polarized components of the electric field. The characteristics of these synchronization regimes are similar to the characteristics of the anticipating and isochronous regimes identified in edge-emitting lasers.

The optical injection of only one of the linearly-polarized components of the electric field clearly favors the corresponding component at the slave laser. For sufficiently large injection levels, the component parallel to the injection synchronizes isochronously with the injected field. If this component is inactive at the slave laser, the polarized optical injection activates it, and if the orthogonal component is active, the optical injection kills it. In the case of orthogonal injection, and for intermediate injection levels, the two linearly-polarized components of the slave electric field can be active contemporaneously, and antiphase dynamics

between the two components is often observed. In this case, the component parallel to the direction of the polarized injection tends to synchronize with the injected field, while the other component experiences antisynchronization with the injected field. The component of the electric field perpendicular to the injection is usually killed, however, before good synchronization (and antisynchronization) occurs. We are confident that some modifications of the operating conditions, and especially the inclusion of frequency detuning between the lasers, should lead to the observation of good synchronization and antisynchronization, consistently with the experimental results of Hong *et al.* [106, 107].

Finally, preliminary results indicate that it should be possible to realize chaotic communications, between external-cavity VCSELs, in which the information-bearing signal is coded on the polarization state of the master laser.

In chapter 4, we have used specific techniques for delay systems, based on local linear models of the dynamics, to analyze experimental and numerically-generated time series of different chaotic delay systems.

We have shown that the identification of the delay is possible for systems that can be modeled by a scalar delay-differential equation (Mackey-Glass system, optoelectronic generator of wavelength chaos, and electronic system producing frequency chaos, when a low-pass filter is used), as well as for vectorial systems modeled by an integro-differential delay equation (electronic generator of frequency chaos using a band-pass filter, optoelectronic system producing chaos in intensity). We have observed that, contrary to the identification techniques based on autocorrelation and mutual information, the technique based on local linear approximations leads to the exact (non-overestimated) delay value. We have also found that this technique is very robust. In particular, we have observed that the identification is possible for a large range of values of the internal parameters of the identification procedure, and in presence of an information-bearing signal. It has also been possible to estimate, from time series, the nonlinear function of the Mackey-Glass system and of the generator of wavelength chaos.

Finally, we have estimated the Lyapunov spectrum, the chaos dimension, and entropy, from numerically-generated time series of a Mackey-Glass system, and from experimental

time series produced by the generator of wavelength chaos. In both case, we have compared the spectrum estimated from time series with the spectrum estimated from the dynamical model. In the case of the Mackey-Glass system, we have observed a very good correspondence between the two spectra. We have verified that the dimension increases linearly with the delay, while the entropy is independent of the value of the delay. In the case of wavelength chaos, the computation of the spectrum from the dynamical model shows that the dimension increases linearly with the delay and the feedback strength, while the entropy also increases linearly with the feedback strength, but does not increase with the delay. The estimation of the Lyapunov spectrum from experimental time series has proved to be more problematic. We have not been able to find a satisfactory agreement between the spectrum calculated from the time series and from the model. We believe the discrepancy is due to the presence of noise in the time series, and to the concomitant fact that we try to estimate the spectrum of a very hyperchaotic system, whose nonlinear function has many active extrema. We have nevertheless been able to confirm that the dimension and entropy tend to vary linearly with the feedback strength.

Cryptosystems with a single delayed feedback loop do not appear to be secure because several techniques exist to identify the value of the delay. Once the delay is known, the cryptosystem can usually be broken. Cryptosystems that use several delayed feedback loops have been suggested to be more secure. We have examined three different types of chaotic cryptosystems subjected to two delayed feedbacks. We have shown that in the case of the generalization of the generator of wavelength chaos in which a nonlinear function is applied to each delayed term separately, and in the case of a semiconductor laser subjected to two optical feedbacks, it is possible to identify the delays using the same techniques that work for single-delay systems. In the case of the generalization of the generator of wavelength chaos in which a nonlinear function is applied to the sum of the delayed terms, however, these techniques fail. We have proposed some adapted techniques that have enabled us to identify this latter type of system too. An eavesdropper will have a harder time identifying the delays, however, since these adapted techniques involve longer computation times. Additionally, we have found that it is interesting to use strong feedbacks, since this makes

the identification of the delays more difficult. Finally, we mention that adaptations of the identification techniques, performed in the spirit of the work done here, should lead to the identification of the three delays of the cryptosystem recently proposed in Ref. [152].

Preliminary results show that when two different, and suitably chosen, filtering elements are used in two delayed feedback loops, only one of the delays can be identified, even when the specific techniques for systems with two delays are used. This type of configuration could be interesting for cryptographic purposes. Another way to hide the delay value of a chaotic cryptosystem is to modulate it at the emitter. It has been shown [161, 162] that, under certain circumstances, the modulation makes the identification of the delay impossible with standard techniques, while it is still possible to synchronize the receiver and decode the message. Using the techniques described in this chapter, we have been unable so far to identify the delay in this kind of system, and it would be particularly interesting to determine some techniques to do so.

APPENDIX A

NEIGHBOR SEARCHING TECHNIQUES

The problem of neighbor searching often arises when the time series analyst tries to determine some local properties in the phase space of a system, or in a projection of this phase space¹. For example, noise reduction, local prediction, and the estimation of the Lyapunov spectrum require to work in the neighborhood of a state. During the thesis, it has been necessary to search for neighbors to model locally a chaotic delay system (section 4.2).

This appendix is devoted mainly to present the simple and efficient technique we have used to find the neighbors of an element of a k -dimensional space. A detailed description of the different methods to search for neighbors can be found in Refs. [163, 31].

Assuming that we have a set of N vectors x_n in a k -dimensional space, the aim of a neighbor searching method is to determine, for each x_n , the set of all the vectors x_m , that are inside the ball centered in x_n and of radius ϵ (ϵ is the neighborhood size). Equivalently, it is necessary to determine the set of indices

$$\mathcal{U}_n(\epsilon) = \left\{ m \mid \|x_m - x_n\|_p < \epsilon \right\} , \quad (150)$$

where $\|\cdots\|_p$ is the L_p norm.²

The simplest way to find the neighbors of a set of N points is to compute the $N^2/2$ distances between all the pairs of points. Though simple, this method is often impractical because of the large computation times involved when the number of points is important. More efficient techniques must be used. Box-assisted methods provide a substantial gain in computation time and are at the same time easy to implement. In the remainder of this appendix, we present the principles of box-assisted methods.

¹This latter case makes reference to the specific analysis techniques for delay systems.

²The L_p norm of a vector x_n is defined by $\|x_n\|_p = \left(\sum_{i=1}^k |x_{n,i}|^p \right)^{1/p}$, where $x_{n,i}$ represents a component of the vector x_n . The special case $p = 2$ corresponds to the standard Euclidean norm.

In a box-assisted method, the k -dimensional space is divided into a grid of boxes (or hypercubes) of side length ϵ , and all the vectors are placed in one of the boxes. The search for neighbors of a vector is thus limited to the hypercube that contains this vector and to the adjacent hypercubes³. When implementing the method, it is important to be able to place the vectors in the boxes without wasting memory. In particular, since each box contains a different number of vectors, it is important to allocate the correct memory size to each box. The elements of every box will be contained in a N -dimensional vector POINTS. An

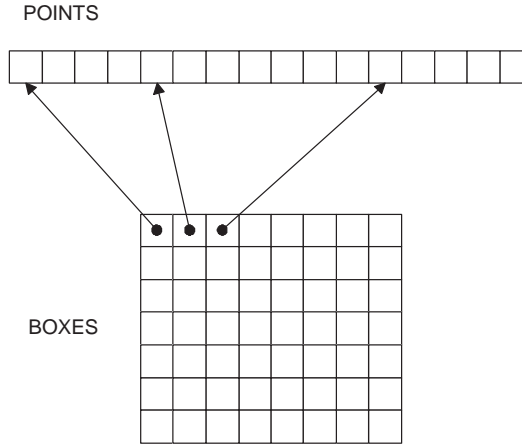


Figure 118: Matrix BOXES and vector POINTS.

analysis of the set of N vectors tells us how many vectors fall in each box. The information on the number of elements of each box enables us to divide POINTS in such a way that to each box is associated a contiguous section of memory, whose size is exactly that needed to contain all the vectors of the box. Moreover, to minimize the memory required by the algorithm, the space of dimension k is divided in boxes of dimension *two*, whatever the value of k is. This means that we work on a projection of the k -dimensional space on a plane, and subsequently extract the neighbors in dimension k among the neighbors in dimension two. The vector POINTS is represented in Fig. 118. It contains the indices of the vectors that lie in the boxes. The indices of vectors that are in the same box follow each other in POINTS. The matrix BOXES, represented in Fig. 118, is used to determine the location

³This reasoning is valid for any type of norm. We have chosen arbitrarily to use the Euclidean norm ($p = 2$).

of the boxes in the vector POINTS. Each element of this matrix corresponds to a box, and points toward the section of POINTS that contains the indices of the vectors of that box. Before beginning to look for neighbors, it is necessary to determine the matrix BOXES by counting the number of vectors that fall into each box. The vector POINTS is then filled using the information contained in BOXES.

When it is necessary to look for the neighbors of a vector, the first thing to do is to determine the box in which it lies, i.e. the element of BOXES that points towards this box. The indices of the neighbors are then found in the vector POINTS, at the position determined by BOXES. This box-assisted technique leads to a significant decrease of the computation time.

REFERENCES

- [1] E. N. Lorenz, “Deterministic nonperiodic flow,” *J. Atmos. Sci.*, vol. 20, pp. 130–141, 1963.
- [2] T. Li and J. A. Yorke, “Period three implies chaos,” *Amer. Math. Monthly*, vol. 82, pp. 985–992, 1975.
- [3] F. P. Romeiras and E. Ott, “Strange nonchaotic attractors of the damped pendulum with quasiperiodic forcing,” *Phys. Rev. A*, vol. 35, pp. 4404–4413, 1987.
- [4] K. T. Alligood, T. D. Sauer, and J. A. Yorke, *CHAOS An introduction to dynamical systems*. Textbooks in mathematical sciences, Springer, 1996.
- [5] M. J. Feigenbaum, “Quantitative universality for a class of a class of nonlinear transformations,” *J. Statist. Phys.*, vol. 19, pp. 25–52, 1978.
- [6] K. Pyragas, “Continuous control of chaos by self-controlling feedback,” *Phys. Lett. A*, vol. 170, pp. 421–428, 1992.
- [7] S. Bielawski, D. Derozier, and P. Glorieux, “Controlling unstable periodic orbits by a delayed continuous feedback,” *Phys. Rev. E*, vol. 49, pp. 971–974, 1994.
- [8] M. C. Mackey and L. Glass, “Oscillations and chaos in physiological control systems,” *Science*, vol. 197, no. 287, pp. 287–289, 1977.
- [9] F. T. Arecchi, G. L. Lippi, G. P. Puccioni, and J. R. Tredicce, “Deterministic chaos in lasers with injected signal,” *Opt. Commun.*, vol. 51, pp. 308–314, 1984.
- [10] F. T. Arecchi, R. Meucci, G. P. Puccioni, and J. R. Tredicce, “Experimental evidence of subharmonic bifurcations, multistability and turbulence in a q-switched gas laser,” *Phys. Rev. Lett.*, vol. 49, pp. 1217–1220, 1982.
- [11] H. G. Winful, Y. C. Chen, and J.-M. Liu, “Frequency locking, quasiperiodicity and chaos in a modulated self-pulsing semiconductor laser,” *Appl. Phys. Lett.*, vol. 48, pp. 616–618, 1985.
- [12] J. Sacher, D. Baums, P. Pankin, W. Elsasser, and E. O. Gobel, “Intensity instabilities of semiconductor laser under current modulation, external light injection, and delayed feedback,” *Phys. Rev. A*, vol. 45, pp. 1893–1905, 1992.
- [13] G. Giacomelli, M. Calzavara, and F. T. Arecchi, “Instabilities in a semiconductor laser with delayed optoelectronic feedback,” *Opt. Commun.*, vol. 74, 1989.
- [14] N. A. Loiko and A. M. Samson, “Possible regimes of generation of a semiconductor laser with a delayed optoelectronic feedback,” *Opt. Commun.*, vol. 93, 1992.
- [15] S. Tang and J. M. Liu, “Chaotic pulsing and quasi-periodic route to chaos in a semiconductor laser with delayed opto-electronic feedback,” *IEEE J. Quantum Electron.*, vol. 37, no. 3, pp. 329–336, 2001.

- [16] J.-L. Chern, K. Otsuka, and F. Ishiyama, "Coexistence of two attractors in lasers with incoherent optical delayed feedback," *Opt. Commun.*, vol. 93, p. 259, 1993.
- [17] F. Rogister, A. Locquet, D. Pieroux, and M. Sciamanna, "Secure communication scheme using chaotic laser diodes subject to incoherent optical feedback and incoherent optical injection," *Optics Letters*, vol. 26, no. 19, pp. 1486–1488, 2001.
- [18] D. Sukow, K. Blackburn, A. R. Spain, K. Babcock, J. Bennet, and A. Gavrielides, "Experimental synchronization of chaos in diode lasers with polarization-rotated feedback and injection," *Opt. Lett.*, vol. 29, no. 20, pp. 2393–2395, 2004.
- [19] D. W. Sukow, A. Gavrielides, T. Erneux, M. Baracco, Z. A. Parmenter, and K. Blackburn, "Two-field description of chaos synchronization in diode lasers with incoherent optical feedback and injection," *to appear in Phys. Rev. A*, 2005.
- [20] K. Green, B. Krauskopf, and K. Engelborghs, "Bistability and torus break-up in a semiconductor laser with phase-conjugate feedback," *Physica D*, vol. 173, pp. 114–129, 2002.
- [21] A. Locquet, F. Rogister, M. Sciamanna, P. Megret, and M. Blondel, "Synchronization of chaotic semiconductor lasers with phase-conjugate feedback," in *Proceedings of the CLEO/Pacific Rim 2001 conference on lasers and electro-optics*, pp. II–388, 2001.
- [22] L. Larger, J. Goedgebuer, and J. Merolla, "Chaotic oscillator in wavelength : A new setup for investigating differential difference equations describing nonlinear dynamics," *IEEE J. Quantum Electron.*, vol. 34, no. 4, pp. 594–601, 1998.
- [23] J. Goedgebuer, L. Larger, H. Porte, and F. Delorme, "Chaos in wavelength with a feedback tunable laser diode," *Physical Review E*, vol. 57, no. 3, pp. 2795–2798, 1998.
- [24] J.-P. Goedgebuer, P. Levy, L. Larger, C. Chang, and W. T. Rhodes, "Optical communication with synchronized hyperchaos generated electrooptically," *IEEE J. Quantum Electron.*, vol. 38, pp. 1178–1183, 2002.
- [25] N. Gastaud, S. Poinot, L. Larger, J.-M. Merolla, M. Hanna, J.-P. Goedgeuer, and F. Malassenet, "Electro-optical chaos for multi-gbit/s optical transmissions," *Electron. Lett.*, vol. 40, pp. 898–899, 2004.
- [26] E. Genin, L. larger, J.-P. Goedgebuer, M. Lee, R. Ferriere, and X. Bavard, "Chaotic oscillations of the optical phase for multigigahertz-bandwidth secure communications," *IEEE J. Quantum Electron.*, vol. 40, pp. 294–298, 2004.
- [27] L. Larger, M. W. Lee, J.-P. Goedgebuer, W. Elflein, and T. Erneux, "Chaos in coherence modulation: bifurcations of an oscillator generating optical delay fluctuations," *J. Opt. Soc. Am. B*, vol. 18, pp. 1063–1068, 2001.
- [28] M. W. Lee, L. Larger, and J.-P. Goedgebuer, "Transmission system using chaotic delays between lightwaves," *IEEE J. Quantum Electron.*, vol. 39, pp. 931–935, 2003.
- [29] L. Larger, *Cryptage de signaux par chaos en longueur d'onde*. PhD thesis, U.F.R des Sciences et Techniques de l'Université de Franche-Comté, 1997.

- [30] J.-B. Cuenot, *Système optoelectronique de communication sécurisée par chaos en longueur d'onde*. PhD thesis, U.F.R des Sciences et Techniques de l'Université de Franche-Comté, 2002.
- [31] H. Kantz and T. Schreiber, *Nonlinear Time Series Analysis*. Cambridge University Press, 1996.
- [32] P. Manneville, "Systèmes dynamiques et chaos," 1998. cours de DEA.
- [33] V. I. Oseledec, "A multiplicative ergodic theorem. lyapunov characteristic exponents for dynamical systems.," *Trans. Moscow Math. Soc.*, vol. 19, pp. 197–230, 1968.
- [34] G. Benettin, L. Galgani, A. Giorgilli, and J. M. Strelcyn, "Lyapunov characteristic exponents for smooth dynamical systems and for hamiltonian systems; a method for computing all of them. part 1: theory," *Meccanica*, pp. 9–20, 1980.
- [35] G. Benettin, L. Galgani, A. Giorgilli, and J. M. Strelcyn, "Lyapunov characteristic exponents for smooth dynamical systems and for hamiltonian systems; a method for computing all of them. part 2: numerical application," *Meccanica*, pp. 21–30, 1980.
- [36] J. Farmer, E. Ott, and J. Yorke, "The dimension of chaotic attractors," *Physica D*, vol. 7, pp. 153–180, 1983.
- [37] Y. B. Pesin, "Characteristic lyapunov exponents and smooth ergodic theory," *Russ. Math. Surveys*, vol. 32, p. 55, 1977.
- [38] D. T. Kaplan and J. Yorke, *Chaotic behavior in of multidimensional difference equations*. Springer, 1979. in Functional differential equations and approximation of fixed points.
- [39] F. Takens, *Detecting strange attractors in turbulence*, vol. 898 of *Lecture notes in mathematics*. Springer-Verlag, 1981.
- [40] M. B. Kennel, R. Brown, and H. D. I. Abarbanel, "Determining embedding dimension for phase-space reconstruction using a geometrical construction," *Phys. Rev. A*, vol. 45, p. 3403, 1992.
- [41] J. P. Eckmann and D. Ruelle, "Ergodic theory of chaos and strange attractors," *Rev. Mod. Phys.*, vol. 57, p. 617, 1985.
- [42] M. Sano and Y. Sawada, "Measurement of the lyapunov spectrum from a chaotic time series," *Phys. Rev. Lett.*, p. 1082, 1985.
- [43] J.-P. Eckmann, S. O. Kamphorst, D. Ruelle, and S. Ciliberto, "Lyapunov exponents from time series," *Phys. Rev. A*, vol. 34, pp. 4971–4979, 1986.
- [44] H. Fujisaka and T. Yamada, "Stability theory of synchronized motion in coupled-oscillator systems. ii. the mapping approach," *Prog. Theor. Phys.*, vol. 70, p. 1240, 1983.
- [45] H. Fujisaka and T. Yamada, "Stability theory of synchronized motion in coupled-oscillator systems," *Prog. Theor. Phys.*, vol. 69, p. 32, 1983.

- [46] T. Yamada and H. Fujisaka, "Stability theory of synchronized motion in coupled-oscillator systems. iii. mapping model for continuous system," *Prog. Theor. Phys.*, vol. 72, p. 885, 1984.
- [47] L. M. Pecora and T. L. Carroll, "Synchronization in chaotic systems," *Physical Review Letters*, vol. 64, no. 8, pp. 821–824, 1990.
- [48] L. M. Pecora and T. Carroll, "Driving systems with chaotic systems," *Phys. Rev. A*, vol. 44, pp. 2374–2383, 1991.
- [49] L. M. Pecora and T. Carroll, "Synchronizing chaotic circuits," *IEEE Trans. Circ. syst*, vol. 38, pp. 453–456, 1991.
- [50] N. F. Rulkov, L. S. T. M.M. Sushchik, and H. D. I. Abarbanel, "Generalized synchronization of chaos in directionally coupled chaotic systems," *Phys. Rev. E*, vol. 51, pp. 980–994, 1995.
- [51] D. Y. Tang, R. Dykstra, W. Hamilton, and N. R. Heckenberg, "Observation of generalized, predictability and equivalence of unidirectionally coupled dynamical systems," *Phys. Rev. E*, vol. 57, 1998.
- [52] K. M. Cuomo and A. V. Oppenheim, "Circuit implementation of synchronized chaos with applications to communications," *Physical Review Letters*, vol. 71, no. 1, pp. 65–68, 1993.
- [53] L. Larger, J.-P. Goedgebuer, and F. Delorme, "An optical encryption system using hyperchaos generated by an optoelectronic wavelength oscillator," *Physical Review E*, vol. 57, no. 6, pp. 6618–6624, 1998.
- [54] J. Goedgebuer, L. Larger, and H. Porte, "Optical cryptosystem based on synchronization of hyperchaos generated by a delayed feedback tunable laser diode," *Physical Review Letters*, vol. 80, no. 10, pp. 2249–2252, 1998.
- [55] S. Hayes, C. Grebogi, and E. Ott, "Communicating with chaos," *Phys. Rev. Lett.*, vol. 70, p. 3031, 1993.
- [56] S. Hayes, C. Grebogi, E. Ott, and A. Mark, "Experimental control of chaos for communication," *Phys. Rev. Lett.*, vol. 73, p. 1781, 1994.
- [57] M. S. Baptista and L. Lopez, "Information transfer in chaos-based communication," *Phys. Rev. E*, vol. 65, p. 055201, 2002.
- [58] T. Matsumoto, "A chaotic attractor from chua's circuit," *IEEE Trans. Circ. Syst.*, vol. 31, p. 1055, 1984.
- [59] L. Kocarev, K. S. Halle, K. Eckert, L. O. Chua, and U. Parlitz, "Experimental demonstration of secure communications via chaotic synchronization," *Int. J. Bifurcation and Chaos*, vol. 2, p. 709, 1992.
- [60] U. Parlitz, L. Chua, L. Kocarev, K. Halle, and A. Shang, "Transmission of digital signals by chaotic synchronization," *Int. J. Bifurcation and Chaos*, vol. 2, p. 973, 1992.
- [61] K. M. Cuomo and A. V. Oppenheim, "Synchronization of lorenz-based chaotic circuits with applications to communications," *IEEE Trans. Circ. Syst. I*, vol. 32, p. 626, 1993.

- [62] R. Roy and K. S. Thornburg, "Experimental synchronization of chaotic lasers," *Phys. Rev. Lett.*, vol. 72, p. 2009, 1994.
- [63] P. Colet and R. Roy, "Digital communications with synchronized chaotic lasers," *Opt. Lett.*, vol. 19, p. 2056, 1994.
- [64] G. VanWiggeren and R. Roy, "Communication with chaotic lasers," *Science*, vol. 279, pp. 1198–1200, 1998.
- [65] G. VanWiggeren and R. Roy, "Optical communication with chaotic waveforms," *Physical Review Letters*, vol. 81, no. 16, pp. 3547–3550, 1998.
- [66] L. G. Luo, P. L. Chu, and H. F. Liu, "1-ghz optical communication system using chaos in erbium-doped fiber laser," *IEEE Phot. Tech. Lett.*, vol. 12, p. 269, 2000.
- [67] C. Mirasso, P. Colet, and P. Garcia-Fernandez, "Synchronization of chaotic semiconductor lasers : Application to encoded communications," *IEEE Photonics Technology Letters*, vol. 8, no. 2, pp. 299–301, 1996.
- [68] S. Sivaprakasam and K. A. Shore, "Demonstration of optical synchronization of external-cavity lasers," *Opt. Lett.*, vol. 24, p. 466, 1999.
- [69] H. Fujino and J. Ohtsubo, "Experimental synchronization of chaotic oscillations in external-cavity semiconductor lasers," *Opt. Lett.*, vol. 25, p. 625, 2000.
- [70] I. Fischer, Y. Liu, and P. Davis, "Synchronization of chaotic semiconductor laser dynamics on subnanosecond time scales and its potential for chaos communication," *Physical Review A*, vol. 62, no. 011801, 2000.
- [71] J. Paul, M. W. Lee, and K. A. Shore, "3.5 ghz signal transmission in an all-optical chaotic communication scheme using 1550-nm diode lasers," *to appear in IEEE Phot. Tech. Lett.*, 2005.
- [72] A. Sanchez-Diaz, C. Mirasso, P. Colet, and P. Garcia-Fernandez, "Encoded gbit/s digital communications with synchronized chaotic semiconductor lasers," *IEEE J. Quantum Electron.*, vol. 35, no. 3, pp. 292–297, 1999.
- [73] A. Bogris, D. Kanakidis, A. Argyris, and D. Syvridis, "Performance characterization of a closed-loop chaotic communication system including fiber transmission in dispersion-shifted fibers," *IEEE J. Quantum electron.*, vol. 40, p. 1326, 2004.
- [74] S. Tang and J. M. Liu, "Message-encoding at 2.5 gbit/s through synchronization of chaotic pulsing semiconductor lasers," *Opt. Lett.*, vol. 26, p. 1843, 2001.
- [75] K. M. Short, "Unmasking a modulated chaotic communications scheme," *Int. J. Bifurc. Chaos*, vol. 6, p. 367, 1996.
- [76] K. M. Short and A. T. Parker, "Unmasking a hyperchaotic communication scheme," *Phys. Rev. E*, vol. 58, p. 1159, 1998.
- [77] L. Kocarev and U. Parlitz, "General approach for chaotic synchronization with applications to communication," *Phys. Rev. Lett.*, vol. 74, p. 957, 1995.

- [78] T. Beth, D. E. Lazic, and A. Mathias, “Cryptanalysis of cryptosystems based on remote chaos replication,” in *Lecture Notes in Computer Science*, vol. 839, pp. 318–331, Springer-Verlag, 1994.
- [79] R. Hegger, M. J. Bunner, H. Kantz, and A. Giaquinta, “Identifying and modeling delay feedback systems,” *Phys. Rev. Lett.*, vol. 81, no. 3, pp. 558–561, 1998.
- [80] C. Zhou and C. Lai, “Extracting messages masked by chaotic signals of time-delay systems,” *Physical Review E*, vol. 60, no. 1, pp. 320–323, 1999.
- [81] V. S. Udaltsov, J.-P. Goedgebuer, L. Larger, J.-B. Cuenot, P. Levy, and W. T. Rhodes, “Cracking chaos-based encryption systems ruled by nonlinear delay differential equations,” *Phys. Lett. A*, vol. 308, pp. 54–60, 2003.
- [82] G. Agrawal and N. Dutta, *Semiconductor Lasers*. Van Nostrand Reinhold, second edition ed., 1993.
- [83] R. Lang and K. Kobayashi, “External optical feedback effects on semiconductor injection laser properties,” *IEEE J. Quantum Electron.*, vol. 16, pp. 347–355, 1980.
- [84] T. Heil, I. Fischer, W. Elsasser, and A. Gavrielides, “Dynamics of semiconductor lasers subject to delayed optical feedback: the short cavity regime,” *Phys. Rev. Lett.*, vol. 87, no. 243901, 2001.
- [85] T. Heil, I. fischer, W. Elsasser, B. Krauskopf, K. Green, and A. Gavrielides, “Delay dynamics of semiconductor lasers with short external cavities: Bifurcation scenarios and mechanisms,” *Phys. Rev. E*, vol. 67, no. 066214, 2003.
- [86] C. Masoller, “Coexistence of attractors in a laser diode with optical feedback from a large external cavity,” *Phys. Rev. E*, vol. 50, p. 2569, 1994.
- [87] C. Masoller and N. B. Abraham, “Stability and dynamical properties of the coexisting attractors of an external-cavity semiconductor laser,” *Phys. Rev. A*, vol. 57, pp. 1313–1322, 1998.
- [88] G. H. M. van Tartwijk, A. M. Levine, and D. Lenstra, “Sisyphus effect in semiconductor lasers with optical feedback,” *IEEE J. Sel. Top. Quantum Electron.*, vol. 1, p. 466, 1995.
- [89] G. van Tartwijk, *Semiconductor laser dynamics with optical injection and feedback*. PhD thesis, Vrije Universiteit te Amsterdam, 1994.
- [90] W. van der Graaf, *Nonlinear dynamis of semiconductor lasers driven by external optical fields*. PhD thesis, Vrije Universiteit te Amsterdam, 1997.
- [91] A. Locquet, C. Masoller, and C. R. Mirasso, “Synchronization regimes of optical-feedback-induced chaos in unidirectionally coupled semiconductor lasers,” *Phys. Rev. E*, vol. 65, no. 056205, 2002.
- [92] S. Sivaprakasam, E. M. Shahverdiev, and K. A. Shore, “Experimental verification of the synchronization condition for chaotic external cavity diode lasers,” *Phys. Rev. E*, vol. 62, no. 5, pp. 7505–7507, 2000.

- [93] A. Locquet, F. Rogister, M. Sciamanna, P. Megret, and M. Blondel, “Two types of synchronization in unidirectionally coupled chaotic external-cavity semiconductor lasers,” *Phys. Rev. E*, vol. 64, no. 045203, 2001.
- [94] A. Locquet, C. Masoller, P. Megret, and M. Blondel, “Comparison of two types of synchronization of external-cavity semiconductor lasers,” *Opt. Lett.*, vol. 27, pp. 31–33, 2002.
- [95] A. Murakami and J. Ohtsubo, “Synchronization of feedback-induced chaos in semiconductor lasers by optical injection,” *Phys. Rev. A*, vol. 65, no. 033826, 2002.
- [96] I. V. Koryukin and P. Mandel, “Two regimes of chaos synchronization in unidirectionally coupled semiconductor lasers,” *Phys. Rev. E*, vol. 65, no. 26201, 2001.
- [97] R. Lang, “Injection locking properties of a semiconductor laser,” *IEEE J. Quantum Electron.*, vol. 18, p. 976, 1982.
- [98] J. K. White and J. V. Moloney, “Multichannel communication using an infinite dimensional spatiotemporal chaotic system,” *Phys. Rev. A*, vol. 59, pp. 2422–2426, 1999.
- [99] C. Masoller, “Anticipation in the synchronization of chaotic semiconductor lasers with optical feedback,” *Phys. Rev. Lett.*, vol. 86, pp. 2782–2785, 2001.
- [100] H. U. Voss, “Anticipating chaotic synchronization,” *Phys. Rev. E*, vol. 61, pp. 5115–5119, 2000.
- [101] J. Revuelta, C. R. Mirasso, P. Colet, and L. Pesquera, “Criteria for synchronization of coupled chaotic external-cavity semiconductor lasers,” *IEEE Photon. Technol. Lett.*, vol. 14, no. 2, pp. 141–142, 2002.
- [102] Y. Liu, H. F. Chen, J. M. Liu, P. Davis, and T. Aida, “Synchronization of optical-feedback-induced chaos in semiconductor lasers by optical injection,” *Phys. Rev. A*, vol. 63, p. 031802(R), 2001.
- [103] Y. Liu, P. Davis, Y. Takiguchi, T. Aida, S. Saito, and J.-M. Liu, “Injection locking and synchronization of periodic and chaotic signals in semiconductor lasers,” *IEEE J. Quantum Electron.*, vol. 39, pp. 269–278, 2003.
- [104] P. S. Spencer and C. R. Mirasso, “Analysis of optical chaos synchronisation in frequency detuned external cavity vcsels,” *IEEE J. Quantum Electron.*, vol. 58, p. 803, 1999.
- [105] K. Kusumoto and J. Ohtsubo, “Anticipating synchronization based on optical injection-locking in chaotic semiconductor lasers,” *IEEE J. Quantum electron.*, vol. 39, no. 12, pp. 1531–1536, 2003.
- [106] Y. Hong, M. W. Lee, P. Spencer, and K. A. Shore, “Synchronization of chaos in unidirectionally coupled vertical-cavity surface-emitting semiconductor lasers,” *Opt. Lett.*, vol. 29, no. 11, pp. 1215–1217, 2004.
- [107] M. W. Lee, Y. Hong, and K. A. Shore, “Experimental demonstration of VCSEL-based chaotic optical communications,” *IEEE Phot. Tech. Letters*, vol. 16, no. 16, pp. 2392–2394, 2004.

- [108] P. Spencer, C. R. Mirasso, P. Colet, and K. A. Shore, "Modelling of optical synchronization of chaotic external-cavity vcsels," *IEEE J. Quantum Electron.*, vol. 34, p. 1673, 1998.
- [109] S. F. Yu, P. Shum, and N. Q. Ngo, "Performance of optical chaotic communication systems using multimode vertical cavity surface emitting lasers," *Optics Commun.*, vol. 200, p. 143, 2001.
- [110] M. Torre, C. Masoller, and K. Shore, "Synchronization of unidirectionally coupled multi-transverse-mode vertical-cavity surface-emitting lasers," *J. Opt. Soc. Am. B*, vol. 21, p. 1772, 2004.
- [111] A. Scire, J. Mulet, J. Danckaert, and M. S. Miguel, "Polarization message encoding through vectorial chaos synchronization in vertical-cavity surface-emitting lasers," *Phys. Rev. Lett.*, vol. 90, no. 113901, 2003.
- [112] M. San Miguel, Q. Feng, and J. Moloney, "Light polarization dynamics in surface-emitting semiconductor lasers," *Phys. Rev. A*, vol. 52, pp. 1728–1739, 1995.
- [113] W. Chow and S. Koch, *Semiconductor-laser fundamentals—Physics of the gain material*. Springer, 1999.
- [114] C. Chang-Hasnain, J. Harbison, G. Hasnain, A. V. Lehmen, L. Florez, and N. G. Stoffel, "Dynamic polarization, and transverse mode characteristics of vertical-cavity surface-emitting lasers," *IEEE J. Quantum Electron.*, vol. 27, p. 1402, 1991.
- [115] A. J. van Doorn, M. van Exter, M. Travagnin, and J. P. Woerdman, "Polarization behavior of surface-emitting lasers in an axial magnetic field," *Opt. Commun.*, vol. 133, p. 252, 1997.
- [116] J. Martin-Regalado, F. Prati, M. S. Miguel, and N. Abraham, "Polarization properties of vertical-cavity surface-emitting lasers," *IEEE J. Quantum Electron.*, vol. 33, p. 765, 1997.
- [117] R. Azzam and N. Bashara, *Ellipsometry and polarized light*. Elsevier, 2003.
- [118] C. Masoller and N. Abraham, "Low-frequency fluctuations in vertical-cavity surface-emitting semiconductor lasers with optical feedback," *Phys. Rev. A*, vol. 59, p. 3021, 1999.
- [119] M. Sciamanna, C. Masoller, N. Abraham, F. Rogister, P. Megret, and M. Blondel, "Different regimes of low-frequency fluctuations in vertical-cavity surface emitting lasers," *J. Opt. Soc. Am. B*, vol. 20, p. 37, 2003.
- [120] Y. C. Chung and Y. H. Lee, "Spectral characteristics of vertical-cavity surface emitting lasers with external optical feedback," *IEEE Photonics Technol. Lett.*, vol. 3, p. 43, 1993.
- [121] M. Giudici, S. Balle, T. Ackemann, S. Barland, and J. Tredicce, "Polarization dynamics in vertical-cavity surface-emitting lasers with optical feedback: experiment and model," *J. Opt. Soc. Am. B*, vol. 16, p. 2114, 1999.

- [122] S. Bandyopadhyay, Y. Hong, P. Spencer, and K. A. Shore, “Experimental observation of anti-phase polarization dynamics in vcsels,” *Opt. Commun.*, vol. 202, p. 145, 2002.
- [123] J. Farmer, “Chaotic attractors of an infinite-dimensional dynamical system,” *Physica D*, vol. 4, pp. 366–393, 1982.
- [124] R. Hegger, “Estimating the lyapunov spectrum of time delay feedback systems from scalar time series,” *Physical Review E*, vol. 60, no. 2, pp. 1563–1566, 1999.
- [125] H. Kantz and E. Olbrich, “Scalar observations from a class of high-dimensional chaotic systems: limitations of the time-delay embedding,” *Chaos*, vol. 7, pp. 423–429, 1997.
- [126] H. S. Greenside, A. Wolf, J. Swift, and T. Pignataro, “Impracticality of a box-counting algorithm for calculating the dimension of strange attractors,” *Phys. Rev. A*, vol. 25, pp. 3453–3456, 1982.
- [127] M. J. Bunner, M. Popp, T. Meyer, A. Kittel, U. Rau, and J. Parisi, “Recovery of scalar time-delay systems from time series,” *Phys. Lett. A*, vol. 211, 1996.
- [128] M. J. Bunner, M. Popp, T. Meyer, A. Kittel, and J. Parisi, “Tool to recover scalar time-delay systems from experimental time series,” *Phys. Rev. E*, vol. 54, no. 4, pp. 3082–3085, 1996.
- [129] M. J. Bunner, T. Meyer, A. Kittel, and J. Parisi, “Recovery of time-evolution equation of time-delay systems from time series,” *Phys. Rev. E*, vol. 56, no. 5, pp. 5083–5089, 1997.
- [130] M. J. Bunner, M. Ciofini, A. Giaquinta, R. Hegger, H. Kantz, and A. Politi, “Reconstruction of systems with delayed feedback: I. theory,” *Eur. Phys. J. D*, vol. 10, pp. 165–176, 2000.
- [131] M. J. Bunner, M. Ciofini, A. Giaquinta, R. Hegger, H. Kantz, R. Meucci, and A. Politi, “Reconstruction of systems with delayed feedback: II. application,” *Eur. Phys. J. D*, vol. 10, pp. 177–187, 2000.
- [132] M. Casdagli, “A dynamical systems approach to modeling input-output systems,” in *Nonlinear modeling and forecasting, SFI Studies in the sciences of complexity* (M. Casdagli and S. eubank, eds.), vol. XII, pp. 265–281, Addison-Wesley, 1992.
- [133] M. W. Lee, *Etude des comportements chaotiques en modulation de coherence et application a la cryptographie*. PhD thesis, Universite de Franche-Comte, 2002.
- [134] T. M. Cover and J. A. Thomas, *Information theory*. Wiley series in telecommunications, 1991.
- [135] J. Goedgebuer, L. Larger, H. Porte, and F. Delorme, “Chaos in wavelength with a feedback tunable laser diode,” *Physical Review E*, vol. 57, no. 3, pp. 2795–2798, 1998.
- [136] V. Udaltsov, J.-P. Goedgebuer, L. Larger, and W. Rhodes, “Dynamics of non-linear feedback systems with short time-delays,” *Optics Communications*, vol. 195, pp. 187–196, 2001.

- [137] X. Bavard, *Numrisation du chaos et applications aux systemes de communication securises par chaos en longueur d'onde*. PhD thesis, U.F.R des Sciences et Techniques de l'Université de Franche-Comté, 2004.
- [138] N. Gastaud, L. Larger, F. Malassenet, J.-M. Merolla, M. Hanna, and Y. C. Kouomou, "Application de cryptage par chaos aux communications optiques multi-gigabit," in *Compte-rendu de la septieme rencontre du non-lineaire* (Y. Pomeau and R. Ribotta, eds.), pp. 109–114, 2004.
- [139] N. Gastaud, *Systeme de Communication Haut Debit Securise par Chaos en Intensite*. PhD thesis, Universite de Franche-Comte.
- [140] L. Larger, V. Udaltsov, J. Goedgebuer, and W. Rhodes, "Chaotic dynamics of oscillators based on circuits with VCO and nonlinear delayed feedback," *Electronics Letters*, vol. 36, no. 3, pp. 199–200, 2000.
- [141] L. Larger, J.-P. Goedgebuer, V. Udaltsov, and W. Rhodes, "Radio transmission system using fm high dimensional chaotic oscillator," *Electronics Letters*, vol. 37, no. 9, pp. 594–595, 2001.
- [142] V. S. Udaltsov, L. Larger, J.-P. Goedgebuer, M. W. Lee, E. Genin, and W. T. Rhodes, "Bandpass chaotic dynamics of electronic oscillator operating with delayed nonlinear feedback," *IEEE Trans. Circ. Syst. I*, vol. 49, pp. 1006–1009, 2002.
- [143] A. Pallavisini, L. Larger, V. Udaltsov, and J.-P. Goedgebuer, "Cryptage par chaos en frequence applique aux telecommunications hertziennes," in *Compte-rendu de la septieme rencontre du non-lineaire* (Y. Pomeau and R. Ribotta, eds.), pp. 227–232, 2004.
- [144] B. Dorizzi, B. Grammaticos, M. L. Berre, Y. Pomeau, E. Ressayre, and A. Tallet, "Statistics and dimension of chaos in differential delay systems," *Physical Review A*, vol. 35, no. 1, pp. 328–339, 1987.
- [145] M. L. Berre, E. Ressayre, A. Tallet, H. Gibbs, D. L. Kaplan, and M. H. Rose, "High-dimension chaotic attractors of a nonlinear ring cavity," *Physical Review Letters*, vol. 56, no. 4, pp. 274–277, 1986.
- [146] K. Ikeda, "Multiple-valued stationary state and its instability of the transmitted light by a ring cavity system," *Opt. Commun.*, vol. 30, pp. 257–261, 1979.
- [147] S. Ortin, J. Guttierrez, L. Pesquera, and H. Vasquez, "Nonlinear dynamics extraction for time-delay systems using modular neural networks synchronization and prediction," *Physica A*, vol. 351, p. 133, 2005.
- [148] S. Ortin, L. Pesquera, A. Cofino, A. Valle, and J. Gutierrez, "Extraction of nonlinear dynamics for laser diodes with feedback in chaotic regime," in *SPIE Proceedings*, vol. 5452, 2004.
- [149] V. S. Udaltsov, A. Locquet, L. Larger, J. P. Goedgebuer, and D. S. Citrin, "Time delay identification in chaotic cryptosystems ruled by delay-differential equations," *Journal of Optical Technology*, vol. 72, p. 23, 2005.

- [150] M. W. Lee, L. Larger, V. Udaltsov, E. Genin, and J.-P. Goedgebuer, "Demonstration of chaos generator with two delays," *Opt. Lett.*, vol. 29, no. 4, pp. 325–327, 2004.
- [151] M.W.Lee, P. Rees, K.A.Shore, L.Pesquera, and A. Valle, "Dynamical characterization of laser diode subject to double optical feedback for chaotic optical communications," *IEE Proc. Optoelectron.*, vol. 152, p. 97, 2005.
- [152] C.-M. Kim, W.-H. Kye, S. Rim, and S.-Y. Lee, "Communication key using delay times in time-delayed chaos synchronization," *Phys. Lett. A*, vol. 333, p. 235, 2004.
- [153] Y. Liu and J. Ohtsubo, "Dynamics and chaos stabilization of semiconductor lasers with optical feedback from an interferometer," *IEEE J. Quantum Electron.*, vol. 33, no. 7, pp. 1163–1169, 1997.
- [154] F. Rogister, P. Megret, O. Deparis, and M. Blondel, "Suppression of low-frequency fluctuations and stabilization of a semiconductor laser subjected to optical feedback from a double cavity: theoretical results," *Opt. Lett.*, vol. 24, no. 17, pp. 1218–1220, 1999.
- [155] F. Rogister, D. W. Sukow, A. Gavrielides, P. Megret, O. Deparis, and M. Blondel, "Experimental demonstration of suppression of low-frequency fluctuations and stabilization of an external-cavity laser diode," *Opt. Lett.*, vol. 25, no. 11, pp. 808–810, 2000.
- [156] I. Fischer, O. Hess, W. Elssser, and E. Gbel, "High-dimensional chaotic dynamics of an external cavity semiconductor laser," *Phys. Rev. Lett.*, vol. 73, no. 16, pp. 2188–2191, 1994.
- [157] L. Larger, V. Udaltsov, D. Nirouset, A. Locquet, A. Pallavisini, and S. Poinot, "Multiple highly nonlinear delayed feedbacks in a wavelength chaotic oscillator," in *Technical Digest of the PHASE International Workshop* (M. Sciamanna and K. Panaiotov, eds.), p. 37, 2005.
- [158] A. Locquet, V. Udaltsov, L. Larger, and J. Goedgebuer, "Time delay identification in chaotic cryptosystems ruled by delay-differential equations," in *Proc. of the Third International Conference "Basic problems of Optics"-Topical Meeting on Optoinformatics* (A. V. Pavlov, ed.), p. 11, 2004.
- [159] A. Locquet, V. Udaltsov, L. Larger, D. S. Citrin, and J.-P. Goedgebuer, "Delay time identification in chaotic cryptosystems with two delayed feedback loops," in *Technical Digest of the PHASE International Workshop* (M. Sciamanna and K. Panaiotov, eds.), p. 26, 2005.
- [160] L. L. J.-P. G. V. Udaltsov, A. Locquet and D. Citrin, "Some aspects of security of chaos-based communications," in *invited presentation at the International Topical Meeting on Optoinformatics, Saint Petersburg*, October 2005.
- [161] W.-H. Kye, M. Choi, S. Rim, M. Kurdoglyan, and C.-M. Kim, "Characteristics of a delayed system with time-dependent delay time," *Phys. Rev. E*, vol. 69, p. 055202, 2004.

- [162] W.-H. Kye, M. Choi, M.-W. Kim, S.-Y. Lee, S. Rim, C.-M. Kim, and Y.-J. Park, “Synchronization of delayed systems in the presence of delay time modulation,” *Phys. Lett. A*, vol. 322, p. 338, 2004.
- [163] T. Schreiber, “Efficient neighbor searching in nonlinear time series analysis,” *Int. Journal Bif. Chaos*, vol. 5, p. 348, 1995.